ATMÓSFERA

Revista trimestral publicada por el
Instituto de Ciencias de la Atmósfera y Cambio Climático
de la Universidad Nacional Autónoma de México

Volumen 36
Número 1
1 de enero de 2023

CONTENTS

MÉXICO 2023

INFORMATION FOR CONTRIBUTORS

ATMOSFERA seeks contributions on theoretical, empirical and applied research in all the areas of atmospheric sciences, with emphasis on meteorology, climatology, aeronomy, physics, chemistry, and aerobiology. Interdisciplinary contributions are also accepted; especially those related with oceanography, hydrology, ecology, forestry, glaciology, agriculture, environmental pollution, and other topics related to economy and society as they are affected by climate variability and change, and atmospheric hazards.

ATMOSFERA publishes articles, short contributions and correspondence in English. The submission of a contribution to be considered an article is assumed to indicate that no similar paper, other than an abstract or preliminary report, has been or will be submitted for publication elsewhere. Short contributions should not exceed 1000 words. Correspondence is intended for discussion of papers published in the journal and should not exceed 250 words.

Manuscripts. Please submit an electronic copy of your final version of the manuscript, preferably prepared with MS Word or compatible software, through the journal's webpage at http://www.revistascca.unam.mx/atm/index.php/atm/about/submissions#onlineSubmissions. It should be formatted with wide margins, double-spacing and all pages numbered. Footnotes to the text should be avoided. When symbols in mathematical work could be in doubt, the authors should submit a list identifying typographically the symbols used. Equations will be numbered in parentheses to the right.

Title, name, address. Provide the title in full and suggest a short title for headers on odd-numbered pages. Author's name, affiliation, e-mail and present postal address will not be included in the document, but they should be captured in the "Submission Metadata" section.

Abstract. All articles shall include an abstract, both in Spanish and in English. Abstracts are not required for short contributions.

Text. The text should be divided into sections, each with a separate heading.

Acknowledgements. Brief.

Appendices. Supplementary materials and lengthy mathematical analyses, whose details are subordinate to the main theme of the paper, should normally appear in an appendix. Each appendix should have a title.

Units, abbreviations and symbols. The International System of Units (m, kg, s, K) should be used. Only standardized terms that have been generally accepted should be used. Unfamiliar abbreviations must be defined when first used. Particular care should be taken to ensure that all symbols are clearly identified. The minus sign should be –.

References. Articles should be fully documented with references in the text and a reference listing ordered alphabetically by author's names at the end of the paper. Digital object identifiers (DOIs) should be provided whenever possible for each reference. Authors are encouraged to adjust to the citation system. Examples:

Articles in journals: Hoerling M.P. and Kumar A., 2002. Atmosphere response patterns associated with tropical forcing. J. Climate 15, 2184-2203.

Chapters in books: Magaña V. and Conde C., 2003. Climate variability and climate change and their impacts on the freshwater resources in the border region: A case study for Sonora, México. In: Climate and water-transboundary challenges in the Americas (Díaz H.F. and Morehouse B.S., Eds.). Kluwer Academic Publishers, Dordrecht, 373-393.

Articles in proceedings: Gallardo L., Córdova A.M., Rojas M., Quintana J., Alcafuz R. and Ramos I., 2004. Stratosphere-troposphere exchange (STE) over Easter Island and Cerro Tololo stations in South America: analysis and simulation of an intensive sounding campaign. 8th International Global Atmospheric Chemistry Conference, Christchurch, New Zealand, September 2004.

Books: Thompson R.D., 1998. *Atmospheric processes and systems.* Routledge, New York, 194 pp.

References cited in the text should indicate, within parenthesis, the last name of each author and the year of publication. If there are more than two authors, the last name of the first author should be followed by et al. When the name forms part of the content of the article, and does not appear solely as a reference, the year of publication is parenthesized. For example:

...a weekly cycle has been observed in surface temperature (Gordon, 1994).
...Gordon (1994) has observed a weekly cycle in surface temperature.

Illustrations and tables. Vector graphics should be supplied in a vector format (eps, ps, ai, etc.) or as pdfs. Photographs should be provided as tiff or jpeg images (with at least 300 dpi); the same applies to line drawings (with at least 1000 dpi). Graphics created in Microsoft Office applications should be supplied in their original format. Figure captions should be self-explanatory and printed on a separate sheet of paper. All figures should be numbered and specifically mentioned in the text by number. Please number all tables with Roman numerals and include a short title.

Proofs. Copies of the proofs will be sent to the author. Revised proofs should be returned to the publisher without delay. The only changes that could be accepted in proofs are on grammar or related to printing errors.

Authors can print copies of their articles from: http://www.revistascca.unam.mx/atm/index.php/atm.

Copyright notice: Once an article is accepted for publication, the author(s) agree that, from that date on, the owner of the copyright of their work(s) is the journal ATMÓSFERA. Reproduction of the published articles (or sections thereof) for non-commercial purposes is permitted, as long as the source is provided and acknowledged. Authors are free to upload their published manuscripts at any non-commercial open access repository. Accepted, but not published articles (preprints), are not allowed to be distributed by any means. The violation of this rule may end in the withdrawal of the accepted article.

ATMÓSFERA

Revista trimestral publicada por el
Instituto de Ciencias de la Atmósfera y Cambio Climático
de la Universidad Nacional Autónoma de México

MÉXICO 2023

Atmósfera is included in: Web of Science (WoS), SCOPUS, SCISEARCH, Research Alert, GeoBase, Current Contents Connect, and Aquatic Sciences and Fisheries Abstracts (ASFA).

Registrada en el Sistema de Clasificación de Revistas Mexicanas de Investigación Científica y Tecnológica del Consejo Nacional de Ciencia y Tecnología (CONACyT), e indizada en PERIÓDICA.

Manuscripts should be submitted through our website at: https://www.revistascca.unam.mx/atm/.

Subscriptions and all correspondence should be sent to:
Editor of *Atmósfera*, Instituto de Ciencias de la Atmósfera y Cambio Climático, UNAM, Circuito Exterior, Ciudad Universitaria, 04510 Coyoacán, Ciudad de México. Tel.: 52 (55) 5622-4240 Ext. 81888; fax: 52 (55) 5616-0789; e-mail: editorial@atmosfera.unam.mx

Subscription information: Institutional rate: US $90.00 per volume (4 issues); Private rate: US $70.00 per volume (4 issues).

The complete texts of Atmósfera are available in digital format at:
https://www.revistascca.unam.mx/atm/; Redalyc: https://redalyc.org; SciELO: https://www.scielo.org.mx/.

Atmósfera, vol. 36, núm. 1, enero-marzo de 2023, es una publicación trimestral editada por la Universidad Nacional Autónoma de México, Ciudad Universitaria, 04510 Coyoacán, Ciudad de México, teléfono (55) 5622-4240, ext.81888, https://www.revistascca.unam.mx/atm/. Editor responsable: Graciela B. Raga. Reserva de derechos al uso exclusivo del título núm. 001559/94 otorgado por el Instituto Nacional del Derecho de Autor. ISSN: 0187-6236. Certificado de licitud de título y contenido 7719 y 5464 otorgados por la Comisión Calificadora de Publicaciones y Revistas Ilustradas de la Secretaría de Gobernación. Las opiniones expresadas por los autores no necesariamente reflejan la postura del editor de la publicación.

Printed in Mexico.

Chief Editor
Graciela B. Raga
Founding Editor
Julián Adem

EDITORIAL BOARD

President
Jorge Zavala Hidalgo

Atmospheric Composition and Remote Sensing
Michel Grutter (*Mexico*) • Luis Gerardo Ruiz (*Mexico*) • Telma Castro Romero (*Mexico*)

Climatology and Climate Variability
Tereza Cavazos (*Mexico*) • Henry F. Diaz (*USA*) • Carlos Gay (*Mexico*)
José Luis Labajo (*Spain*) • Carlos Nobre (*Brazil*) • Matilde Rusticucci (*Argentina*)

Meteorology and Atmospheric Physics
Isidoro Orlanski (*USA*) • Yuri Skiba (*Mexico*)

Observations and Numerical Modeling of the Atmosphere-Ocean System
Julio Sheinbaum Pardo (*Mexico*)

ASSOCIATE EDITORS

Dr. Paola Arias Gómez
Universidad de Antioquia, Colombia

Dr. Deniz Bozkurt
Universidad de Valparaíso, Chile

Dr. Moira Doyle
Universidad de Buenos Aires, Argentina

Dr. Iván Y. Hernández Paniagua • Dr. Paulina Ordóñez Pérez • Dr. Wolfgang Stremme
Instituto de Ciencias de la Atmósfera y Cambio Climático, UNAM, Mexico

Dr. Daniel Martínez
INAIGEM, Peru

Dr. Manuel Mendoza Ramírez • Dr. Irma Beatriz Rumbos Pellicer
Instituto Tecnológico Autónomo de México, Mexico

Dr. Álvaro Osornio
University of Alberta, Canada

Dr. Michelle Reboita
Universidade Federal de Itajubá, Brazil

Dr. Alfredo Ruiz Barradas
University of Maryland, United States

Dr. Luis Zavala Sansón
Centro de Investigación Científica y de Educación Superior de Ensenada, Baja California, Mexico

Assistant editors Irene Romero Nájera • Aline E. Maza Vázquez • *Copy editor* Alberto Alazraki
Layout editor and webmaster Pietro Villalobos Peñalosa

Atmósfera 36(1), 1-21 (2023)
https://doi.org/10.20937/ATM.52953

Classification of the flood severity of the Guadalquivir River in the Southwest of the Iberian Peninsula during the 13th to 19th centuries

Leoncio GARCÍA-BARRÓN[1], Mónica AGUILAR-ALBA[2], Julia MORALES[3] and Arturo SOUSA[3]*

[1]*Departamento de Física Aplicada, Universidad de Sevilla, E-41012 Sevilla, España.*
[2]*Departamento de Geografía Física y AGR, Universidad de Sevilla, E-41004 Sevilla, España.*
[3]*Departamento de Biología Vegetal y Ecología, Universidad de Sevilla, E-41012 Sevilla, España.*
*Corresponding author: asousa@us.es

Received: July 31, 2020; accepted: June 15, 2021

RESUMEN

Este estudio estima la severidad de las inundaciones durante los siglos XIII a XIX en el suroeste de la Península Ibérica. Para ello nos basamos en las crónicas históricas de los impactos provocados por las inundaciones del río Guadalquivir en la ciudad de Sevilla (España). La principal fuente documental fue la monografía *Historia crítica de las riadas o grandes avenidas del Guadalquivir en Sevilla* (1878), que recopila noticias de distintos observadores contemporáneos de cada inundación. Por ello, desde el punto de vista metodológico, ha sido necesario transferir la información procedente de fuentes documentales variadas a índices ordinales, para hacerlas comparables. Esto implica elaborar criterios de asignación por los impactos de las diferentes inundaciones. A partir del índice anual de severidad asignado a cada inundación, se genera la serie interanual. Mediante la ponderación interanual de los índices de inundación se deduce la duración e intensidad de las secuencias de periodos de inundación desde 1250 hasta 1850. De las 10 inundaciones clasificadas como más destructivas en los cinco siglos estudiados (1280-1880), cinco se concentran en poco más de un siglo, de 1598 a 1701. Los resultados obtenidos contribuyen al conocimiento multisecular de la pluviometría regional y son una nueva aportación a la climatología e hidrología histórica.

ABSTRACT

This study estimates the flood severity between the 13th and 19th centuries on the southwestern Iberian Peninsula based on the historic records of impacts of the Guadalquivir River flooding on the city of Seville (Spain). The main documentary source was *Historia crítica de las riadas o grandes avenidas del Guadalquivir en Sevilla* (Critical history of the floods of the Guadalquivir in Seville) (1878), which compiles news from different observers that were contemporaries of each flood. Regarding the methodology, it was necessary to transfer the information from different documentary sources to ordinal indices, which required developing allocation criteria per flood impact. From the annual severity index assigned to the different floods, an interannual series was generated. Through interannual weighing of the flooding indices, it was possible to deduce the durations and intensities of sequences of flood periods between 1250 and 1850. Of the 10 floods classified as most destructive during the five centuries analyzed (i.e., from 1280 to 1880), five occurred during little more than a century (1598-1701). The obtained results contribute to knowledge on regional rainfall, as well as to historical climatology and hydrology, over multiple centuries.

Keywords: floods, Guadalquivir River, documentary sources, historical climatology.

1. Introduction

Knowledge on the evolution of climate over past centuries, before instrumental records, is based on multiple sources that provide information directly or indirectly (i.e., proxy data). Historical, botanical, and geological evidence are worthy sources of flood information. Wilhelm et al. (2019) show the historical development of different methodological approaches and the type of information that these files provide. Fundamentally, there are two types of proxy data: natural and documentary data. This study is exclusively focused on proxy data from documentary sources. One of the frequently used types of documentary proxy data is ecclesial documents related to tithe and rogation ceremonies. A tithe payment (i.e., an economic tax of one tenth of a harvest) shows the annual agricultural production associated with meteorological factors, although it is not always easy to interpret. Moreover, in the face of meteorological adversity, the Catholic Church regulated liturgical celebrations of intercession: pro-pluvia rogations, in the case of prolonged droughts, or pro-serenitate rogations, in the case of persistent rainfall with floods (Martín-Vide and Barriendos, 1995; Tejedor et al., 2019). The advantage of the rogation method is that it maintained the spatial and temporal uniformity of the applicable type of ceremony, which indicates the severity attributed to each event (Cremades, 2017).

Other relevant documentary sources of historic climatology are the records and annals of historians who included unique meteorological circumstances in their stories (Rodrigo et al., 2012), minutes of local corporations and institutions that gathered information on exceptional situations such as droughts or floods (Barriendos et al., 2019), and reports of trustees of noble houses about the economic results of agriculture they considered to be affected by meteorological conditions (Fernández-Fernández et al., 2014). This information is frequently scattered and must be filtered from the main focus of the set of consulted documents. In general, literary information on climatic phenomena is linked to the subjectivity and inaccuracy of the chroniclers and may be influenced by external factors. To develop temporal series from this information, it is necessary to establish ordinal levels of intensity that allow the creation of quantifiable scales (Pfister et al., 1999).

Different authors with varied orientations have investigated historical floods in Europe (Brázdil et al., 2006; Glaser et al., 2010; Kjeldsen et al., 2014; Benito et al., 2015; Blöschl et al., 2020), as well as their frequency and intensity in the main Spanish drainage basins (Benito et al., 2003; Machado et al., 2011; Fragoso et al., 2015; Balasch et al., 2019). Regarding the floods of the Guadalquivir River, the geomorphological studies of Uribelarrea and Benito (2008) and Baena et al. (2019) are worthy of mentioning. Despite the large number of historical documents on the Guadalquivir River floods, according to Zamora (2014) the impacts of these floods have not been addressed thoroughly, unlike other European rivers, except the compilation by Francisco de Borja Palomo: *Historia crítica de las riadas o grandes avenidas del Guadalquivir en Sevilla: desde su reconquista hasta nuestros días* (Critical history of the floods of the Guadalquivir in Seville: From its reconquest to today) (Palomo, 1878). Among the studies focusing on the historic climate of the southern Iberian Peninsula, it is worth highlighting studies on South Portugal (Alcoforado et al., 2000; Do Ó and Roxo, 2008), the Doñana wetlands (Sousa et al., 2010), and southern Extremadura and Andalusia (Rodrigo et al., 1999, 2012; Barriendos, 2007; Rodrigo, 2007, 2017, 2018).

Barriendos and Rodrigo (2006) compared historic floods of the main Spanish drainage basins. According to these authors, it is possible to differentiate the typology between the Atlantic and Mediterranean watersheds, although the drainage basin is the adequate reference unit for the analysis of the chronology of floods. Thus, the Guadalquivir basin, in the South Atlantic side of the Iberian Peninsula, only experienced synchronous catastrophic floods with the Segura basin in 1778 A.D. and with the Douro basin in 1545 A.D. (Fig. 1). García-Codrón (2004) stated that in the Iberian Peninsula, the highest seasonal risk of flooding appears in spring for the central plateau under Atlantic influence (Douro, Tagus, and Guadiana), during autumn for the Mediterranean watershed (Jucar and Segura), and in winter for the Guadalquivir basin. Therefore, this information highlights the need to conduct historical climatological studies that are thoroughly focused on the main basins, such as the Guadalquivir basin object of this study.

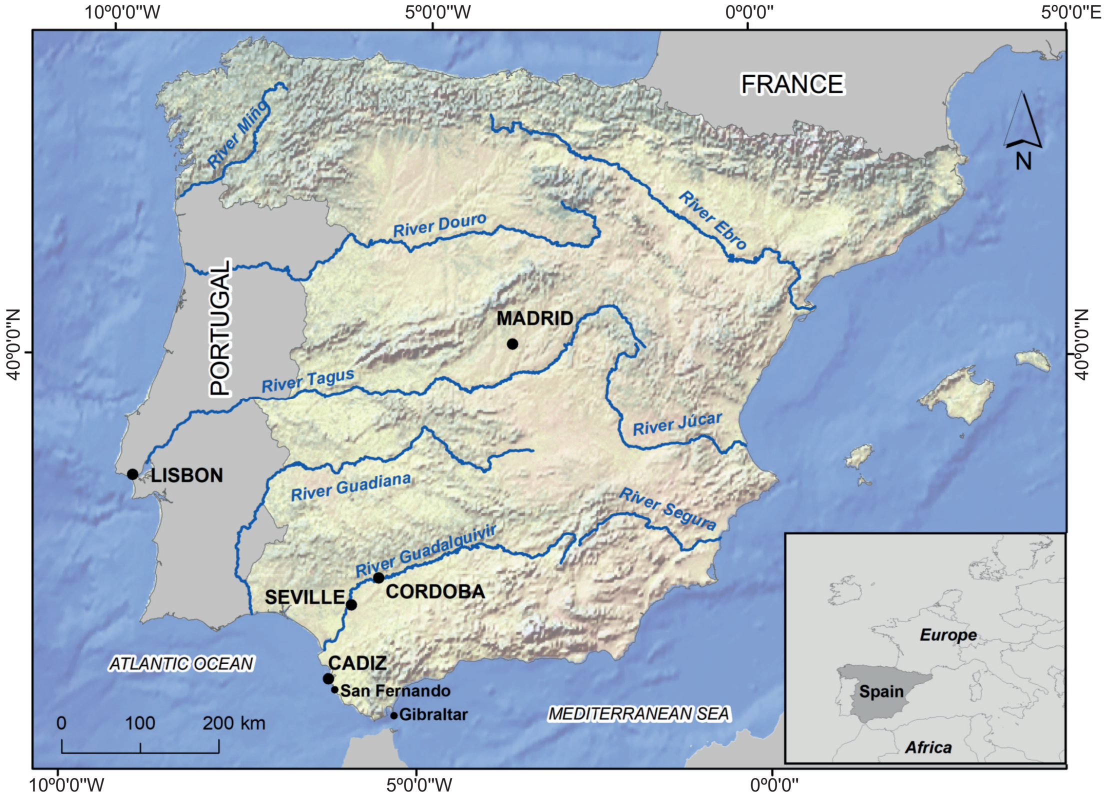

Fig. 1. Location of Seville and the Guadalquivir River on the Iberian Peninsula.

In southern Spain, it is possible to distinguish two causes of flooding:

1. Persistent rainfall due to a long and continuous period of precipitation (or melting) in Atlantic basins, as the Guadalquivir basin. These are more frequent in winter.
2. Torrential rains caused by periods of very intense and short rains. These are frequent in Mediterranean basins as a consequence of cold drops, with greater probability in the months of autumn.

In the Guadalquivir river basin, although floods can be caused by brief torrential rainfalls, they are generally influenced by prolonged and persistent rains, with subsequent runoff from an upper river basin.

The risk of flooding in the Guadalquivir basin is essentially influenced by pluviometric and orographic factors. With respect to the former, it is worth highlighting an important irregularity in precipitation at both the seasonal and interannual scales, with a high frequency of intense rainfall in wide areas of the basin. The annual precipitation average for the entire watershed is of 640 mm. This, however, hides very relevant variations, with over 1000 mm yr^{-1} in some areas compared to other areas with only 300 mm yr^{-1} (García-Barrón et al., 2011). This is mainly due to frontal precipitation that responds to the entry of Atlantic storms through the Gulf of Cádiz (Vallejo, 2000).

Flooding in the lower Guadalquivir River basin has a high flow rate, which is surprising, given the slight slope in that region and the deceleration exerted by the sinuosities of its course (García, 2003). As stated by Vanney (1970), this scenario is due to the acceleration caused by the local volume contributions.

The aim of this work is to classify the floods of the Guadalquivir River in the city of Seville from the 13th to the 19th century using historical records gathered by Palomo (1878).

2. Study area and data

The following sections describe the urban circumstances of the city and its relationship with the river to better understand the subsequent categorization of the impacts caused by the floods of the Guadalquivir River on the city of Seville. Most of the studies that analyze the floods of the Guadalquivir focus on their effects on the urban transformation of Seville and on hydraulic works during the 19th and 20th centuries (del Moral, 1991, 1992). On the other hand, studies of the floods of previous centuries are very scarce. We analyze the main source of documentary proxy data used in this study (Palomo, 1878) that were subsequently compared with instrumental meteorological data.

2.1 Study area: The city of Seville and its relationship with the floods of the Guadalquivir River

The Guadalquivir River is the most important river in the southern part of the Iberian Peninsula (657 km long). It crosses Córdoba and Seville (Fig. 1) and discharges in Sanlúcar de Barrameda, next to Doñana National Park. The Guadalquivir River is situated in the southwest of Spain, where there is a Mediterranean climate influenced by the Atlantic Ocean (García-Barrón et al., 2013).

The city of Seville (37.38° N, 5.97° W) is built on an alluvial plain. Historically, it was a walled city surrounded from the northeast to the southwest by the Guadalquivir River (Fig. 2). This river separates the traditional neighborhood of Triana from the remainder of the historic urban center of Seville. Therefore, the extramural neighborhood of Triana was connected to the intramural area of the city of Seville by a floating (or pontoon) bridge that crossed the Guadalquivir River (Fig. 2). This floating bridge, originally built in 1171 A.D., consisted of a set of tall boats anchored to the bottom, joined together by iron chains, with wooden columns that held the platform of the bridge. By observing old lithographs, it is possible to deduce that the distance between the water surface and the platform of the bridge was no more than two and a half meters. It was reported that the bridge was damaged several times and even ripped and broken apart by the current in 1794 (Palomo, 1878).

The walls of the city of Seville have historically served two defensive purposes: military and hydrological. The initial construction of the wall dates from the period of Julius Caesar (1st century B.C.). Since the Roman Age, it has been rebuilt and expanded. In the late Middle Ages, the wall was 7 km long and had 166 turrets, with 19 gates and wickets. Since the 16th century, its military purpose has been less important, and it was maintained to protect the city against the flooding river. It is the fundamental protective element of the city. During flood events, its

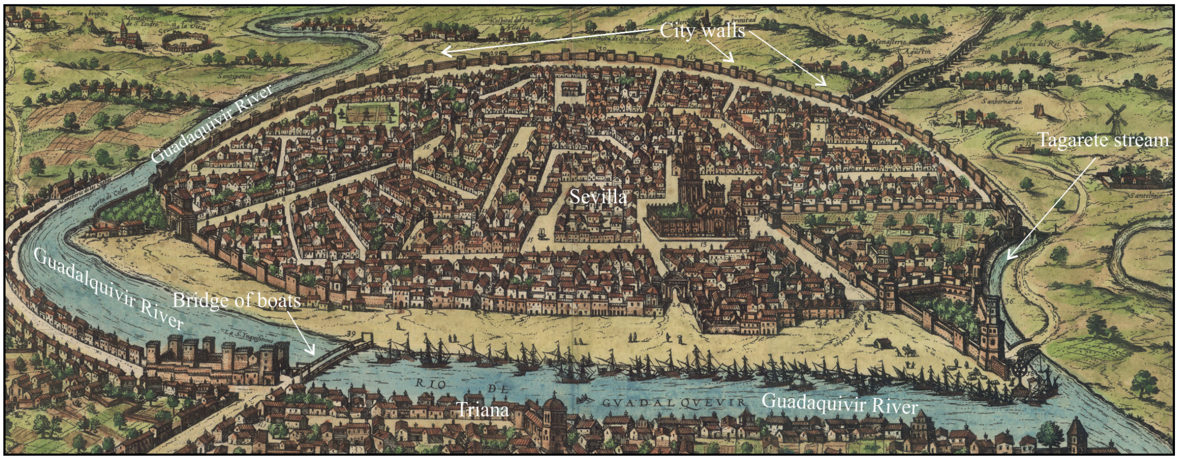

Fig. 2. View of Seville with the Guadalquivir River in the 17th century. This map shows the floating bridge or bridge of boats at the lower left side and the Torre del Oro at the right end of the harbor. Source: detail of the enlarged facsimile version of Braun and Hogenberg, *Civitates Orbis Terrarum* (1588). It can be found online at the National Geographic Institute of Spain: https://www.ign.es/web/catalogo-cartoteca/resources/html/023677.html (accessed on April 16, 2020).

gates were externally reinforced with caulked planks inserted in lateral guides. It is important to highlight that in 1868, after great political debate, the gates and walls were torn down with the justification that this would favor the expansion of the city. However, this would also influence the impact of floods on the city, as described in subsequent sections.

Similarly, the drain spindles of the city of Seville were closed during floods to prevent them from working in the reverse direction (i.e., introducing water from outside of the city into the walled urban center). In the river plain of the opposite riverbank, next to the neighborhood of Triana, cloisters and monasteries were built, which appear frequently in historical records as being affected by river flooding. After floods, a serious additional problem was the permanent ponding of the low areas of the river plain, where poor quality water bodies formed, with pests and the risk of disease transmission, as was reported for different periods by Palomo (1878).

Two tributaries flowed through the west side of the city, which are currently channeled and hidden: the Tamarguillo, currently a ring road for traffic, and the Tagarete, closer to the walls (Fig. 2), which crossed under the bridge that provided access to the Xerez Gate in the southwest of the city. This location is very relevant since the height of the old city wall is a reference used by some chroniclers to alert about the danger of floods. Both tributaries increased the destructive flood effects on the city. Moreover, Guadalquivir River is influenced by the rhythm of the tides at its mouth; high tides oppose the flow of the river current, which hinders river discharge during floods.

In the 7th century, the old canal of La Vega was opened to serve as a natural drain that prevented the risk of overflow into the city and that was maintained and improved during Muslim rule. However, with the Christian reconquest (13th century), the maintenance of the canal was neglected, and its depth decreased, which increased the flood risk. During the 17th-19th centuries, important containment and diversion works were proposed, although most of them were never implemented.

In 1776 the sewerage system was enhanced and a pier was built that improved the defense of the city against floods. In 1816, different reformations were carried out along the course of the Guadalquivir River between its mouth and the city of Seville to facilitate navigation throughout the river and reduce the risk of flooding.

It is worth mentioning the severe floods of 1892 and 1895, when the city was not protected by the wall. In the 20th century, several overflows also occurred, generally with small impacts, of which there is extensive journalistic and graphic documentation. During the 19th century and especially the 20th century, hydraulic works were carried out in the river and in the flood plain, such as the cutting of meanders and canals or reservoirs (García-Martínez and Baena, 2006), which have substantially modified the natural dynamics of the river and the risk of flooding.

2.2 Historical documentary sources

The present study is fundamentally based on the documentary proxy data obtained from the historical monograph by Palomo (1878) (Fig. 3), who gathered data on the historical floods of Seville and their effects on the city between the 13th and 19th centuries, and for all years with floods, he compiled all the known documentary sources. Francisco de Borja Palomo was a scholar and bibliophile, professor of jurisprudence at the University of Seville

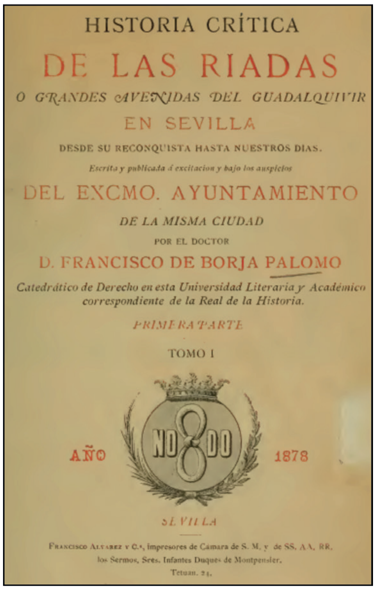

HISTORIA CRÍTICA
DE LAS RIADAS
O GRANDES AVENIDAS DEL GUADALQUIVIR
EN SEVILLA
DESDE SU RECONQUISTA HASTA NUESTROS DIAS.
Escrita y publicada á excitacion y bajo los auspicios
DEL EXCMO. AYUNTAMIENTO
DE LA MISMA CIUDAD
POR EL DOCTOR
D. FRANCISCO DE BORJA PALOMO
Catedrático de Derecho en esta Universidad Literaria y Académico
correspondiente de la Real de la Historia.
PRIMERA PARTE
TOMO I

AÑO 1878

SEVILLA

Francisco Alvarez y C.ª, impresores de Cámara de S. M. y de SS. AA. RR.
los Sermos. Sres. Infantes Duques de Montpensier.
Tetuan. 24.

Fig. 3. Original cover of *Historia crítica de las riadas o grandes avenidas del Guadalquivir en Sevilla*, vol. I, published in Seville in 1878.

and official receiver of the city hall of Seville in the late 19th century. In addition to the detailed critical compilation of annual floods, he also included notes, biographical comments of distinguished figures, descriptions of relevant and catastrophic events (earthquakes, hurricanes, epidemics, famines, etc.) and a description of some monuments. He provided paintings with a view of the city and its relationship with the river, as well as images of the old gates of the city wall. His complex book is divided into two volumes. The first volume covers the period between the Christian Reconquista (13th century) and 1800 A.D. and compiles and expands upon the articles that were previously published by the author. The second volume is focused on the 19th century and was published later (1884), incorporating other manuscripts. In each of the years when there were reports about floods, the book includes comments on the primary documents written by chroniclers who were contemporary to the event or had direct references. Similarly, the second volume includes texts of historians who highlighted the effects of the floods with a broader perspective. We have consulted primary sources in files and historical records of different institutions that corroborate the reliability of the corresponding comments by Palomo (1878). As an interesting example, we highlight the dissertations presented at the Regia Sociedad de Medicina y Ciencia of Seville after the floods of the 18th century, focused on the medical damages that floods can cause.

Data of Palomo (1878) have been used in studies that analyze changes in the geomorphology of the Guadalquivir River during the Holocene (Uribelarrea and Benito, 2008), the sinking of the flood plain as a consequence of the growth of the city of Seville (Ruiz-Constán et al., 2017) and the flood risk of the Guadalquivir River (García-Martínez and Baena, 2006), as well as the fact that it has been cited as a source of studies on historical floods in Andalusia in the 16th century (Pfister et al., 1999) and throughout the 20th century (León et al., 2020).

One of the most laborious tasks involved in acquiring information related to historical climatology and hydrology is consulting multiple documents with varied content in archives and libraries of diverse ownership. Palomo (1878) gathered over 400 works, most of them related to the history of Seville and the floods of the Guadalquivir River: records, annals, memorials, ephemerides, relations, appendices, speeches, dissertations, etc., of numerous authors throughout history. Among this vast number of documents, he highlighted, based on the number of citations and the authority granted to its comments, the *Ecclesiastical and secular annals of Seville* by D. Diego Ortiz de Zúñiga (1638-1680). This author gathered, in his memoirs, data on the period between 1246 and 1671 A.D. According to León et al. (2020), the book of Palomo (1878) is a bibliographic source of inestimable value for its clarity and detailed information. It is also cited in the National catalogue of historical floods of Spain (DGPCE, 2019).

2.3 Links of floods with meteorological instrumental records

Similarly, the Royal Institute and Observatory of the Navy of San Fernando (Cádiz, southwestern Spain) has uninterrupted pluviometric records from 1805, although with homogeneous monthly series from 1837. It is considered as a reference observatory due to the homogeneity of its temporal series, which is the longest series for southern Spain (Rodrigo, 2002; Sousa et al., 2010). A recent study, which analyzed 25 423 pluviometric observatories in 32 geographical areas worldwide, highlighted that the observatory of San Fernando has the longest uninterrupted daily series (Morbidelli et al., 2020). San Fernando is not located in the Guadalquivir Valley (it is 30 km away from the mouth of the Guadalquivir River), although it is in the same drainage basin, i.e., the Andalusian South Atlantic basin. Different authors have applied the evolution of monthly precipitation series of San Fernando as an indicator for the entire southwestern region of the Iberian Peninsula (Sousa et al., 2009, 2015; García-Barrón et al., 2013, 2018). During the 19th century, reports about floods partially overlapped with the instrumental rainfall records of the observatory of San Fernando.

After the summer period, in which the monthly precipitation of July and August is frequently null, the precipitation of the beginning of autumn is incorporated into the subsoil; therefore, except for occasional torrential rains, the runoff of streams and the flow in the tributaries of the Guadalquivir does not present a notable increase until the end of autumn.

3. Methodology

3.1 Methodology used to estimate the severity of the floods between the late 13th century and the 18th century

To calculate the severity of floods reported between the 13th and 18th centuries, so that the severity values can be compared, we must standardize the information obtained from documentary sources of different origin (by author, date and content). Thus, we established source-contrast systems that allowed the subsequent classification of very different flood events, selecting the following main criteria: (a) the height reached by the overflow on the wall or on one of the gates of the city, (b) the damage caused by the collapse of buildings, and (c) the number of people drowned.

Other secondary criteria to standardize the range of severity of the floods were: (a) the evacuation of exterior buildings (private homes and cloisters), (b) livestock mortality in the flood plain of the Guadalquivir River in the vicinity of Seville, (c) effects on the floating bridge or on the ships of the harbor, and (d) rogations and other religious ceremonies.

Apart from these criteria, and with the aim of establishing the severity of the flood events, we used a triple filter that modulated the classification assigned to them by different documentary sources, in order to compare their severity levels:

- The relevance of the social and urban impacts in the urban area of Seville with which they appear in the compilation of events conducted by Palomo (1878).
- The appreciation of the authors themselves and the comparison with similar events gathered in records and annals of long periods.
- Whether they were gathered in the main records or only in particular references.

Appendix 1 in the supplementary material shows, in a comparative manner, the main and secondary criteria employed to assign the overflow level and impact of different flood indices, as well as the filters applied to modulate the classification of the severity of floods.

Guided by these criteria, we assigned an ascending index of flood severity as a function of the level of the overflow and its impact:

- Flood I. Flooding with the gates and spindles of Seville being closed and flooding of the extramural neighborhoods, with the evacuation of the flood plain of the Guadalquivir River in the vicinity of Seville.
- Flood II. Alarm in the city with the rampart or gates endangered, collapsed buildings and flooding in the lower intramural areas.
- Flood III. Serious generalized catastrophic situations in the entire city, except in higher areas.

Each of the testimonies about specific events highlights some of the above-mentioned aspects, without the possibility of establishing a common typology. Thus, it was necessary to conduct a comparative evaluation of the information provided in each case. We recognize that the application of the previous criteria to each year with a registered flood is subject to personal valuation margins of the authors of the original documentary sources. To control this subjectivity, the descriptions of the different documentary sources were transformed into numerical tables based on the flood indices (see Appendix 2 in the supplementary material). Other documentary sources consulted can be seen in Appendix 3 in the supplementary material.

3.2. Methodology used to calculate the severity of the floods reported in the 19th century and their relationship with instrumental meteorological records

The second volume of Palomo (1878) is focused on the floods that took place in Seville during the 19th century. The information provided by different documents compiled by this author is not uniform throughout the 19th century. The description about the effects of the overflow cannot be directly compared to those in previous centuries, mainly due to the large construction works carried out in 1776 with the building of a pier in front of the walls, and later in 1816 with the construction of a canal that reduced the risk of flooding. Thus, these elements modified the severity of the impacts that served as classification criteria in this study for previous centuries.

The average of the instrumental series from the 19th century shows that in the Guadalquivir River Valley, the intra-annual distribution of precipitation increases in autumn until it reaches a monthly maximum in November-December and decreases progressively in spring (García-Barrón et al., 2013). The interannual variability of the seasonal changes of the precipitation regime is associated with the North Atlantic Oscillation (NAO) in the Iberian Peninsula (Trigo et al., 2004), which, in its negative phase, favors the entry of storms in the Guadalquivir River Valley (Gallego et al., 2006; García-Barrón et al., 2018). This current behavior can be extrapolated to previous centuries (Luterbacher et al., 2002).

During the first half of the 19th century, the classification of the severity of floods of the Guadalquivir River was based on the description of the effects caused by the floods. However, from 1858 to the end of the 19th century, we generated a quantified series of river overflows that allowed us to establish the possible degree of synchronous correspondence between the temporal series of both climatic manifestations: precipitation vs. overflow. For each flood, we identified the height of the river over the usual level. In the Guadalquivir River basin, floods are generally due to persistent rainfall and not to very short and intense rainfall events. This period of persistent rains precedes the more intense rainfall that ends up leading to the overflow of the channel. According to the revised historical documentation, in the surroundings of Seville, the floods used to last several weeks. For this reason, we used the data for the month in which the maximum overflow occurred and also the data for the previous month (bimonthly). For that reason, the meteorological variable used for the correlation test was the excess of bimonthly precipitation at San Fernando with respect to the average of the period 1837-1890.

To synthesize the temporal development, we generated a new series, based on the flood index, that shows the rainy sequences or periods between the late 13th and 19th centuries using the centered moving average calculated for 11-yr periods. In general, from the 16th century the number of documentary sources available for the same event has progressively increased. This means that the information available is also greater, which does not necessarily imply that the number of floods is therefore more frequent or intense.

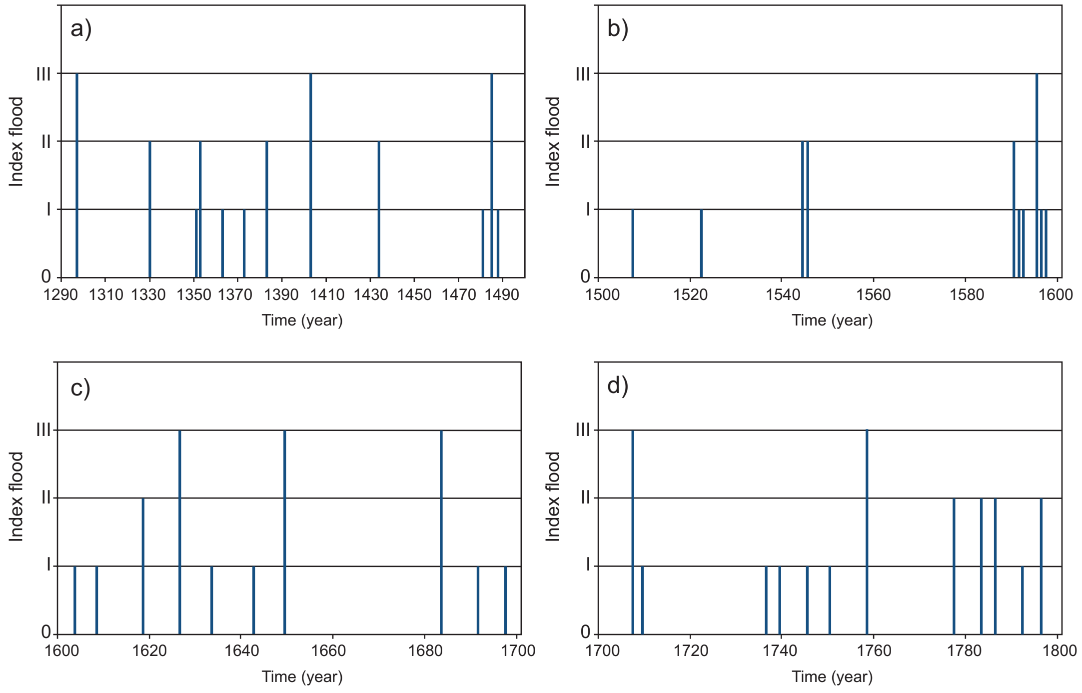

Fig. 4. Flood index estimated for the Guadalquivir River in Seville: (a) 1290 A.D. to the 15th century, (b) 16th century, (c) 17th century, and (d) 18th century.

4. Results and interpretation

4.1 Severity of the floods between the late 13th century and the 19th century

A classification of the Guadalquivir River floods, based on the flood severity index assigned, between 1290 A.D. and the late 18th century is shown in Figure 4. Although there is temporal continuity, to visualize the flood events in more detail, they were grouped by century. More specifically, Figure 4a represents the 13th, 14th and 15th centuries; Figure 4b shows the 16th century; Figure 4c displays the 17th century; and Figure 4d shows the 18th century.

4.1.1 13th-15th centuries

Despite the limited number of authors and the difficulty in preserving documents disseminated by copyists before the arrival of printing, news of floods before 1500 A.D. have been transmitted. Some of these reports are focused on the spread of diseases rather than on direct property damage. We interpreted that because this information had been recorded as extraordinary events by chroniclers, they were relevant.

In the 250 years of the late Medieval period (1250 to 1500 A.D.), 12 floods of remarkable impact were described (Fig. 4a). Three of them were classified as extremely disastrous (indexed as Flood III), specifically in 1297, 1403 and 1485. Before 1290, there are no records of floods in the book of Palomo (1878). During the first half of the 14th century, the incidence of floods was very low, and then, in the second half, there were floods of different categories.

Between the floods of 1403 and 1481, only that of 1435 was reported, which suggests that the pluviometric regime for that period in the Guadalquivir River valley was characterized by scarce overflow. Considering the number and effects of the floods, we can estimate that globally, over the studied time period, the 15th century, except for the two last decades, was the period with the lowest flood incidence.

4.1.2 16th century

Ten floods were recorded throughout the 16th century, although six of them took place in the last decade of that century. The flood reported in 1595 was classified as a generalized catastrophe in the city (indexed as Flood III). This suggests that the last decade of the 16th century was very rainy and that the remainder of the century had very few flood events.

4.1.3 17th century

Although only 10 floods were reported in the 17th century (in 1626, 1649, and 1683), these floods can be considered among the most catastrophic floods during the analyzed centuries (indexed as Flood III). Except for 1650-1682, in which no overflow of the Guadalquivir River was recorded, the remainder of the century presents a relatively uniform distribution, with a trend of approximately 7-10 yrs. Precisely, this period of 1650-1682 coincides with the first half of the Maunder minimum (1645-1715) (Eddy, 1976; Usokin, 2017) which, under our criteria, supports the idea that the decreased insular activity corresponded to a dry period in southern Spain, although the continuity of the Maunder minimum from 1683 to 1715 was relatively more humid (Alcoforado et al., 2000).

Through the analysis of the ecclesiastical tithe between 1589 and 1708, Rodrigo (2007) established that in the area of Seville, 30 years of bad harvests were recorded, of which 16 could be attributed to excess precipitation, among other possible causes such as frost and locust plagues and the Plague epidemics. In the same period, 19 floods of different categories were recorded. Over nine years, the excess rainfall coincided with floods. However, among the bad harvests, such analysis did not include the serious floods of 1595 and, especially, 1626; the latter was called “el año de diluvio” (“the year of deluge”). No floods were recorded in any of the seven years classified as bad harvest years.

The solemn public supplications are important means for understanding the historical evolution of the climate. In the investigations based on ecclesial documents they take on a remarkable weight. Although Palomo (1878) collects multiple news on supplications related to the Guadalquivir River, his analysis is even broader, since he also includes other documentary sources that directly describe the level reached by water in each flood and its urban and social impacts.

4.1.4 18th century

Twelve overflows of the Guadalquivir River occurred in the 18th century, and those in 1707 and 1758 had catastrophic effects (indexed as Flood III). During the second half of the 18th century, the occurrence of moderate and serious events increased (indexed as Floods II and III). García-Martínez and Baena

(2006) also found an increase in the frequencies of Guadalquivir River floods from 1750 with respect to the previous centuries. The greatest rainfall variability was detected in 1730 and 1780. The first years of the 1780s were very dry; during the winter and spring of 1780-1781 and the spring of 1782, there were marked episodes of drought, as confirmed by the pro-pluvia rogations. On the other hand, strong rains prevailed from 1784 (when the floating bridge of the Guadalquivir River was moved) onwards.

In summary, Table I shows the number of reported floods between 1280 and 1800 as a function of the flood impact index assigned, the probability of occurrence per decade and the average period of recurrence in years.

Table I. Distribution of floods based on the annual index flood, with probability of occurrence and average recurrence period.

Flood index	Number	Average probability of occurrence per decade	Average recurrence period (years)
I	23	0.44	22.6
II	12	0.23	43.3
III	9	0.17	57.8
Total	44	0.85	11.8

Table I shows that, on average, the city of Seville has had approximately one flood every 12 years, of which one every 58 years had catastrophic effects. Therefore, it is possible to confirm that the flood risk in the urban area of Seville was a historically usual element. Thus, flooding was a consistent focus and concern for the authorities and the population.

4.2 Severity of the floods during the 19th century

Section I of volume II (1800-1858) of Palomo (1878) describes 10 overflows of the Guadalquivir River. The recorded documentary sources differ in the type of information they provide in different years, although they are consistent in the use of platforms ("borriquetes" in Spanish) raised above the floating bridge of the Guadalquivir River to connect to the neighborhood of Triana (1803, 1830, and 1841). In January 1823, the main catastrophic flood of this period took place, which inundated the entire neighborhood of Triana and reached the height of the previous great flood of 1796. We can assert that in the first half of the 19th century, the frequency of floods of different intensities was high. Section II describes historical episodes of the city that were not directly related to the river flooding. As a novelty, section III provides uninterrupted data from 1858 on the height (feet) reached by the river during each flooding event. Table II shows the years and months of maximum overflow and the corresponding elevation over the usual level of the river.

Moreover, as noted in the methodology section, we used the monthly rainfall series of the San Fernando Observatory (southwestern Spain) to calculate the bimonthly excess precipitation with respect to the average of that in 1837-1890, coinciding with the floods. The flood of 1876-1877 was not used in the calculations since after the demolition of most of the gates and the walls of the city in the preceding years, the river flooded the city. Therefore, without protection, there was no longer a uniform criterion to compare the effects of previous floods.

Figure 5 shows a pair diagram between the synchronous series of bimonthly excess rainfall p (l m^{-2}) and the overflow level d (inches). Although the number of data points is small, it can be observed that the dots are roughly aligned.

Table II. Month and year of the most relevant floods and the corresponding elevations of the level of the river (in inches).

Date	November 1858	December 1860	January 1862	January 1867	January 1872	December 1876*
Elevation of the level of the river	21	12	16	28	22	37

*The impacts of this year cannot be compared with the other floods of the 19th century.

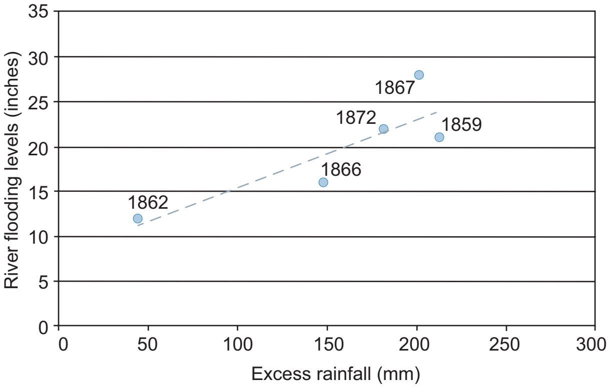

Fig. 5. Scatter plot of the elevation of the river level, measured in inches, and bimonthly excess rainfall, measured in millimeters, with the regression line indicated.

The small number of events and the type of variables that led to Eq. (1) do not allow extrapolation to previous centuries, although R^2 explains more than 70% of the variance (Pearson's correlation coefficient R = 0.84, p = 0.073, and the standard error of the estimates is 3.78).

$$p = 9.4\, d - 28.5 \tag{1}$$

The average of the instrumental series from the 19th century shows that in the Guadalquivir River valley, the intra-annual distribution of precipitation increases in autumn until it reaches a monthly maximum in November-December and decreases progressively in spring (García-Barrón et al., 2013). The precipitation regime is associated with the NAO in the Iberian Peninsula (Trigo et al., 2004) which, in its negative phase, favors the entry of storms in the Guadalquivir River valley (Gallego et al., 2006; García-Barrón et al., 2018). This current behavior can be extrapolated to previous centuries (Luterbacher et al., 2002). Figure 6 shows the intra-annual rainfall distribution (Fig. 6a) and the intra-annual distribution in the number of floods (Fig. 6b), exhibiting the delay in the month with the highest probability of floods (January) with respect to the maximum of the intra-annual rainfall distribution (November-December). This could be due to the fact that floods are frequently influenced not only by immediate direct rain but also accumulated rain in a drainage basin.

Between the starting date of the uninterrupted instrumental series of rainfall records (1837) and the year of the last reports about floods gathered by Palomo (1878), the following is observed:

- In each of the 16 years with floods (see Appendix II in the supplementary material), the total annual precipitation was above the average precipitation of the entire period.
- The average annual precipitation of the years with floods was 847 mm, which is significantly different from the average of 580 mm for the entire period 1837-1878, that is, 46% over the annual arithmetic mean of the same period.
- For this period the average rainfall in the two wettest months of the year was 125 mm in November and 119 mm in December. However, in the years with floods the average of the month when the flood occurred was 143 mm and the average of the previous month was 184 mm. Therefore, the excess of the bimonthly accumulation corresponding to flood events is 35% higher than that of the wet bimesters.

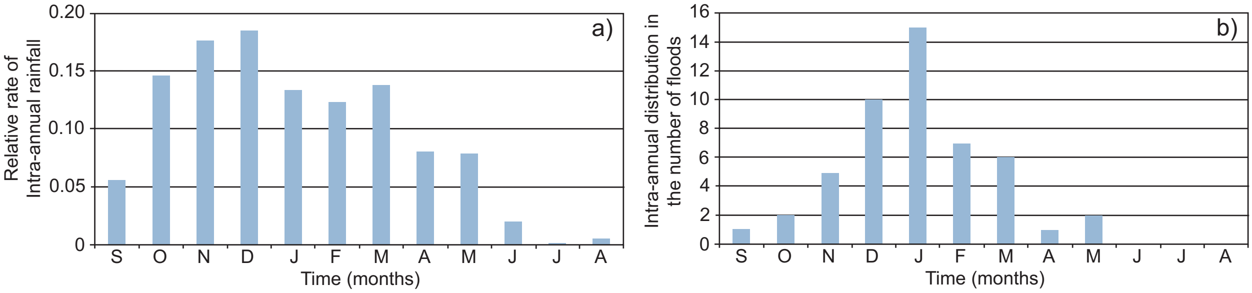

Fig. 6. Intra-annual distribution: (a) relative rate of monthly rainfall during the instrumental period and (b) intra-annual distribution in the number of floods.

4.3 Interdecadal-scale estimation of the pluviometric evolution in the Guadalquivir River basin based on the records of floods in Seville

Frequently the floods of the Guadalquivir River are due to the accumulation of intense rains for several days in the context of a wide period of some weeks with rainy conditions. In general, this type of temporary distribution of rainfall is usually associated with the existence of west-south-west Atlantic fronts.

Using the results obtained in sections 4.1 and 4.2, it was possible to generate an inter-annual series of the flood index from the 13th to the 19th century. From the results of the annual flood indices for 1297-1796 (Fig. 4 and Appendix II), the centered moving average was calculated for 11-yr periods (Fig. 7). The values of the *Y* coordinate represent the temporal variation of the flood index. This allows to establish a comparable ordinal scale for more than five centuries, which estimates the historical evolution of floods in the southwestern Iberian Peninsula.

Figure 7 shows a non-periodic alternation of years with flooding and non-flooding intervals. During the 14th century, a moderate level of floods can be observed; however between 1580 and 1650 there is a long sequence of flooding. Finally, from 1680, three discontinuous pulses are shown with a greater amount of flooding episodes: 1680 to 1710, 1730 to 1760, and 1770 until the end of the 18th century.

Rodrigo et al. (1999) presented conclusions on the temporal development of precipitation in southern Spain based on several types of historical reports in different localities between 1500 and 2000, with instrumental records for the 19th and 20th centuries. We observed a generalized likelihood between their pluviometric evolution and the one obtained in the present study for the same periods in both studies (1500-1800 A.D.). The authors highlighted the positive anomaly or the humid period from the late 16th century to the mid-17th century.

Through a documentary analysis of institutional sources and ecclesiastic pro-pluvia rogations, Barriendos (2007) used two complementary ordinal indices of precipitation and drought. This author highlighted that in Seville, two periods of floods, one from 1580 to 1620 and the other from 1760 to 1800, occurred. He also identified two drought periods: 1560-1580 and 1660-1730. Generally, his results are globally consistent with those presented in this study, with no discrepancies at the multi-decadal scale. The results obtained by García-Martínez and Baena (2006) from a geomorphological analysis of the study of floods in the lower Guadalquivir River are also in line with our results.

It seems probable that the effects of the Little Ice Age (LIA) on the Mediterranean latitudes were markedly more humid and with greater variability with respect to those on the northern latitudes of Europe (Sousa and García-Murillo, 2003). Pfister et al. (1999) stated that climate change on the Iberian Peninsula could be more associated with precipitation and less associated with temperature. Grove (2001) highlighted that the same climatic conditions that induced the advance of glaciers during the LIA were also responsible for an increase in the frequency of

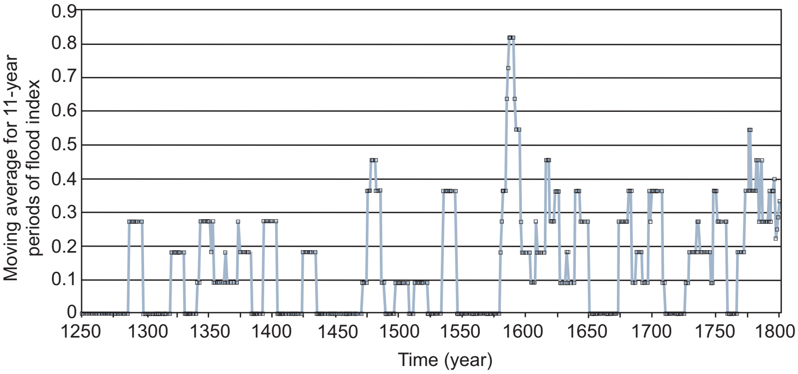

Fig. 7. Decadal-scale estimation of the flood index evolution in the Guadalquivir River basin based on the flood records for Seville between 1250 and 1800 A.D

floods and sedimentation in Mediterranean Europe. Several studies (Barriendos and Martín-Vide, 1998; Rodrigo et al., 1999, 2000) detected, with different aspects, humid periods during the LIA in Andalusia (1570-1630, 1780-1800, and 1830-1870), which alternated with dry periods and with great variability (Benito, 2006; Rodrigo, 2018). Similarly, different studies have detected greater aridity in the climatic conditions of the Doñana biosphere reserve, which coincided with the end of the last of the humid periods of the LIA on the southern Iberian Peninsula, and these conditions influenced the deterioration of lagoons (Sousa et al., 2010), hygrophytic plants (Sousa et al., 2013) and coastal streams (Sousa et al., 2015).

In comparison with other studies, based on different types of qualitative sources of information and through different assignation procedures, the results of this study must be interpreted in their own context. The concept of drought can result in multiple interpretations in general, which refer to a deficit of precipitation. Therefore, although different authors that documented historic climatology used terms that, in a simplified manner, identify with dry/rainy, these do not have an unambiguous meaning, but they introduce conceptual differences depending on the applied methodology and the type of precipitation variable estimated.

5. Conclusions

This study briefly presents the impact of the Guadalquivir River floods on the urban area of Seville, especially highlighting the city walls as a protective element against such events. These particular conditions influenced the levels of impacts cited in texts. From the literary description of the historical floods of the Guadalquivir River, we generated an index flood series from the late 13th century to the 19th century. In addition, we created transference criteria that numerically assigned three ascending levels of severity as a function of the described impacts. We developed graphs for each century that show the intensity of the floods and, complementarily, multi-annual sequences with no floods. Of the 10 floods classified as most destructive in the five centuries analyzed (1280-1880), five were concentrated during little more than a century (i.e., between 1598 and 1701).

We consider that a multiple-century application of floods is an adequate procedure that, in addition to other proxy data, contributes to the knowledge of the historical climatic evolution on the southern Iberian Peninsula.

Acknowledgments

We would like to thank the Royal Institute and Observatory of the Navy of San Fernando for providing records on precipitation from its historical archive. This study was partially funded by project PID2019-104343RB-I00.

References

Alcoforado MJ, Nunes MF, García JC, Taborda JP. 2000. Temperature and precipitation reconstruction in southern Portugal during the late Maunder minimum (AD 1675-1715). The Holocene 10: 333-340. https://doi.org/10.1191/095968300674442959

Baena R, Rinaldi M, García-Martínez B, Guerrero-Amador I, Nardi L. 2019. Channel adjustments in the lower Guadalquivir River (southern Spain) over the last 250 years. Geomorphology 337: 15-30. https://doi.org/10.1016/j.geomorph.2019.03.027

Balasch JC, Pino D, Ruiz-Bellet JL, Tuset J, Barriendos M, Castelltort X, Peña JC. 2019. The extreme floods in the Ebro River basin since 1600 CE. Science of the Total Environment 646: 645-660. https://doi.org/10.1016/j.scitotenv.2018.07.325

Barriendos M, Martín-Vide J. 1998. Secular climatic oscillations as indicated by catastrophic floods in the Spanish Mediterranean coastal area (14th-19th centuries). Climatic Change 38: 473-491. https://doi.org/10.1023/A:1005343828552

Barriendos M, Rodrigo FS. 2006. Study of historical flood events on Spanish rivers using documentary data. Hydrological Sciences Journal 51: 765-783. https://doi.org/10.1623/hysj.51.5.765

Barriendos M. 2007. Climatic variability on Spain for past centuries. Reconstruction from historical documentary sources. In: Climate change in Andalusia: Evolution and environmental consequences (Sousa A, García-Barrón L, Jurado V, Eds.). Consejería de Medio Ambiente de la Junta de Andalucía, Seville, Spain, 45-54. Available at: http://www.juntadeandalucia.es/medioambiente/web/Bloques_Tematicos/

Educacion_Y_Participacion_Ambiental/Educacion_Ambiental/el_cambio_climatico_en_andalucia/capitulo2.pdf

Barriendos M, Gil-Guirado S, Pino D, Tuset J, Pérez-Morales A, Alberola A, Costa J, Balasch JC, Castelltort X, Mazón J, Ruiz-Bellet JL. 2019. Climatic and social factors behind the Spanish Mediterranean flood event chronologies from documentary sources (14th-20th centuries). Global and Planetary Change 182: 102997. https://doi.org/10.1016/j.gloplacha.2019.102997

Benito G, Díez-Herrero A, Fernández de Villalta M. 2003. Magnitude and frequency of flooding in the Tagus basin (Central Spain) over the last millennium. Climatic Change 58: 171-192. https://doi.org/10.1023/A:1023417102053

Benito G. 2006. Riesgos de inundaciones: tendencias históricas y perspectivas de acuerdo con el cambio climático. Cuaternario y Geomorfología 20: 29-44. https://core.ac.uk/download/pdf/36016472.pdf

Benito G, Brázdil R, Herget J, Machado MJ. 2015. Quantitative historical hydrology in Europe. Hydrology and Earth System Sciences 19: 3517-3539. https://doi.org/10.5194/hess-19-3517-2015

Blöschl G, Kiss A, Viglione A, Barriendos M, Böhm O, Brázdil R, Coeur D, Demarée G, Llasat MC, Macdonald N, Retsö D, Roald L, Schmocker-Fackel P, Amorim I, Bělínová M, Benito G, Bertolin C, Camuffo D, Cornel D, Doktor R, Elleder L, Enzi S, Garcia JC, Glaser R, Hall J, Haslinger K, Hofstätter M, Komma J, Limanówka D, Lun D, Panin A, Parajka J, Petrić H, Rodrigo FS, Rohr C, Schönbein J, Schulte L, Silva LP, Toonen WHJ, Valent P, Waser J, Wetter O. 2020. Current European flood-rich period exceptional compared with past 500 years. Nature 583: 560-566. https://doi.org/10.1038/s41586-020-2478-3

Brázdil R, Kundzewicz ZW, Benito G. 2006. Historical hydrology for studying flood risk in Europe. Hydrological Sciences Journal 51: 739-764. https://doi.org/10.1623/hysj.51.5.739

Cremades CV. 2017. Rogativas pro-pluvia y pro-serenitate en la cuenca del Segura durante la PEH: la información suministrada por el Archivo Diocesano de Orihuela. In: Riesgo, desastre y miedo en la península Ibérica y México durante la Edad Moderna (Alberola Romá A, Ed.). Universidad de Alicante/El Colegio de Michoacán, 47-69. Available at: https://rua.ua.es/dspace/bitstream/10045/71200/1/2017_Cremades-Prieto_Rogativas-pro-pluvia-y-pro-serenitate.pdf

Del Moral L. 1991. La obra hidráulica en la cuenca baja del Guadalquivir (siglos XVIII-XX). Gestión del agua y organización del territorio. Junta de Andalucía y Universidad de Sevilla, Spain.

Del Moral L. 1992. El Guadalquivir y la transformación urbana de Sevilla (siglos XVIII-XX). Ayuntamiento de Sevilla, Spain.

DGPCE. 2019. Catálogo nacional de inundaciones históricas. Dirección General de Protección Civil y Emergencias, Ministerio del Interior de España. Avalaible at: https://www.proteccioncivil.es/catalogo/naturales/cnih/cnih2014/Presentacion.html (accessed on September 11, 2019).

Do Ó A, Roxo MJ. 2008. Drought events in Southern Portugal from the 12th to the 19th centuries: Integrated research from descriptive sources. Natural Hazards 47: 55-63. https://doi.org/10.1007/s11069-007-9196-0

Eddy JA. 1976. The Maunder minimum. Science 192: 1189-1202. https://doi.org/10.1126/science.192.4245.1189

Fernández-Fernández MI, Gallego MC, Domínguez-Castro F, Trigo RM, García JA, Vaquero JM, González JMM, Durán JC. 2014. The climate in Zafra from 1750 to 1840: history and description of weather observations. Climatic Change 126: 107-118. https://doi.org/10.1007/s10584-014-1201-5

Fragoso M, Marques D, Santos JA, Alcoforado MJ, Amorim I, Garcia JC, Silva L, De Fátima Nunes M. 2015. Climatic extremes in Portugal in the 1780s based on documentary and instrumental records. Climate Research: 66: 141-159. https://doi.org/10.3354/cr01337

Gallego MC, García JA, Vaquero JM, Mateos VL. 2006. Changes in frequency and intensity of daily precipitation over the Iberian Peninsula. Journal of Geophysical Research 111: D24105. https://doi.org/10.1029/2006JD007280

García Codrón J. 2004. Las ciudades españolas y el riesgo de inundación: permanencia y cambio de un problema crónico. Boletín de la Asociación de Geógrafos Españoles 37: 85-99.

García Martínez B. 2003. Interpretación paleohidrológica (ss. XVI-XX) del tramo bajo continental del río Guadalquivir a través de sus inundaciones y meandros. In: Geografía de Andalucía. Asociación de Profesores de Geografía e Historia de Bachillerato de Andalucía, Spain, 173-213.

García-Barrón L, Aguilar-Alba M, Sousa A. 2011. Evolution of annual rainfall irregularity in the southwest of the Iberian Peninsula. Theoretical and Applied

Climatology 103: 13-26. https://doi.org/10.1007/s00704-010-0280-0

García-Barrón L, Morales J, Sousa A. 2013. Characterization of the intra-annual rainfall and its evolution (1837-2010) in the southwest of the Iberian Peninsula. Theoretical and Applied Climatology 114: 445-457. https://doi.org/10.1007/s00704-013-0855-7

García-Barrón L, Aguilar-Alba M, Morales J, Sousa A. 2018. Intra-annual rainfall variability in the Spanish hydrographic basins. International Journal of Climatology 38: 2215-2229. https://doi.org/10.1002/joc.5328

García-Martínez B, Baena R. 2006. El impacto de las infraestructuras de la ciudad de Sevilla sobre el paisaje fluvial del río Guadalquivir. In: Ríos y ciudades europeas: espacios naturales, culturales y productivos (Baena R, Guerrero I, Posada JC, López E, Eds.). I Encuentro Internacional de Ciudades Fluviales Europeas. Universidad de Sevilla, Spain, 119-128. Available at: https://idus.us.es/handle/11441/62088#.XxWDv3p_at0.mendeley

Glaser R, Riemann D, Schönbein J, Barriendos M, Brázdil R, Bertolin C, Camuffo D, Deutsch M, Dobrovolný P, van Engelen A, Enzi S, Halíčková M, Koenig SJ, Kotyza O, Limanówka D, Macková J, Sghedoni M, Martin B, Himmelsbach I. 2010. The variability of European floods since AD 1500. Climatic Change 101: 235-256. https://doi.org/10.1007/s10584-010-9816-7

Grove AT. 2001. The “Little Ice Age” and its geomorphological consequences in Mediterranean Europe. Climatic Change 48: 121-136. https://doi.org/10.1023/A:1005610804390

Kjeldsen TR, Macdonald N, Lang M, Mediero L, Albuquerque T, Bogdanowicz E, Brazdil R, Castellarin A, David V, Fleig A, Gül GO. 2014. Documentary evidence of past floods in Europe and their utility in flood frequency estimation. Journal of Hydrology 517: 963-973. https://doi.org/10.1016/j.jhydrol.2014.06.038

León P, García-Martínez B, Langa Nuño C. 2020. El estudio de las inundaciones históricas en Sevilla a través de fuentes periodísticas (siglo XX). Estudios sobre el Mensaje Periodístico 26: 177-188. https://doi.org/10.5209/esmp.67297

Luterbacher J, Xoplaki E, Dietrich D, Rickli R, Jacobeit J, Beck C, Gyalistras D, Schmutz C, Wanner H. 2002. Reconstruction of sea level pressure fields over the Eastern North Atlantic and Europe back to 1500. Climate Dynamics 18: 545-562. https://doi.org/10.1007/s00382-001-0196-6

Machado MJ, Benito G, Barriendos M, Rodrigo FS. 2011. 500 Years of rainfall variability and extreme hydrological events in southeastern Spain drylands. Journal of Arid Environments 75: 1244-1253. https://doi.org/10.1016/j.jaridenv.2011.02.002

Martín-Vide J, Barriendos M. 1995. The use of rogation ceremony records in climatic reconstruction: a case study from Catalonia (Spain). Climatic Change 30: 201-221. https://doi.org/10.1007/BF01091842

Morbidelli R, García-Marín AP, Mamun AA, Atiqur RM, Ayuso-Muñoz JL, Taouti MB, Baranowski P, Bellocchi G, Sangüesa-Pool C, Bennett B, Oyunmunkh B, Bonaccorso B, Brocca L, Caloiero T, Caporali E, Caracciolo D, Casas-Castillo MC, Catalini CG, Chettih M, Chowdhury AFMK, Chowdhury R, Corradini C, Custò J, Dari J, Diodato N, Doesken N, Dumitrescu A, Estévez J, Flammini A, Fowler HJ, Freni G, Fusto F, García-Barrón L, Manea A, Goenster-Jordan S, Hinson S, Kanecka-Geszke E, Kar KK, Kasperska-Wołowicz W, Krabbi M, Krzyszczak J, Llabrés-Brustenga A, Ledesma JLJ, Liu T, Lompi M, Marsico L, Mascaro G, Moramarco T, Newman N, Orzan A, Pampaloni M, Pizarro-Tapia R, Torres AP, Rashid MDM, Rodríguez-Solà R, Manzor MS, Siwek K, Sousa A, Timbadiya PV, Filippo T, Vilcea MG, Viterbo F, Yoo C, Zeri M, Zittis G, Saltalippi C. 2020. The history of rainfall data time-resolution in a wide variety of geographical areas. Journal of Hydrology 590: 125258. https://doi.org/10.1016/j.jhydrol.2020.125258

Palomo y Rubio, Francisco de Borja. 1878. Historia crítica de las riadas o grandes avenidas del Guadalquivir en Sevilla: desde su reconquista hasta nuestros días. Francisco Álvarez y Compañía, Seville, Spain. Available at: http://www.bibliotecavirtualdeandalucia.es/catalogo/es/consulta/registro.cmd?id=7818

Pfister C, Brázdil R, Glaser R, Barriendos M, Camuffo D, Deutsch M, Dobrovolný P, Enzi S, Guidoboni E, Kotyza O, Militzer S, Rácz L, Rodrigo FS. 1999. Documentary evidence on climate in sixteenth-century Europe. Climatic Change 43: 55-110. https://doi.org/10.1023/A:1005540707792

Rodrigo FS, Esteban-Parra MJ, Pozo-Vázquez D, Castro-Díez Y. 1999. A 500-year precipitation record in Southern Spain. International Journal of Climatology 19: 1233-1253. https://doi.org/10.1002/(SICI)1097-0088(199909)19:11<1233::AID-JOC413>3.0.CO;2-L

Rodrigo FS, Esteban-Parra MJ, Pozo-Vázquez D, Castro-Díez Y. 2000. Rainfall variability in southern Spain on decadal to centennial time scales. International Journal of Climatology 20: 721-732. https://doi.org/10.1002/1097-0088(20000615)20:7<721::AID-JOC520>3.0.CO;2-Q

Rodrigo FS. 2002. Changes in climate variability and seasonal rainfall extremes: A case study from San Fernando (Spain), 1821-2000. Theoretical and Applied Climatology 72: 193-207. https://doi.org/10.1007/s007040200020

Rodrigo FS. 2007. El clima de Andalucía a través de los registros históricos. In: Climate change in Andalusia: Evolution and environmental consequences (Sousa A, García-Barrón L, Jurado V, Eds.). Consejería de Medio Ambiente de la Junta de Andalucía, Sevilla, Spain, 25-41. Available at: http://www.juntadeandalucia.es/medioambiente/web/Bloques_Tematicos/Educacion_Y_Participacion_Ambiental/Educacion_Ambiental/el_cambio_climatico_en_andalucia/capitulo1.pdf

Rodrigo FS, Gómez-Navarro JJ, Montávez Gómez JP. 2012. Climate variability in Andalusia (southern Spain) during the period 1701-1850 based on documentary sources: Evaluation and comparison with climate model simulations. Climate of the Past 8: 117-133. https://doi.org/10.5194/cp-8-117-2012

Rodrigo FS. 2017. Variabilidad climática e inundaciones en Sevilla en la década de 1780 a partir de fuentes documentales. SÉMATA, Ciencias Sociais e Humanidades 29: 165-183.

Rodrigo FS. 2018. A review of the Little Ice Age in Andalusia (Southern Spain): results and research challenges. Cuadernos de investigación geográfica/Geographical Research Letters 44: 245-65. http://doi.org/10.18172/cig.3316

Ruiz-Constán A, Ruiz-Armenteros AM, Galindo-Zaldívar J, Lamas-Fernández F, Sousa JJ, Sanz de Galdeano C, Pedrera A, Martos-Rosillo S, Caro Cuenca M, Delgado JM, Hanssen RF, Gil AJ. 2017. Factors determining subsidence in urbanized floodplains: evidence from MT-InSAR in Seville (southern Spain). Earth Surface Processes and Landforms 42: 2484-2497. https://doi.org/10.1002/esp.4180

Sousa A, García-Murillo P. 2003. Changes in the wetlands of Andalusia (Doñana Natural Park, SW Spain) at the end of the Little Ice Age. Climatic Change 58: 193-217. https://doi.org/10.1023/A:1023421202961

Sousa A, García-Murillo P, Morales J, García-Barrón L. 2009. Anthropogenic and natural effects on the coastal lagoons in the Southwest of Spain (Doñana Natural Park). ICES Journal of Marine Science 66: 1508-1514. https://doi.org/10.1093/icesjms/fsp106

Sousa A, García-Murillo P, Sahin S, Morales J, García-Barrón L. 2010. Wetland place names as indicators of manifestations of recent climate change in SW Spain (Doñana Natural Park). Climatic Change 100:525-557. https://doi.org/10.1007/s10584-009-9794-9

Sousa A, Morales J, García-Barrón L, García-Murillo P. 2013. Changes in the *Erica ciliaris* Loefl. ex L. peat bogs of southwestern Europe from the 17th to the 20th centuries. The Holocene 23: 255-269. https://doi.org/10.1177/0959683612455545

Sousa A, García-Barrón L, García-Murillo P, Vetter M, Morales J. 2015. The use of changes in small coastal Atlantic brooks in southwestern Europe as indicators of anthropogenic and climatic impacts over the last 400 years. Journal of Paleolimnology 53: 73-88. https://doi.org/10.1007/s10933-014-9809-z

Tejedor E, de Luis M, Barriendos M, Cuadrat JM, Luterbacher J, Saz MÁ. 2019. Rogation ceremonies: A key to understanding past drought variability in northeastern Spain since 1650. Climate of the Past 15: 1647-1664. https://doi.org/10.5194/cp-15-1647-2019

Trigo R, Pozo-Vázquez D, Osborn T, Castro-Díez Y, Gámiz-Fortis S, Esteban-Parra MJ. 2004. North Atlantic oscillation influence on precipitation, river flow and water resources in the Iberian Peninsula. International Journal of Climatology 24: 925-944. https://doi.org/10.1002/joc.1048

Uribelarrea D, Benito G. 2008. Fluvial changes of the Guadalquivir river during the Holocene in Córdoba (Southern Spain). Geomorphology 100: 14-31. https://doi.org/10.1016/j.geomorph.2007.04.037

Usokin IG. 2017. A history of solar activity over millennia. Living Reviews in Solar Physics 14: 3. https://doi.org/10.1007/s41116-017-0006-9

Vallejo I. 2000. Las inundaciones en la cuenca del Guadalquivir. Serie Geográfica 9: 133-149.

Vanney JR. 1970. L´hydrologie du bas Guadalquivir. Consejo Superior de Investigaciones Científicas (CSIC), Departamento de Geografía Aplicada, Madrid.

Wilhelm B, Ballesteros-Cánovas JA, Macdonald N, Toonen WHJ, Baker V, Barriendos M, Benito G, Brauer A, Corella JP, Denniston R, Glaser R, Ionita M, Kahle M, Liu T, Luetscher M, Macklin M, Mudelsee M, Munoz S, Schulte L, George SS, Stoffel M, Wetter O. 2019. Interpreting historical, botanical, and geological evidence to aid preparations for future floods. Wiley Interdisciplinary Reviews: Water 6: 1-22. https://doi.org/10.1002/wat2.1318

Zamora F. 2014. “Quando el agua llegare aquí Sevilla...”. La avenida del río Guadalquivir en 1626 según un documento de la Biblioteca da Ajuda (Portugal). Historia. Instituciones. Documentos 41: 407-431. https://doi.org/10.12795/hid.2014.i41.13

Supplementary material

Appendix I. Impact and overflow levels applied to the three flood indices with which the historical floods of the Guadalquivir River between 1250 and 1800 A.D. were characterized, as well as the criteria and filters used to categorize the impacts.

Index Flood	Overflow level and impact	Main criteria	Secondary criteria	Filters to modulate the classification of the impact
I	Closing the gates of the city of Seville and the spindles. Flooding of extramural neighborhoods, with the evacuation of the flood plain in the vicinity of Seville.	a) Height reached by the overflow on the wall. b) Damage caused by the collapse of buildings. c) Number of people drowned.	d) Evacuation of extramural buildings. e) Livestock mortality. f) Effects on the floating bridge or on the ships in the harbour. g) Rogations and other religious ceremonies.	The relevance with which a flood appears in the compilation of events. The recognition of a flood byte authors and comparisons with similar events. Whether the floods are included in the main records or only in particular references.
II	Alarm in the city with the rampart or gates endangered. Collapsed buildings. Inundation in the lower intramural areas.			
III	Serious generalized catastrophic situation in the entire city, except in higher areas.			

Appendix II. Years of significant Guadalquivir River flooding (1297-1876) with indication of the month of the maximum overflow of the river and estimated severity index. For the 13th and 14th centuries the historical source only indicates the year and during the 19th century the severity index is not applicable.

Century	Year	Month	Index
13th	1297	-	3
14th	1330	-	2
	1351	-	1
	1353	-	2
	1363	-	1
	1373	-	1
	1383	-	2
15th	1403	November	3
	1435	February	2
	1481	December	1
	1485	February	3
	1488	December	1
16th	1507	November	1
	1522	January	1
	1544	January	2
	1554	January	2
	1590	March	2
	1591	March	1
	1592	December	1
	1595	November	3
	1596	Mai	1
	1597	January	1
17th	1603	December	1
	1608	March	1
	1618	March	2
	1626	January	3
	1633	September	1
	1642	January	1
	1649	April	3
	1683	January	3
	1691	March	1
	1697	Mai	1

Appendix II. Years of significant Guadalquivir River flooding (1297-1876) with indication of the month of the maximum overflow of the river and estimated severity index. For the 13th and 14th centuries the historical source only indicates the year and during the 19th century the severity index is not applicable.

Century	Year	Month	Index
18th	1707	March	3
	1709	February	1
	1736	April	1
	1739	December	1
	1740	January	0
	1745	February	1
	1750	October	1
	1758	January	3
	1777	February	2
	1784	January	2
	1786	March	1
	1792	January	1
	1796	November	2
19th	1802	December	-
	1804	January	-
	1806	April	-
	1821	January	-
	1823	January	-
	1830	January	-
	1831	January	-
	1838	February	-
	1839	December	-
	1841	January	-
	1843	March	-
	1845	January	-
	1846	January	-
	1852	December	-
	1855	March	-
	1856	January	-
	1858	November	-
	1860	December	-
	1862	January	-
	1866	March	-
	1867	January	-
	1872	January	-
	1876	December	-

Appendix III. Other documentary sources consulted

Ariño F de. 1873. Sucesos de Sevilla de 1592 á 1604. Imprenta de Rafael Tarascó y Lassa. Biblioteca virtual de Andalucía. Available at: http://www.bibliotecavirtualdeandalucia.es/catalogo/es/consulta/registro.cmd?id=1017773 (accessed on September 22, 2019).

Barrantes Maldonado P. 1868. Corónica de rey don Enrique Tercero deste nombre en la casa de Castilla y de León, que otros llaman el doliente, hijo del rey don Juan el primero. 1541. Biblioteca Digital Real Academia de la Historia. Available at: https://bibliotecadigital.rah.es/es/consulta/registro.do?control=RAH20100000502 (accessed on September 26, 2019).

Bernáldez A. 1870. Historia de los Reyes Católicos Don Fernando y Doña Isabel. S. XVII. Biblioteca virtual de Andalucía. Available at: http://www.bibliotecavirtualdeandalucia.es/catalogo/es/consulta/registro.cmd?id=1000499 (accessed on September 6, 2019).

Delgado F. 1785. Leccion histórico-político-médica de las enfermedades que pueden seguirse de resultas de la pasada inundacion del Guadalquivir. Memorias Académicas de la Real Sociedad de Medicina y demás ciencias de Sevilla, tomo III, pp. 58-77.

Nieto Piña C. 1785. Varias reflexiones sobre las inundaciones del río en Sevilla, sus efectos y causas evitables. Memorias Académicas. Tomo III. Archivo de la Regia Sociedad. Real Academia de Medicina, pp. 336-360.

Ortiz de Zúñiga D. 1677. Anales eclesiásticos y seculares de la muy noble y muy leal ciudad de Sevilla. Imprenta Real. Madrid. Biblioteca virtual Andalucía. Available at: http://www.bibliotecavirtualdeandalucia.es/catalogo/es/consulta/registro.cmd?id=1013983 (accessed on September 11, 2019).

Trigueros CM. 1784. La riada. Ofic. de Vázquez y Comp. Available at: https://archive.org/details/A253289 (accessed on September 11, 2019).

Vera Limón D. 1797. De los perjuicios médicos que causan las inundaciones del Guadalquivir, modo de precaver y de corregirlo. Memorias Académicas de la Regia Sociedad de Medicina y demás ciencias de Sevilla, leg. 1797.

Ximénez de Lorite B. 1778. Causas físicas de las inundaciones de Sevilla. Perjuicios que causan a la salud pública y modo de remediarlos. Academia de Medicina de Sevilla, leg. 1778.

Zapata C. 1787. Si el agua de los ríos en sus inundaciones tengan algunos perjuicios para el uso interno o externo de ellas, quáles sean, y modo de examinarlas. En: Memorias académicas de la Regia Sociedad de Medicina y demás Ciencias de Sevilla, V, leg. 1786, pp. 95-107

Atmósfera 36(1), 23-39 (2023)
https://doi.org/10.20937/ATM.53017

Behavior of the ITCZ second band near the Peruvian coast during the 2017 coastal El Niño

Vannia ALIAGA-NESTARES*, Diego RODRÍGUEZ-ZIMMERMANN and Nelson QUISPE-GUTIÉRREZ

Subdirección de Predicción Meteorológica, Servicio Nacional de Meteorología e Hidrología, Jesús María, 15072, Lima, Perú.
*Corresponding author; email: valiaga@senamhi.gob.pe

Received: December 11, 2020; accepted: May 31, 2021

RESUMEN

En este estudio se analiza el comportamiento de la segunda banda de la Zona de Convergencia Intertropical (ZCIT) cerca de la costa peruana a inicios de 2017 usando precipitación, vientos superficiales, temperatura superficial del mar y variables atmosféricas en diferentes niveles isobáricos. Además, se propone un índice diario (Ia) para identificar de manera oportuna la formación de esta segunda banda y se considera el análisis de los términos de energía de Lorenz en la región. Esta banda estuvo presente desde los últimos días de enero hasta los primeros días de abril de 2017, asociada con un dipolo anómalo de presión reducida a nivel del mar hacia el este y el oeste del Pacífico Ecuatorial oriental, lo cual configuró vientos superficiales anómalos del norte y relajación de los vientos alisios del sur cerca de la costa peruana. En niveles medios de la troposfera, a inicios de marzo, se observó una anomalía positiva de relación de mezcla proveniente del este sobre la región de la segunda banda de la ZCIT, asociada con sistemas de precipitación intensos sobre la costa norte de Perú. En el mismo periodo se observaron anomalías positivas de divergencia en niveles altos. El índice diario Ia permitió la detección oportuna de la segunda banda de la ZCIT 11 días antes del máximo de precipitación en el norte de la costa peruana, y los términos de energía de Lorenz mostraron picos de energía cinética de las perturbaciones (K_E) en enero y febrero, así como contribución de la inestabilidad barotrópica en regiones ecuatoriales.

ABSTRACT

The behavior of the second band of the Intertropical Convergence Zone (ITCZ) near the Peruvian coast during early 2017 is studied, using precipitation, surface winds, sea surface temperature (SST) and atmospheric variables in different isobaric levels. The proposal of a daily index (Ia) to identify opportunely the formation of this band and the Lorenz energy terms in the region is also considered. This band was present from late January to early April 2017, associated with an anomalous dipole of sea level pressure between the east and west eastern Equatorial Pacific that configured anomalously northerly surface winds and the release of southeasterly trade winds near Peru. In medium levels, a zonally oriented positive mixing ratio anomaly was observed in early March over the ITCZ second band, associated with heavy rain systems over the northern Peruvian coastal region. In the same period, positive anomalies of divergence in high tropospheric levels were observed. The daily Ia index allowed an effective detection of the ITCZ second band 11 days before the maximum coastal precipitation, and the Lorenz energy terms showed eddy kinetic energy (K_E) peaks in January and February and a contribution of barotropic instability in equatorial regions.

Keywords: ITCZ, 2017 coastal El Niño, Lorenz energy.

1. Introduction

Between February and March of 2017, extreme precipitation was registered along the north and central coast and highlands of Peru, reaching values over 120 mm/day in north coastal cities, where the monthly average is 28 mm (Figs. 1 and 2), associated with an abnormal warming of the sea surface temperature (SST) above 28 ºC (Garreaud, 2018) in El Niño 1+2 region, mainly during March.

According to Rodríguez-Morata et al. (2018), the rainfall recorded between January and March 2017 can only be compared with the extreme El Niño events of the last 40 years, and exceeded the 90th percentile (1981-2017), causing floods and landslides (locally known as huaicos) in the arid coast zone. These hydrometeorological events were caused by an unusual type of El Niño, the coastal El Niño (Takahashi and Martínez, 2017; Takahashi et al., 2018).

According to Ramírez and Briones (2017), economic losses due to coastal El Niño-related precipitation were estimated at USD 3.1 billion and affected over 1 million people (INDECI, 2017), with at least 113 killed and nearly 40 000 homes destroyed (Fraser, 2017). The most affected Peruvian regions were Piura, Lambayeque, La Libertad and Lima. An array of infectious diseases, like dengue, chikungunya, zika and leptospirosis, also were reported (Ramírez and Briones, 2017), triggered by stagnant water, increased humidity and warm air temperatures observed during this period (1-2.5 ºC above its normal between January and March) (ENFEN, 2017a, b).

2. The 2017 coastal El Niño (CEN)

Echevin et al. (2018) did a complete analysis of the 2017 CEN and concluded that the initial warming was

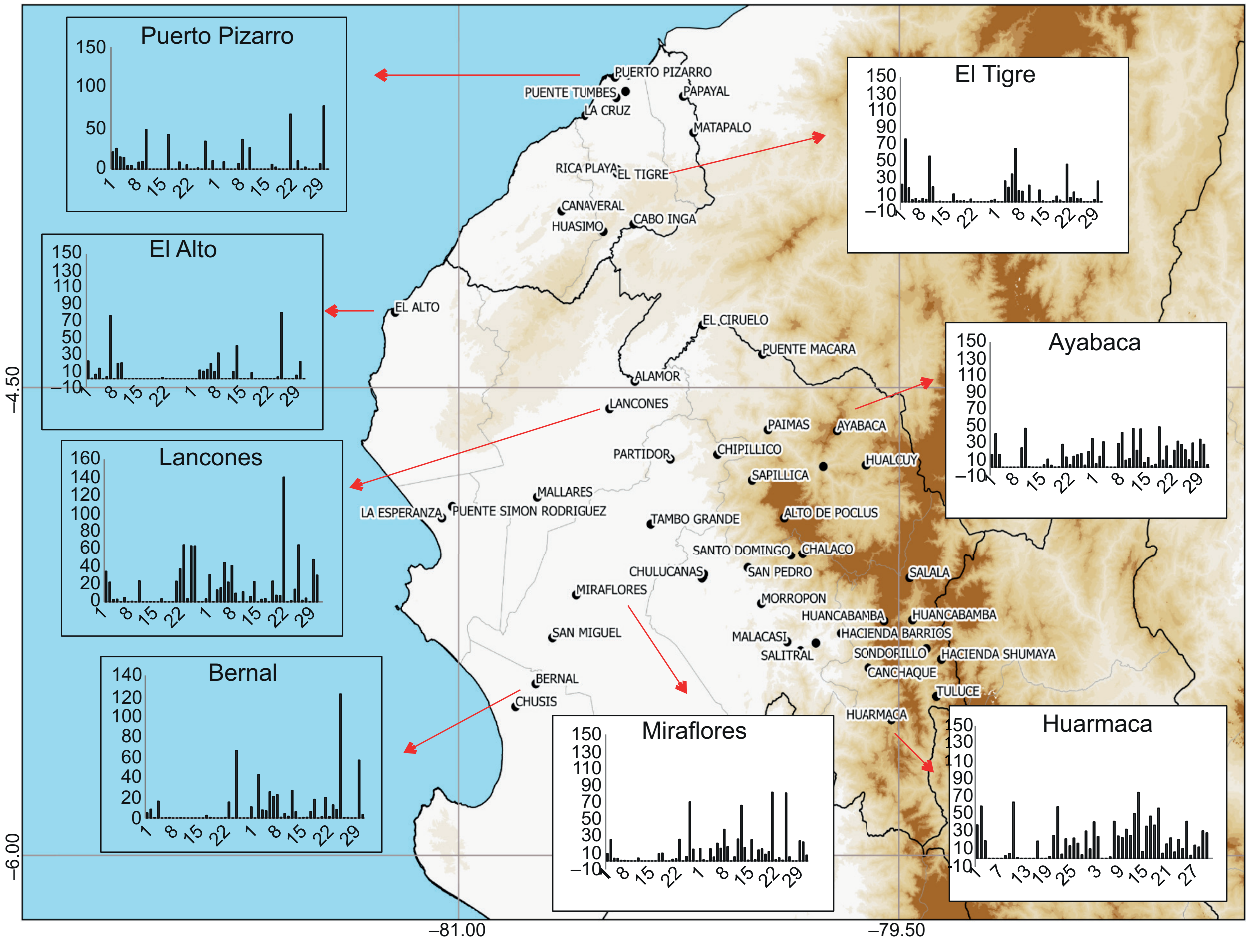

Fig. 1. Daily precipitation during February and March, 2017 in Tumbes and Piura.

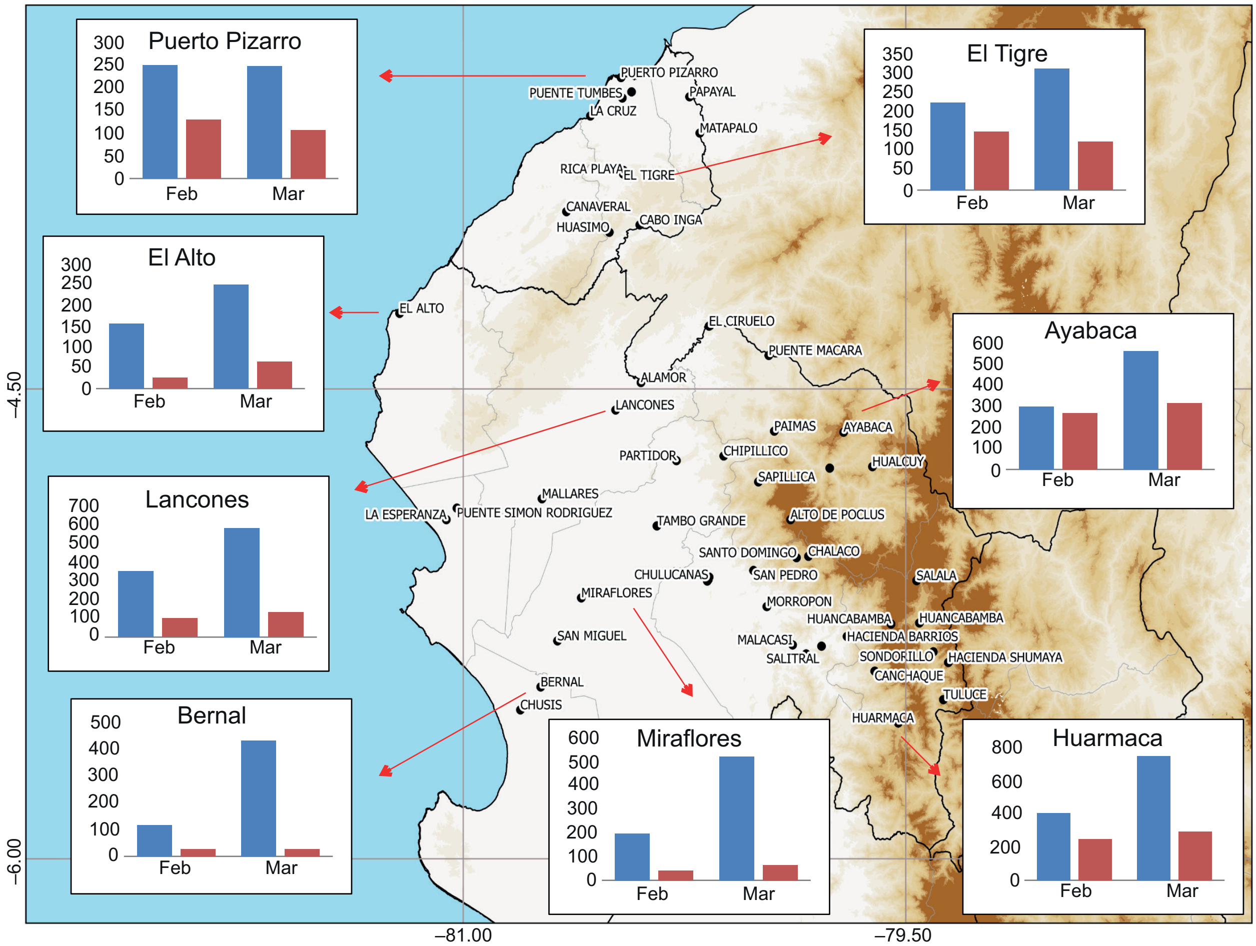

Fig, 2. Monthly precipitation during February and March, 2017 in Tumbes and Piura (2017 monthly accumulated: blue; normal monthly accumulated: red).

mainly associated with a regional decrease of winds in the far-eastern Pacific from late 2016 to January 2017. This wind relaxation reduced the coastal upwelling and vertical mixing in the top ocean layers, generating a positive SST anomaly off northern Peru and Ecuador, which resulted on an alongshore temperature gradient.

During February and March (FM), the Ekman pumping negative anomaly may have deepened the thermocline, generating anomalously warm source waters. Peng et al. (2019) concluded that both the downwelling oceanic Kelvin waves, observed in December 2016 (ENFEN, 2017a), and local northerly alongshore wind anomalies were necessary for an extreme CEN. The latter caused the average magnitude of the southeast trade winds in the austral summer of 2017 to be one of the lowest in the 1948-2016 period, favored by anomalous easterly winds in the mid- and upper troposphere, which did not contribute to the tropospheric sinking and strengthening of the trade winds (Garreaud, 2018). According to Hu et al. (2019), the formation of the 2017 CEN was largely driven by ocean heat flux anomalies, associated with westerly surface wind anomalies in the equatorial far-eastern Pacific, mainly during January, the biggest for that month since 1981 (Takahashi et al., 2018).

Although coastal El Niño and basin-scale El Niño occur simultaneously most of the time, so that Niño 3.4 and Niño 1+2 indices are positively correlated (Hu et al., 2019), FM Peruvian coastal warming is not always preceded by a basin-scale Niño. In fact, the strong event of 2017 was preceded by a weak basin-scale La Niña (Xie et al., 2018; Peng et al., 2019).

The first CEN analyzes were done by Takahashi and Martínez (2017), focused on the events of 1891 and 1925. These CEN were generated by strong northerly winds across the equator in the equatorial eastern Pacific and the strengthening of the Intertropical Convergence Zone (ITCZ) south of the equator.

Hu et al. (2019) identified seven CEN between 1979 and 2017, which were driven by three different mechanisms. The CEN of 1983, 1987 and 1998, as they occurred immediately after extreme/strong El Niño, were driven by an equatorially centered ITCZ that generated anomalously strong convection in the eastern tropical Pacific, leading to the relaxation of the southeast trade winds suppressing the wind-forced upwelling and resulting in warming in the eastern tropical Pacific. The CEN of 2014 and 2015 were associated with thermocline fluctuations driven by eastward propagation of a downwelling Kelvin wave, warming the eastern tropical Pacific. Lastly, the CEN of 2008 and 2017 were associated with westerly surface wind anomalies in the eastern equatorial Pacific and largely driven by ocean surface heat flux. As far as the frequency of extreme CEN, there is an increase in a warming climate (Peng et al., 2019).

One of the main factors that favored the extreme rain in the CEN was related to the development of the second band (south band) of the eastern Pacific ITCZ. Here, we show a detailed analysis of the behavior of this band during early 2017, associated with a synoptic circulation and energetic analysis. A description of the ITCZ second band is detailed in section 2, followed by a description of the data and methodology used in this research (section 3). In section 4 the results are shown and discussed. Finally, in part V the conclusions of this study are presented.

3. The ITCZ second band

The interannual variability of eastern Pacific convection during February-March-April (FMA) has two modes. One with intensified deep convection centered on the equator (single ITCZ), and one with a meridional dipole with little signals on the equator (double ITCZ) (Xie et al., 2018; Yu and Zhang, 2018), due to a cold tongue or lower SST present between the two bands of the ITCZ (Zhang, 2001; Gu et al., 2005). In the latter, there are maximum precipitation anomalies to either side of the equator. These two ITCZ bands develop early during the austral autumn (March-April) in the eastern Pacific (90º-130º W), which coincides with the maximum SST in the equator and south of it, and with the seasonal weakening of southeasterly trade winds (Gu et al., 2005). Likewise, during El Niño events, the ITCZ bands vary according to the ENSO pattern present over the eastern Pacific; an extreme El Niño pattern has a strong ITCZ presence over the equator, while a moderate El Niño pattern presents an ITCZ north to the Equator (Peng et al., 2020).

Haffke et al. (2016) carried out a daily analysis of the ITCZ in the eastern Pacific with satellite information, using an identification method proposed by Henke et al. (2012), and found five states of the ITCZ: the double ITCZ state (dITCZ), where an ITCZ is visible on both sides of the equator; the northern state (nITCZ), and the southern state (sITCZ), where only one ITCZ is formed accordingly; the state of non-presence (aITCZ), where there is no significant ITCZ signal; and the equatorial state (eITCZ), where convection in the eastern Pacific is located on the equator and covers a broad north-south band. The sITCZ state can be viewed as an extreme case of the dITCZ state. The ocean-atmosphere interaction in the Central Pacific (CP) La Niña conditions favor the dITCZ and sITCZ states, with higher correlation in the last one (Yang and Magnusdottir (2016); Yu and Zhang (2018).

From 2000 to 2017 there was an increase of the sITCZ (ITCZ second band) formation (Son et al., 2019); hence, its analysis and relationship with the precipitation in the northern coast of Peru is important.

4. Data and methodology

4.1 ITCZ identification Index

Yu and Zhang (2018) proposed an index to identify the ITCZ second band formation, working with monthly precipitation averaged in three areas (Fig. 3), the northeastern equatorial Pacific (NEP; 180º-85º W, 2º-10º N), the southeastern equatorial Pacific (SEP; 150º-85º W, 10º-2º S), and the eastern equatorial Pacific (EEP; 180º-85º W, 2º S-2º N). In this work, these areas are used to calculate the Yu and Zhang index

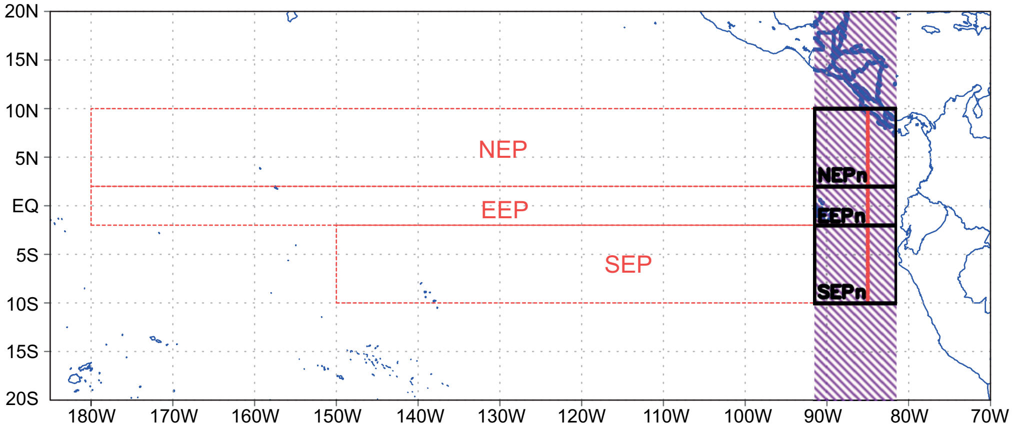

Fig. 3. Areas taken into account for analyzing the ITCZ second band. Yu and Zhang areas (red boxes): NEP (180º-85º W, 2º-10º N), EEP (180º-85º W, 2º S-2º N), SEP (150º-85º W, 10º-2º S). New areas (black boxes): NEPn (91.5º-81.5º W, 2º-10º N), EEPn (91.5º-81.5º W, 2º S-2º N), SEPn (91.5º-81.5º W, 10º-2º S). Purple region is the area considered for temporal wind and precipitation analysis (Fig. 5).

with monthly and daily satellite estimated precipitation data; also, a new area to identify the formation of the ITCZ second band near the Peruvian coast is proposed. The longitudinal limits of this new area are 91.5º-81.5º W (purple area in Fig. 3), and the same latitudinal limits of NEP, SEP and EEP.

To show the behavior of the early 2017 rain in the Peruvian western north, we selected eight stations of the National Service of Meteorology and Hydrology (SENAMHI) network distributed in Tumbes and Piura (Figs. 1 and 2).

Daily and monthly estimated precipitation from of TRMM Multi-Satellite Precipitation Analysis (TMPA) January 1 to April 30, with 0.25º of spatial resolution, were used in this work (Huffman and Bolvin, 2017),

For SST and its anomalies (SSTA), data of the Operational Sea Surface Temperature and Sea Ice Analysis (OSTIA) reanalysis was used with a spatial resolution of 0.25º and 1-day temporal resolution (Donlon et al., 2012).

Data from the Era-Interim reanalysis (Dee et al., 2011) was also used with a spatial resolution of 79 km (~0.75º), a temporal resolution of 6 h and 37 pressure levels (from 1000 to 10 hPa). The data used is of 12:00 UTC from January 1 to April 30 2017, while the 1981-2010 period was used for the climatology, as recommended by WMO (2014).

For the synoptic analysis, 5-day anomalies of surface winds, sea level pressure, 600 hPa mixing ratio and 200 hPa divergence and winds were considered.

The ITCZ could be identified with analyzes of cloud, precipitation or surface winds (Haffke et al., 2016), and precipitation estimated by TMPA-TRMM, which was used in this paper.

To determine the formation of the ITCZ second band, two indices proposed by Yu and Zhang (2018) to characterize interannual variability of the eastern Pacific ITCZ during boreal spring (February to April) were used: the asymmetric index (Ia) and double ITCZ index (Id):

$$Ia = \frac{P_{NEP} - P_{SEP}}{P_m} \quad (1)$$

$$Id = \frac{P_{NEP} - 2P_{EEP} + P_{SEP}}{P_m} \quad (2)$$

where P_{NEP} is the boreal spring precipitation rate averaged in the NEP, P_{SEP} is the precipitation averaged in the SEP, P_{EEP} is the precipitation averaged in EEP, and P_m is the mean precipitation rate in the three regions:

$$P_m = \frac{1}{3}\left(P_{NEP} + P_{EEP} + P_{SEP}\right) \quad (3)$$

A negative Id index indicates single precipitation maximum at the equator, while positive a Id index indicates double ITCZ. The Ia index distinguishes the preference of the ITCZ to the north (Ia > 0) or south (Ia < 0) of the equator, or a symmetric double ITCZ (Ia = 0).

Using these indices with precipitation between 1979 and 2017, Yu and Zhang (2018) identified 13 years with maximum precipitation anomalies to the south of the equator: 1984, 1986, 1989, 1996, 1999, 2000, 2001, 2006, 2008, 2009, 2011, 2012, and 2017.

4.2. Lorenz Energy Cycle

The general circulation of the atmosphere may be approximated as a composition of the mean zonal motion and eddies superposed upon it. This allows the division of kinetic (K) and available potential (A) energy of the atmosphere in two types: zonal (Z) and eddy (E). The zonal component of energy surges due to variance of zonally averaged temperature, while the eddy component of energy is associated with the variance of temperature within the latitude circles. Each type of energy is a source or sink of another type (Lorenz, 1955).

Applying the equations of continuity, thermodynamic and motion, and considering transfer of energy across the boundaries in a limited area, Michaelides (1987) proposed the next equations to express the local variation of A_Z, A_E, K_Z and K_E as:

$$\frac{\partial A_Z}{\partial t} = C_Z\left(K_Z, A_Z\right) - C_A\left(A_Z, A_E\right) + G_Z + BA_Z \tag{4}$$

$$\frac{\partial A_E}{\partial t} = C_A\left(A_Z, A_E\right) - C_E\left(A_E, K_E\right) + G_E + BA_E \tag{5}$$

$$\begin{aligned} \frac{\partial K_Z}{\partial t} = {} & -C_Z\left(K_Z, A_Z\right) + \\ & C_K\left(K_E, K_Z\right) - D_Z + BK_Z + B\Phi_Z \end{aligned} \tag{6}$$

$$\begin{aligned} \frac{\partial K_E}{\partial t} = {} & C_E\left(A_E, K_E\right) - \\ & C_K\left(K_E, K_Z\right) - D_E + BK_E + B\Phi_E \end{aligned} \tag{7}$$

where *Z* and *E* represent zonal and eddy energies, respectively.

According to Lorenz (1967), A_Z represents the amount of available potential energy that would exist if the mass field was replaced by its zonal average, and A_E the excess of available potential energy over A_Z. Likewise, K_Z represents the amount of kinetic energy which would exist if the existing zonally averaged motion, but no eddy motion was present, and K_E, the excess of kinetic energy over K_Z.

In Eqs. (4-7), G_Z represents the generation of zonal available potential energy (A_Z) through the latitudinal differential heating, produced by the diabatic heat sources (Asnani, 1993, 2005). G_E represents the generation of eddy potential energy (A_E) along the same latitude, heating the warm regions and cooling the cold regions, generating gradients of temperature in the same latitude. Physically, the latent heat released due to convection should be an important source of heat and, and consequently of eddy available potential energy (G_E) (Dias, 2010). C_A (A_Z, A_E) represents the conversion of the available potential energy between zonal and eddy forms, associated with meridional and vertical gradients of temperature, transporting sensible heat. In physical terms, the zonal averaged temperature in the troposphere decreases toward the poles, and this gradient generates transport of warm tropical air to polar latitudes and cold polar air to warm latitudes through meridional motions. This process decreases the thermal gradient between latitudes, diminishing A_Z, and increases the thermal gradient at the same latitude, resulting in A_E increases, related to wave motion (troughs and ridges) and it is an intermediate process in the baroclinic chain. C_Z (K_Z, A_Z) indicates the conversion of zonal kinetic energy (K_Z) into zonal available potential (A_Z) through upward movements of warm air in low latitudes and downward movements of cold air in high latitudes. According to Asnani (2005), the Hadley and Ferrel circulations are manifestations of this conversion. Meanwhile, C_E (A_E, K_E) represents the conversion of eddy available potential (A_E) into eddy kinetic energy (K_E) through upward motions of warm air and downward movements of cold air along the same latitude circle. The equatorial Walker circulation would be a manifestation of this process (Aliaga, 2017). C_K (K_E, K_Z) represents the conversion of the kinetic energy between eddy and zonal types. According to Lorenz (1967), there is no process that converts A_Z into K_E or A_E into K_K. D_K and D_E represent the effects of friction (dissipation) by zonal and eddy motions, respectively. Terms with *B* represent energy flux across the boundary. All these terms can be expressed in the diagram in Figure 4.

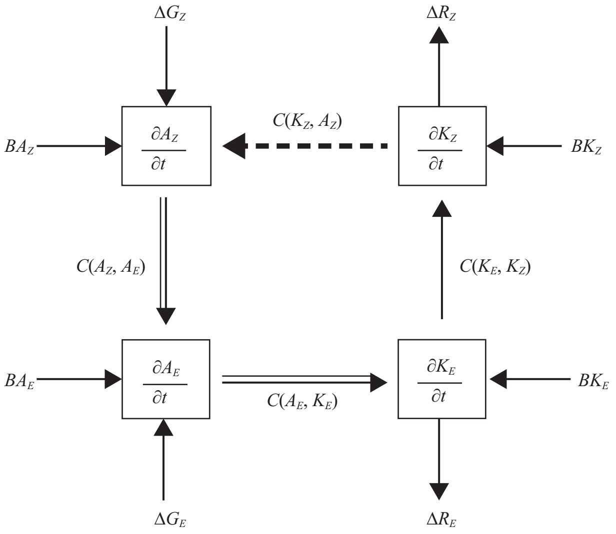

Fig. 4. Diagram of the Lorenz energy cycle (LEC) in a limited area (Michaelides, 1987). Arrows denote the most likely direction of the conversion between energy components for a large-scale mid-latitude region averaged over the passage of many disturbances.

In terms of physical processes in the atmosphere, C_K (K_K, A_K) and C_E (A_E, K_E) are denominated baroclinic terms because they are strongly related to the processes that presents baroclinic instability (Dias, 2010) or thermal gradients. On the other hand, C_K (K_E, K_Z) is called barotropic term (Asnani, 1993, 2005; Dias, 2010).

Studies of the energetics of synoptic systems using Lorenz cycle in a limited area (considering the transfer of energy across boundaries) proposed by Muench (1965) were performed by different authors such as Brennan and Vincent (1980), Michaelides (1987), and Dias and Da Rocha (2011) while researching cyclones; Veiga et al. (2013) used it to study the Walker circulation and its relationship with ENSO; Norquist et al. (1977) and Hsieh and Cook (2007) to evaluate African easterly waves; Da Silva and Satyamurty (2013) in the ITCZ in the South American sector of the Atlantic Ocean; Ramírez et al. (2009) in a work about the energy of the South American rainy season.

Here, the daily temporal variation of integrated energy components in the atmospheric volume in the ITCZ second band near the Peruvian coast was studied, using the LEC in a new SEP area (SEPn) (from –10º to –2º S and from 91.5º to 81.5º W) (Fig. 3) from January 1 to April 30, 2017.

5. Results

5.1. *Temporal variability of the ITCZ's second band near the coast*

The temporal variability of precipitation, SST, and 10 m wind, as well as its anomalies, averaged between 91.5º and 81.5º W in early 2017 (Fig. 4) shows the presence of the ITCZ second band between the end of January and the beginning of April. The highest intensity of the second band occurred during February and March. The south trade wind relaxation reported by Garreaud (2018) and Hu et al. (2019), even with anomalies from the north, is observed during January, February and March, mainly between 5º N and 10º S, and in April returned to its normality (Fig. 4b).

There were two defined periods with formation of the ITCZ second band, determined only by precipitation anomalies: one from the last days of January to the first half of February, and another during March (purple boxes in Fig. 4b). These periods were preceded by an anomalously warm SST since the beginning of January, and by anomalous winds from the north 10 days before (Fig. 4b). It is possible that the relaxation of the southeast trade winds is associated with the behavior of the South Pacific Anticyclone.

Fig. 4b shows that the surface winds were anomalously from the north between January and March, with two main episodes: the second half of January and March, in the 5º N to 10º S strip. This is similar to Echevin et al. (2018), who found that the anomalies of wind stress nearshore and offshore in January 2017 were poleward.

It is observed that the nuclei of maximum precipitation in the ITCZ second band are toward the south of the SST maximum. This is consistent with Gu et al. (2005), who found that the precipitation maximum is out of phase toward the poles of the SST maxima.

SST exceeding the threshold of 27 ºC is one of the main factors that favor the development of the ITCZ second band near the coast (mainly when this value is above its normal by 2º C during FM, at least). This threshold is not necessarily required to maintain the first band (Fig. 4). However, a warming of the SST is not sufficient to generate precipitation alone, the behavior of the wind is also important. According to Yu and Zhang (2018) in the SEP there is no significant relationship between the local SST and precipitation, as there is in the NEP.

In early January, an anomalous westerly wind over the equatorial Pacific was observed, which preceded the formation of the ITCZ second band near the coast between January 31 and February 4, 2017 (Fig. 5). This is congruent with Peng et al. (2019), who manifested that these strong westerly winds, which were the largest for January since 1981 (Takahashi et al., 2018), together with anomalous northerly coastal winds, caused the downwelling Kelvin waves, also found by ENFEN (2017a).

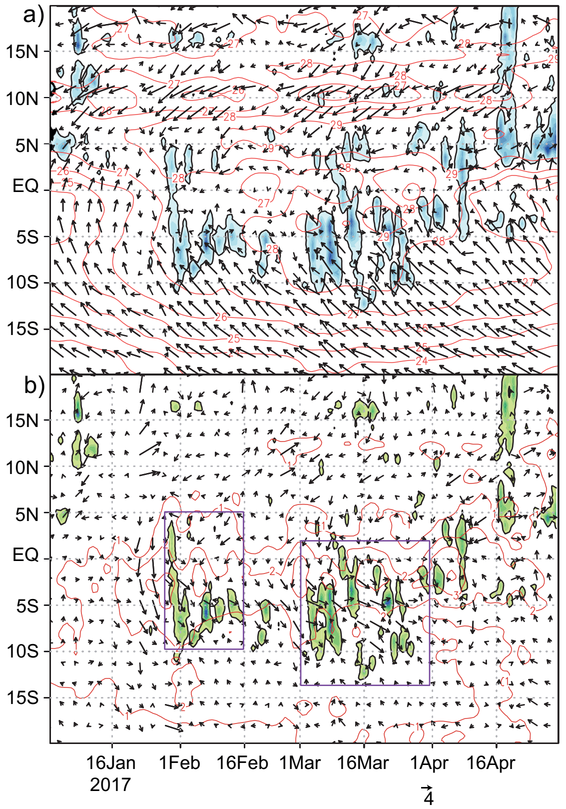

Fig. 5. (a) Daily SST (ºC, contours), daily precipitation (mm day^{-1}, shaded) and 10 m wind (m s^{-1}, vectors). (b) Daily SST anomalies (ºC, contours), daily precipitation anomalies (mm day^{-1}, shaded) and 10 m wind anomalies (m s^{-1}, vectors). The values are averaged between 91.5º and 81.5º W. Purple boxes represent the ITCZ second band events.

Between January 21 and 25 the northerly anomalies in the wind were most prevalent in the analysis region. In the period between February 10-14, the highest intensity of westerly anomalously winds over 110º-90º W was observed, while March was characterized by westerly and northerly anomalous winds (Fig. 5). It is also clear that in the second half of February there was an absence of rainfall in the region.

5.2. Atmospheric circulation

In Fig. 6 we can see that, between January and the first 10 days of February, the MSLP was below its normal in the east of the South Pacific, contrasting with the positive anomaly of MSLP in the equator from 100º W to the west. This contrast of pressure can be associated with the intensification of westerly and northerly winds in the equator close to the Peruvian coast (Fig. 7). This is congruent with Takahashi (2004), who suggested that rainy days during 1997-1998 and 2002 El Niño events were associated with an enhanced onshore westerly low-level flow, which may help the triggering of convection by orographic lifting over the western slope of the Andes.

After that and until February 24, the MSLP was above its normal in the Southeast Pacific, causing a decrease of rainfall in the second half of February (Fig. 5). Then, between the last days of February and the first half of March, the negative MSLP anomaly in the east of the South Pacific returned, favoring a new increase in rainfall close to the equator, near and over the Peruvian coast. During this period, the MJO was more active and influenced the intensification of surface westerlies in the oriental Pacific near the Equator, as explained in Tang and Yu (2008).

The positive SST anomaly near the Peruvian coast was increasing in intensity and area since January 16, which favored the convection producing low-level convergence of the thermally driven boundary layer winds (Lindzen and Nigam, 1987 apud Takahashi, 2004).

In 600 hPa (Fig. 8), the positive anomalies of mixing ratio (MIXR) in the region of the ITCZ second band near the coast developed around January 21-25, with highest intensity between January 31 and February 4 and positive MIXR flux from east to west. From February 10 to March 1, negative anomalies of MIXR in the region of the ITCZ second band can be observed near the coast, associated with the decrease of rainfall in the second half of February (Figs. 5 and 7). In the first half of March, positive anomalies of MIXR were observed in the region of analysis and the flux was from the west (second band of the ITCZ region)

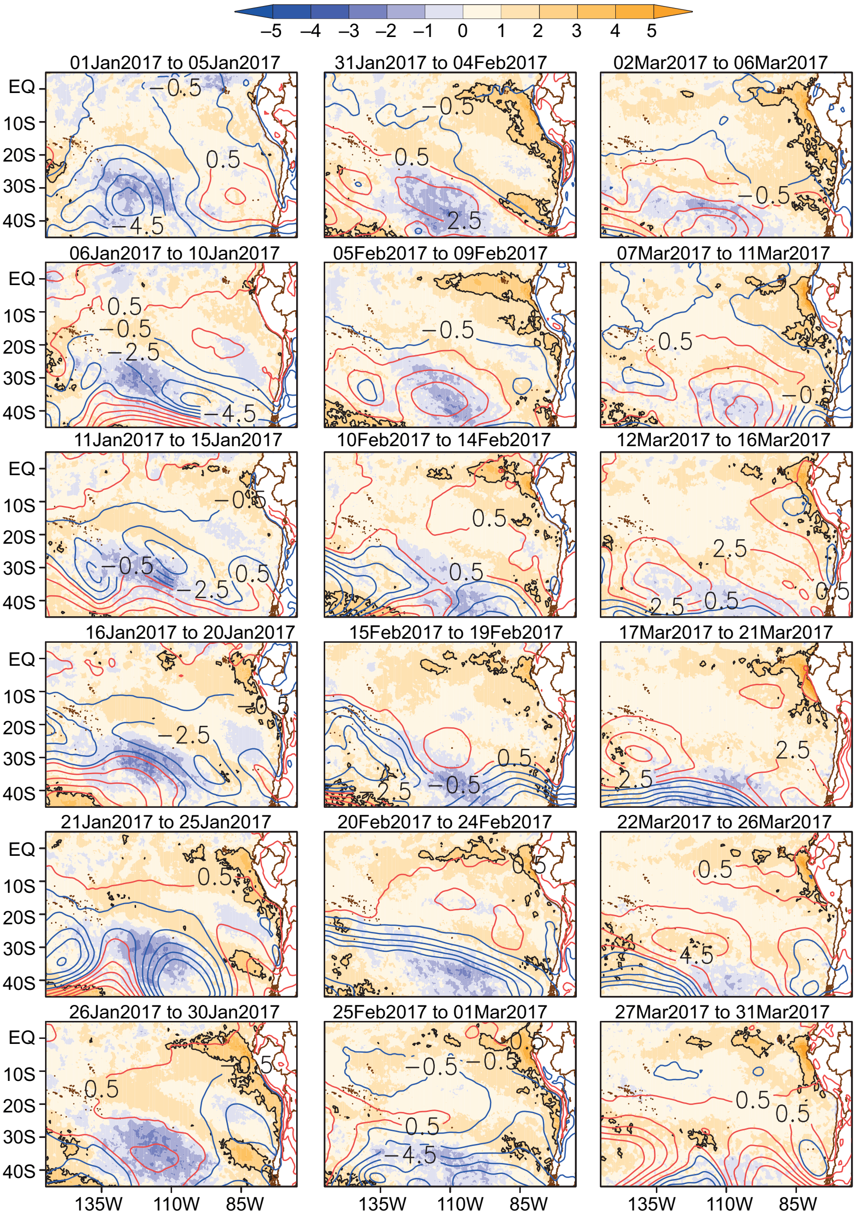

Fig. 6. Five-days mean sea level pressure (hPa, contours) and sea surface temperature (ºC, shaded) anomalies.

to the east (north of Peru), this is similar to what Sulca et al. (2017) found for the the ITCZ eastern Pacific configuration (ITCZE).

In upper levels of the troposphere (250 hPa) (Fig. 9) the anomalous configuration of two anticyclonic systems, one north and another south of the equator (better observed between January 31 and February 4) encouraged the positive anomaly of divergence and anomalous easterly winds in the second band of ITCZ near the coastal region and over the north of Peru, similar to Sulca et al. (2017) and the ITCZE configuration and El Niño 1997-1998 pattern found by Takahashi (2004) and in CEN 2017 (Quispe, 2018). In the second half of February a decrease in divergence was observed, related to a decrease of rainfall in the same period; and an increase between March 7-16 associated to a positive anomaly of precipitation was observed (Fig. 5).

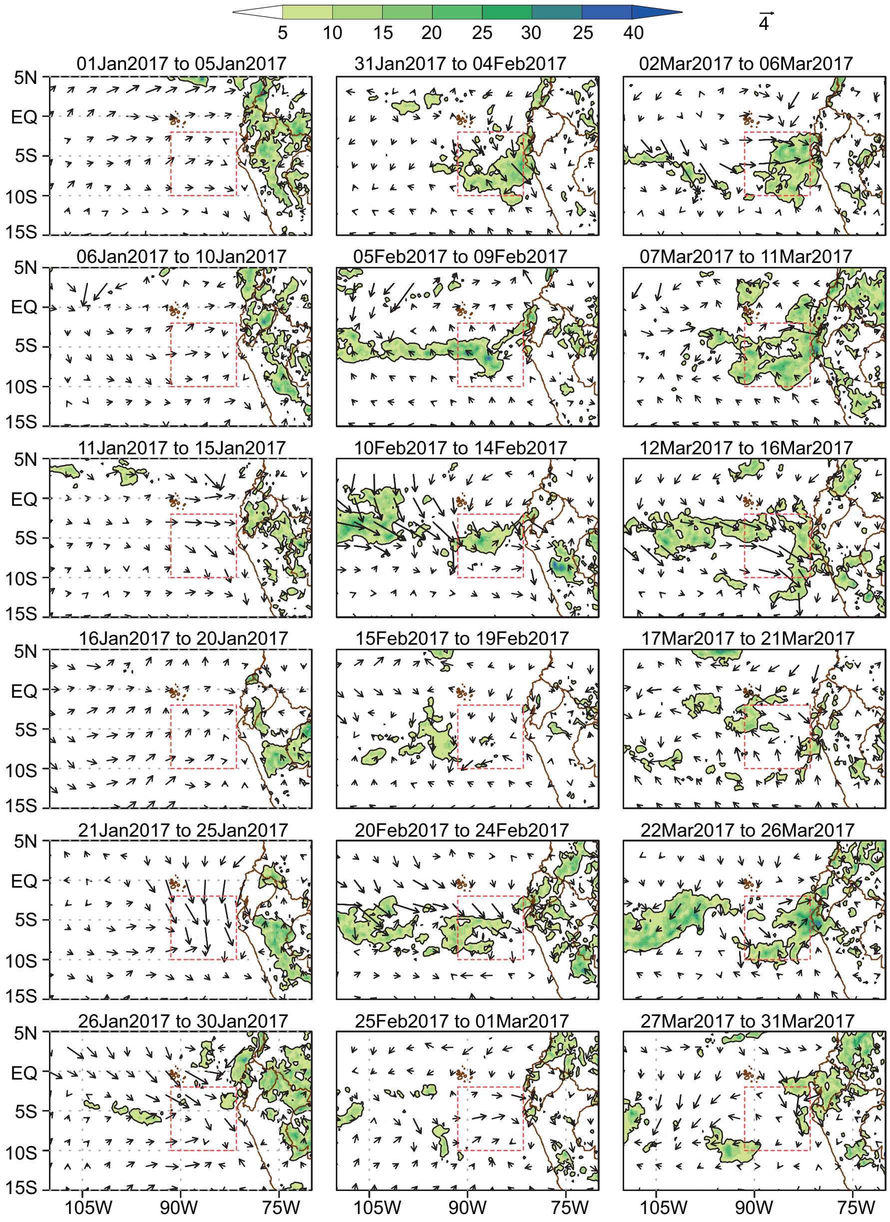

Fig. 7. Five-days precipitation (mm day^{-1}, shaded) and 10 m wind (m s^{-1}, vectors) anomalies. Red boxes represent the new SEP area (SEPn).

5.3. Relationship between precipitation in the Peruvian northwestern region and the formation of the ITCZ second band

Using TRMM monthly precipitation and the Yu and Zhang (2018) methodology (considering Ia < 0.5), we identified eight years with maximum precipitation anomalies to the south of the equator: 1998, 1999, 2000, 2001, 2006, 2009, 2012, and 2017. The majority of these years (80%) coincide with the years found by Yu and Zhang (2018). The differences may be explained by the climatology and the hierarchical clustering used in this research.

With the aim of identifying the daily ITCZ second band formation, we calculated the Ia index considering the areas proposed by Yu and Zhang (2018) (Fig. 10, upper panel) and a new proposed area (Fig. 10, lower panel), and compared them with the daily precipitation gauged in the Bernal coastal station (Fig. 10, middle

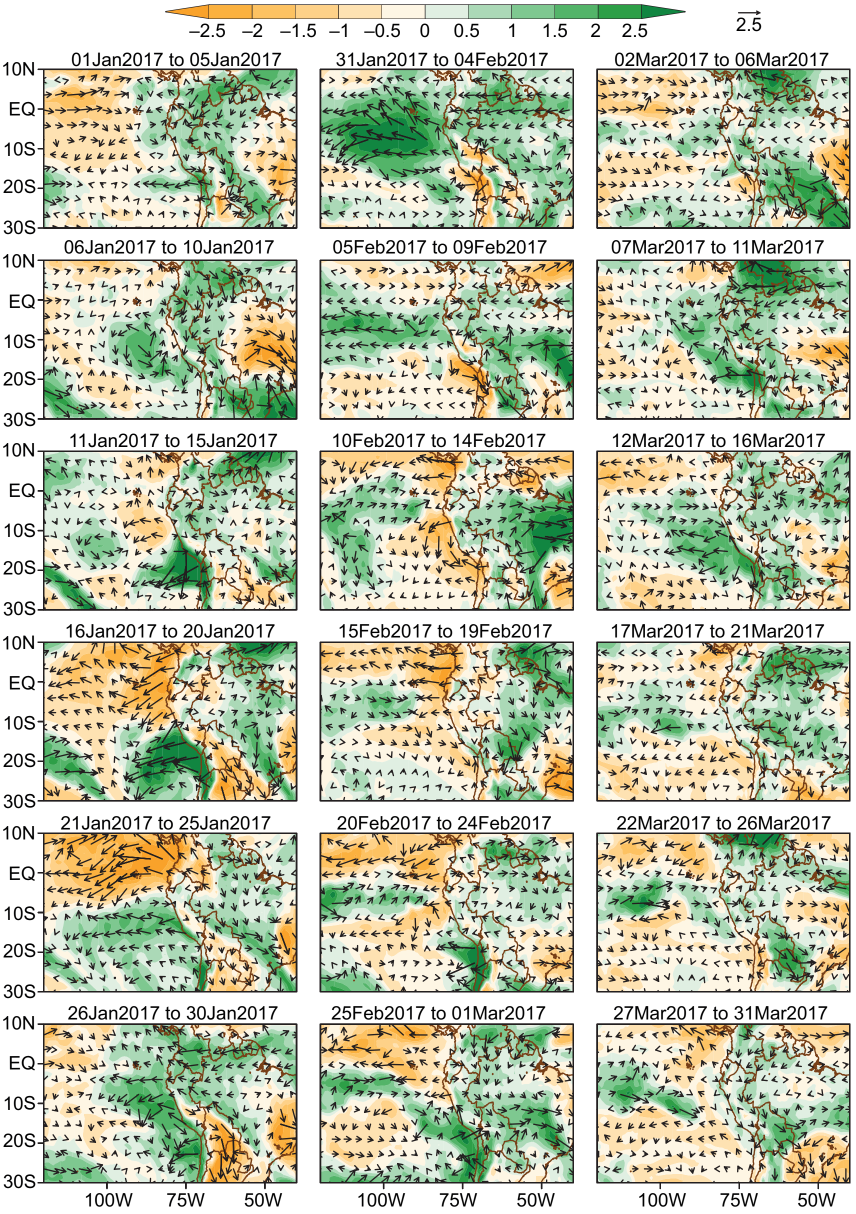

Fig. 8. Five-days anomalies of mixing ratio in 600 hPa (g kg^{-1}, shaded) and anomalies of mixing ratio flux in 600 hPa (vectors).

panel). The first day with an important daily precipitation in Bernal (30 mm) was January 30, and the identification of the ITCZ second band (negative Ia) in new proposed areas was on January 19, 11 days prior to the occurrence of a maximum precipitation. This lag would allow anticipating the occurrence of rain on the coast with more than 10 days of advance; however, this is not possible with the Ia calculated in a total area, which showed a negative value on February 6, one week after the first important daily precipitation in Bernal. This lag may be explained by Sulca et al. (2017), who showed that the integrated moisture transport in periods with positive ITCZE index (ITCZ for the eastern Pacific) is from the west to the east in northwest Peru; as such, the ITCZ second band formation becomes more important in the prediction of rain in that region, especially if it can be identified with days of anticipation.

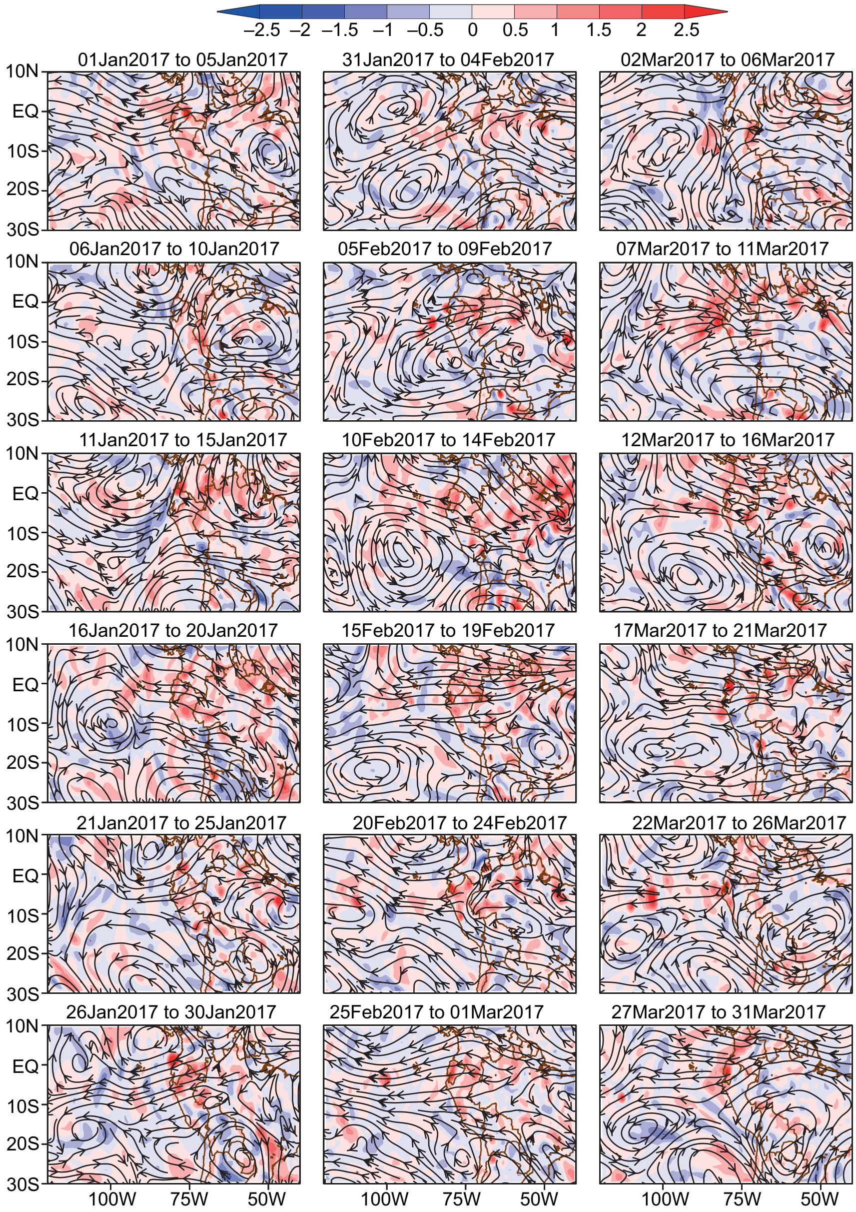

Fig. 9. Five-days of wind (m s^{-1}, stream) and divergence anomalies in 250 hPa (s^{-1} 10^{-5}, shaded).

5.4. Lorenz energy terms

The daily temporal energy analysis (Fig. 11) shows the greatest increase of K_E and K_Z (K_Z is an order of magnitude more than K_E, similar to what was found in the ITCZ of the Atlantic by Da Silva and Satyamurti [2013]) in the first half of January, showing an increase of kinetic energy conditions since early January due to the intensification of wind velocity. Other peaks of K_E were present in the first half of February and March, but with values close to half of those obtained in January. This decrease in K_E can be related to the presence of a CEN event, which was also found by Veiga et al. (2013) and Sátyro and Veiga (2017) in warm ENSO episodes, due to the decrease in the transfer of K_E from the environment to the area of the second band, as the warming generated

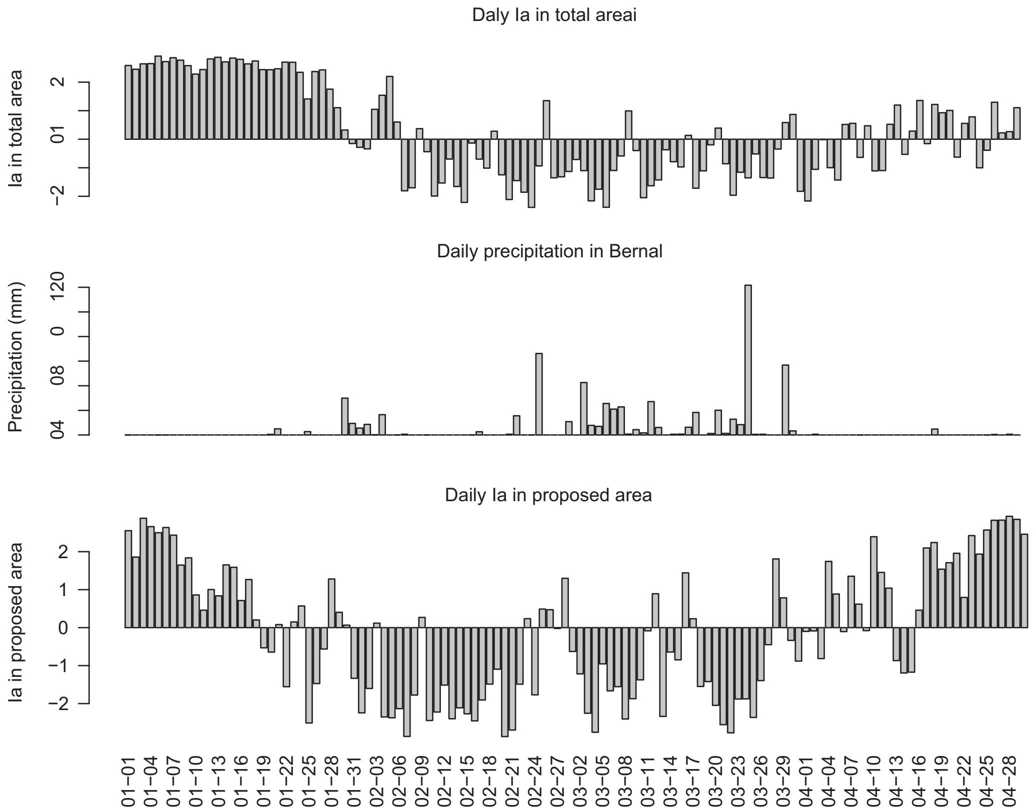

Fig. 10. Upper panel: daily Ia index calculated in total areas (considered in Yu and Zhang, 2018). Middle panel: daily precipitation in the Bernal station (coast of Piura, northwest of Peru). Lower panel: daily Ia index calculated in the new proposed areas.

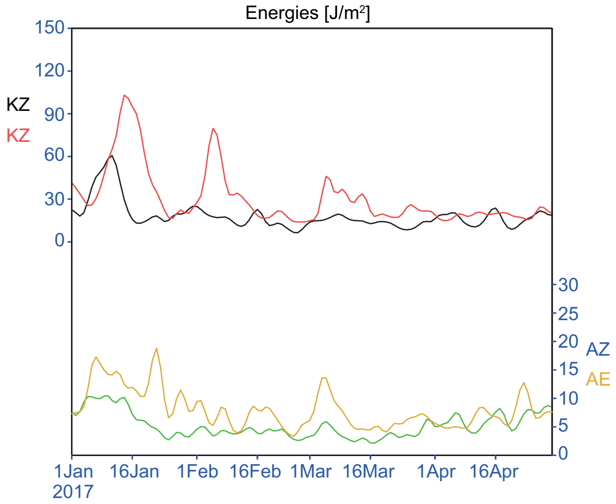

Fig. 11. Time series of volume-integrated Lorenz energy terms ($K_Z \times 10^4$, $K_E \times 10^3$, $A_Z \times 10^3$ and $A_E \times 10^3$) in the SEPn area (values in J m^{-2}).

by CEN in the entire eastern Pacific region near Peru did not allow for significant thermal gradients that generate energy transfer. The peaks of K_E in the first half of February and March are related to maximums of precipitation in the ITCZ second band (Fig. 5), which can be explained by the increased of convection during this period.

Values of A_Z and A_E are smaller than K_E and K_Z (similar to Da Silva and Satyamurti [2013] for the south Atlantic ITCZ) in the equator regions as the horizontal thermal variations are not significant. The peaks of A_E and A_Z (the former was greater than the latter) are registered in January and in the first 10 days of March, indicating that, in these days, the thermal gradients in the same latitude were greater than the meridional temperature gradients. Physically, the peaks of A_E and A_Z on January can be explained by the meridional and zonal thermal gradients in the lower troposphere and sea surface; then, in the first half of March, as it gradually warms up because the CEN occurrence, the convection became important because it generated thermal differences in regions in the same latitude, increasing the values of A_E.

Figure 12 shows that among all types of energy conversion, C_A (conversion of A_Z in A_E) has the smallest order of magnitude, followed by C_Z (conversion of K_Z in A_Z), which is due to very small horizontal thermal gradients in the ITCZ region. On the other hand, similar to Da Silva and Satyamurti (2013), C_E (conversion of A_E in K_E) and C_K (conversion of K_E in K_Z) have the same order of magnitude, as the barotropic instability has a great contribution in equatorial regions.

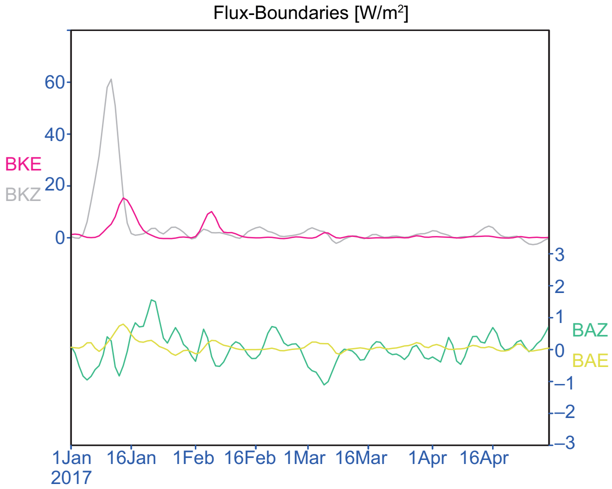

Fig. 12. Time series of volume-integrated energy conversions of the Lorenz energy cycle ($C_A \times 10^{-2}$, $C_Z \times 10^{-1}$, $C_\mathrm{K} \times 10^0$ and $C_E \times 10^0$) in SEPn area (values in W m^{-2}).

The conversion from A_E to A_Z (negative C_A) in January, in the second half of February and in the second half of March ahead indicates that, due to the northerly motions, the zonal thermal variations slightly increase the thermal gradient between latitudes and generates A_Z gain. Contrary, positive C_A in the first half of February and March (periods with more convection) indicate transport of warm tropical air to polar latitudes and cold polar air to warm latitudes through meridional motions. This transport could be enhanced by the ascending movements in the convergence zone and subsident movements over southern regions.

The barotropic process (C_K) has high values in January and the first half of February, with positive values indicating conversion from K_E to K_Z. Considering this process, the increase of K_Z observed in the first half of January in Figure 11 is due, mainly, to the energy transferred from the eddies (K_E).

On the other hand, C_Z has more variability, mainly in February and March, oscillating between negative and positive values, changing the flux of conversion, manifesting the similar importance of K_Z and A_Z during the convection of ITCZ second band region. CE has only positive values, with a maximum in the second half of March, indicating that the increase of K_E observed in this period in Figure 11 is due to conversion from A_E.

At the boundaries, the flux of A_Z has the smallest order of magnitude, related to minimum horizontal variations of temperature in the equatorial region (Fig. 13).

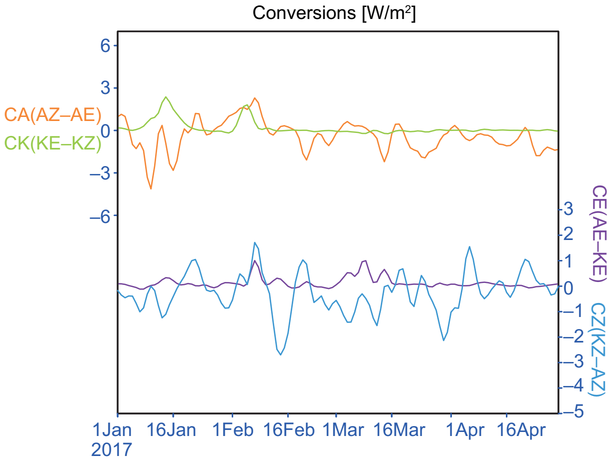

Fig. 13. Time series of volume-integrated boundary energy transports of the Lorenz energy cycle ($BA_Z \times 10^{-1}$) in SEPn area (values in W m^{-2}).

The flux of kinetic energy (K_Z and K_E) is from the exterior to the area of the ITCZ second band (positive values) in January and the first half of February; as a result, part of maximums of K_Z and K_E observed in this period were obtained from the environment. During the rest of the period of the study, the transfer of kinetic energy from the boundaries is almost null.

In the case of the flux of A_E, almost all values are positive, indicating flux from the exterior to the area of the ITCZ, with a maximum around January 15. While the flux of A_Z has values oscillating between positive and negative, indicating, mainly, flux from exterior to the ITCZ second band region in the second half of January, and flux in the opposite direction in the first half of January and early March, possibly due to the greater warming of the ITCZ second band region compared to its surroundings.

6. Summary and conclusions

During the beginning of 2017, the ITCZ second band was present near the coast of northern Peru between the last days of January and the first days of April, with two periods of maximum precipitation during the first half of February and March, which were preceded by positive SST anomalies since January and, mainly, by anomalous north winds and the weakening of the southeast trade winds in a previous period.

A key factor for the development of the second band of the ITCZ is an SST positive anomaly of at least 2 ºC, and at the same time the SST needs to be over 27 ºC, during February and March. However, the determining factor is the behavior of the wind, which must exhibit a constant anomaly from the north (Fig. 4b) and from the west, at least 10 days before the maximum development of precipitation in the second band of the ITCZ.

The behavior of the winds in the ITCZ second band and surroundings were associated with the predominance of an anomalous sea level pressure dipole in the Pacific, with values lower than its normal in the eastern South Pacific (associated with the weakening of the trade winds in the Peruvian coast) and higher than its normal near the equator (from 100 ºW towards the west), generating anomalous west and north winds in the Eastern Pacific near the Peruvian coast.

The mixing ratio in the mid-troposphere had an anomalously positive behavior in the region of the second band of the ITCZ since the last days of January, with a maximum in the first days of February, but with a flow from east to west. However, the change in direction of the flow of the mixing ratio and the positive anomalies over the region (from the Pacific to the continent) occurred only in the first half of March, associated with the development of the maximum convective systems on the northwest coast of Peru. This behavior of flow at medium levels was coupled with the anomalous divergence at high levels, mainly in the region of the ITCZ second band.

The application of the Ia index with daily precipitation and the modified area allows the timely detection of the formation of the ITCZ second band 11 days prior to the occurrence of a maximum precipitation in the Peruvian northwest coast.

According to Lorenz energy terms, the first two peaks of K_E (first half of January and second half of February) are related to the boundaries flux from to exterior to the ITCZ second band region. The last peak of K_E is related to the conversion from to A_E into K_E, indicating a change of energy from differential heating in the same latitude to movement, and the values of C_K similar to C_E show a great contribution of barotropic instability in equatorial regions.

References

Aliaga VJ. 2017. Lorenz energetic applied to understanding of squall lines propagation over the Amazon basin. M.Sc. thesis. University of São Paulo.

Asnani GC. 1993. Tropical meteorology. Climatology of the tropics. Vol. 1. Indian Institute of Tropical Meteorology, 157-166.

Asnani GC. 2005. Tropical meteorology. Climatology of the tropics. Vol. 1. Indian Institute of Tropical Meteorology, 166-186.

Brennan F, Vincent D. 1980. Zonal and eddy components of the synoptic-scale energy budget during intensification of hurricane Carmen (1974). Monthly Weather Review 108(7): 954-965. https://doi.org/10.1175/1520-0493(1980)108<0954:ZAECOT>2.0.CO;2

Da Silva LG, Satyamurty P. 2013. Evolution of the Lorenz energy cycle in the Intertropical Convergence Zone in the South American sector of the Atlantic Ocean. Journal of Climate 26: 3466-3481. https://doi.org/10.1175/JCLI-D-11-00426.1

Dee DP, Uppala SM, Simmons AJ, Berrisford P, Poli P, Kobayashi S, Andrae U, Balmaseda, MA, Balsamo G, Bauer P, Bechtold P, Beljaars ACM, van de Berg L, Bidlot J, Bormann N, Delsol C, Dragani R, Fuentes

M, Geer AJ, Heimberger L, Healy SB, Hersbach H, Hólm EV, Isaksen L, Hallberg P, Kohler M, Matricardi M, McNally AP, Monge-Sanz BM, Morcrette JJ, Park BK, Peubey C, De Rosnay P, Tavolato C, Thépaut JN, Vitart F. 2011. The ERA-Interim reanalysis: Configuration and performance of the data assimilation system. Quarterly Journal of the Royal Meteorological Society 137: 553-597. https://doi.org/10.1002/qj.828

Dias J. 2010. Estudo da estrutura e energia dos distúrbios de escala sinótica na costa leste da América do Sul. M.Sc. thesis. University of São Paulo.

Dias J, Da Rocha R. 2011. The energy cycle and structural evolution of cyclones over southeastern South America in three cases studies. Journal of Geophysical Research 116: 1-17. https://doi.org/10.1029/2011JD016217

Donlon CJ, Martin M, Stark J, Roberts-Jones J, Fiedler E, Wimmer W. 2012. The Operational Sea Surface Temperature and Sea Ice Analysis (OSTIA) system. Remote Sensing of Environment 116: 140-158. https://doi.org/10.1016/j.rse.2010.10.017

Echevin V, Colas F, Espinoza-Morriberon D, Vásquez L, Anculle T, Gutiérrez D. 2018. Forcings and evolution of the 2017 coastal El Niño off northern Peru and Ecuador. Frontiers in Marine Science 5: 1-16. https://doi.org/10.3389/fmars.2018.00367

ENFEN. 2007a. Comunicado oficial ENFEN Nº 01-2017. Comisión Multisectorial encargada del Estudio Nacional del Fenómeno "El Niño", Peru. Available at: https://www.dhn.mil.pe/comunicado_oficial_enfen (accessed on November 2, 2020).

ENFEN. 2007b. COMUNICADO OFICIAL ENFEN Nº 07-2017. Comisión Multisectorial encargada del Estudio Nacionalndel Fenómeno "El Niño", Peru. Available at: https://www.dhn.mil.pe/comunicado_oficial_enfen (accessed on November 2, 2020). Fraser B. 2017. Peru's floods teach tough lessons. Springer Nature 544: 405-406. Available at: https://go.nature.com/2TNP9M0 (accessed on November 2, 2020).

Garreaud R. 2018. Short communication: A plausible atmospheric trigger for the 2017 coastal El Niño. International Journal of Climatology 38: e1296-e1302. https://doi.org/10.1002/joc.5426

Gu G, Adler R, Sobel A. 2005. The eastern ITCZ during the boreal Spring. Journal of the Atmospheric Sciences 62: 1157-1174. https://doi.org/10.1175/JAS3402.1

Haffke C, Magnusdottir G, Henke D, Smyth P, and Peings Y. 2016. Daily states of the March-April East Pacific ITCZ in three decades of high-resolution satellite data. Journal of Climate 29: 2981-2995. https://doi.org/10.1175/JCLI-D-15-0224.1

Henke D, Smyth P, Haffke C, Magnusdottir G. 2012. Automated analysis of the temporal behavior of the double Intertropical Convergence Zone over the east Pacific. Remote Sensing of Environment 123: 418-433. https://doi.org/10.1016/j.rse.2012.03.022

Hsieh J, Cook K. 2007. A study of the energetics of African easterly waves using a regional climate model. Journal of the Atmospheric Sciences 64: 421-440. https://doi.org/10.1175/JAS3851.1

Hu Z, Huang B, Zhu J, Kumar A, McPhaden M. 2019. On the variety of coastal El Niño events. Climate Dynamics 52: 7537-7552. https://doi.org/10.1007/s00382-018-4290-4

Huffman G, Bolvin D. 2017. Real-time TRMM multi-satellite precipitation analysis data set documentation. TRMM 3B4XRT_doc_V7. Available at: https://gpm.nasa.gov/sites/default/files/document_files/3B4XRT_doc_V7_180426.pdf (accessed on May 28, 2021).

INDECI. 2017. Información de emergencias y daños por el "Niño Costero", 07 agosto 2017 (procesamiento al 96%). Instituto Nacional de Defensa Civil. Available at: https://bit.ly/3irKRnl (accessed 2020 November 2)

Lorenz EN. 1955. Available potential energy and the maintenance of the general circulation. Tellus VII 2: 157-167. https://doi.org/10.1111/j.2153-3490.1955.tb01148.x

Lorenz EN. 1967. The nature and theory of the general circulation of the atmosphere. World Meteorological Organization, 161 pp.

Michaelides SC. 1987. Limited area energetics of Genoa cyclogenesis. Monthly Weather Review 115: 13-26. https://doi.org/10.1175/1520-0493(1987)115%3c0013:LAEOGC%3e2.0.CO;2

Muench HS. 1965. On the dynamics of the wintertime stratosphere circulation. Journal of Atmospheric Sciences 22: 349-360. https://doi.org/10.1175/1520-0469(1965)022%3c0349:OTDOTW%3e2.0.CO;2

Norquist DC, Reckeer EE, Reed RJ. 1977. The energetics of African wave disturbances as observed during phase III of GATE. Monthly Weather Review 105: 334-342. https://doi.org/10.1175/1520-0493(1977)105%3c0334:TEOAWD%3e2.0.CO;2

Peng Q, Xie S, Wang D, Zheng X, Zhang H. 2019. Coupled ocean-atmosphere dynamics of the 2017 extreme coastal El Niño. Nature Communications 10, 298: 1-10. https://doi.org/10.1038/s41467-018-08258-8

Peng Q, Xie S, Wang D, Kamae Y, Zhang H, Hu S, Zheng X, Wang W. 2020. Eastern Pacific wind effect on the evolution of El Niño: Implications for ENSO diversity. Journal of Climate: 33: 3197-3212. https://doi.org/10.1175/JCLI-D-19-0435.1

Quispe K. 2018. El Niño Costero 2017: Precipitaciones extraordinarias en el norte de Perú. M.Sc. thesis. University of Barcelona.

Ramírez GE, Silva Dias PL, Veiga JA, Camayo R. and Dos Santos A. 2009. Multivariate analysis of the energy cycle of the South American rainy season. International Journal of Climatology 29: 2256-2269. https://doi.org/10.1002/joc.1858

Ramírez IJ, Briones F. 2017. Understanding the El Niño Costero of 2017: The definition problem and challenges of climate forecasting and disaster responses. International Journal of Disaster Risk Science 8: 489-492. https://doi.org/10.1007/s13753-017-0151-8

Rodríguez-Morata C, Díaz HF, Ballesteros-Canovas JA, Rohrer M, Stoffel M. 2018. The anomalous 2017 coastal El Niño event in Peru. Climate Dynamics 52: 5605-5622. https://doi.org/10.1007/s00382-018-4466-y

Sátyro ZC, and Veiga J. 2017. An analysis of the energetics of tropical and extra-tropical regions for warm ENSO composite episodes. Revista Brasileira de Meteorologia 32: 39-51. https://doi.org/10.1590/0102-778632120150114

Son R, Wang AU, Simon S, Tseng WL, Barreto-Schuler C, Becker E, Yoon J-H. 2019. Climate diagnostics of the extreme floods in Peru during early 2017. Climate Dynamics 54: 935-945 https://doi.org/10.1007/s00382-019-05038-y

Sulca J, Takahashi K, Espinoza JC, Vuille M, Lavado Casimiro W. 2017. Impacts of different ENSO flavors and tropical Pacific convection variability (ITCZ, SPCZ) on austral summer rainfall in South America, with a focus on Peru. International Journal of Climatology 38: 420-435. https://doi.org/10.1002/joc.5185

Takahashi K, 2004. The atmospheric circulation associated with extreme rainfall events in Piura, Peru, during the 1997-1998 and 2002 El Niño events. Annales Geophysicae 22: 3917-3926. https://doi.org/10.5194/angeo-22-3917-2004

Takahashi K, Martínez A. 2017. The very strong coastal El Niño in 1925 in the far-eastern Pacific. Climate Dynamics 52: 7389-7415. https://doi.org/10.1007/s00382-017-3702-1

Takahashi K, Aliaga-Nestares V, Ávalos G, Bouchon M, Castro A, Cruzado L, Dewitte B, Gutiérrez D, Lavado-Casimiro W, Marengo J, Martínez A, Mosquera-Vásquez K, Quispe N. 2018. The 2017 coastal El Niño. In: (J Blunden, DS Arndt, G Hartfield, Eds.). Bulletin of the American Meteorological Society 99: 210-211. https://doi.org/10.1175/2018BAMSStateoftheClimate.1

Tang Y and Yu B. 2008, MJO and its relationship to ENSO. Journal of Geophysical Research: Atmospheres 113: D14106. https://doi.org/10.1029/2007JD009230

Veiga J, Pezza A, Ambrizzi T, Rao B, Franchito S, Yoshida M. 2013. The energy cycle associated to the Pacific Walker circulation and its relationship to ENSO. Atmospheric and Climate Sciences 3: 627-642. https://doi.org/10.4236/acs.2013.34065

WMO. 2014. Commission for Climatology. Sixteenth session. Abridged final report with resolutions and recommendations (WMO-No. 1137). World Meteorological Organization, Geneva. Available at: https: https://library.wmo.int/doc_num.php?explnum_id=5560 (accessed on June 7, 2021).

Xie S, Peng Q, Kamae Y, Zheng X, Tokinaga H, Wang D. 2018. Eastern Pacific ITCZ dipole and ENSO diversity. Journal of Climate 31: 4449–4462. https://doi.org/10.1175/JCLI-D-17-0905.1

Yang W, Magnusdottir G. 2016. Interannual signature in daily ITCZ states in the East Pacific in boreal spring. Journal of Climate 29: 8013-8025. https://doi.org/10.1175/JCLI-D-16-0395.1

Yu H, Zhang M. 2018. Explaining the year-to-year variability of the Eastern Pacific Intertropical Convergence Zone in the boreal spring 123: 3847-3856. https://doi.org/10.1002/2017JD028156

Zhang C. 2001. Double ITCZs. Journal of Geophysical Research 106: 11785-11792. https://doi.org/10.1029/2001JD900046

Atmósfera 36(1), 41-56 (2023)
https://doi.org/10.20937/ATM.52858

CONTENTS

Surface shortwave cloud radiative effect of cumulus and stratocumulus-cumulus cloud types in the Caribbean area (Camagüey Cuba, 2010-2016)

Boris BARJA[1,2]*, Jorge ROSAS[2], Victoria Eugenia CACHORRO[3], Carlos TOLEDANO[3],
Juan Carlos ANTUÑA-MARRERO[3], Rene ESTEVAN[2] and Ángel DE FRUTOS[3]

[1]Laboratorio de Investigaciones Atmosféricas, Universidad de Magallanes, Av. Bulnes 01855, Punta Arenas, 6101042, Chile.
[2]Grupo de Óptica Atmosférica de Camagüey, Centro Meteorológico de Camagüey, km 7 ½ Av. Finlay, Camagüey, 70100, Cuba.
[3]Grupo de Óptica Atmosférica (GOA-UVA), Departamento de Física Teórica, Atómica y Óptica, Facultad de Ciencias, Universidad de Valladolid, Paseo de Belén 7, 47011, Valladolid, España.
*Corresponding author; email: bbarja@gmail.com

Received: March 25, 2020; accepted: June 2, 2021

RESUMEN

Los efectos de las nubes tipo cúmulos (Cu) y de la combinación de los tipos estratocúmulos-cúmulos (Sc-Cu) sobre la radiación solar en la superficie terrestre de Camagüey, Cuba, fueron estudiados durante seis años (de junio de 2010 a mayo de 2016). El efecto radiativo de las nubes (CRE, por su sigla en inglés) fue calculado por dos métodos. El primero (CRE_m) utiliza valores de irradiancia solar medidos mediante observaciones actinométricas en condiciones de nubosidad, donde el tipo de nube es reportado de manera visual. En el segundo método (CRE_0) se calculó la irradiancia solar en la superficie, tanto en casos de nubosidad como despejados, con un modelo de transferencia radiativa 1-D, utilizando como entrada principal los valores de espesor óptico de nubes (COD) obtenidos de un fotómetro solar de AERONET. Se aplicó un criterio de correspondencia temporal entre los valores de COD y las observaciones actinométricas, con el fin de clasificar los valores de COD por tipo de nube. Al aplicar este criterio, se eliminaron los COD pertenecientes a las nubes ópticamente finas. Finalmente, se seleccionaron 255 y 732 observaciones de COD para los tipos de nubes Cu y Sc-Cu, respectivamente. Los resultados muestran diferencias estadísticamente significativas al nivel de confianza del 95% entre la CRE para Sc-Cu y Cu, utilizando ambos métodos. Los valores medios de CRE_m y CRE_0 para el tipo de nube Cu (Sc-Cu) fueron −442 (−390) y −460 (−417) Wm^{-2}, respectivamente. La CRE_0 muestra una relación lineal con ln(COD), siendo más fuerte a medida que disminuye el ángulo cenital solar. La eficiencia del efecto de las nubes (CEE) para Cu y Sc-Cu disminuye bruscamente con el aumento del valor de COD hasta 20, disminuyendo lentamente para valores mayores de COD.

ABSTRACT

The effects of cumulus (Cu) clouds and the combination of stratocumulus-cumulus (Sc-Cu) clouds on solar radiation at the Earth's surface were evaluated at Camagüey, Cuba, during a 6-yr period (from June 2010 to May 2016). Two methods to calculate the cloud radiative effect (CRE) were employed. The first method (CRE_m) uses solar irradiances in cloudy conditions from actinometric observations, where cloud information was also reported by visual observation. In the second method (CRE_0) surface solar irradiances were estimated for both cloudy and clear sky conditions using a 1-D radiative transfer model, and cloud optical depth (COD) retrieved from an AERONET sun-photometer as the main input. A temporal correspondence criterion between COD retrievals and actinometric observations was performed in order to classify the COD of each cloud type. After the application of this criterion, the COD belonging to the optically thin clouds was removed. Finally, 255 and 732 COD observations for Cu and Sc-Cu, respectively, were found. Results show a statistically significant difference at the 95% confidence level between CRE calculated for Sc-Cu and Cu, using both methods. Mean values of CRE_m and CRE_0 for Cu (Sc-Cu) were −442 (−390) and −460 (−417) Wm^{-2}, respectively. CRE_0 shows a linear relation with ln(COD), with stronger correlation at a lower solar zenith angle. The shortwave cloud effect efficiency (CEE) for the two cloud types sharply decreases with the increase of the COD value up to 20. For larger COD, the CEE is less sensitive to the increase of COD.

Keywords: cloud effects on solar radiation (CRE) at surface, cloud optical depth (COD), cumulus and stratocumulus, cloud effect efficiency (CEE).

1. Introduction

Clouds are an important component of climate due to their complex interactions with other components of the climatic system. The main interaction is thwir influence on the radiative transfer in solar or shortwave radiation (spectral interval: 0.2 to 4 μm) and in terrestrial or longwave radiation (spectral interval higher than 4 μm). Those interactions occur via the scattering and absorption within the solar spectrum, and mainly by absorption and emission within the terrestrial spectrum. The main effect of clouds on solar radiation is the large backward scattering produced by cloud droplets and ice crystals (Liou, 1986; Stephens, 2005; Mitchell and Finnegan, 2009). As a result, the earth-atmosphere system albedo basically depends on clouds and their properties.

At the Earth's surface, the clouds effect on solar radiation basically depends on the microphysical (i.e., particle size) and macrophysical (i.e., cloud base and cloud top) properties of clouds and the sun disk location with respect to the measuring point. For instance, when a cloud completely or partially obstructs the sun disk, the result is a reduction of downward irradiance at the Earth's surface, producing a radiative cooling effect. In addition, in partially cloud-covered situations, such as low broken cloud fields, the surface irradiance can exceed the expected clear sky irradiance value, causing radiative heating at surface. This phenomenon is known as cloud enhancement effect and can be observed all around the world (Gueymard, 2017). The enhancement is produced under a clear sun disk by the increase of diffuse shortwave irradiance due to the presence of clouds. To detect this effect, it is necessary to perform continuous solar radiation measurements and to estimate the expected instantaneous cloudless radiation. Hereinafter the terms cooling or heating will refer to the radiative cooling or heating.

One of the first results reported in scientific literature about the clouds effect on solar radiation was reported in the 1940s (Neiburger, 1949). The author computed the cloud radiative properties using downward and upward shortwave radiation measurements below, inside and above the coastal stratus clouds in the USA. In the 1980s there was an increase in studies estimating the cloud radiative properties (reflectivity, absorptivity and transmissivity), and their relationship with macr physical, microphysical and optical properties of the clouds (e.g., Ackerman and Stephens, 1987). After the creation of the International Satellite Cloud Climatology Project (ISCCP) (Schiffer and Rossow, 1983) these studies were substantially increased. This project enabled an improvement in the estimation of the cloud radiative effects and cloud optical depth (COD) (Chou and Zhao, 1997; Chen et al., 2000).

More recent polar orbit satellite-based projects have helped to improve in depth these studies, such as the A-Train constellation, which comprises the Cloud Aerosol Lidar and Infrared Pathfinder Satellite Observation (CALIPSO) (Winker et al., 2007), Cloud Sattleite (CloudSat) (Stephens et al., 2008), MODerate-resolution Imaging Spectroradiometer (MODIS) (Barnes et al., 1998) and the Clouds and the Earth's Radiant Energy System (CERES) (Wielicki et al., 1996) instruments onboard Aqua and Terra satellites. These instruments allow for analyzing the cloud radiative effects considering the vertical structure of the clouds (L'Ecuyer et al., 2008; Li et al., 2011; Ham et al., 2017; Dolinar et al., 2019).

In the Caribbean region, there have been few studies about this topic. This is specifically the case of Cuba, despite its tropical location and the high frequency of low clouds. Martínez and Pomares (2002) evaluated the effect of cloud cover on the UV radiation transmittance, without specifying the cloud type. The pioneering study in Cuba about the effect of cirrus clouds on solar radiation was carried out by Barja and Antuña-Marrero (2008, 2010, 2011), estimating the microphysical properties of cirrus clouds and their shortwave radiative effect. The authors reported a daily mean value of shortwave cloud radiative effect (SWCRE, formerly shortwave cloud radiative forcing, hereinafter CRE) of -5.6 Wm^{-2} and a cloud effect efficiency (formerly cloud radiative efficiency, hereinafter CEE) of -26 Wm^{-2} COD^{-1}, both at the surface. Cirrus cloud properties have also been described for Cuba and the Wider Caribbean (Barja and Antuña-Marrero, 2010; Barja et al., 2012).

Despite the important role of clouds in the Earth's radiation budget, the number of experimental sites conducting measurements of cloud properties is not yet enough to produce detailed information on the different regions of the Earth. For that reason, the cloud radiative effect at surface has been less reported by the scientific community than cloud effects at the top of atmosphere (Boucher et al., 2013). This whole scenario demonstrates the importance of studies about clouds and their interaction with solar radiation at the Earth's surface.

Therefore, this paper presents an estimation of the effect of cumulus (Cu) and stratocumulus-cumulus (Sc-Cu) cloud types on the solar irradiance at the surface at Camagüey, Cuba (21.42º N, 77.85º W, 122 masl), 2 h before and after 12:00 LT. Sun-photometric and actinometric measurements at the site were used in conjunction with a 1-D atmospheric radiative transfer model (RTM) and satellite-derived products. A brief description of the instruments, datasets and RTM calculations is shown in section 2. Section 3 shows the results and the discussion. Finally, section 4 concludes and summarizes this study.

2. Data and methods

2.1 COD, actinometric datasets, and correspondence criterion

Our study period spans six years from June 2010 to May 2016, at the Meteorological Station of Camagüey, Cuba. At this site, in addition to the meteorological devices, an actinometric station and the AERONET Cimel sun-photometer were installed as close as tens of meters.

The Cimel CE 318 sun-photometer was installed at the Camagüey Meteorological Station (21.42º N, 77.85º W, 122 masl) as part of AERONET (AErosol RObotic NETwork) (Holben et al., 1998) in 2006, due to a research collaboration agreement between the Cuban Meteorological Institute at Camagüey and the University of Valladolid (Spain). It has nine interference filters centered at 340, 380, 440, 500, 675, 870, 935, 1020, and 1640 nm nominal wavelengths. The main objective of this instrument is to retrieve the spectral aerosol optical depth (AOD) from direct solar irradiance at the surface. When the clouds block the sun disk, it is not possible to retrieve the AOD. Under such conditions, the instrument carries out 10 radiance measurements towards the zenith for all spectral channels, in the so-called "cloud mode". Using these zenith radiance measurements at 440 and 870 nm as inputs into lookup-tables created using a radiative transfer algorithm (Chiu et al., 2010), the COD parameter can be retrieved. For the study period, a total of 8997 COD observations were carried out with the AERONET cloud mode level 2.

Barja et al. (2012) developed a 1-yr preliminary study in order to evaluate the AERONET COD measurements at the Camagüey site. An algorithm was used to determine the "correct" COD values. The term correct must be understood in two senses: first, there was a cloud present in the sky and therefore the decision to make a COD measurement with the sun-photometer was correct; second, this COD value is related to cloud type and cloud cover information recorded in the actinometric report (more details of the algorithm are provided in Barja et al., 2012). The authors showed that a high percentage of COD data from AERONET was correct and in very good agreement with CALIPSO data for COD values lower than 5.

In the actinometric station of the site, visual observations of clouds and manual irradiance measurements were conducted 12 min after each hour during daytime. A Yanishevsky pyranometer (M-80-M or M-115-M) connected to an analogic galvanometer (GSA-1MA or GSA-1MB) along with a shadow cover, were manually operated to measure broadband global, diffuse, and direct components of solar irradiance at the surface.

Before, during and after measurements in the actinometric station, the observer reported some characteristics of the weather and surface (e.g., air temperature, wind speed, color of the sky, cloud types, cloud cover, temperature of the soil surface, visibility range, and state of the sun disk). Cloud types observed in the sky, including those at the zenith, were reported by the observer, following the classification of clouds given by the World Meteorological Organization (WMO, 2017).

The state of the sun disk is classified in four categories: (1) sun disk not covered by clouds: no traces of clouds, mist, haze or dust on the disk of the sun and within a radius of 5º; (2) sun disk partially covered by thin clouds: the sun shines through clouds, fog or smoke and the actinometer tube can collimate the sun; (3) sun disk totally covered by thick clouds: the sun disk is weakly visible through a layer of dense clouds, and it is impossible to aim the actinometer tube at the sun, and (4) sun disk totally covered by dense clouds: the sun is not visible through dense clouds (Yanishevsky 1957; Ross et al., 1969; Antuña-Marrero et al., 2008; Eerme and Aun, 2012; Chervyakov and Neishtadt, 2018).

Manually operated solar radiation stations are becoming practically extinct, replaced by automatic instruments. But in Cuba these manual stations are still functional and the plan is to continue operating them during the next years. Therefore, data provided by these instruments are useful to obtain and study atmospheric parameters such as clouds. The dataset was subjected to an improved quality control and processing algorithm (Antuña-Marrero et al., 2008, 2018, 2019). In the present work we used shortwave global downward irradiance (*G*), shortwave upward irradiance (*R*), cloud type and low cloud amount from actinometric measurements.

Measurements with the actinometric station made when the sun disk is partially and completely covered by thin and thick clouds (sun disk 2-4) were employed for this study. In addition, in order to find COD and irradiance measurements in the presence of the cloud types of interest, a correspondence criterion was applied. The combination of COD measurements and the visual reports of clouds from the actinometric observations is the aim of this correspondence criterion, whose conditions are:

1. Select visual reports with only Sc-Cu or Cu cloud types.
2. Time range is set between 15:00 and 19:00 UTC (from 10:00 to 14:00 LT). In this time interval the solar zenith angle is smaller, therefore it increase the probability that the sun-photometer measures the same clouds as the actinometric instrument.
3. The coincident COD measurements with Sc-Cu or Cu visual reports are selected in the time interval of 2 min before and 30 min after the start time of the actinometric observation (it must be noted that actinometric measurements last about 30 min and the report of the cloud is done 2 min before the radiation measurement, which is why this asymmetrical time interval is chosen).

When the first condition of the criterion was applied, a total of 1447 and 852 cases of actinometric reports in presence of Sc-Cu and Cu were found, respectively. Finally, after the application of all conditions of the correspondence criterion, a total of 876 and 314 actinometric measurements were coincident with COD retrievals corresponding to Sc-Cu and Cu, respectively.

2.2 Atmospheric Radiative Transfer model, CRE and CEE computations

A 1-D radiative transfer of the National Oceanic and Atmospheric Administration (NOAA) is used to calculate the solar radiation fluxes at the surface (Freidenreich and Ramaswamy, 1999, 2005). The RTM solves the atmospheric radiative transfer equation using the delta Eddington and double adding method and only considers the term related to atmospheric extinction in the solar (or shortwave) spectrum.

The model has a high vertical resolution with the atmosphere divided in 122 layers and pressure levels ranging from 3.10 to 1013.25 hPa. It also includes gas absorption (water vapor, CO_2, O_2, and O_3), Rayleigh scattering, scattering and absorption of aerosols, water droplets and ice particles. The model assumes clouds as a homogeneous and in a parallel plane layer (conditions similar to overcast sky), with the parameterization scheme for water clouds provided by Slingo (1989).

This RTM was adapted to the Camagüey meteorological conditions and has demonstrated a good agreement with experimental solar radiation measurements for clear sky and cloudy conditions (Barja and Antuña-Marrero, 2011; Freidenreich and Ramaswamy, 2011). Water vapor mixing ratio vertical profiles were collected using a radiosounding dataset carried out at Camagüey from 1991 to 1988. A surface albedo average value of 0.22, obtained from actinometric measurements at the site, was used in the calculations. The vertical profile of ozone mass mixing ratio was taken from the mid-latitude summer (MLS) atmosphere of McClatchey et al. (1972).

The effect of low clouds on solar radiation was estimated by calculating the shortwave cloud radiative effect at the surface (CRE). Two methods were used to calculate CRE: in the first one, actinometric measurements for cloudy conditions and modeling of the clear sky to generate CRE_m were used (Eq. [1]); the second one was carried out using only the modeling of both clear and cloudy conditions to obtain CRE_0 (Eq. [2]).

CRE_m was calculated through the difference between measured net solar surface irradiance in cloud presence (I_{cloud}^{meas}) and the modeled one in clear sky conditions at the same time (I^0_{clear}). Net solar irradiance on the surface in the presence of clouds was estimated by with Eq. (3) (*G* and *R* were defined above).

$$CRE_m = I_{cloud}^{meas} - I_{clear}^{0} \quad (1)$$

$$I_{cloud}^{meas} = G - R \quad (2)$$

$$CRE_o = I_{cloud}^{0} - I_{clear}^{0} \quad (3)$$

From the theoretical evaluation of I^0_{clear}, the most important component is aerosol, hence AOD values were estimated as a temporal interpolation of the daily mean AOD (500 nm) obtained by the AERONET sun-photometer. Vertical distribution of aerosol in the RTM was assumed in a layer between ground and 3 km.

The main inputs in cloudy conditions to obtain CRE_0 were COD, the effective radius of the cloud droplet distribution (r_e) and cloud geometrical properties. Because no measurements of geometrical cloud properties and r_e are available at our site, cloud properties used in the model were taken from literature and MODIS data (see Table I). Cloud base (Z_b) and top (Z_t) height for each cloud type were included in their respective pressure levels by the interpolation with the tropical atmosphere profile from McClatchey et al. (1972). Note that Z_b and Z_t have the same values for both Sc-Cu and Cu.

Table I. Cloud properties assumed in this study.

Cloud type	Z_b (km)	Z_t (km)	r_e (μm)
Cu	1.7	2.15	12
Sc-Cu	1.7	2.15	15

Z_b: cloud base; Z_t: cloud top; r_e: cloud droplet distribution; Cu: cumulus; Sc-CU: stratocumulus-cumulus.

The selection of the mean r_e was based on literature (e.g., Zhang et al., 1995; Kim et al., 2003; Allan et al., 2008; Spiegel et al., 2014) and from climatological data obtained from the Goddard Earth Sciences Data and Information Services Center (GES DISC) Interactive Online Visualization and Analysis Infrastructure (Giovanni). MODIS provides a mean value for r_e of 15.6 μm within the range from 8 to 26 μm, without any identification relative to cloud type, based on daily average values for the period 2000 to 2014. To assume a fixed value for the effective radius r_e may appear non-realistic, but we must note that r_e is far less sensitive to shortwave surface transmitted radiation as has been demonstrated in various studies (e.g., McBride et al., 2011). Chiu et al. (2010) retrieved COD assuming a fixed value of 8 μm, but a 25% error in this parameter only implies a 4% error in the COD. Therefore, we used a fixed r_e for each cloud type (see Table I) as the most adequate value for the modeling of radiative fluxes in the presence of clouds.

We computed the CRE using the net flux (Eq. [3]), similar to other studies (e.g., Berg et al., 2011), rather than using only the downward flux (e.g., McFarlane et al., 2012). Therefore, care must be taken when comparisons are made. The main errors in the estimation of CRE are associated with instrumental errors and errors in the modeling of radiative fluxes, because of the assumption of 1-D RTM for non-overcast conditions. Due to the ageing of the actinometric instruments, the magnitude of error associated with the broadband pyranometer is estimated to be about 10% (Antuña-Marrero et al., 2008). The error of radiative flux calculations with the RTM is 10% for clear sky (Freidenreich and Ramaswamy, 2011) and between 20 and 30% in cloudy conditions (Li and Trishchenko, 2001).

Considering all the above-mentioned errors, the total uncertainty of the methods used to determine CRE and CEE is between 20 and 40%. In the case of overcast sky, the error can be higher, between 30 and 40% (20 to 30% related with model calculations plus 10% of the observations); and 20% for clear sky (10% related with the model calculations plus 10% of the observations).

The number of CRE_m cases was higher than CRE_0 because of the lower number of coincident actinometric measurements in presence of clouds with available COD data. As expected, CRE exhibits negative values, showing a reduction of solar radiation at the surface by the presence of clouds. High absolute values of CRE correspond to a higher decrease of the solar radiation. Hence, hereinafter we will not consider the sign in the CRE when we talk about higher or lower values.

CRE provides the actual radiative effect of clouds, but in order to make a consistent comparison between different clouds (clouds with different microphysical and macrophysical properties) the shortwave cloud effect efficiency (CEE), also known in the literature as cloud forcing efficiency (Mateos et al., 2014) is a more appropriate magnitude defined as the rate at which the cloud radiative effect is forced per unit of COD. CEE is then calculated in order to evaluate the change in the cloud effect per unit of COD, and can be obtained as the following relation, using small intervals of SZA (Mateos et al., 2014):

$$CEE = \frac{m}{COD} \tag{4}$$

where m is the slope of the linear fit between CRE and ln(COD) (in Wm^{-2}) for each SZA interval. Therefore, the units of CEE are Wm^{-2} per COD unit, presenting dependence on both SZA and COD. The physical meaning of m is related to absolute changes in CRE due to relative changes on COD. However, in order to evaluate cloud efficiency in terms of radiative effects with the absolute change of COD, we need to check this change in COD units, which is not directly retrieved from the slope. CEE is a useful parameter to compare different cloud types with the same COD, because the influence of other factors such as absorbing and scattering cloud properties may become more evident. Nonetheless, when analyzing the efficiency values, it is necessary to be careful with high CODs (Mateos et al., 2014), since for these values a high concentration of cloud droplets is expected and hence the saturation of CEE due the increase in multiple scattering. In this study, CEE was only calculated for CRE_0 values because enough COD data are only available for these cases.

2.3 Cleaning of the data set to remove doubtful measurement cases

Preliminary analyses of the frequency distribution of CRE for Cu and Sc-Cu near noon, calculated with the two methods, are shown in Figure 1. For Cu (Fig. 1a) 852 and 314 cases of CRE_m and $CRE_{0,}$ respectively, were found. There were 1447 and 876 cases of CRE_m and CRE_0 for Sc-Cu (Fig. 1b). The cases that satisfied the first condition of the correspondence criterion were used to calculate CREm. The cases that successfully met all conditions of the correspondence criterion were used to calculate CRE_0. Figure 1a shows differences between both CRE histograms for Cu. The highest frequency value (27%) of CRE_0 is placed in the range from 0 to −100 Wm^{-2}. However, the highest frequency value (36%) for CRE_m is in the interval from −400 to −500 Wm^{-2}, with no frequency values in the range from 0 to −100 Wm^{-2}. Figure 1b shows CRE histograms for Sc-Cu. As with Cu, there are no values for CRE_m in the interval from 0 to −100 Wm^{-2}. The maximum frequencies for both CRE_m and CRE_0 are observed in the interval from −300 to −400 Wm^{-2}, with 36 and 27%, respectively.

T-Student tests were applied to check the differences between CRE_m and CRE_0, showing statistically significant differences at the 95% confidence level for Cu and Sc-Cu. This is largely due to the differences observed in the range of 0 to −100 Wm^{-2}, which could be due to the fact that COD values employed in the modeling were not related to the same cloud types measured with the actinometric technique.

When zenith sky radiance is measured in cloud mode with the sun-photometer and there are interstices between clouds, the instrument can measure a different cloud type than the one reported by the observer. Low COD values causing CRE values below −100 Wm^{-2} are considered doubtful because they do not correspond to low water clouds near

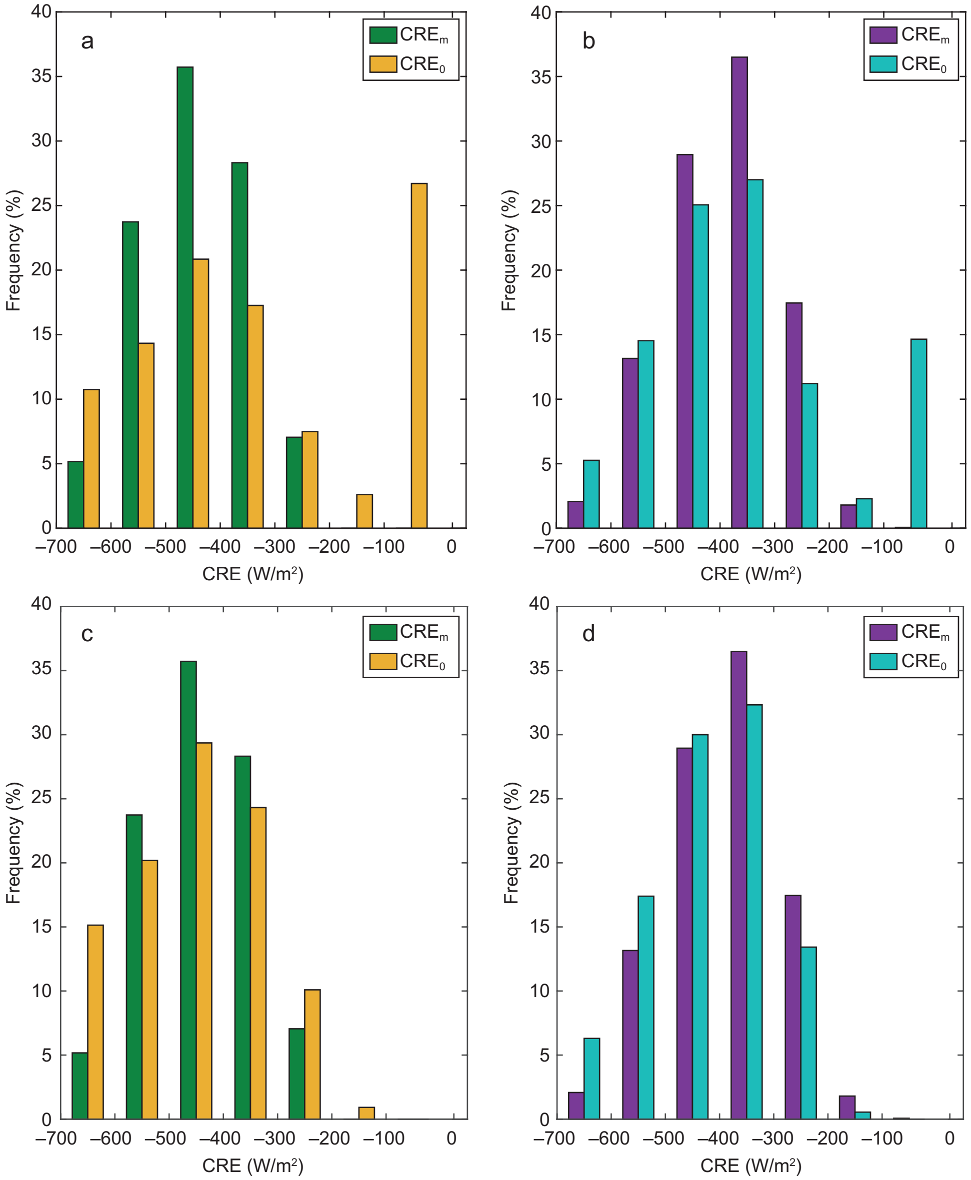

Fig. 1. Frequency distributions of CRE$_m$ and CRE$_0$ for (a) Cu and (b) Sc-Cu cloud types. (c) and (d) as in (a) and (b) after discarding doubtful COD values. (CRE: cloud radiative effect at the surface; CRE$_m$: CRE from actinometric measurements; CRE$_0$: modeled CRE; Cu: cumulus; Sc-CU: stratocumulus-cumulus).

noon. The term doubtful is used, hereinafter, for these COD measurements with low values producing high differences with CRE values determined with both methods. The Sc-Cu morphology is closer to cloud representation in the radiative transfer code (plane-parallel) than Cu. In addition, this cloud combination has great horizontal extension, which leads to lesser occurrence of interstices and therefore lower occurrence of small COD values when CODs from sun-photometric measurement are compared to actinometric measurements reports.

In order to clean the dataset to reduce the amount of doubtful COD values, it is necessary to check the consistency between the values of CRE methods and the reported cloud type. Differences between CRE$_m$ and CRE$_0$ for each cloud type, as a function of COD, were calculated for cases with stricter coincident criterion (Fig. 2). This criterion was set between 12 and 20 min in each measurement hour. After applying this criterion, 79 and 280 cases of COD were found for Cu and Sc-Cu, respectively.

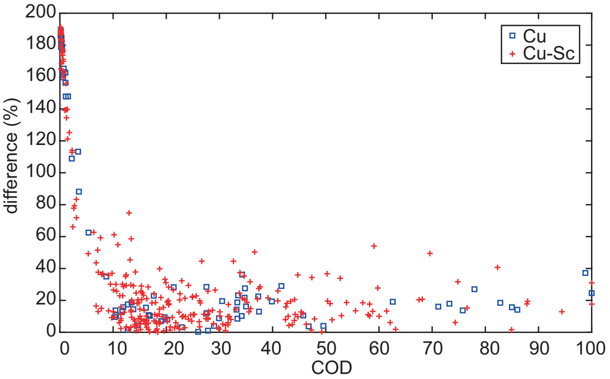

Fig. 2. Percentage differences between CRE_m and CRE_0 for coincident cases in relation with COD for the two cloud types, Cu and Cu-Sc. (CRE: cloud radiative effect at the surface; CRE_m: CRE from actinometric measurements; CRE_0: modeled CRE; Cu: cumulus; Sc-CU: stratocumulus-cumulus; COD: cloud optical depth).

In Figure 2, higher differences (> 150%) in the small-COD values region (which corresponds to the range of doubtful COD values) were found. Therefore, it is evident that these COD values are not related with the reported cloud type. These COD values are characteristic of optically thin clouds, such as subvisible cirrus clouds or low minor clouds that cannot be sufficiently measured by the actinometric method. Hence, a threshold COD value for each cloud type was determined by a minimum COD value of the subset of COD with differences below 60%. The selection of this difference value was based on the fact that 70% of the studied cases are below it. For both cloud types, the threshold COD was found to be 5, thus any lower COD was removed from the analysis.

The number of cases resulting from the correspondence criterion which remain after the removal of doubtful COD values were 225 and 732 for Cu and Sc-Cu, respectively. The cleaned dataset was used for further analysis and results.

Figure 3 shows the frequency distributions of COD for Cu and Sc-Cu after the removal of doubtful COD cases. The COD frequency distribution for Cu (Fig. 3a) has its 15% peaks in the COD interval with central values of 10 and 15, with 80% of the distribution below 45. In the case of Sc-Cu (Fig. 3b), the COD frequency distribution has its maximum frequency (18%) in the COD interval with central values of 10 and 15, similar to Cu, with 85% of the distribution below 45. The mean values of COD for Sc-Cu and Cu were 29.6 and 34.2, respectively. As

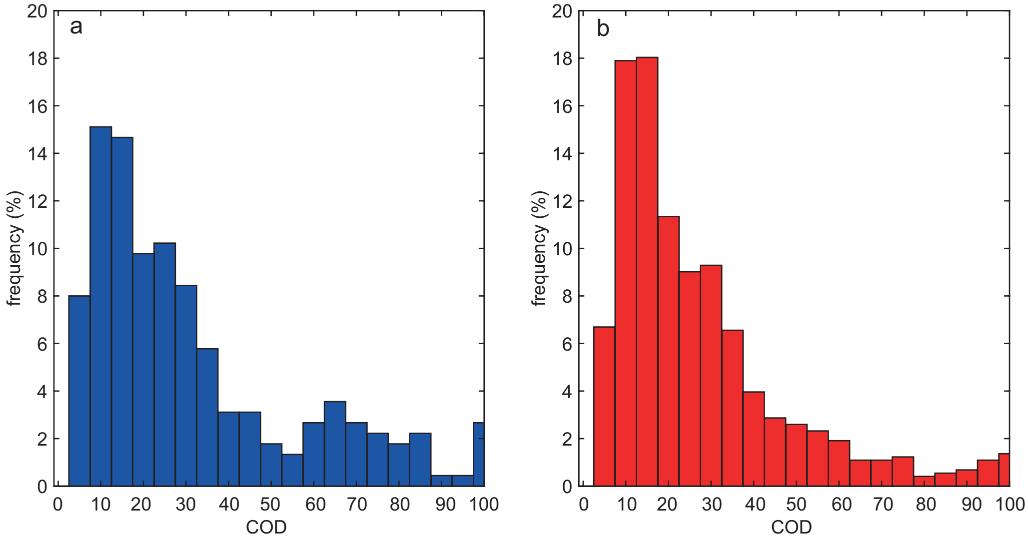

Fig. 3. Frequency distributions of COD for (a) Cu and (b) Sc-Cu. (COD: cloud optical depth; Cu: cumulus; Sc-CU: stratocumulus-cumulus).

observed above, the COD frequency distributions for both cloud types are similar, but the Sc-Cu maximum is higher than the Cu maximum, and the distribution of Cu has a secondary maximum of 4% in the COD interval of 65.

3. Results and discussion

3.1 Frequency and statistical values of CRE

The CRE frequency distribution for Cu and Sc-Cu after discarding doubtful values is shown in Figure 1c, d, where a decrease in the frequency within doubtful intervals of CRE_0 is observed. There is not data in the interval from 0 to −100 Wm^{-2}, where the maximum frequency was previously located for both cloud types. Only a low value of 1% for CRE_0 in the frequency interval from −100 to −200 Wm^{-2} was observed for both cloud types. The maximum frequencies of CRE_0 after discarding doubtful COD values are observed in the intervals from −400 to −500 and −300 to −400 Wm^{-2} for Cu and Sc-Cu, respectively. Similar behavior was found regarding the CRE_m frequency distribution.

Hypothesis t-Student tests for Cu and Sc-Cu were applied showing no statistically significant differences between CRE_m and CRE_0 at the 95 % confidence level. However, the existing differences between CRE_m and CRE_0 for a given cloud type are due to different causes, e.g., the uncertainties related to the input parameters for the modeled data and the assumption of 1-D RTM for non-overcast conditions, which can overestimate the surface irradiances for cloudy conditions. In addition, temporal differences in measurement methodologies between the actinometric and sun-photometer measurements can also be an important factor.

Table II shows statistics (mean, standard deviation [std], maximum [max], minimum [min], and percentiles 5, 95 and 50 [median]) of CRE_m and CRE_0 for each cloud type after discarding doubtful COD values. We consider the absolute value when referring to CRE maximum or minimum. As shown in Table II, Cu clouds have smaller differences between CRE_m and CRE_0 than Sc-Cu. For Cu, the mean values of CRE are −442 and −460 Wm^{-2} for CRE_m and CRE_0, respectively. In the case of Sc-Cu, CRE is lower than Cu, with mean values of −390 and −417 Wm^{-2} for CRE_m and CRE_0, respectively. There is a slightly higher dispersion of CRE_0 than CRE_m values because of the possible existence of non-discarded doubtful COD values. We found statistically significant differences at the 95% confidence level between Cu and Sc-Cu for both CRE_m and CRE_0. Percentiles 95 and 5 show higher values for the Cu cloud type. CRE_m values of percentiles 95 (5) for Cu and Sc-Cu were −603 (−292) and −567 (−230) Wm^{-2}, respectively. Therefore, we can conclude that Sc-Cu clouds produce a lower effect on solar radiation than Cu clouds.

3.2 Relationship between CRE and the cosine of solar zenith angle (CSZA)

The dependence of solar irradiance to the sun position is transmitted to CRE values, and this behavior is analyzed here in relation to the cosine of solar zenith angle (CSZA). In Figure 4, CRE_m and CRE_0 versus CSZA for both studied cloud types are shown. Note that for Cu (Fig. 4a), CRE_m and CRE_0 decrease

Table II. Statistical values of CRE_m and CRE_0 for each cloud type. CRE maxima and minima are determined with the modulus or absolute value.

Cloud type	CRE (Wm^{-2})	Mean	Standard deviation	Percentiles			Maximum	Minimum
				5th	50th	95th		
Cu	CRE_m	−442	95	−292	−442	−603	−700	−208
	CRE_0	−460	131	−250	−448	−682	−722	−180
Sc-Cu	CRE_m	−390	102	−230	−384	−567	−722	−99
	CRE_0	−417	111	−251	−417	−619	−728	−121

CRE: cloud radiative effect at the surface; CREm: CRE from actinometric measurements; CRE0: modeled CRE.

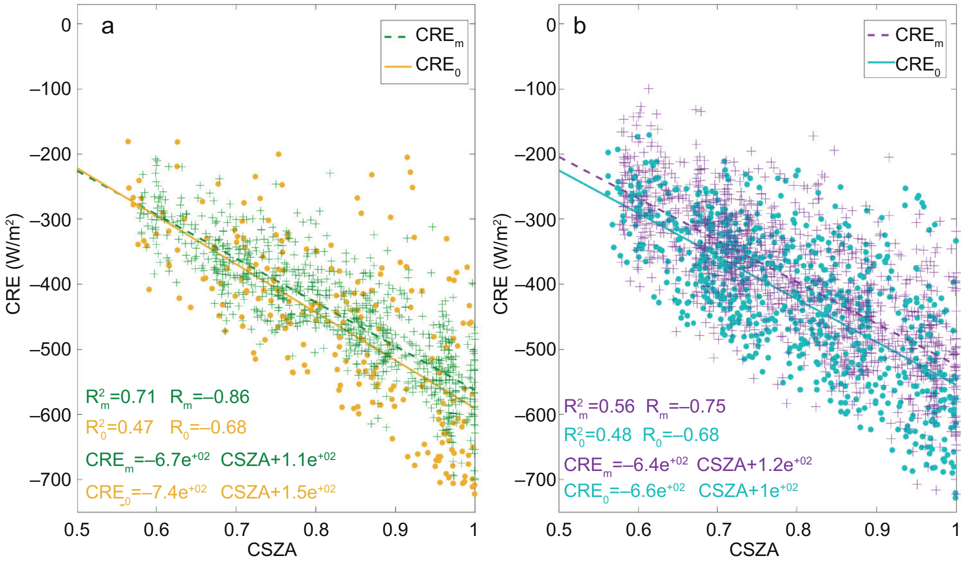

Fig. 4. Relation between CRE (for both CRE$_m$ and CRE$_0$) and CSZA for (a) Cu and (b) Sc-Cu. (CRE: cloud radiative effect at the surface; CRE$_m$: CRE from actinometric measurements; CRE$_0$: modeled CRE; CSZA: cosine of solar zenith angle; Cu: cumulus; Sc-CU: stratocumulus-cumulus).

linearly as CSZA increases (CRE is more negative as CSZA increases). Spearman's correlation coefficient of −0.86 and −0.68 for CRE$_m$ and CRE$_0$, respectively, confirm the relative high correlation with CSZA. The determination coefficient of 0.7 for CRE$_m$ is higher than for CRE$_0$.

In the case of Sc-Cu, Figure 4b also shows a decrease of CRE as function of CSZA, with a Spearman's correlation coefficient of −0.75 and −0.68 for CRE$_m$ and CRE$_0$, respectively. Similar to Cu, the determination coefficient for Sc-Cu is 0.56 for CRE$_m$, higher than for CRE$_0$. Thus, there are similarities in the behavior of CRE respect to CSZA for the two cloud types. The presence of any of these two cloud types obscuring the sun disk strongly decreases the direct sun irradiance, but at near noon (CSZA close to 1), solar irradiance has its maximum, and hence the maximum cloud effect on solar radiation at the surface is present.

3.3 Relationship between CRE and COD

CRO is a function of COD, although other dependencies exist, as the one produced by surface albedo (beyond the scope of this study). However, it is not easy to derive an expression from the radiative transfer theory and hence empirical relationships are frequently obtained. The relation between CRE and COD calculated with both methods is shown in Figure 5. CRE is more negative as COD increases, as can be expected. As it was reported in Mateos et al. (2014), there is a linear relation between CRE$_0$ and COD based on the natural logarithm of COD, with a high Spearman's correlation coefficient of 0.73 and 0.69 for Cu and Sc-Cu, respectively.

COD and actinometric measurements conducted between the first 12 and 20 minutes of each hour were considered as coincident measurements and used to analyze the relationship between CREm and COD (Fig. 5b). The relation between CRE$_m$ and ln(COD) shows a very poor Spearman's correlation coefficient (0.2 for both cloud types). Obviously, this is due to the great dispersion of data and the considerable reduction in the number of experimental data (54 and 238 for Cu and Sc-Cu, respectively). This poor correlation may be in part attributable to the fact that measurements of COD and irradiances were acquired with instruments of very different characteristics, hence there are time-delays between measurements in spite of the coincidence criterion. The radiometer used in the actinometric station measures basically the diffuse solar irradiance under

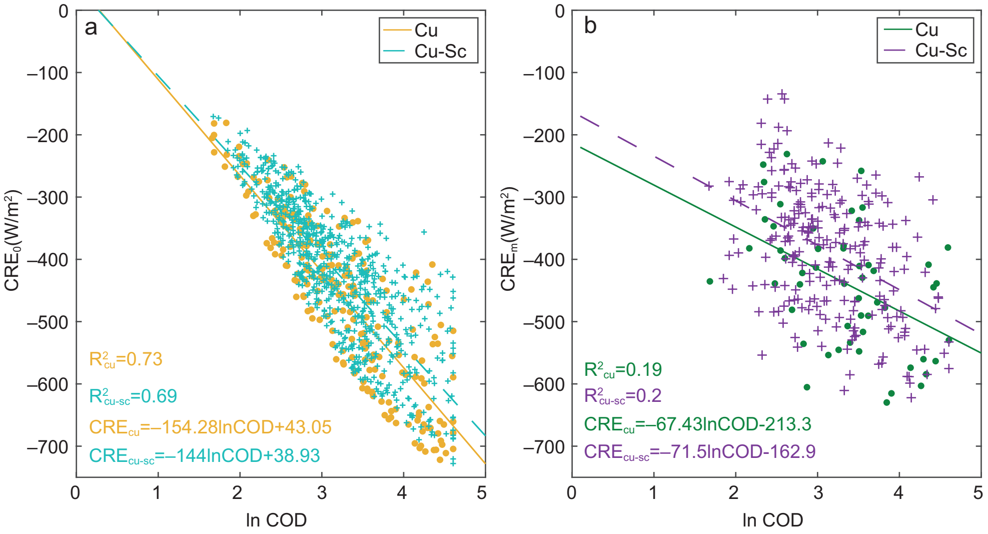

Fig. 5. Relation between (a) CRE_0 and ln(COD) and (b) CRE_m vs. ln(COD). (CRE: cloud radiative effect at the surface; CRE_m: CRE from actinometric measurements; CRE_0: modeled CRE; Cu: cumulus; Sc-CU: stratocumulus-cumulus; lnCOD: natural logarithm of cloud optical depth).

cloudiness conditions, while COD is determined by measuring solar radiation (sky radiance) in the zenith direction. Therefore, the sun-photometer only observes clouds at the zenith.

Table III summarizes the coefficients of the linear regression equation for the CRE_0- ln(COD) relation in several CSZA ranges. It shows the slope of the fitted line (m), the intersection with the ordinate (n), the determination coefficient (R^2) and the number of data in the range (N_0). Linear relations between CRE and ln(COD) have a high determination coefficient ($R^2 > 0.85$) for all intervals.

3.4 Dependence of the cloud effect efficiency (CEE) on CSZA and COD

The relation of CEE vs. CSZA and COD was analyzed only for CRE_0 in different ranges of these variables. Figure 6 shows the CEE behavior in relation to COD in six CSZA ranges (the same than in Table III) for both cloud types. Note that the slope values of m in the selected CSZA ranges do not differ much.

The absolute values of CEE for the two cloud types sharply decrease with the increase of the COD value up to 20. After this value, CEE slowly decreases as COD increases. This behavior is explained by the

Table III. Coefficients *m* and *n* of linear correlation [CRE_0 = m ln(COD) + n], determination coefficient (R^2) and number of data (N_o) for Cu and Sc-Cu at six CSZA ranges.

CSZA	Cu				Sc-Cu			
	m	*n*	R^2	N_o	*m*	*n*	R^2	N_o
0.64 ≥ CSZA > 0.50	–94.7	–24.7	0.96	22	–89.5	–34	0.93	72
0.77 ≥ CSZA > 0.64	–108.6	–45.7	0.91	57	–104.1	–44.6	0.90	259
0.87 ≥ CSZA > 0.77	–114.4	–82.1	0.86	51	–131.5	–9.9	0.93	177
0.94 ≥ CSZA > 0.87	–152.7	2.8	0.96	39	–149.0	5.7	0.95	103
0.98 ≥ CSZA > 0.94	–141.9	–76.9	0.93	38	–159.4	4.4	0.95	87
1 ≥ CSZA > 0.98	–156.7	–33.5	0.97	18	–143.4	–69.8	0.93	34

Cu: cumulus; Sc-CU: stratocumulus-cumulus; CSZA: cosine of solar zenith angle; CRE_m: cloud radiative effect at the surface from actinometric measurements; CRE_0: modeled cloud radiative effect at the surface; lnCOD: natural logarithm of cloud optical depth).

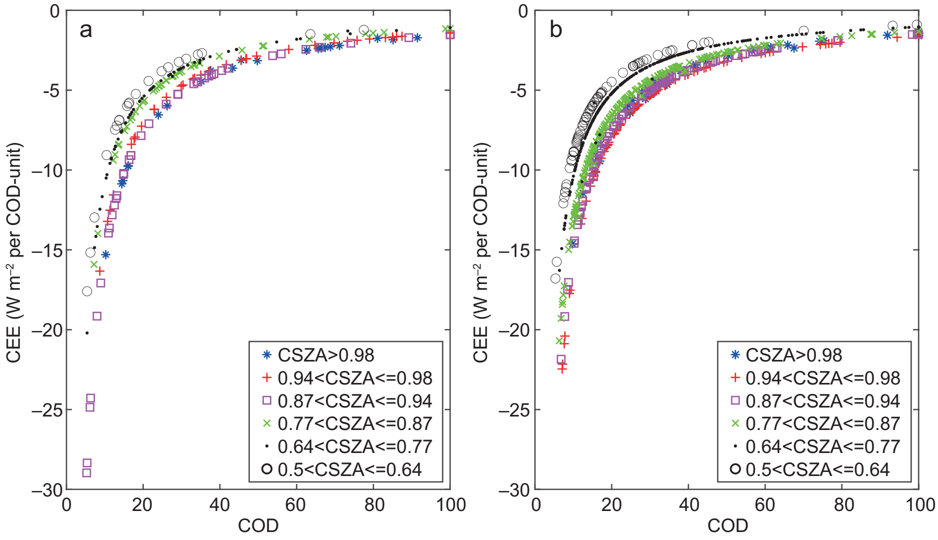

Fig. 6. CEE vs. COD for several CSZA ranges for (a) Cu and (b) Sc-Cu. (CEE: cloud effect efficiency; COD: cloud optical depth; CSZA: cosine of solar zenith angle; Cu: cumulus; Sc-CU: stratocumulus-cumulus).

increase of multiple scattering in the clouds with the increase of COD, and saturation as a consequence of the increase of drops overlapping in the cross section (Mateos et al., 2014). Figure 6 also shows that for both cloud types, CEE is less sensitive to changes in COD due to low values of CSZA (lower Sun position).

Figure 7 shows the relation between CEE and CSZA in four ranges of COD values (5-10, 10-50, 50-75, 75-100). These ranges were chosen to improve

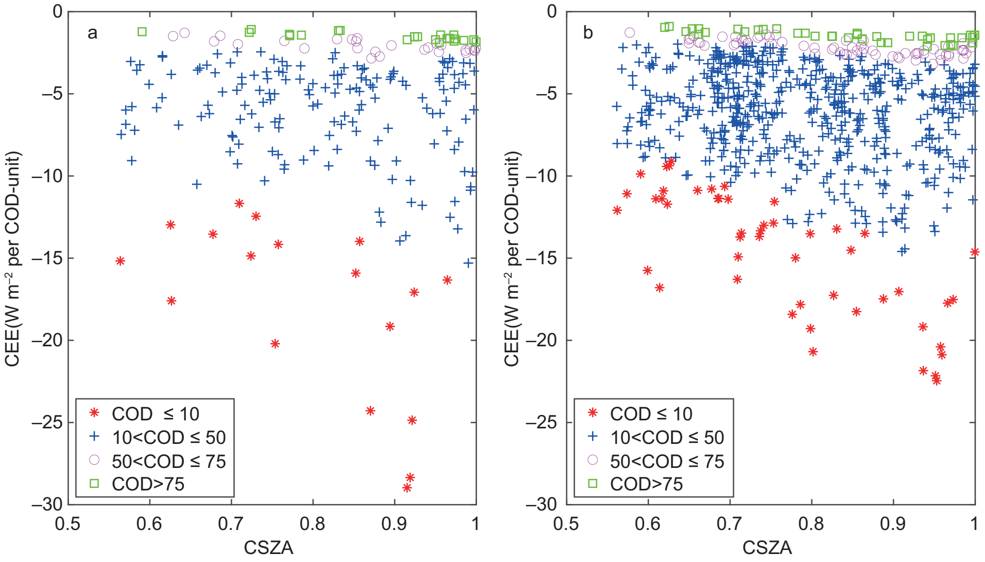

Fig. 7. CEE vs. CSZA at four COD ranges for (a) Cu and (b) Sc-Cu. (CEE: cloud effect efficiency; CSZA: cosine of solar zenith angle; COD: cloud optical depth; Cu: cumulus; Sc-CU: stratocumulus-cumulus).

the understanding of CEE behavior respect to CSZA. In the analysis of both cloud types, the increase of CSZA produces a higher effect per COD unit. This behavior is notable in the range of COD below 10. The maximum value (in modulus) of CEE for Cu is −29 $\mathrm{Wm^{-2}}$ per COD unit with a COD value of 5.3 and CSZA of 0.91, and the minimum is −1 $\mathrm{Wm^{-2}}$ per COD unit for a COD of 100 and CSZA of 0.72. Sc-Cu have a maximum value of −22 $\mathrm{Wm^{-2}}$ per COD unit for a COD of 7.1 and CSZA of 0.95. The minimum value for CEE is −1 $\mathrm{Wm^{-2}}$ per COD unit occurring at a COD of 99.5 (the highest COD value) and CSZA of 0.62.

4. Conclusions

The focus of this paper is to evaluate the clouds radiative effect (CRE) of Cu and Sc-Cu clouds at surface around noon in Camagüey, Cuba. Two methods for the estimation of CRE were applied: (1) using only computations of clear sky irradiances by a 1-D radiative transfer model (RTM) and measurements of irradiances from an actinometric station ($\mathrm{CRE_m}$), and (2) computations of both cloudy and clear sky irradiances by the RTM, using cloud optical depth (COD) from a sun-photometer as main cloud input ($\mathrm{CRE_0}$).

A correspondence criterion between the COD database and the actinometric visual reports of clouds was carried out, in order to assign CODs to a certain cloud type. In addition, a quality control was conducted to remove doubtful COD values to ensure the consistency between the two databases. This quality control consisted in comparing percentages differences between $\mathrm{CRE_0}$ and $\mathrm{CRE_m}$ as function of COD. Doubtful COD values appear in a range of 0-5. Once these doubtful COD values were discarded, $\mathrm{CRE_m}$ (experimental data) and $\mathrm{CRE_0}$ (theoretical data) values were in better agreement, with the maximum frequency of data in the same range, which enabled the comparison between the two methods for evaluating CRE. After the correspondence criterion and the removing of doubtful values, 255 and 732 COD values for Cu and Sc-Cu clouds around noon, respectively, were selected.

The Sc-Cu cloud type has its maximum CRE in the range from −300 to −400 $\mathrm{Wm^{-2}}$; for Cu, the maximum was in the interval from −400 to −500 $\mathrm{Wm^{-2}}$. There are no statistically significant differences between both methods for each cloud type.

For Cu we observed mean values of $\mathrm{CRE_m}$ and $\mathrm{CRE_0}$ of −442 and −460 $\mathrm{Wm^{-2}}$, respectively, while for of Sc-Cu they were −390 and −417 $\mathrm{Wm^{-2}}$, respectively. $\mathrm{CRE_m}$ values of the 95th (5th) percentile were −603 (−292) and −567 (−230) $\mathrm{Wm^{-2}}$ for Cu and Sc-Cu, respectively. Differences between CRE mean values for Cu and Sc-Cu confirm that the latter has less radiative effects in comparison with Cu at our study site. There are statistically significant differences at the 95% confidence level between CRE for Cu and Sc-Cu with both computing methods.

A linear decrease of CRE vs. ln(COD) with a high correlation was found for $\mathrm{CRE_0}$. No linear correlation was found between $\mathrm{CRE_m}$ and ln(COD) because of the lower number of experimental points and their high dispersion due to radiation enhancement effects and also to the fact that measurements of COD and solar irradiance were acquired from instruments with different characteristics, thus having a high time-delay between them.

Cloud effect efficiency (CEE) and its relation with the cosine of the solar zenithal angle (CSZA) and COD were analyzed. The maximum CEE value for Cu (Sc-Cu) was −29 (−22) $\mathrm{Wm^{-2}}$ per COD-unit, with corresponding values of COD of 5.3 (7.1) and CSZA of 0.91 (0.95). On the other hand, the minimum value of CEE for Cu (Sc-Cu) was −1 $\mathrm{Wm^{-2}}$ per COD unit with a COD of 100 (99.5) and CSZA of 0.72 (0.62). CEE values for both cloud types, Sc-Cu and Cu, show a clear dependency with CSZA and COD, decreasing in absolute value with increasing COD.

The results obtained in this research improve the understanding of the relationship between low clouds and solar radiation, which is of great importance for climate studies. Sc and Cu clouds reflect much of the incoming shortwave radiation in the Earth. These low cloud types are the most frequent in our region; they have a great importance in the interaction with irradiances reaching the surface and are related to temperature and further development of other cloud types.

Due to the short period covered by experimental data, it was only possible to evaluate the theoretical method for CEE. However, for the first time, CEE was analyzed as a function of SZA and COD for two different cloud types that have a high occurrence and a great effect on solar radiation in the region.

Acknowledgments

Authors from GOAC-INSMET want to thank the GOA-UVA team for their support and logistics. Our gratitude to AERONET NASA and RIMA networks for including the Camagüey site in AERONET. Authors want to acknowledge the anonymous referees that helped to improve the quality of the manuscript.

This work has been supported by the Cuban National Climate Change Research Program under the contract number 01301204 and by the Collaboration Agreement between the Atmospheric Optics Group (GOA-UVA) and the Atmospheric Optics Group of Camagüey (GOAC-INSMET). Partial financial support from GOA-UVA was provided by Spanish projects from MINECO and MICCIN from 2015 to 2021 (CMT2015-66742-R, RTI2018-097864-B-I00) and by ACSUCYL (Junta de Castilla y León) (projects VA100P17 and VA227P20). Partial financial support from FONDECYT 11181335 was provided to principal author Boris Barja.

Analyses used in this study relates with MODIS data were produced with the Giovanni online data system, developed and maintained by NASA GES DISC. Authors also acknowledge the MODIS mission scientists and associated NASA personnel for the production of data used in this research effort.

References

Ackerman SA, Stephens GL. 1987. The absorption of solar radiation by clouds droplets: An application of anomalous diffraction theory. Journal of the Atmospheric Sciences 44, 1574-1588. https://doi.org/10.1175/1520-0469(1987)044<1574:TAOSRB>2.0.CO;2

Allan JD, Baumgardner D, Raga GB, Mayol-Bracero OL, Morales-García F, García-García F, Montero-Martínez G., Borrmann S, Schneider J, Mertes S, Walter S, Gysel M, Dusek U, Frank GP, Kramer M. 2008. Clouds and aerosols in Puerto Rico—A new evaluation. Atmospheric Chemistry and Physics 8, 1293-1309. https://doi.org/10.5194/acp-8-1293-2008

Antuña-Marrero JC, Fonte A, Estevan R, Barja B, Acea R, Antuña-Sánchez JC. 2008. Solar radiation data rescue at Camagüey, Cuba. Bulletin of the American Meteorological Society 89, 1507-1511, https://doi.org/10.1175/2008BAMS2368.1

Antuña-Marrero JC, Cachorro V, García F, de Frutos A, Rodríguez A, Mateos D, Estevan R, Toledano C. 2018. Comparison of aerosol optical depth from satellite (MODIS), sun photometer and broadband pyrheliometer ground-based observations in Cuba. Atmospheric Measurement Techniques 11, 2279-2293. https://doi.org/10.5194/amt-11-2279-2018

Antuña-Marrero JC, García F, Estevan R, Barja B, Sánchez-Lorenzo A. 2019. Simultaneous dimming and brightening under all and clear sky at Camagüey, Cuba (1981-2010). Journal of Atmospheric and Solar-Terrestrial Physics 190, 45-53. https://doi.org/10.1016/j.jastp.2019.05.004

Barnes WL, Pagano TS, Salomonson VV. 1998. Prelaunch characteristics of the moderate resolution imaging spectroradiometer (MODIS) on EOS-AM1. IEEE Transactions on Geoscience and Remote Sensing 36, 1088-1100. https://doi.org/10.1109/36.700993

Barja B, Antuña-Marrero JC. 2008. Numerical simulation of cirrus cloud radiative forcing using lidar backscatter data. Preliminary results. Óptica Pura y Aplicada 41, 89-95.

Barja B, Antuña-Marrero JC. 2010. Cirrus clouds physical and spatiotemporal features in the Wider Caribbean. Atmósfera 23, 185-196.

Barja B, Antuña-Marrero JC. 2011. The effect of optically thin cirrus clouds on solar radiation in Camagüey, Cuba. Atmospheric Chemistry and Physics 11, 8625-8634. https://doi.org/10.5194/acp-11-8625-2011.

Barja B, Bennouna Y, Toledano C, Antuña-Marrero JC, Cachorro V, Hernández C, de Frutos A, Estevan R. 2012. Cloud optical depth measurements with the sun-photometer in Camaguey, Cuba. Optica Pura y Aplicada 45, 389-396. https://doi.org/10.7149/opa.45.4.389

Berg LK, Kassianov EI, Long CN, Mills DL Jr. 2011. Surface summertime radiative forcing by shallow cumuli at the Atmospheric Radiation Measurement Southern Great Plains site, Journal of Geophysical Research: Atmospheres 116, D01202. https://doi.org/10.1029/2010JD014593

Boucher O, Randall D, Artaxo P, Bretherton C, Feingold G, Forste P, Kerminen VM, Kondo Y, Liao H, Lohmann U, Rasch P, Satheesh SK, Sherwood S, Stevens B, Zhang XY. 2013. Clouds and aerosols. In: Climate Change 2013: The Physical Science Basis. Contribution of Working Group I to the Fifth Assessment Report of the Intergovernmental Panel on Climate Change (Stocker TF, Qin D, Plattner GK, Tignor M, Allen SK, Boschung J, Nauels A, Xia Y, Bex V, Midgley PM, Eds.). Cambridge University Press, Cambridge, United Kingdom and New York, NY, USA. 571-657, https://doi.org/10.1017/CBO9781107415324.016

Chen T, Rossow WB, Zhang Y. 2000. Radiative effects of cloud-type variations. Journal of Climate 13, 264-286. https://doi.org/10.1175/1520-0442(2000)013<0264:REOCTV>2.0.CO;2

Chervyakov MY, Neishtadt JA. 2018. Actinometric methods of measurements. Textbook for students of the Faculty of Geography. Saratov Publishing house of the Saratov State University, Russia, 42 pp. (in Russian).

Chiu JC, Huang CH, Marshak A, Slutsker I, Giles DM, Holben BN, Knyazikhin Y, Wiscombe WJ. 2010. Cloud optical depth retrievals from the Aerosol Robotic Network (AERONET) cloud mode observation. Journal of Geophysical Research 115, D14202. https://doi.org/10.1029/2009JD013121

Chou MD, Zhao W. 1997. Estimation and model validation of surface solar radiation and cloud radiative forcing using TOGA COARE measurements. Journal of Climate 10, 610-620. https://doi.org/10.1175/1520-0442(1997)010<0610:EAMVOS>2.0.CO;2

Dolinar EK, Dong X, Xi B, Jiang J, Loeb N, Campbell J, Su H. 2019. A global record of single-layered ice cloud properties and associated radiative heating rate profiles from an A-Train perspective. Climate Dynamics 53, 3069–3088. https://doi.org/10.1007/s00382-019-04682-8

Eerme K, Aun M. 2012. A review of the variations of optical remote sensing conditions over Estonia in 1958-2011. International Journal of Remote Sensing Applications 2, 12-19.

Freidenreich SM, Ramaswamy V. 1999. A new multiple-band solar radiative parameterization for general circulation models. Journal of Geophysical Research 104, 31389- 31409. https://doi.org/10.1029/1999JD900456

Freidenreich SM, Ramaswamy V. 2005. Refinement of the geophysical fluid dynamics laboratory solar benchmark computation and improved parameterization for climate models. Journal of Geophysical Research 110, D17105. https://doi.org/10.1029/2004JD005471

Freidenreich SM, Ramaswamy V. 2011. Analysis of the biases in the downward shortwave surface flux in the GFDL CM2.1 general circulation model. Journal of Geophysical Research 116, D08208. https://doi.org/10.1029/2010JD014930

Gueymard CA. 2017. Cloud and albedo enhancement impacts on solar irradiance using high-frequency measurements from thermopile and photodiode radiometers. Part 1: Impacts on global horizontal irradiance. Solar Energy 153, 755-765. https://doi.org/10.1016/j.solener.2017.05.004

Ham S, Kato S, Rose F, Winker D, L'Ecuyer T, Mace G, Painemal D, Sun-Mack S, Chen Y, Miller WF. 2017. Cloud occurrences and cloud radiative effects (CREs) from CERES-CALIPSO-CloudSat-MODIS (CCCM) and CloudSat radar-lidar (RL) products. Journal of Geophysical Research 122, 8852-8884. https://doi.org/10.1002/2017JD026725

Holben BN, Eck TF, Slutsker I, Tanré D, Buis JP, Setzer A, Vermote E, Reagan JA, Kaufman YJ, Nakajima T, Lavenu F, Jankowiak I, Smirnov A. 1998. AERONET—A federated instrument network and data archive for aerosol characterization. Remote Sensing of Environment 66, 1-16. https://doi.org/10.1016/S0034-4257(98)00031-5

Kim BG, Schwartz SE, Miller MA, Min Q. 2003. Effective radius of cloud droplets by ground-based remote sensing: Relationship to aerosol. Journal of Geophysical Research 108, 4740. https://doi.org/10.1029/2003JD003721.

L'Ecuyer TS, Wood NB, Haladay T, Stephens GL, Stackhouse PWJr. 2008. Impact of clouds on atmospheric heating based on the R04 Cloudsat fluxes and heating rates data set. Journal of Geophysical Research 113, D00A15. https://doi.org/10.1029/2008JD009951

Li J, Yi Y, Minnis P, Huang J, Yan H, Ma Y, Wang W, Ayers J. 2011. Radiative effect differences between multi-layered and single-layer clouds derived from CERES, CALIPSO, and CloudSat data. Journal of Quantitative Spectroscopy and Radiative Transfer 112, 361-375. https://doi.org/10.1016/J.JQSRT.2010.10.006

Li Z, Trishchenko AP. 2001. Quantifying uncertainties in determining SW cloud radiative forcing and cloud absorption due to variability in atmospheric conditions. Journal of the Atmospheric Sciences 58, 376-389. https://doi.org/10.1175/1520-0469(2001)058<0376:QUIDSC>2.0.CO;2

Liou KN. 1986. Influence of Cirrus Clouds on Weather and Climate Processes: A Global Perspective. Monthly Weather Review 114, 1167-1199. https://doi.org/10.1175/1520-0493(1986)114%3C1167:IOCCOW%3E2.0.CO;2

Martínez E, Pomares I. 2002. Evaluation of the solar radiation transmission in clouds from measurements in Havana (in Spanish). In: Proceedings of the first workshop Physics in Meteorology. Havana, Cuba, February 4-6.

Mateos D, Antón M, Valenzuela A, Cazorla A, Olmo FJ, Alados-Arboledas L. 2014. Efficiency of clouds on shortwave radiation using experimental data. Applied Energy 113, 1216-1219. http://dx.doi.org/10.1016/j.apenergy.2013.08.060

McBride PJ, Schmidt KS, Pilewskie P, Kittelman AS, Wolfe DE. 2011. A spectral method for retrieving cloud optical thickness and effective radius from surface-based transmittance measurements. Atmospheric Chemistry and Physics 11, 7235-7252, https://doi.org/10.5194/acp-11-7235-2011.

McClatchey RA, Fenn RW, Selby JE, Volts FE, Garing JS. 1972. Optical properties of the atmosphere. 3rd ed. Air Force Cambridge Research Labs, Hanscom, MA. Available at: https://apps.dtic.mil/sti/pdfs/AD0753075.pdf (accessed on January 25, 2021).

McFarlane S, Long CN, Flaherty J. 2012. A climatology of surface cloud radiative effects at the ARM tropical western Pacific sites. Journal of Applied Meteorology and Climatology 52, 996-1031. https://doi.org/10.1175/JAMC-D-12-0189.1

Mitchell DL, Finnegan W. 2009. Modification of cirrus clouds to reduce global warming. Environmental Research Letters 4, 045102. https://doi.org/10.1088/1748-9326/4/4/045102

Neiburger M. 1949. Reflection, absorption, and transmission of insolation by stratus cloud.

Journal of the Atmospheric Sciences 6, 98-104. https://doi.org/10.1175/1520-0469(1949)006<0098:RAATOI>2.0.CO;2

Ross YK, Ashcheulov SV, Mikhailov VV. 1969. 2. Methods of actinometric measurements. International Geophysics 12, 49-83. https://doi.org/10.1016/S0074-6142(08)62774-6

Schiffer RA, Rossow WB. 1983. The International Satellite Cloud Climatology Project (ISCCP): the first project of the World Climate Research Programme. Bulletin of the American Meteorological Society 64. 779-784. https://doi.org/10.1016/0169-8095(88)90026-9

Slingo A. 1989. A GMC Parameterization for the shortwave radiative properties of water clouds. Journal of Atmospheric Sciences 46, 1419-1427. https://doi.org/10.1175/1520-0469(1989)046<1419:AGPFTS>2.0.CO;2

Spiegel JK, Buchmann N, Mayol-Bracero OL, Cuadra-Rodriguez LA, Valle-Díaz CJ, K. Prather A, Mertes S, Eugster W. 2014. Do cloud properties in a Puerto Rican tropical montane cloud forest depend on occurrence of long-range transported African dust? Pure Applied Geophysics 171, 2443-2459. https://doi.org/10.1007/s00024-014-0830-y

Stephens GL. 2005. Cloud feedbacks in the climate system: A critical review. Journal of Climate 18, 237-273. https://doi.org/10.1175/JCLI-3243.1

Stephens GL, Vane DG, Tanelli S, Im E, Durden S, Rokey M, Reinke D, Partain P, Mace GG, Austin L, L'Ecuyer T, Haynes J, Lebsock M, Suzuki K, Waliser D, Wu D, Kay J, Gettelman A, Wang Z, Marchand R. 2008. CloudSat mission: Performance and early science after the first year of operation. Journal of Geophysical Research 113, D00A18, https://doi.org/10.1029/2008JD009982

Winker DM, Hunt WH, McGill MJ. 2007. Initial performance assessment of CALIOP. Geophysical Research Letters 34, L19803., https://doi.org/10.1029/2007GL030135

Wielicki BA, Barkstorm BR, Harrison EF, Lee III RB, Smith GL, Cooper JE. 1996. Clouds and the Earth's radiant energy system (CERES): An Earth observing system experiment. Bulletin of the American Meteorological Society 77, 853-868. https://doi.org/10.1175/1520-0477(1996)077<0853:CATERE>2.0.CO;2

WMO. 2017. International cloud atlas: Manual on the observation of clouds and other meteors. WMO No. 407. Secretariat of the World Meteorological Organization, Geneva, Switzerland. Available at: https://cloudatlas.wmo.int/home.html (accessed on November, 2020).

Yanishevsky YD. 1957. Aktinometricheskie pribory i metody nablyudenij (Actinometric receivers and measurement methods). Gidrometeorol. Izd., Leningrad, Russia, 416 pp. (in Russian).

Zhang G, Xu L, Chen H. 1995. A new parameterization for shortwave radiative properties of water clouds. Journal of Applied Meteorology 34, 101-106. https://doi.org/10.1175/1520-0450-34.1.101

Atmósfera 36(1), 57-76 (2023)
https://doi.org/10.20937/ATM.53025

Summer dry events on synoptic and intraseasonal timescales in the Southeast Region of Brazil

Anderson Augusto BIER[1]*, Simone Erotildes Teleginski FERRAZ[2] and Tercio AMBRIZZI[1]

[1]Department of Atmospheric Sciences, University of São Paulo, São Paulo, 05508-090, SP, Brazil.
[2]Department of Physics, Federal University of Santa Maria, Santa Maria, 97105900, RS, Brazil.
*Corresponding author: bier.anderson@iag.usp.br

Received: December 30, 2020; accepted: May 18, 2021

RESUMEN

La ocurrencia de eventos secos en la región Sudeste de Brasil (SEB, por sus siglas en inglés) durante el verano (temporada de lluvias) se ha evidenciado en los últimos años, principalmente debido a eventos extremos previos en las temporadas 2013/14 y 2014/15. Los análisis de sequía se suelen realizar con datos mensuales. Aquí nuestra metodología aborda el tema con datos diarios para generar un análisis exhaustivo. Los eventos secos se evaluaron en diferentes subregiones de precipitación homogénea dentro del SEB, durante 37 temporadas diciembre-febrero (DJF, por sus siglas en inglés) y con dos escalas de tiempo diferentes de duración: sinóptica (5-9 días) e intraestacional (≥10 días). Se encontraron dos patrones dinámicos principales distintos para los eventos secos en las partes sur y centro-norte de SEB, respectivamente, pero no se identificaron diferencias importantes en las diferentes escalas de tiempo de ocurrencia. Los eventos del sur se caracterizaron por una cresta estacionaria que actuaba sobre todo el sur de América del Sur, lo que dificultó la aproximación de los sistemas transitorios al SEB del sur. Al mismo tiempo, este patrón mostró una configuración de Zona de Convergencia del Atlántico Sur (SACZ, por sus siglas en inglés) desplazada hacia el norte. En los eventos centro-norte, una alta presión centrada entre las regiones sur y sureste de Brasil se asoció con las condiciones de sequía. También se verificó un desplazamiento anómalo hacia el sur de los sistemas meteorológicos característico del verano sudamericano para estos eventos. Sobre el Atlántico Sur, se identificó una configuración de anomalía SST opuesta entre los eventos del sur y del centro-norte.

ABSTRACT

The occurrence of dry events in the Southeast Region of Brazil (SEB) during summer (rainfall season) has been in evidence in the last years, mainly due to previous extreme events in the 2013/14 and 2014/15 seasons. Drought analyses are usually carried out with monthly data. Here our methodology addresses the issue with daily data to generate a thorough analysis. Dry events were evaluated in different homogeneous precipitation sub-regions within the SEB, over 37 December-February (DJF) seasons and with two different timescales of duration: synoptic (5-9 days) and intraseasonal (≥10 days). Two main distinct dynamic patterns were found for dry events in southern and central-northern parts of SEB, respectively, but no significant differences were identified in the different timescales of occurrence. Southern events were characterized by a stationary ridge acting over the whole of southern South America, making the approximation of the transient system to southern SEB difficult. At the same time, this pattern showed a northern-shifted South Atlantic Convergence Zone (SACZ) configuration. In the central-northern events, a high pressure centered between Brazil's South and Southeast regions was associated with the dryness conditions. An anomalous southward shift of meteorological systems characteristic of the South American summer was also verified for these events. Over the South Atlantic, an opposite SST anomaly configuration was identified between southern and central-northern events.

Keywords: synoptic dry events, intraseasonal dry events, rainfall season.

1. Introduction

The Southeast Region of Brazil (SEB) is located between 14ºS and 26ºS latitudes and 39ºW to 52ºW longitudes. The region is made up of the states of São Paulo, Rio de Janeiro, Minas Gerais and Espírito Santo. The population consists of more than 80 million inhabitants and represents approximately 42.1% of the Brazilian population (IBGE, 2010). Its economy is based upon industry, services sector, mineral extraction, and agriculture, besides holding about 55% of the national gross domestic product (GDP) (IBGE, 2014). SEB has different climate regimes, with most of its land in tropical areas and a small portion, in the southern half of the state of São Paulo, in the subtropics. When considering the topic of rainfall, the region is located in a transition zone between a permanently wet regime, typical of the Southern Brazil, and a regime with seasonal variation in precipitation observed in central Brazil, which has large rainfall accumulations over the summer months contrasting with dry winters (Nunes et al., 2009). The main atmospheric system to produce precipitation over the SEB during the summer is the South Atlantic Convergence Zone (SACZ), which shows a timescale that varies between synoptic and intraseasonal (Kodama, 1992, 1993; Quadro, 1994; Carvalho et al., 2004; Ambrizzi and Ferraz, 2015). It is worth noting that the highest rainfall occurs in the summer due to the convective systems (often associated with SACZ episodes), which are typical of this season, more frequent, and bring a greater amount of rain when compared with winter frontal systems (Nunes et al., 2009; Cavalcanti and Kousky, 2009).

In this context, summer drought events have an immense potential to cause economic and social impact in the region if mitigation measures are not adopted. Services and activities essential for the population, such as food production, water, and electric power supply, can be seriously affected. SEB has a large number of hydroelectric plants, which represents the primary current Brazilian energy matrix. Approximately 65,2% of the domestic supply in Brazil comes from this matrix (Ministério de Minas e Energia, 2018), being highly dependent on the regional rainfall regime. Other inconveniences, such as fires, agricultural damage, respiratory health diseases, and the disablement of waterways (Toloi et al., 2016), are also more common during shortage periods and are aggravating factors. Large precipitation deficits associated with drought periods, such as those that occurred during the summer of 2014 and 2015, have led to a decrease in the level of water supply and hydroelectric power plants dams in the SEB being at extreme levels never seen before (e.g., Watts, 2015; Nobre et al., 2016). Such events have motivated new studies that seek to understand these phenomena better.

Atypical summer dry periods over the SEB result from complex interactions between natural oscillations across different time scales and local factors. The causes may include many factors that are not well known and can be further investigated. Some of these factors are documented in the current literature but are not yet a closed issue. For instance, the Pacific-South America (PSA) teleconnection pattern, especially the PSA2 mode, is commonly associated with dry episodes over SEB (Mo and Paegle, 2001; Castro-Cunningham and De Albuquerque-Cavalcanti, 2006). Some works like Seth et al. (2015) and Coelho et al. (2016) identified a teleconnection pattern between anomalous convective activities over the western tropical Pacific Ocean, and the consequent establishment of a blocking high close to SEB, as the main source of the 2014 and 2015 summer droughts. In their turn, Rodrigues and Woolings (2017) showed that wave-breaking events associated with convection over the Indian Ocean coinciding with phases 1 and 2 of Madden-Julian Oscillation (MJO) have an important role in triggering such blocking highs near the SEB. Expressive marine heatwaves in the adjacent Atlantic Ocean are also very common in such conditions (Rodrigues et al., 2019). Finke et al. (2020), through numerical simulations, argued that neither the tropical Pacific nor the Indian SST anomalies are the main cause of generating the wave train pattern associated with the SEB summer dry event in 2013/14, but rather the South Pacific and the local Atlantic SST anomalies that have a more critical role.

Regarding local factors contributing to drier summers over SEB, a possibility is presented by Grimm et al. (2007) and Grimm and Zilli (2009), in which the authors found a negative relationship between precipitation observed during spring and summer. As for rainy springs and dry summers, the authors suggest that the precipitation observed over the region during spring contributes to a decrease in the temperature throughout this season. Consequently, the initial conditions of summer are mild temperatures, which are favorable to an increase in atmospheric pressure over the continent during the season, thus reducing atmospheric conditions for precipitation. The opposite circumstance is also true; in other words, dry and warm spring in the region contributes to a rainy summer, these conditions being more common in El Nino's years.

Some regional aspects of atmospheric dynamics and ocean-atmosphere interactions, which occur during dry periods in the SEB and are present at various timescales, are well recognized and have been reported in several works. One of these is the intensification and displacement of the South Atlantic Subtropical High (SASH) towards the southeastern Brazilian coast, which is associated with dry periods in the SEB in practically all seasons of the year (Nogués-Paegle and Mo, 1997; Doyle and Barros, 2002; Muza et al., 2009; Pampuch, 2014; Coelho et al., 2016). Such SASH configuration favors a blocked flow over the region, diverting passages of baroclinic disturbances and also contributing to an increase in subsidence and consequent atmosphere stabilization over the SEB. Also, SEB dry periods are commonly associated with positive precipitation anomalies over southeastern South America (SESA), a region that involves northwestern Argentina, Paraguay, Uruguay, and southern Brazil (Nogués-Paegle and Mo, 1997; Barros et al., 2000; Robertson and Mechoso, 2000; Ferraz, 2004; Castro-Cunningham and De Albuquerque-Cavalcanti, 2006; Muza et al., 2009; Grimm and Zilli, 2009, Gonzalez and Vera, 2014). This relationship corresponds to a phase of a meridional dipole between such regions that is verified in the main mode of precipitation variability over Brazil during the austral summer (Grimm, 2009), associated with the alternating channeling of moisture from Amazon to SESA and central-eastern Brazil. Some studies show the relationship between the precipitation dipole and wave trains' propagation from midlatitudes or teleconnection patterns like the PSA (Mo and Paegle, 2001; Carvalho et al., 2004; Castro-Cunningham and De Albuquerque-Cavalcanti, 2006). Another frequent feature connected to dry events in the most of SEB, as a result of ocean-atmosphere interactions, is an elongated strip of positive sea surface temperature (SST) anomalies over subtropical South Atlantic(e.g., Barros et al., 2000; Doyle and Barros, 2002; Coelho et al., 2016; Pampuch et al., 2016; Pattnayak et al., 2018; Rodrigues et al., 2019). Rodrigues et al. (2019) demonstrate that this pattern is mainly due to the increased incident shortwave radiation and negative anomalies of latent heat flux (from the ocean to the atmosphere). Results of numerical simulations from Finke et al. (2020) suggest that these positive SST anomalies contribute to establishing a high-pressure system south of SEB and then favoring the dry periods over SEB.

A better comprehension of the atmospheric mechanisms associated with the dry summer periods in SEB contributes to improving the diagnosis and the forecast of similar conditions in the future. As seen in the last paragraphs, many studies have addressed dry periods in SEB. However, most analyzed monthly data, which may attenuate some atmospheric signatures related to such events. In this study, daily data was employed to analyze dry periods over the SEB in a synoptic and intraseasonal timescale to describe the dynamic and thermodynamic aspects verified in the dry events. Seasonal rainfall deficits over a given region may have more causes than isolated dry events with a synoptic and intraseasonal duration scale, such as those presented here. However, when such events occur frequently, they contribute to expressive precipitation deficits, as will be verified. Besides that, detailed analyses of the mean atmospheric and oceanic conditions related to the dry events were performed, focusing on the behavior of large-scale meteorological systems typical during the South American summer.

2. Data and methodology

2.1 Data

Daily precipitation data were obtained from *Climate Hazards Group InfraRed Precipitation with Station* (CHIRPS) (Funk et al., 2015) with a spatial resolution of 0.25 degrees. These data were employed to determine dry events over the SEB. Another dataset was composed of *ERA-Interim reanalysis* (Dee et al., 2011; Berrisford et al., 2011) from the *European Centre for Medium-Range Weather Forecasts* (ECMWF). This dataset was used to calculate mean fields and composites, aiming to describe the mean atmospheric and oceanic features of drought events. The data resolution is 0.75º x 0.75º, and the variables used were 500 mb geopotential height, mean sea level pressure (MSLP), 200 mb and 850 mb wind, 850 mb specific humidity, sea surface temperature (SST), and outgoing longwave radiation (OLR). OLR was chosen because it is a variable that correlates well with rain, especially in tropical latitudes (Peixoto and Oort, 1992). The mean annual cycle of daily data was removed from both datasets. As the summer precipitation regime was targeted, only data from the December-February (DJF) season (austral summer) were used for the period 1981/82 to 2017/18.

2.2 Methodology

2.2.1 Determination of homogeneous precipitation regions

Precipitation regimes are spatially variable through the SEB in all year seasons, especially in the summer. For this reason, the cluster analysis method was used to group areas with homogeneous characteristics in the daily precipitation regime. As can be seen in figure 1, the method was applied over a rectangular region that encompasses the SEB (states of São Paulo, Rio de Janeiro, Minas Gerais, and Espírito Santo, referenced respectively as SP, RJ, MG, and ES in figure 1b) and part of neighboring states.

According to Wilks (2006), in the cluster analysis, *n* grid points are considered *n* vectors with *K* dimensions each (*K* steps in time). In an initial moment, each vector is treated as a cluster (*n* clusters with *K* dimensions each). The next step is to join the two closest vectors to each other (with the smallest vector differences) to form a new cluster, and thus, the number of clusters becomes *n-1*. Ward's minimum variance hierarchical method (Ward 1963) was employed to join the two closest clusters, aiming to minimize the sum of the internal vector distance variance for each cluster (*W*). The process of cluster merging (clustering) is repeated continuously until a given number of clusters is reached when the differences between the members of a specific cluster are minimized, and the differences between members of different clusters are maximized, or from another viewpoint, it is the creation of groups with homogeneous data.

Some methods identify the stage in which the clustering process must be interrupted, a way of doing this for methods based on distance matrix is through the analysis of the graph showing the distance between clusters as a function of the clustering process stage (Wilks, 2006). Analogously, for Ward's method, which is not based on the distance matrix, this step must be done by analyzing the graph showing *W* as a function of the number of merged clusters. The distances in the first cluster merge are usually small, and *W* increases slowly. This pattern tends to remain the same until the last stages of clustering, when

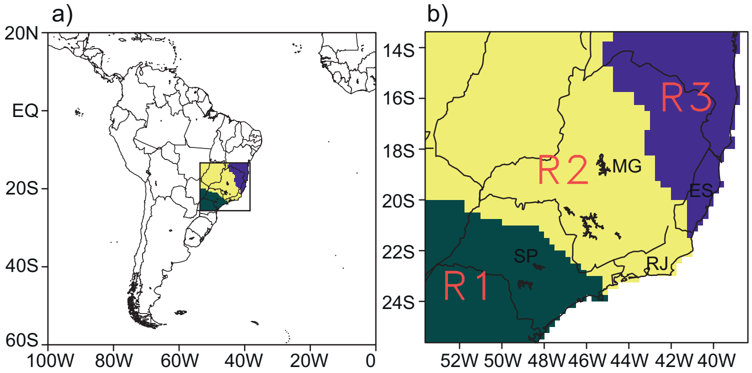

Fig. 1. (a) Area of study (rectangle) where the Southeast Region of Brazil (SEB) is encompassed. (b) Regions with homogeneous precipitation were determined from the cluster analysis. From south to north, we have R1, R2, and R3, respectively. The SEB states are identified on the map with the acronyms SP (São Paulo), RJ (Rio de Janeiro), MG (Minas Gerais) and ES (Espírito Santo).

clusters become more distant, and *W* increases faster, precisely because the differences between the clusters are more accentuated. Seen in *W* as a function of the number of remaining clusters scheme, this transition is identified by an important "jump" in the growth trend of *W* from one stage to another. Evaluating it by this subjective method, the moment to interrupt the process is exactly the moment when this "jump" occurs because it is the moment in which the distances between the clusters become considerably larger.

The graph shown in figure 2 presents W as a function of the number of clusters for the precipitation dataset of this work. Note that the figure only indicates the last 15 steps (from a total of 3100 initial clusters, or 3100 grid points within the study region), which is the progression of the clustering process between the time that there are 15 clusters and when there is only one cluster left. Note the continuous increase of W, from left to right of the graph, and the "jump" in the growth trend between points 4 and 3, indicated by an arrow. From this analysis, 3 clusters were found as representative. When these three groups of grid points are disposed of geographically, three regions with homogeneous daily precipitation data are identified, which is presented in figure 2. The regions were named, from south to north, R1, R2, and R3, respectively.

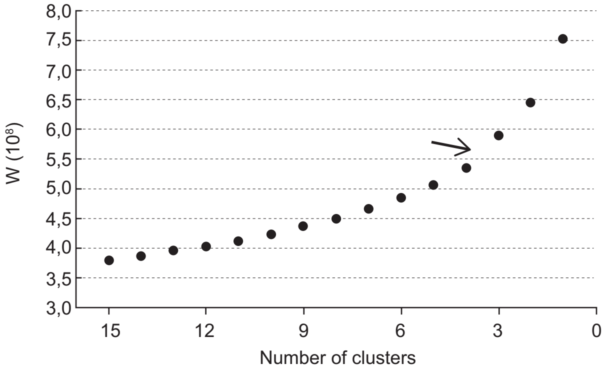

Fig. 2. Sum of the variance of each cluster (W) internal vector distance as a function of the number of clusters.

2.2.2 Determination of dry events

There is no universal index for determining droughts due to the various possible definitions for this phenomenon (Heim, 2002). We aim to determine drought events over a broad area and for a daily data series when there are no significant spatially or temporally precipitation episodes. For this task, two methods were employed: the consecutive dry days method (CDDM) and the variable threshold method (VTM). Van Huijgevoort et al. (2012) proposed this combination of two methods for the detection of hydrological drought events consistently and for regions with different runoff climatic regimes. Pampuch et al. (2016) adapted the two methods for meteorological droughts, taking this model as a basis for the script adopted here. According to Van Huijgevoort et al. (2012), in comparison with other methods widely adopted in the detection of droughts, such as SPI (Standard Precipitation Index) and PDSI (Palmer Drought Standard Index), the advantages of using these two methods are that knowledge of probability distributions is not needed, besides the creation of essential aspects of a drought event, such as frequency, duration, and severity. Also, even during summer shortage periods, the predominantly wet and tropical climate of SEB presents localized precipitation events. The CDDM makes a spatial assessment of droughts, where it is possible to identify dry periods in which such isolated rain events occur. On the other hand, VTM evaluates regional average rainfall as a whole.

The CDDM is simply based on a cumulative count of the dry days following some parameters. Here, the CDDM involves the following steps:

1. The days in which the precipitation was less than 1 mm were identified for each grid point. In theory, this threshold was supposed to be equal to 0 mm, but the value adopted here was due to the interpolated nature of the precipitation data.
2. If precipitation recorded at 75% of the grid points in a given region shows precipitation below 1 mm on a given day, that day is considered a "dry day."
3. The consecutive "dry days" are counted until the day when the requirements in item 2 are no longer accomplished; that is, precipitation above 1 mm occurs in more than 25% of grid points, except for the condition listed in item 4.
4. It is allowed that up to one day, within a sequence of consecutive dry days, in a given region presents less than 75% of grid points with values lower than 1 mm, but at least 50% of grid points must meet this requirement.

The VTM shows whether the precipitation recorded on a given day characterizes an extreme dry value over the evaluated region as a whole. Unlike the CDDM, which uses the precipitation series at each grid point, the VTM is applied over the mean regional precipitation. The method utilizes a threshold to determine dry periods within a precipitation series, which is usually the 20th percentile, and it can be used either as a fixed or time-varying threshold (e.g.: seasonally, monthly, or daily) (Van Huijgevoort et al., 2012). A time-varying threshold is used to consider the seasonal precipitation cycle. For example, a daily-varying threshold considers a data series composed of every day of the year throughout the study period. In other words, for January 21st, we have a series of 37 data (37 days on January 21st throughout the 37 years of the data series).

Since a sample size of 37 would be too small to form a sample of appreciable size and without disregarding the local seasonal precipitation cycle, in this work, a time-varying threshold was chosen for a 10-day interval. Considering that the DJF is composed of 90 days (excluding the leap years), representing a total of 3330 days over the 37 years, nine series of 370 days each were created from this dataset. Therefore, the first series consists of the 1st to 10th of December days, the second one of 11th to 20th, and so on. To simplify, the nine daily precipitation data corresponding to the February 29th, present throughout the study period, were included in the last of the nine series described above, with the latter having 379 elements. The 20th percentiles were determined as the "dry thresholds" within each series, called P(20). A "dry day" is identified at the time that the daily precipitation of a given day falls below this threshold. A boxplot with the distribution of the precipitation data series over the 10-day intervals for each of the three sub-regions is shown in figure 3. The P(20) values in each interval are labeled and indicated by the red dots.

In order to determine possible differences in the atmospheric and oceanic characteristics present during the dry events, which were identified by the methods at different timescales, two temporal thresholds were used. Firstly, dry events persisting for a minimum period of 5 consecutive days and a maximum of 9 consecutive days were called "synoptic dry events" (SDEs), while events lasting ten days or longer were named "intraseasonal dry events" (IDEs). In the combination of CDDM and VTM, a "dry event" is detected at the moment the CDDM requirements are met at the synoptic (5 days) or intraseasonal (10 days) dry threshold period, at the same time that it is confirmed at least 50% of "dry days" by the VTM along the same period determined by the CDDM. As previously mentioned, isolated rain events can occur in the CDDM, while VTM potentially inhibits them in part of the days (at least 50%), which reinforces and suits the method to the study region. In figures 4a and 4b, there is a graphical demonstration of how the CDDM acting along with the VTM detected dry events. The methods were applied separately to each homogeneous precipitation region determined by cluster analysis (R1, R2, and R3).

3. Results

3.1 Dry events statistics

As described in the introduction section, SEB is a vast region with somewhat different climatic regimes. Generally, summer is characterized as the rainy season, but with some differences within the region. These differences were the reason we divided the region into three sub-regions with more homogeneous characteristics in precipitation to analyze them better. Considering our precipitation dataset for the study period (DJF 1981/82 to DJF 2017/18), R2 (the central strip area in SEB) has the highest DJF average precipitation with 719 mm, while R1 (southernmost area) has 595.5 mm and R3 (northernmost area) has 393.3 mm. Some notion about how the mean regional precipitation varies seasonally in different aspects and within each sub-region can be obtained through the boxplot analysis in figure 3.

The total numbers of dry events (synoptic and intraseasonal) found by study region (R1, R2, and R3) between DJF 1981/82 and 2017/18 are shown in figure 5. Concerning intraseasonal dry events (IDEs), R3 was the region with the greatest number of occurrences (20 events), followed by R1 (7 events) and R2 (1 event). For synoptic dry events (SDEs), R1 recorded the highest number of cases (56 events), followed by R3 (37 events) and R2 (19 events). Despite the total number of events (SDEs plus IDEs) being greater in R1 (62 events) compared with R3 (57 events), if one considers the sum of "dry days"

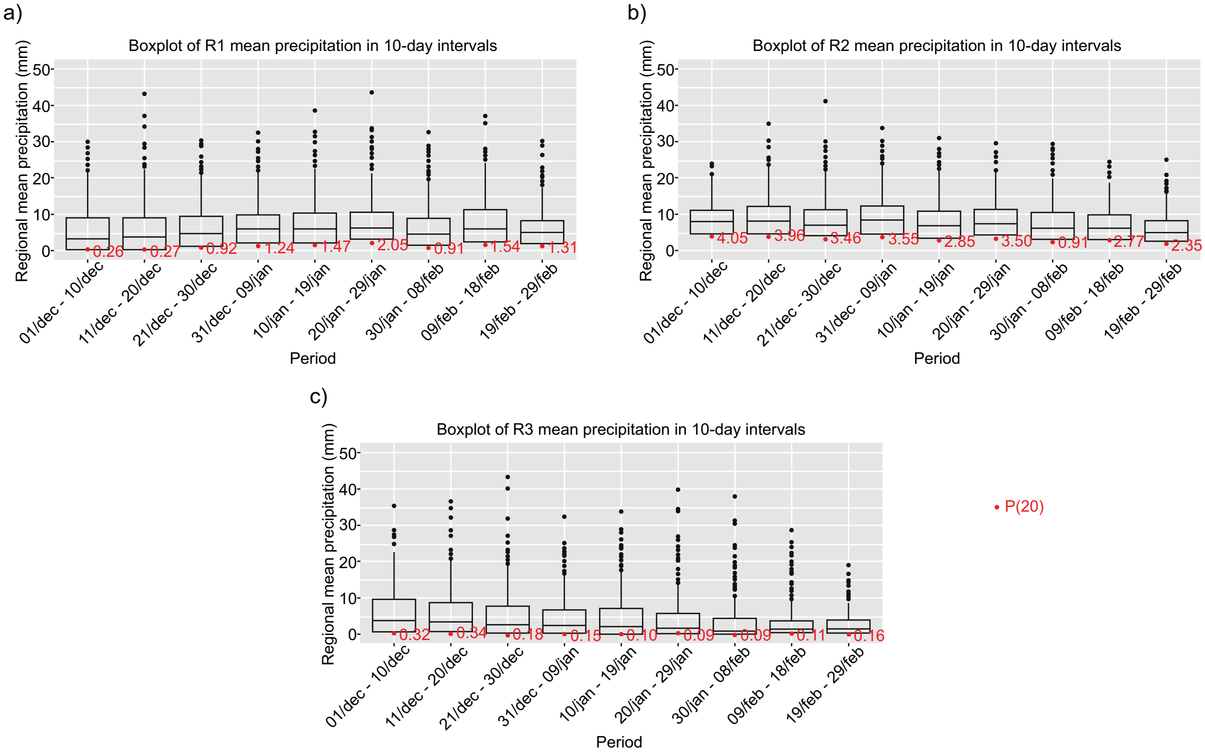

Fig. 3. (a) The Consecutive Dry Days Method (CDDM) and (b) the Variable Threshold Method (VTM) during the DJF 1985/86 period for the R3 region. The dark trace represents the regional mean daily precipitation in both figures. In (a), the moment that the accumulated dry consecutive days determined by the CDDM (red trace) exceeds the synoptic (blue line) or the intraseasonal (green line) thresholds, a dry event is identified by the CDDM. To validate the event, at least 50% of the CDDM event period must consist of dry days found by VTM (red dots) in (b). The arrows in the two figures indicate the synoptic (blue arrows) and intraseasonal (green arrow) dry events identified by the combination of the two methods, while the dotted arrow indicates an event that met the requirements of the CDDM but is not confirmed by the VTM.

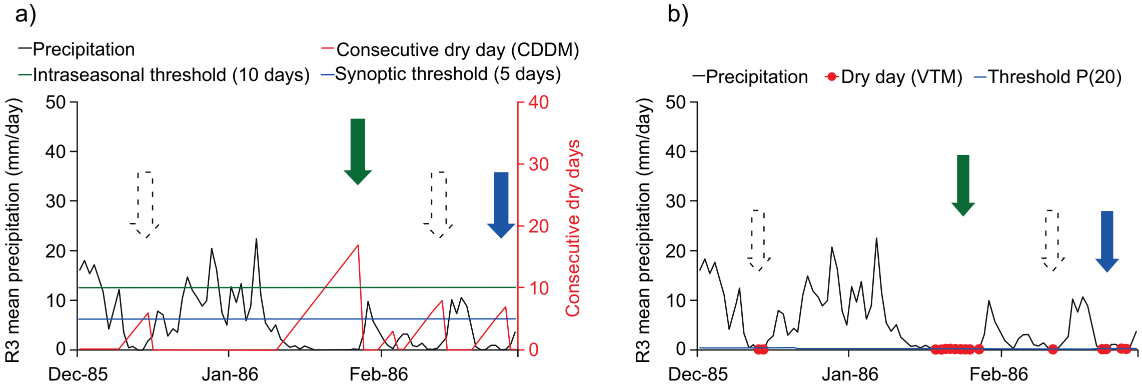

Fig. 4. Boxplot of mean regional precipitation in each of the 10-day intervals used in VTM for (a) R1, (b) R2, and (c) R3. The red dots identify P(20) values in each boxplot.

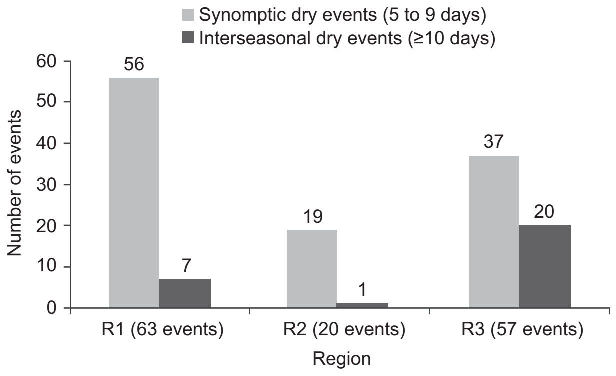

Fig. 5. The number of total synoptic (5 to 9 days) and intraseasonal (≥ 10 days) dry events were recorded in each of the homogeneous precipitation regions (R1, R2, and R3) from DJF 1981/82 to 2017/18.

in such events, R3 has a total of 529 in comparison with 426 in R2. As shown in figure 3c, R3 has lower precipitation values most of the time than the other regions, resulting in more extended dry periods (especially IDEs). This also contributes to a decrease in the number of total events compared to the increase in the duration of dry events. It explains why R1 has more dry events than R3, despite not having the lowest climatological rainfall accumulations among the three regions.

The interannual variations of the DJF precipitation for each of the three homogeneous precipitation regions (R1, R2, and R3) are presented in figures 6a, 6c, and 6e (left side), respectively. A non-linear trend in these series, calculated using the LOESS regression

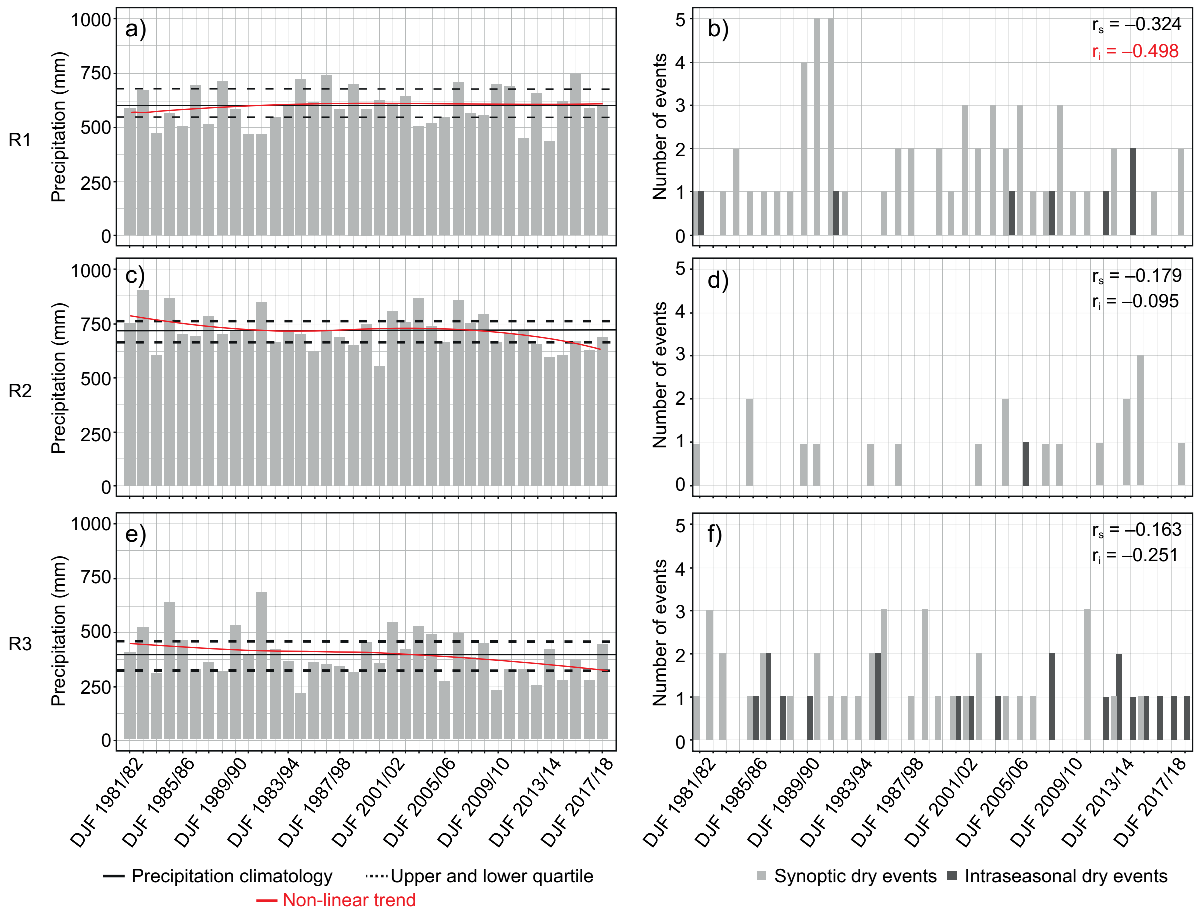

Fig. 6. Interannual variation of precipitation (left side) and a number of dry events (right side) between DJF 1981/82 to 2017/18 for regions R1 (a and b), R2 (c and d), and R3 (e and f). A red line on (a, c, and e) shows a non-linear trend (LOESS regression - Cleveland et al., 1992) in the interannual variation of precipitation series. Correlations indexes for the interannual precipitation series with the interannual number of SDEs (r_s) and with IDEs (r_i) in each region are shown in (b, d, and f). Values in red and bold denote a statistical confidence level above 95%.

(Cleveland et al., 1992), is drawn as a red line. For the same regions, respectively, in figures 6b, 6d, and 6f (right side), the interannual variations of the number of SDEs and IDEs identified by the CDDM and the VTM are shown. The correlation indexes of the interannual variation in the precipitation series with the interannual variations of the number of SDEs (r_s) and the number of IDEs (r_i) for each region are also presented. The figures are shown side by side, according to the region, to show the relationship between the dry events and the precipitation deficits.

The interannual variation of IDEs and SDEs is negatively correlated with the precipitation series in all the regions, as shown by the correlation indexes in the left-sided figures. Although the correlation is significant, above the 95% confidence level only for IDEs in region R1 (as indicated in bold in figure 6b). It demonstrates that the SDEs and IDEs identified here may not be the leading cause of shortage periods for greater timescales (monthly, seasonal and interannual), but they can partially explain them. A relevant number of years with precipitation deficits congruent with the occurrence of SDEs and IDEs can be found comparing the graphs. The dry summers of DJF 1991/92, DJF 2004/05, DJF 2011/12, and DJF 2013/14 were some of the driest seasons in R1 during the study period (Fig. 6a). At the same time, they showed at least 1 IDEs each (Fig 6b), besides presenting other SDEs. In R2, not many dry events were recorded over the sample time, but an increase in the SDEs coincides with the negative precipitation trend in recent years. In region R3, the quarters of DJF 1986/87 (2 SDEs and 2 IDEs), DJF 1994/95 (2 SDEs and 2 IDEs), and DJF 2012/13 (1 SDE and 2 IDEs) (Fig. 6f), three of the driest DJF over the data series (Fig. 6e), also presented expressive amounts of dry events when compared with other years as well as a recurrence of IDEs observed during the last years (Fig. 6f), which were drier than the climatological normal (Fig. 6e).

3.2 Mean fields and composites of anomalies

In this section, the mean fields and composites of several atmospheric and oceanic variables were analyzed for the periods of dry events using ERA-Interim reanalysis. Note that composites refer to mean values of anomalies, and mean fields do not use anomalies in their calculation. For each of the variables, the fields were made for SDEs and IDEs for each of the three homogeneous precipitation regions (R1, R2, and R3). Composites of Outgoing Longwave Radiation (OLR) and 500 mb geopotential height anomalies (Figs. 7 and 8) cover much of the southern hemisphere. The objective is to show, in addition to local atmospheric characteristics, wave train patterns associated with SEB dry events and possible sources. The composites and mean fields of remaining variables (Figs. 9 to 12) focus on local atmospheric and oceanic features, with the analysis domain confined to the surroundings of South America. It is important to emphasize that the mean fields and composites of anomalies show average atmospheric and oceanic behaviors during the dry events. Therefore, if one considers an isolated event, it may display different patterns than those presented here. Also, since only 1 IDE was registered in R2 with a duration of 12 days (small sample size), the composites and mean fields associated with that specific event are not shown.

Composites of OLR anomalies, encompassing an area covering the Pacific and Atlantic Oceans in the Southern Hemisphere, are shown in figure 7. Positive (negative) OLR anomalies are usually associated with lower (greater) cloud cover values and negative (positive) precipitation anomalies. All fields in figure 7 show significant positive OLR anomalies over the regions reporting dry events. When considering the South American continent, some OLR patterns can be observed simultaneously with the dry periods over the study regions. A noticeable pattern is a meridional precipitation dipole, which varies in location according to the region of interest. In R2 SDEs (Fig. 7c), this pattern is located between the central-eastern region of Brazil (positive OLR anomalies) and SESA (negative OLR anomalies). In the R1 and R3 cases (Figs. 7a, 7b, 7d, and 7e), this dipole is practically between such regions, plus part of southern Brazil (in the R1 pole) and part of northeastern Brazil (in the R3 pole). This pattern is prevalent during drought events in the central-eastern portion of Brazil, and it has been reported in many works (e.g., Nogués-Paegle and Mo, 1997; Barros et al., 2000; Robertson and Mechoso, 2000; Ferraz, 2004; Castro-Cunningham and De Albuquerque-Cavalcanti, 2006; Muza et al., 2009; Grimm and Zilli, 2009; Gonzalez and Vera, 2014). Another recurring pattern, which was not observed only in R1 SDEs, is the negative OLR anomalies in

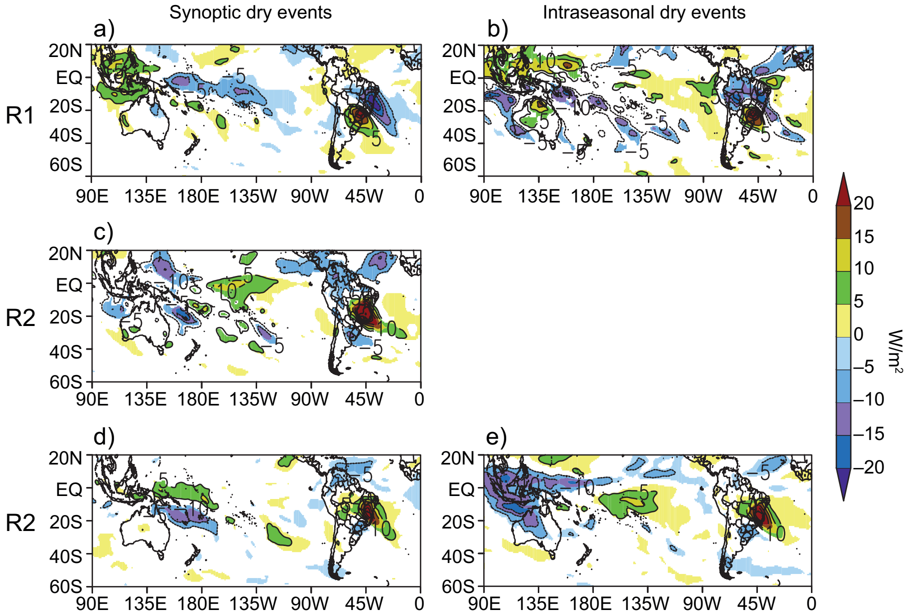

Fig. 7. Composites of outgoing longwave radiation (OLR) anomalies during the synoptic dry events in (a) R1, (c) R2, and (d) R3, and during intraseasonal dry events in (b) R1 and e R3. The shaded anomalies have a statistical confidence level above 95%.

the Intertropical Convergence Zone (ITCZ) region. Considering the equatorial Pacific band, for R2 SDEs, R3 SDEs, and R3 IDEs (Figs. 7c to 7e), is verified significant negative OLR anomalies over Indonesia and positive anomalies over the central part. For R1 cases (Figs. 7a and 7b), negative OLR anomalies are observed more in the central-western equatorial Pacific. It is worth mentioning that such regions of anomalous convective activity over the equatorial Pacific commonly act as a source of teleconnections patterns that may contribute to the dry events over SEB, although it is not the scope of this work to investigate that further.

The 500 mb geopotential height DJF climatology is shown in figure 8a. The same variable mean fields (contours) and their respective anomalies (shaded) for the dry events are shown in figures 8b to 8f. For this variable, it was decided to place the climatology field for a clearer notion of how some atmospheric systems behave on average during dry events in relation to the climatological normal. In all the cases, a positive anomaly is noticed south of the region of the dry events. This configuration makes the approximation of transient disturbances, which are usually associated with the precipitation over the SEB, difficult. For SDEs and IDEs in R1 (Figs. 8b and 8c), a positive anomaly along the Argentine coast (shaded in warm colors) is verified, related to a ridge over the entire southern portion of South America (isohypses) at the same time that it is possible to observe a negative anomaly pole over the SEB coast (shaded in cool colors) related to a trough over this location (isohypses). This pattern can be produced by passages of slow transient systems in the synoptic scale. It is also possible that northern-shifted SACZ episodes could also contribute to that in both timescales. In these possible cases of SACZ, the ridge and the trough associated with the SACZ are more amplified than in the usual cases and with a slight zonal displacement of the trough towards the central Atlantic Ocean, which corresponds to the reallocation of the greatest precipitation region to the north, on the south portion of Northeast region of Brazil.

In contrast, dry conditions are verified in the southern half of the SEB and southern Brazil (as seen in Figs. 7a and 7b). For R2 and R3 cases (Figs. 8d o 8f), a blocking ridge is approximately centered between the coasts of Brazil's southern and south-

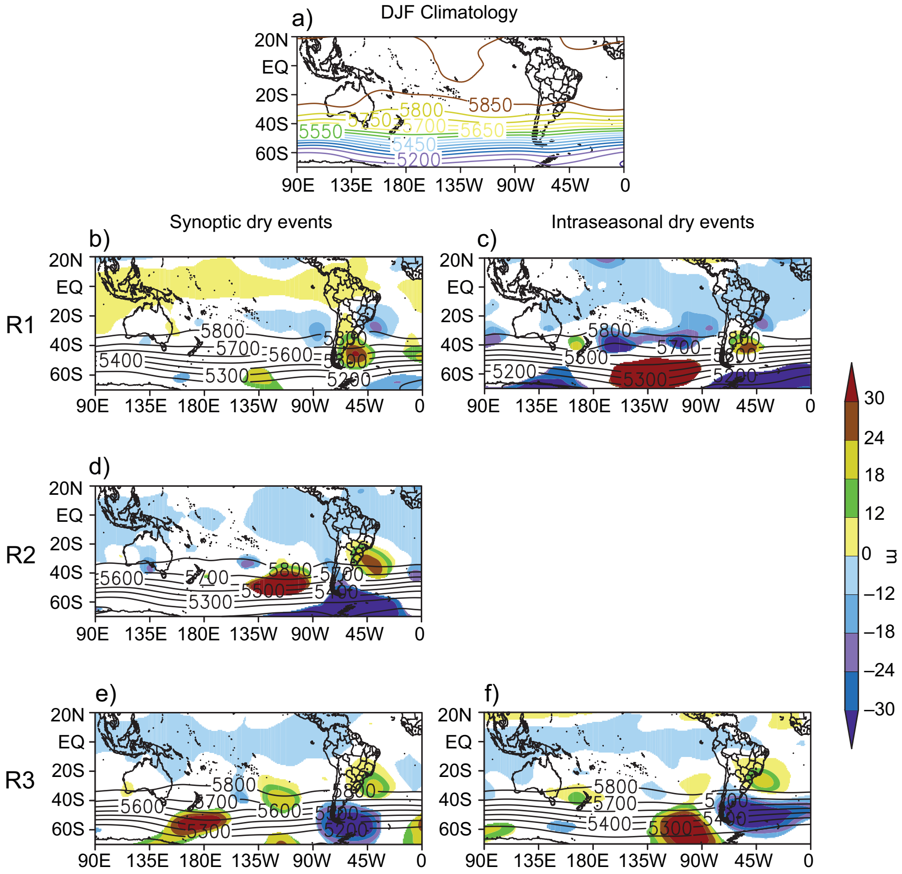

Fig. 8. (a) 500 mb geopotential height December-February (DJF) climatology for the period DJF 1981/82 to 2017/18. Mean fields of 500 mb geopotential (contours) and their respective anomalies (shaded) during the synoptic dry events in (b) R1, (d) R2, and (e) R3, and the intraseasonal dry events in (c) R1 and (f) R3. The shaded anomalies have a statistical confidence level above 95%.

eastern regions. Although with less intense signals, this pattern is similar to those found for the 2014 and 2015 dry events (e.g., Seth et al., 2015; Coelho et al., 2016; Cavalcanti et al., 2017). Further, good similarity exists with the events of those years between the wave train pattern found for SDEs, in R2 and R3 and IDEs in R3 (Figs. 8d to 8f). The wave train extends from the central Pacific Ocean to the South American continent with minor differences between the cases. It displays a trough over the central Pacific subtropics, a ridge over the southwest of Chile, another trough over the southwest Atlantic Ocean, and the blocking ridge over the southern and southeastern Brazilian coasts. This feature, plus the convection over Indonesia for the same class of events (Figs. 7c to 7e), suggests that many times the origin of these events is similar to the teleconnection pattern identified for the 2014 and 2015 dry summers (e.g., Coelho et al., 2016; Rodrigues et al., 2019; Finke et al., 2020).

Now, looking specifically at South American atmospheric conditions, anomalous patterns with some resemblances to those observed in the 500 mb geopotential height fields are also observed in the mean sea level pressure (MSLP) fields (Figs. 9b to 9f), demonstrating the barotropic nature of the anomalies. For events in R1 (Figs. 9b and 9c), it is verified a prevalence of positive (negative) anomalies over the extratropics (tropics) in South America. In contrast, the opposite is noticed in R3 (Figs. 9e and 9f). It denotes a South Atlantic Subtropical High

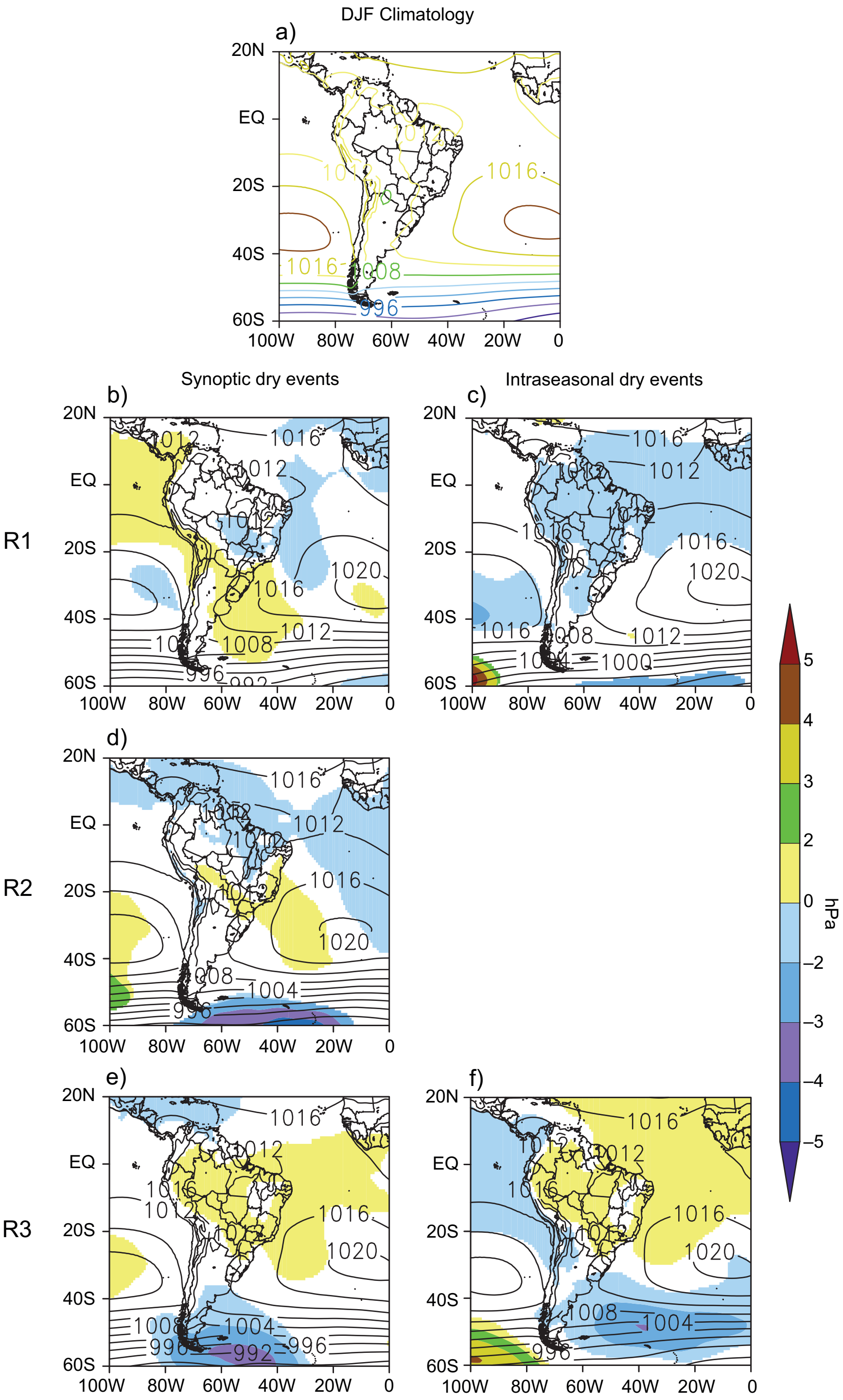

Fig. 9. (a) Mean sea level pressure (MSLP) December-February (DJF) climatology for the period DJF 1981/82 to 2017/18. Mean fields of MSLP (contours) and their respective anomalies (shaded) during the synoptic dry events in (b) R1, (d) R2, and (e) R3, and the intraseasonal dry events in (c) R1 and (f) R3. The shaded anomalies have a statistical confidence level above 95%.

(SASH) inclined and extended to the southwest for events more to the south (R1 cases) and inclined to the northwest in northern cases (R3 cases) when this SASH's continental approach to the South American continent contributes to the atmospheric stabilization over the regions of dry events.

Figure 10a it is shown the 200 mb wind (streamlines), magnitude (contours), and divergence (shaded) DJF climatology, while the mean fields for the dry events in each region and event class are presented in figures 10b to 10f. Upper-tropospheric circulation exhibits a very characteristic pattern during the rainy season of the tropical portion of South America, which occurs on average between mid-spring and early autumn and encompasses our study period. From the DJF climatology (Fig. 10a), it can be seen two typical systems of the tropical upper troposphere: The Bolivian High (BH), anticyclonic circulation due to the grand release of latent heat associated with tropical convection (Lenters and Cook, 1997), centered over Bolivia; and the Atlantic trough (AT), that is observed along the coast of northeastern Brazil, which at times becomes a closed cyclonic circulation, called the upper tropospheric cyclonic vortex of the Brazilian Northeast (VBNE). According to Ferreira et al. (2009), the most favorable regions for upward (downward) movements in the system composed of BH-VBNE or BH-AT circulations are the locations where the most expressive diffluences (confluences) of the flow are found. As mentioned before, in both R1 cases (Figs. 10b and 10c), the dry periods seem to be associated with a post-frontal situation or a northern-shifted SACZ condition. A second trough is observed over a subtropical latitude near the southern coast of Brazil, beyond the AT at tropical latitudes, resembling a typical SACZ trough, also verified in the mid-troposphere (Figs. 8b and 8c). Divergence is verified downstream of this southern trough as well as over a broad area of diffluence between the BH and AT systems in the northern part of Brazil, whereas upstream of the southern trough, a convergence is observed over an area encompassing southern Brazil and the region corresponding to R1 (southern SEB). In R2 and R3 events (Figs. 10d to 10f), the system, composed of BH-AT (SDEs in R3) and BH-VBNE (SDEs in R2 and IDEs in R3), is displaced southwest of its climatological position. The BH is centered approximately over southern Bolivia, while the AT or VBNE acts near the SEB's northern and southern parts of the Brazilian Northeast. For such events, both the AT and the VBNE have a slope towards the eastern part of Brazil. It can be seen that the regions with dry events are generally located under confluence areas of the BH-VBNE or BH-AT systems, just to the west of VBNE or AT location, and present negative values of divergence (i.e., convergence) in the upper troposphere. This atmospheric condition leads to downward movements over these regions, contributing to the persistent stable weather associated with the dry events. The VBNE core lies near SEB by itself (e.g.: SDEs in R2 and IDEs in R3), south of its climatological position, which may contribute to the atmospheric stabilization over such regions because of the typical subsidence within this system (Ferreira et al., 2009). Looking at the other areas in the South American continent, in all cases, we see a region of expressive diffluence in the flow of the BH-VBNE or BH-AT systems in the north of Brazil, where there are large areas of positive values of divergence, which correspond to the vast area of convection over that region. Another point of diffluence is identified over southern Brazil and SESA for events in R2 and R3 (Figs. 10d to 10f), showing positive values of divergence and, hence, rainfall conditions over that place (see Figs. 7c to 7e). In this region, the upper troposphere divergence may also be increased by being located in an equatorial entrance of a reinforced Upper Tropospheric Jet (UTJ) (see contours in Figs. 10d to 10f).

Figure 11 shows wind and specific moisture anomalies at 850 mb. In the R1 events (Figs. 11a and 11b), a cyclonic anomaly is verified near the SEB coast, which contributes to reinforcing the western wet flux over the northern SEB and northeastern Brazil and inducing an anomalous drier eastern flux over the southern part of SEB, where R1 is located. The presence of an anomalous anticyclone is verified near the southern and southeastern coast of Brazil for events in R2 and R3 (Figs. 11c to 11e). Such circulation is associated with the intensification and displacement of SASH towards the east coast of Brazil. In all the R2 and R3 cases, the associated circulation intensifies the South American Low-Level Jet (SALLJ) east of the Andes, channeling the wet stream towards southern Brazil and SESA. One noticeable aspect common to all anomalous wind fields is the eastern

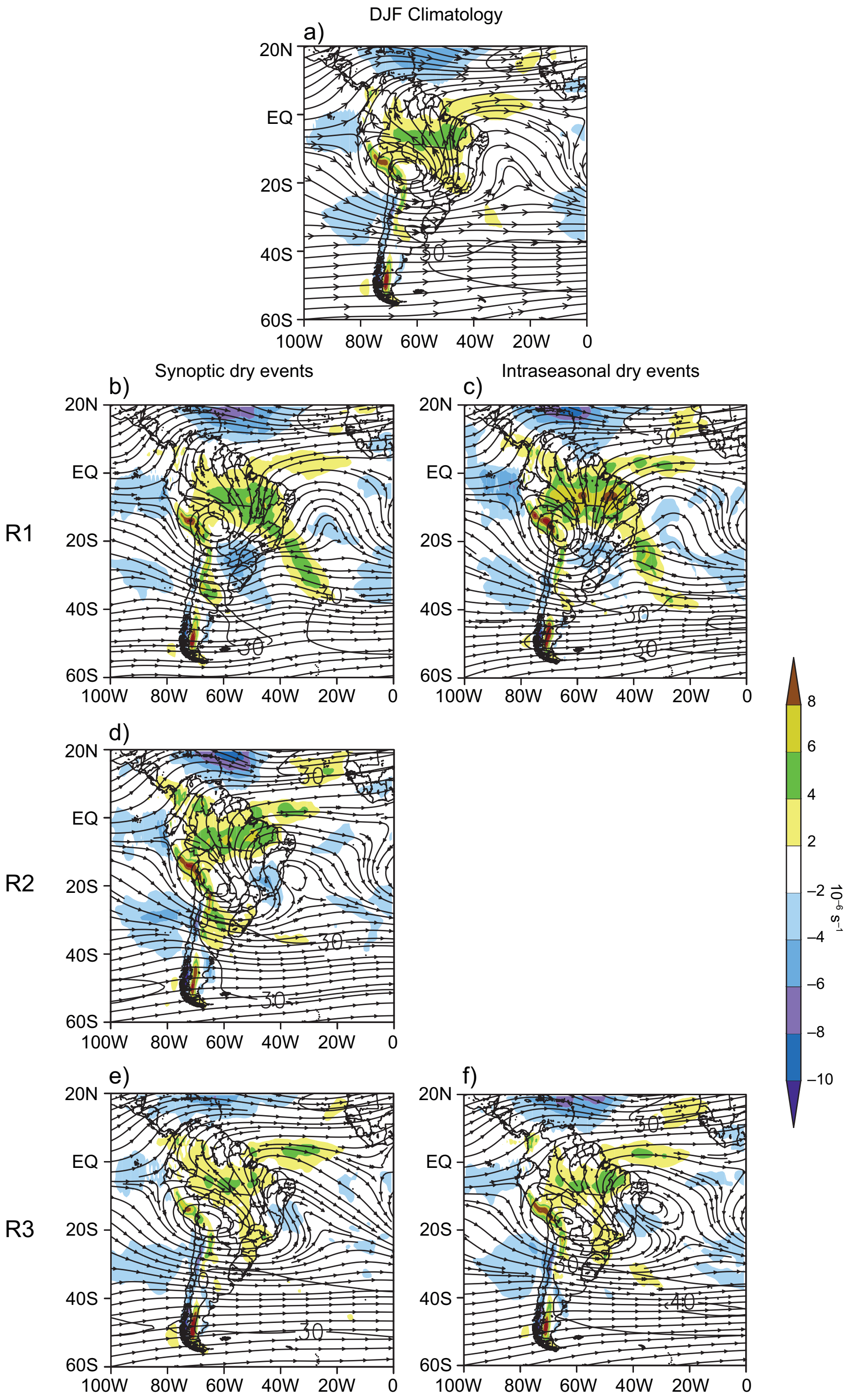

Fig. 10. (a) 200 mb wind (streamlines), magnitude (shaded), and divergence (contours) December-February (DJF) climatology for the period DJF 1981/82 to 2017/18. Mean wind fields (streamlines), magnitude (shaded), and divergence (contours) during the synoptic dry events in (b) R1, (d) R2, and (e) R3, and the intraseasonal dry events in (c) R1 and (f) R3.

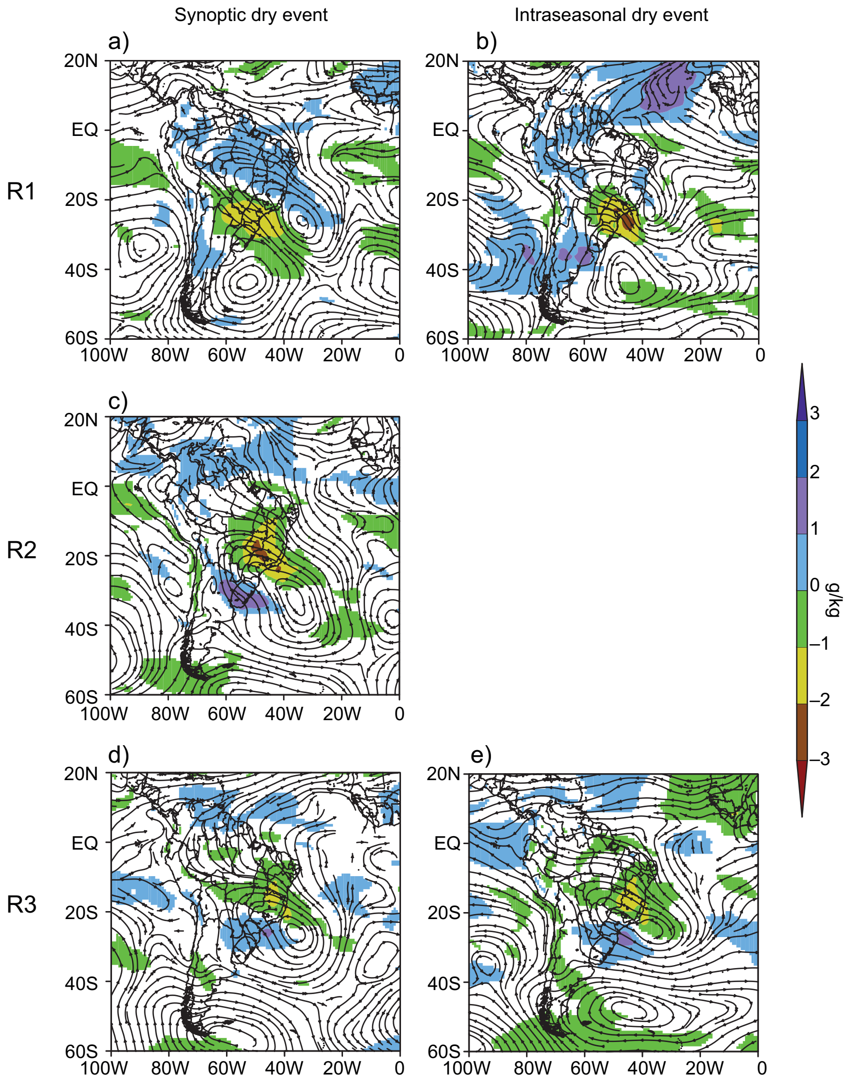

Fig. 11. Composites of 850 mb wind (streamlines) and the specific moisture (shaded) anomalies during the synoptic dry events in (a) R1, (c) R2, and (d) R3, and during the intraseasonal dry events in (b) R1 and (e) R3. The shaded anomalies have a statistical confidence level above 95%.

component with associated moisture deficit over the study regions, as is also verified in Muza et al. (2009) in a study about dry events variability on an intraseasonal and interannual scale. This anomalous eastern component is responsible for weakening the northwestern wet climatological flow over each study region and contributes to the shortage periods.

Lastly, the SST anomaly fields are shown in figure 12. According to Jorgetti et al. (2014), the pattern with a negative anomaly strip between the SEB coast extending zonally over the south Atlantic, as seen for the R1 cases (Figs. 12a and 12b), is typical of northern-shifted SACZ events. It contributes to the origin and the maintenance of the rainy continental band in a northward position, then contributes to the occurrence of the dry events in the southern SEB. The cold anomalies near the southern SEB coast intensify the continent-ocean temperature gradient, characteristic of summer, then favoring an easterly drier anomaly flux (as seen in the Figs. 11a and 11b),

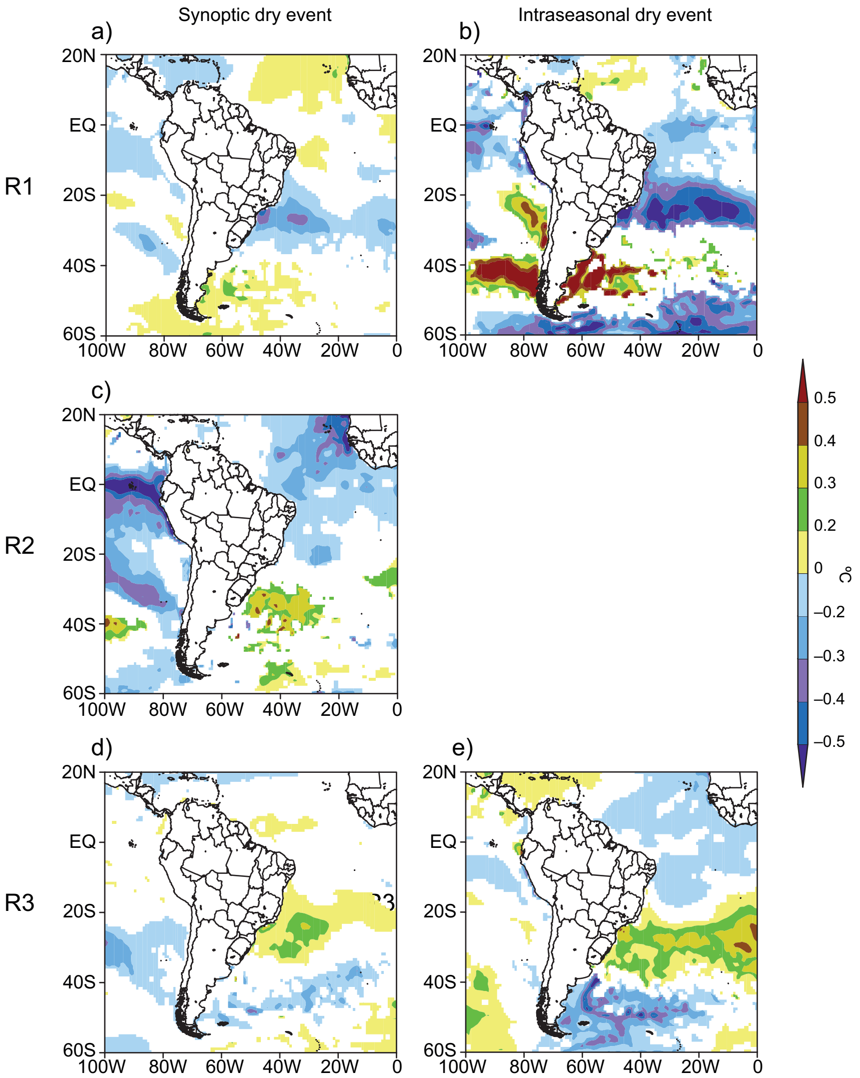

Fig. 12 Composites of sea surface temperature (SST) anomalies during the synoptic dry events in (a) R1, (c) R2, and (d) R3, and during intraseasonal dry events in (b) R1 and (e) R3. The shaded anomalies have a statistical confidence level above 95%.

holding the rainfall pattern to the north (Doyle and Barros, 2002; Jorgetti et al., 2014). For R2 and R3 events (Figs. 12c to 12e), the SST anomaly pattern resembles the typical case found associated with dry events over SEB (Coelho et al., 2016; Pampuch et al., 2016; Pattnayak et al., 2018; Rodrigues et al., 2019), as well as the case of southern SACZ events (Jorgetti et al., 2014). A strip of positive SST anomalies near SEB is verified, which probably responds to the increased incident radiation and negative anomalies of latent heat flux, as shown by Rodrigues et al. (2019). Over mid- and high-latitudes, the main SST anomaly patterns are clearly associated with the dynamic atmospheric conditions shown in the previous figures and mainly respond to them. We compare the SST anomalies with the 500 mb geopotential height anomalies (Fig. 8). Under areas with negative anomalies of 500 mb geopotential height and MSLP, there is usually a greater instability of the environment and a greater cloud cover value, and a consequent decrease in SST due to the smaller amount of incident radiation. The opposite, positive SST anomalies, occur under the areas of positive anomalies of 500 mb geopotential height, where there is a greater atmospheric stabilization, a lower cloud cover value, and a greater amount of incident radiation. As can be seen, for events in R1 (Figs. 12a and 12b), the SST anomalies pattern has almost inverted signals with respect to the other two regions (Figs. 12c to 12e), and the main cause seems to be the configuration of the mid and upper-tropospheric wave train pattern for such cases, which also has signals practically inverted to each other (see Fig. 8). An SST anomaly tripole pattern along the eastern coast of South America, which is more evident in R1 SDEs and R3 IDEs (Figs. 12a and 12e), is also worth noting. It is verified negative (positive) SST anomalies in the central pole and negative (positive) anomalies in the north and south poles for the R1 cases (R3 cases). These patterns are similar to those found by Pampuch et al. (2016) for dry periods in similar areas over the SEB, occurring in the autumn, winter, and spring seasons.

4. Conclusion

This work characterized the atmospheric and oceanic patterns of dry events occurring in the Southeast Region of Brazil (SEB) during the austral summer, the season with the greatest rainfall accumulations in the region. Thirty-seven summers (DJF) between 1981/82 and 2017/18 of daily precipitation data were analyzed to identify dry events in the SEB. Because of the region's broad area, with precipitation regimes varying in time and space, three sub-regions (R1, R2, and R3) with homogeneous precipitation characteristics were identified within the SEB using the cluster analysis method. The R1 region, further south, encompasses the majority of the Brazilian state of São Paulo and small parts of bordering states. R2 region covers a central strip extending diagonally between the Brazilian states of Goiás and Rio de Janeiro. R3, further north, is composed of northern Minas Gerais, Espírito Santo and southern Bahia.

The dry events identification was performed by the consecutive dry days method (CDDM) and the variable threshold method (VTM), applied together to the daily precipitation data. The identification was made separately for the three homogeneous precipitation regions (R1, R2, and R3). The dry events were classified according to their duration as synoptic dry events (SDEs) (between 5 and 9 days in duration) and intraseasonal dry events (IDEs) (10 or more days in duration). The drier the region is, the greater the number of IDEs found, with the R3 region (393.3 mm of DJF average) recording 20 events, R1 (595.5 mm) reporting seven events, and R2 (719.0 mm) recording one event. For SDEs, R1 had the greatest number of events recorded (56 events), followed by R3 (37 events) and R2 (19 events). As expected, interannual variation in precipitation is negatively correlated with the interannual variation of dry events, with a significant value occurring only for R1 IDEs, which can indicate a partial explanation of shortage periods on longer timescales by the dry events identified here.

Considerable differences in atmospheric and oceanic features are seen between dry events taking place in the southern (R1) and central northern (R2 and R3) parts of SEB, while no significant differences were found according to event duration class (SDEs and IDEs). Events in R1 exhibited a pattern that could be produced either by a frontal system with a high pressure behind (over R1) or by a persistent SACZ episode but displaced northward, this last one, especially for IDEs cases. SST cold anomalies over subtropical Atlantic seem to contribute to maintaining a northern-shifted SACZ pattern and, therefore, a drier condition over southern SEB in such cases. For central and northern dry events, in R2 and R3 regions, the atmospheric and oceanic patterns resemble those verified in 2013/14 and 2014/15 summer, with an anomalous blocking high acting close to the SEB coast and a significant strip of positive SST anomalies below.

Other interesting atmospheric conditions over the South American continent, which were associated with the dry events, deserve to be mentioned. A precipitation dipole, which varies its location meridionally according to the homogeneous precipitation region, is verified on the OLR anomaly fields for all study regions (R1, R2, and R3) and in both classes of dry events (SDEs and IDEs). This dipole was characterized by a drier and a wetter pole, which were approximately located between the southern part of Brazil (dry pole) and the northeastern part of Brazil (wet pole) in R1 cases, SEB (dry pole) and SESA (wet pole) in R2 cases, and the opposite of R1 cases in R3.

The DJF climatological low-level flow over the SEB is from the northwest, which commonly brings humidity from the Amazon region. During the dry episodes, the flow presented an eastern anomaly component that represents a weakening of this climatological northwestern flow; therefore, a decrease in humidity over the SEB is seen. This eastern component corresponds to the southern part of an anomalous cyclonic circulation for R1 events, bringing an anomalous moist western flux over northeastern Brazil in its northern flank. For the cases in R2 and R3, the eastern component is the northern part of an anomalous anticyclonic circulation that, in its turn, provides a wetter flux over southern Brazil and SESA. For almost all dry events cases, negative OLR anomalies were also noticed in the Intertropical Convergence Zone (ITCZ) region. A SASH intensification and shift towards the eastern coast of Brazil was identified in the R2 and R3 events. Furthermore, in the upper troposphere, the system composed of BH-VBNE (BH-AT in some cases) is generally displaced south of its climatological position in R2 and R3 events.

This research is important for weather and climate forecasts because it suggests general atmospheric and oceanic patterns linked to extreme dry events. A further investigation on how some oscillations of different timescales may contribute to originate the dry periods over the different parts of SEB, like teleconnections patterns, the Madden-Julian oscillation or the El Niño Southern Oscillation, as well as the SST patterns associated with them, will be the focus of future work.

Acknowledgments

The authors thank *Climate Hazards Group InfraRed Precipitation with Station data* (CHIRPS) and *European Centre for Medium-Range Weather Forecasts* (ECMWF) for meteorological data. The first author thanks *Fundação de Amparo à Pesquisa do Estado de São Paulo* (FAPESP) (Proc. No. 2018/06806-0). The second and third authors were supported by *Conselho Nacional de Desenvolvimento Científico e Tecnológico* (CNPq) with the scholarships 304970/2015-8 and 304298/2014-0, respectively. Simone Erotildes Teleginski Ferraz was also supported by *Fundação de Amparo à Pesquisa do estado do Rio Grande do Sul* (FAPERGS). Tercio Ambrizzi was also supported by the National Institute of Science and Technology for Climate Change Phase 2 under CNPq Grant 465501/2014-1, 301397/2019-8, FAPESP Grants 2014/50848-9 and 2017/09659-6.

References

Ambrizzi T, Ferraz SET. 2015. An objective criterion for determining the South Atlantic Convergence Zone. Frontiers in Environmental Science 3:23. https://doi.org/10.3389/fenvs.2015.00023

Barros V, Gonzalez M, Liebmann B, Camilloni I. 2000. Influence of the South Atlantic convergence zone and South Atlantic sea surface temperature on interannual summer rainfall variability in Southeastern South America. Theoretical and Applied Climatology 67:123-133. https://doi.org/10.1007/s007040070002

Berrisford P, Dee D, Poli P, Brugge R, Fielding K, Fuentes M, Kållberg P, Kobayashi S, Uppala S, Simmons A. 2011. The ERA-Interim archive Version 2.0. ERA Report Series 1:23. Available at https://www.ecmwf.int/sites/default/files/elibrary/2011/8174-era-interim-archive-version-20.pdf (accessed 2020 November 01)

Carvalho LMV, Jones C, Liebmann B. 2004. The South Atlantic convergence zone: Intensity, form, persistence, and relationships with intraseasonal to interannual activity and extreme rainfall. Journal of Climate 17:88-108. https://doi.org/10.1175/1520-0442(2004)017<0088:TSACZI>2.0.CO;2

Castro-Cunningham CA, De Albuquerque-Cavalcanti IF. 2006. Intraseasonal modes of variability affecting the South Atlantic Convergence Zone. International Journal of Climatology 26:1165-1180. https://doi.org/10.1002/joc.1309

Cavalcanti IFA, Kousky VE. 2009. Frentes frias sobre o Brasil. In: Cavalcanti IFA, Ferreira NJ, Alvarez-Justi-Silva MG, Silva-Dias MAF, eds. Tempo e Clima. São Paulo: Oficina de Textos, 135-148.

Cavalcanti IFA, Marengo JA, Alves LM, Costa DF. 2017. On the opposite relation between extreme precipitation over west Amazon and southeastern Brazil: Observations and model simulations. International Journal of Climatology 37:3606-3618. https://doi.org/10.1002/joc.4942

Cleveland WS, Grosse E, Shyu WM. 1992. Local regression models. In: Chambers JM, Hastie TJ, eds. Statistical Models S. Pacific Grove: Wadsworth & Brooks/Cole. Chapter-8.

Coelho CAS, de Oliveira CP, Ambrizzi T, Reboita MS, Carpenedo CB, Campos JLPS, Tomaziello ACN, Pampuch LA, Custódio MS, Mosso-Dutra LM, Rocha RP, Rehbein A. 2016. The 2014 southeast Brazil austral summer drought: regional scale mechanisms and teleconnections. Climate Dynamics 46:3737-3752. https://doi.org/10.1007/s00382-015-2800-1

Dee DP, Uppala SM, Simmons AJ, Berrisford P, Poli P, Kobayashi S, Andrae U, Balmaseda MA, Balsamo G, Bauer P, Bechtold P, Beljaars ACM, van de Berg L, Bidlot J, Bormann N, Delsol C, Dragani R, Fuentes M, Geer AJ, Haimberger L, Healy SB, Hersbach H, Hólm EV, Isaksen L, Kållberg P, Köhler M, Matricardi M, McNally AP, Monge-Sanz BM, Morcrette JJ, Park BK, Peubey C, de Rosnay P, Tavolato C, Thépaut JN, Vitart F. 2011. The ERA-Interim reanalysis: configuration and performance of the data assimilation system. Quarterly Journal of the Royal Meteorological Society 137:553-597. https://doi.org/10.1002/qj.828

Doyle ME, Barros VR. 2002. Midsummer low-level circulation and precipitation in subtropical South America and related sea surface temperature anomalies in the South Atlantic. Journal of Climate 15:3394-3410. https://doi.org/10.1175/1520-0442(2002)015<3394:MLLCAP>2.0.CO;2

Ferraz, SET. 2004. Variabilidade intrasazonal no Brasil e Sul da América do Sul. Doctoral thesis, Universidade de São Paulo. São Paulo.

Ferreira NJ, Ramírez MV, Gan MA. 2009. Vórtices ciclônicos de altos níveis que atuam na vizinhança do Nordeste do Brasil. In: Cavalcanti IFA, Ferreira NJ, Alvarez-Justi-Silva MG, Silva-Dias MAF, eds. Tempo e Clima. São Paulo: Oficina de Textos, 43-60.

Finke K, Jiménez-Esteve B, Taschetto AS, Ummenhofer CC, Bumke K, Domeisen DIV. 2020. Revisiting remote drivers of the 2014 drought in South-Eastern Brazil. Climate Dynamics, 55:3197-3211. https://doi.org/10.1007/s00382-020-05442-9

Funk C, Peterson P, Landsfeld M, Pedreros D, Verdin J, Shukla S, Husak G, Rowland J, Harrison L, Hoell A, Michaelsen J. 2015. The climate hazards infrared precipitation with stations - a new environmental record for monitoring extremes. Scientific Data 2:150066. http://doi.org/10.1038/sdata.2015.66

Gonzalez PLM, Vera CS. 2014. Summer precipitation variability over South America on long and short intraseasonal timescales. Climate Dynamics 43:1993-2007. https://doi.org/10.1007/s00382-013-2023-2

Grimm AM. 2009. Variabilidade interanual do clima no Brasil. In: Cavalcanti IFA, Ferreira NJ, Alvarez-Justi-Silva MG, Silva-Dias MAF, eds. Tempo e Clima. São Paulo: Oficina de Textos, 353-374.

Grimm AM, Pal JS, Giorgi F. 2007. Connection between spring conditions and peak summer monsoon rainfall in South America: Role of soil moisture, surface temperature, and topography in eastern Brazil. Journal of Climate 20:5929-5945. https://doi.org/10.1175/2007JCLI1684.1

Grimm AM, Zilli MT. 2009. Interannual variability and seasonal evolution of summer monsoon rainfall in South America. Journal of Climate 22:2257-2275. https://doi.org/10.1175/2008JCLI2345.1

Heim RR. 2002. A Review of Twentieth-Century Drought Indices Used in the United States. Bulletin of the American Meteorological Society 83:1149-1165. https://doi.org/10.1175/1520-0477-83.8.1149

IBGE. 2010. Sinopse do Censo Demográfico 2010. Instituto Brasileiro de Geografia e Estatística. Available at https://biblioteca.ibge.gov.br/visualizacao/livros/liv49230.pdf (accessed 2019 November 15).

IBGE. 2014. Produto Interno bruto dos municípios. Instituto Brasileiro de Geografia e Estatística. Available at https://www.ibge.gov.br/estatisticas-novoportal/economicas/contas-nacionais/9088-produto-interno-bruto-dos-municipios.html?=&t=series-historicas (accessed 2019 November 15).

Jorgetti T, Silva-Dias PL, Freitas ED. 2014. The relationship between South Atlantic SST and SACZ intensity and positioning. Climate Dynamics 42:3077-3086. https://doi.org/10.1007/s00382-013-1998-z

Kodama Y. 1992. Large-scale common features of subtropical precipitation zones (the Baiu frontal zone, the SPCZ, and the SACZ) Part I: Characteristics of subtropical frontal zones. Journal of the Meteorological Society of Japan 70: 813-836. https://doi.org/10.2151/jmsj1965.70.4_813

Kodama Y. 1993. Large-scale common features of sub-tropical convergence zones (the Baiu frontal zone, the SPCZ, and the SACZ) Part II: conditions of the circulations for generating the STCZs. Journal of the Meteorological Society of Japan 71:581-610. https://doi.org/10.2151/jmsj1965.71.5_581

Lenters JD, Cook KH. 1997. On the Origin of the Bolivian High and Related Circulation Features of the South American Climate. Journal of the Atmospheric Sciences 54:656-678. https://doi.org/10.1175/1520-0469(1997)054<0656:OTOOTB>2.0.CO;2

Ministério de Minas e Energia. 2018. Balanço Energético Nacional. Brasília, Brazil. Available at https://www.epe.gov.br/sites-pt/publicacoes-dados-abertos/publicacoes/PublicacoesArquivos/publicacao-303/topico-419/BEN2018__Int.pdf

Mo KC, Paegle JN. 2001. The Pacific–South American modes and their downstream effects. International Journal of Climatology 21:1211-1229. https://doi.org/10.1002/joc.685

Muza MN, Carvalho LMV, Jones C, Liebmann B. 2009. Intraseasonal and Interannual Variability of Extreme Dry and Wet Events over Southeastern South America and the Subtropical Atlantic during Austral Summer. Journal of Climate 22:1682-1699. https://doi.org/10.1175/2008JCLI2257.1

Nobre CA, Marengo JA, Seluchi ME, Cuartas LA, Alves LM. 2016. Some characteristics and impacts of the drought and water crisis in southeastern Brazil during 2014 and 2015. Journal of Water Resource and Protection 8:252-262. https://doi.org/10.4236/jwarp.2016.82022

Nogués-Paegle J, Mo KC. 1997. Alternating wet and dry conditions over South America during summer. Mon Weather Rev 125:279-291. https://doi.org/10.1175/1520-0493(1997)125<0279:AWADCO>2.0.CO;2

Nunes LH, Vicente AK, Candido DH. 2009. Clima da região Sudeste do Brasil. In: Cavalcanti IFA, Ferreira NJ, Alvarez-Justi-Silva MG, Silva-Dias MAF, eds. Tempo e Clima. São Paulo: Oficina de Textos, 243-258.

Pampuch LA. 2014. Características Sinóticas e Dinâmicas de Períodos Extremos Secos sobre o Sudeste do Brasil e sua Relação com a TSM do Atlântico Sul. Doctoral thesis, Universidade de São Paulo.

Pampuch LA, Drumond A, Gimeno L, Ambrizzi T. 2016. Anomalous patterns of SST and moisture sources in the South Atlantic Ocean associated with dry events in southeastern Brazil. International Journal of Climatology 36:4913-4928. https://doi.org/10.1002/joc.4679

Pattnayak KC, Gloor E, Tindall JC, Brienen RJW, Barichivich J, Baker JCA, Spracklen DV, Cintra BBL, Coelho CAS. 2018. Adding new evidence to the attribution puzzle of the recent water shortage over São Paulo (Brazil). Tellus A: Dynamic Meteorology and Oceanography, 70:1-14. https://doi.org/10.1080/16000870.2018.1481690

Peixoto JP, Oort AH. 1992. Physics of climate. American Institute of Physics. Melville, New York.

Quadro MFL. 1994. Estudo de Episódios de Zona de Convergência do Atlântico Sul ZCAS sobre a América do Sul. Master's thesis, Instituto Nacional de Pesquisas Espaciais.

Robertson AW, Mechoso CR. 2000. Interannual and interdecadal variability of the South Atlantic convergence zone. Monthly Weather Review 128:2947-2957. https://doi.org/10.1175/1520-0493(2000)128<2947:IAIVOT>2.0.CO;2

Rodrigues RR, Woollings TJ. 2017. Impact of Atmospheric Blocking on South America in Austral Summer. Journal of Climate, 30:1821-1837. https://doi.org/10.1175/JCLI-D-16-0493.1

Rodrigues RR, Taschetto AS, Sen Gupta A, Foltz GR. 2019. Common cause for severe droughts in South America and marine heatwaves in the South Atlantic. Nature Geoscience, 12:620-626. https://doi.org/10.1038/s41561-019-0393-8

Seth A, Fernandes K, Camargo SJ. 2015. Two summers of São Paulo drought: Origins in the western tropical Pacific. Geophysical Research Letters 42:10816-10823. https://doi.org/10.1002/2015GL066314

Toloi RC, Freitas-Junior M, Reis JGM, Vendrametto O, Costa-Neto PLO. 2016. Droughts in the Tietê-Paraná waterway: Impacts on the direct, indirect and hidden costs in the transportation of soybean. Independent Journal of Management & Production 7:431-444. https://doi.org/10.14807/ijmp.v7i2.418

Van Huijgevoort MHJ, Hazenberg P, van Lanen HAJ, Uijlenhoet R. 2012. A generic method for hydrological drought identification across different climate regions. Hydrology Earth System Sciences 16:2437-2451. https://doi.org/10.5194/hess-16-2437-2012

Ward JH. 1963. Hierarchical grouping to optimize an objective function. Journal of the American Statistical Association 58:236-244. https://doi.org/10.2307/2282967

Watts J. 2015. Brazil's worst drought in history prompts protests and blackouts. The Guardian. Available at https://www.theguardian.com/world/2015/jan/23/brazil-worst-drought-history (accessed 2015 January 23rd)

Wilks DS. 2006. Statistical methods in the atmospheric sciences. Academic Press.

Atmósfera 36(1), 77-90 (2023)
https://doi.org/10.20937/ATM.53028

Connecting heavy precipitation events to outgoing long wave radiation variability scales: Case analysis in Brazil

Gabriela V. MÜLLER[1,2,*] and Valesca R. FERNANDES[3]

[1] *Consejo Nacional de Investigaciones Científicas y Técnicas (CONICET).*
[2] *Centro de Estudios de Variabilidad y Cambio Climático (CEVARCAM), Facultad de Ingeniería y Ciencias Hídricas, Universidad Nacional del Litoral, Santa Fe (CP: 3000), Argentina.*
[3] *Centro Nacional de Monitoramento e Alertas de Desastres Naturais (CEMADEN) São José dos Campos, São Paulo, Brasil.*
*Corresponding author; email: gvmuller@unl.edu.ar

Received: January 13, 2021; accepted: April 30, 2021

RESUMEN

Se analizan los campos espaciales de la varianza del espectro de radiación de onda larga saliente (OLR, por su sigla en inglés) durante los meses del verano austral 1979-2016 en el sur de Brasil, para diferentes escalas de tiempo: sinóptica, submensual e intraestacional. Los campos de variabilidad difieren tanto en intensidad como en ubicación y resaltan los ciclos de convección dominantes en el área de estudio. La amplitud de la variabilidad submensual es mayor que la de las otras escalas en la región sudeste de Brasil, mientras que la escala sinóptica prevalece en la región sur. Las escalas mencionadas anteriormente muestran mayores amplitudes sobre el Océano Pacífico occidental donde la Oscilación Madden-Julian juega un papel importante, a lo largo de la Zona de Convergencia del Pacífico Sur y sobre las áreas de trayectoria de tormentas sobre el Océano Pacífico sur. También se analiza la influencia de la interacción espectral de OLR asociada con la ocurrencia de dos eventos de lluvia intensa en el sudeste de Brasil en los veranos de 2011 y 2014, cuando la Zona de Convergencia del Atlántico Sur (SACZ) estuvo activa en ambos eventos. Los resultados obtenidos sugieren que la interacción entre escalas espectrales de OLR tiene lugar de forma tal que fortalece la SACZ, ya que los patrones espaciales de la escala temporal de dos a ocho días (sinóptica), la escala temporal de 10 a 30 días (submensual) y la escala temporal de 30 a 60 días (intraestacional), se superponen en la región de estudio.

ABSTRACT

Spatial fields of outgoing long wave radiation (OLR) spectrum variance of the 1979-2016 austral summer months in southern Brazil are analyzed on different timescales: synoptic, sub-monthly, and intra-seasonal. Variability fields differ both in intensity and location and highlight dominant convection cycles in the study area. The results show that the amplitude of sub-monthly variability is greater than that of the other scales in the southeastern region of Brazil, while the synoptic scale prevails in the southern region. The above-mentioned scales show greater amplitudes over the western Pacific Ocean where the Madden-Julian Oscillation plays an important role, along the South Pacific Convergence Zone, and over the storm track areas over the South Pacific Ocean. The influence of spectral OLR scale interaction is also analyzed, associated to the occurrence of two intense rainfall events over the southeastern Brazil in the austral summers of 2011 and 2014 when the South Atlantic Convergence Zone (SACZ) was active in both events. The results obtained suggest that spectral OLR scale interaction takes place in such way that it strengthens the SACZ, since the spatial pattern footprints of the two to eight-day timescale (synoptic), 10 to 30-day timescale (sub-monthly) and 30 to 60-day timescale (intra-seasonal) overlap in the study region.

Keywords: extreme event, scale interaction, outgoing longwave radiation, austral summer.

1. Introduction

Meteorological systems are known to have distinct temporal and spatial scales, which also interact with each other. Such scale variability and interactions can give rise to different weather events or affect their characteristics. A type of such events is heavy precipitation, which can have major socioeconomic impacts on agriculture, energy, or health, among others, and lead to material loss and high death tolls.

In South America, and particularly in Brazil, a series of systems provide a favorable environment for small-scale convective instability that gives rise to clouds with great vertical development and consequent intense storms. Weather systems causing rainfall to occur at different temporal scales, including the synoptic (two-eight days), sub-monthly (10-30 days), and intra-seasonal (30-60 days) scales.

Major synoptic-scale phenomena include frontal systems (Vasconcelos and Cavalcanti, 2010) and persistent systems such as the South Atlantic Convergence Zone (SACZ) (Carvalho et al., 2002, 2004). This system consists of a northwest-southeast oriented cloud band that extends from the Amazon, through the southeast of Brazil, to the subtropical South Atlantic Ocean (Carvalho et al., 2004; Quadro, 1994). According to Sanches (2002), the persistence of this cloud band for several days assigns the SACZ a prominent role in the region's rainfall regime, and is responsible for large amounts of rain.

On the intra-seasonal scale, the main mode of variability is the Madden-Julian Oscillation (MJO), which is characterized by a zonal circulation cell that propagates eastward (Madden and Julian, 1971, 1972). The MJO controls the position and intensity of convection, which locates mainly along the SACZ during the austral summer. In this sense, one of the most striking features of intra-seasonal oscillation in South America is a seesaw pattern between enhanced convection along the SACZ and suppressed convection in the subtropics (Casarin and Kousky, 1986; Cunningham and Cavalcanti, 2006; Shimizu and Ambrizzi, 2017). In addition to the MJO, there is the South Pacific Mode (SPM), an extra-tropical mode of atmospheric circulation over South America. It consists of a mid-latitude wave train that originates in the South Pacific convection area and flows eastward to the continent.

The less understood and studied is the sub-monthly scale, probably because no clearly defined phenomena are associated to it. However, the scale becomes "visible" under certain interactions with phenomena on the intra-seasonal or synoptic scales. According to González and Vera (2013), among other authors, both the sub-monthly and the intra-seasonal scales present similar dipole patterns, although dynamic forcings are different.

Only few studies focus on the meteorological features of scale interaction, e.g., González and Vera (2013); Vera et al. (2018). In this sense, the present paper seeks to contribute to understanding the interaction among the synoptic, sub-monthly, and intra-seasonal scales, by analyzing two selected heavy rainfall events that occurred in southeastern Brazil. Both events had strong sub-monthly components.

The first one of these events took place in Rio de Janeiro, on January 11 and 12, 2011. It caused one of the major disasters in Brazil, which became known as the mega-disaster of the mountain region of Rio de Janeiro. The heavy rainfall (250.8 mm in 48 h) caused thousands of landslides (Netto et al., 2013), flash floods (Cavalcante et. al, 2020), overflow, and floods. More than 1500 people were killed, and infrastructure damage was impressive. Because of its magnitude and consequences, the mega-disaster was (and continues to be) the subject of extended research aimed at contributing to develop early alert systems (Calvello et al., 2015; Ottero et al., 2018).

The second event was selected from a set of SACZ-related severe weather events that took place from January 2007 to December 2014. The 12 events were subjected to wavelet filtering (not shown) to identify those with greater sub-monthly scale influence. The event was selected because the sub-monthly scale was more important than the two other scales. It occurred in the municipality of São Sebastião, in the state of Sao Paulo (SP), Brazil on December 22-25, 2014. An amount of 156 mm fell in 24 h and 208.5 mm in 48 h, causing flash floods and landslides. Nearby cities in SP were also affected, e.g., Ilhabela, Guarujá, and Santos (230, 301, and 272 mm in 48 h, respectively) (Escobar, 2014). According to the National Weather Service of Brazil (INMET), the long-term monthly mean precipitation of December and January in southeastern Brazil varies between 220 and 250 mm, so totals fallen during the selected events represent outstanding values in very short periods.

The main objective of this study is to understand how modes of intra-seasonal, sub-monthly, and synoptic climate variability modulate the main atmospheric systems involved in two heavy rainfall events occurred during the summer (DJF) in the south of Brazil, and explore the physical processes involved. In addition, we seek to improve our understanding of the influence of the sub-monthly scale on precipitation in South America. The structure of this document is as follows: section 2 describes the data and methodology applied; section 3 presents the results of the climatological analysis of OLR and the analysis of interactions among synoptic, sub-monthly, and intra-seasonal variability in the two particular cases. Conclusions are given in section 4.

2. Data and methods

2.1 Data

The influence of the synoptic, sub-monthly, and intra-seasonal scales was examined over the domain bounded by longitudes 110º E-0º and latitudes 10º N-60º S (Figs. 1-4). In this region major rainfall events are driven by meteorological systems such as the SACZ, moisture channels and fronts, among others (Carvalho et al., 2004; Cunningham and Cavalcanti, 2006; Álvarez et al., 2016; Shimizu and Ambrizzi, 2017). The domain was selected for the series of daily records of outgoing longwave radiation (OLR) covering the period from December 1, 1979 to February 28, 2016 (austral summer, DJF), provided by the National Oceanic and Atmospheric Administration (NOAA) with 2.5º × 2.5º resolution (Liebmann and Smith, 1996). ORL is the amount of infrared radiation emitted to space by cloud tops, which depends on cloud temperature and altitude, i.e., OLR is a proxy for enhanced or suppressed convection. Areas of active convection were identified on the basis of the significance of spatial fields of total and filtered OLR power spectra (variance). Scales filtered the synoptic, sub-monthly, and intra-seasonal scales. The filter used here was the wavelets transform (Liebmann and Smith, 1996).

The influence of spectral OLR scale interaction was also analyzed, associated to the occurrence of two intense rainfall events over the southeast of Brazil in the austral summers: January 2011 and December 2014.

Daily meridional and zonal wind data at 200 and 850 hPa made available by the Climate Forecast System Reanalysis (CFSR) (Saha et al., 2010, 2014) with 2.5º × 2.5º resolution were also used in this study.

2.2 Methods

Outgoing longwave radiation power spectra were examined using the wavelet technique (Torrence and Compo, 1998), a common tool for power spectrum analysis of time series. Wavelets make it possible to decompose a series of data into simpler wave-like functions, to identify dominant modes of variability and understand how these modes behave over time. The method has been applied in geophysical studies, such as tropical convection (Weng and Lau, 1994), ENSO (Gu and Philander, 1995), and intra-seasonal oscillations in South America (Vitorino, 2002), among others (Pezzi and Kayano, 2009). A complete list of applications of this technique can be found in Foufoula-Georgio and Kumar (1995). The theory of wavelet analysis is described in Daubechies (1992).

Wavelets are localized wave-like oscillations, in the sense that they grow from zero to reach maximum amplitude, and then decrease back to zero again. Wavelets thus have a location where they peak, a characteristic oscillation period, and also a scale over which they amplify and decline. Consequently, wavelet analysis makes it possible to retain some frequency and time localization. Wavelets are defined in reference to a mother function $\psi(t)$ of some real t variables:

$$\psi_{j,k}\left(t\right)=\frac{1}{\sqrt{j}}\psi_o\left(\frac{t-k}{j}\right) \tag{1}$$

where j is the scaling parameter and k is the translation parameter.

Daughter wavelets are generated by translating $\psi(t) \rightarrow \psi(t+1)$ and scaling $\psi(t) \rightarrow \psi(2t)$ the mother function (Weng and Lau, 1994). The translation and scaling functions are in Eq. (2), above and below, respectively:

$$\psi_j\left(t\right)=\frac{1}{\sqrt{j}}\psi_o\left(\frac{t}{j}\right) \tag{2}$$

The continuous wavelet transform of function $f(t)$ is defined as follows:

$$W_{\psi}f\left(j,k\right)=\frac{1}{\sqrt{j}}\int f\left(t\right)\psi\left(\frac{t-k}{j}\right)dt \tag{3}$$

where $f(t)$ is the function that generates the data series under analysis, which is normalized by $\frac{1}{\sqrt{j}}$

The most suitable wavelets for each type of mother wavelet are selected depending on the accuracy needed for localization in the frequency and/or time domains. This study uses the Morlet wavelet, which provides a good representation of non-stationary signals found in nature. These wavelets are complex, and their features are similar to the features of the meteorological signal under analysis, such as symmetry/asymmetry or sudden/gradual variation (Vitorino, 2002). Further details of the method can be found in Torrence and Compo (1998).

The Morlet time-scale function is given by the following equation:

$$\psi\left(t\right)=e^{iw_o t}e^{\frac{t^2}{2}} \tag{4}$$

where w_o is the dimensionless frequency and t each datum in the time series. The wavelets generated in this study have $w_o = 6$ as suggested in Torrence and Compo (1998) and were calculated as follows:

$$\psi_{\left(j,k\right)}=\frac{1}{\sqrt{j}}e^{iw_o\left(\frac{t-k}{j}\right)_e-\frac{1}{2}\left(\frac{t-k}{j}\right)^2} \tag{5}$$

The wavelet method was applied in this paper to detect, analyze, and characterize the time scales of atmospheric systems over extensive areas. The analysis was made of three spectral OLR modes: (1) two-eight days, representing synoptic variability such as cold fronts and cyclones; (2) 10-30 days, for sub-monthly variability, and (3) 30 to 60 days, for intra-seasonal variability associated to the MJO.

3. Results and discussion

3.1 Spatial OLR patterns

The spatial patterns of total and filtered OLR power spectra of austral summer (December 1-February 28) in the period 1979-2016 were obtained for the synoptic (two to eight days), sub-monthly (10 to 30 days), and intra-seasonal (30 to 60 days) scales. The analysis of the spatial OLR pattern on the filtered scales reveals the most significant convection areas throughout the domain. As shown in Figure 1, there are important values of total OLR variance over the Maritime Continent, Australia, the west Pacific Ocean, and the South Pacific Convergence Zone (SPCZ). Brazil presents revealing OLR variance over the south, south-east, center-east, and northeast of its territory. In the mentioned areas of Brazil, OLR variance values are associated with the SACZ (Carvalho et al., 2004), where convective activity is strong typically during the austral summer, occasionally connecting to portions of the central-eastern, and northeastern Brazil, and the Inter-tropical Convergence Zone (ITCZ). In the Amazon, as convective activity dominates throughout the summer, the variance is small. In the equatorial Pacific Ocean, OLR

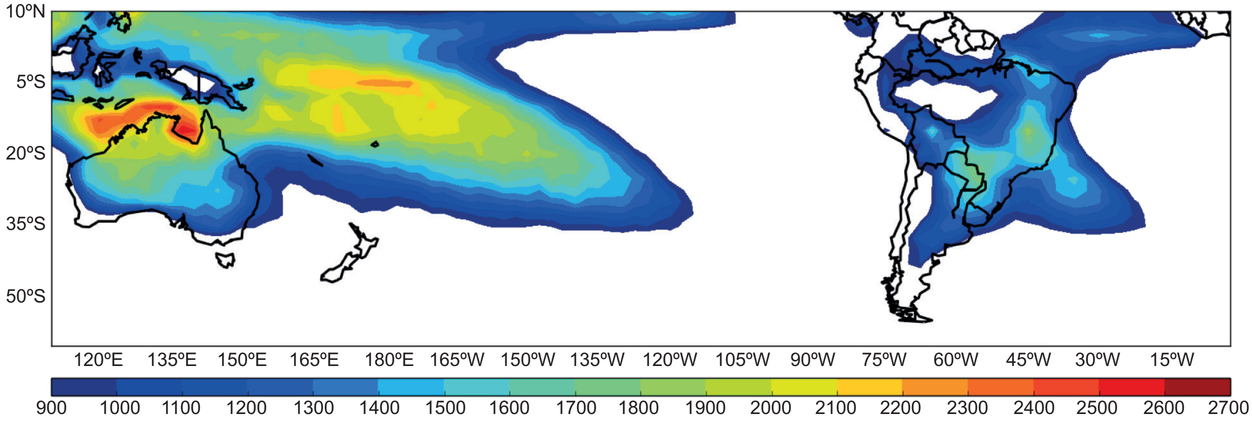

Fig. 1. Total outgoing longwave radiation (OLR) variance ($W^2\ m^{-4}$) for austral summers (DJF) in the period 1979-2016.

variability is mainly associated with convective cells that develop along the ITCZ (Sandeep and Stordal, 2013) and with active convection prevailing in the western subtropical sector, along the SPCZ (Kodama, 1992; Vincent, 1994).

Figure 2 shows OLR variance on the synoptic scale. The core of maximum OLR variance is over Paraguay, northeastern Argentina, Uruguay and the southeast of Brazil, and it extends diagonally towards Bolivia and towards the center-southeast of Brazil, but with lower OLR values. In general, the OLR variance values shown indicate the presence of convective cells over South America. In the south of South America, the variance is explained by frontal systems (Cavalcanti et al., 2009; Reboita et al., 2010) and mesoscale convective systems associated with the low-level jet (Salio et al., 2007; Rodrigues-Alcantara et al., 2014), or the Chaco low (Salio et al., 2002; Seluchi and Saulo, 2012). In addition, Figure 2 shows that in the equatorial Atlantic, the OLR variance along the ITCZ is characterized by intense variable convection, as found in Sandeep and Stordal (2013).

Summertime variance of OLR anomalies at the sub-monthly scale (10-30 days) is presented in Figure 3. The center-west and southeast of Brazil have the highest OLR variance, associated with the establishment of convergence zones such as the SACZ. As widely known, the SACZ causes persistent and

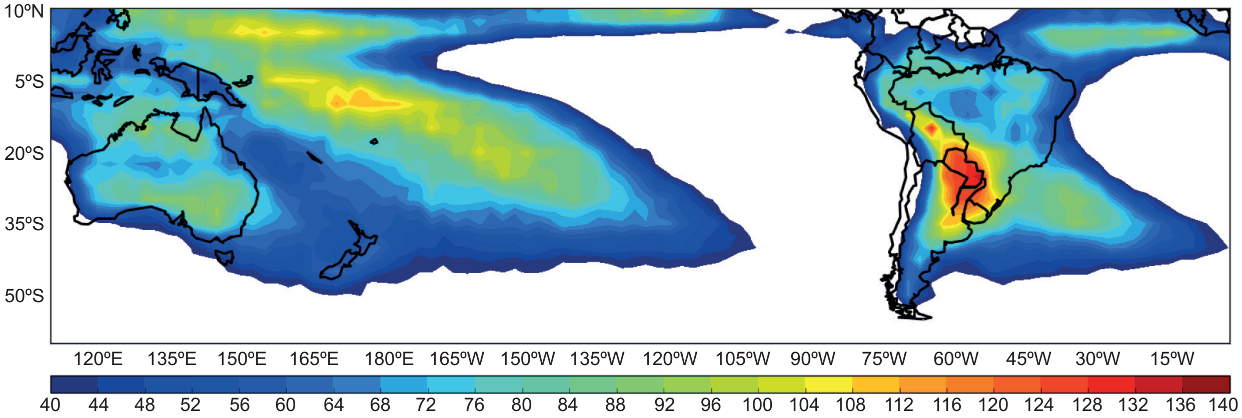

Fig. 2. Spectral OLR variance ($W^2\ m^{-4}$) on the synoptic scale (2 to 8 days) obtained through wavelet transform for austral summers (DJF) in the period 1979-2016.

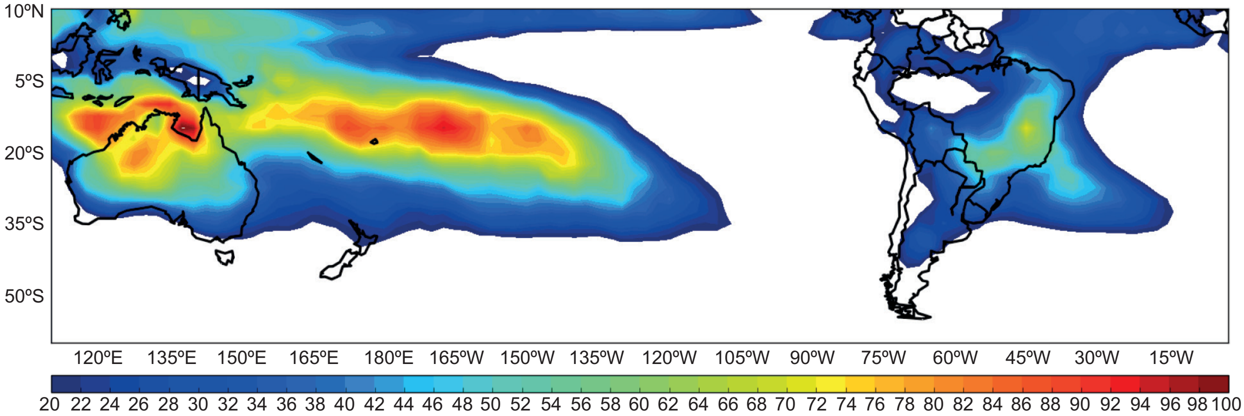

Fig. 3. Spectral OLR variance ($W^2\ m^{-4}$) on the sub-monthly scale (10 to 30 days) obtained through wavelet transform for austral summers (DJF) in the period 1979-2016.

heavy rains over large areas of Brazil. The region is dominated by convergence of water vapor in the lower troposphere and upward motion (Kodama, 1992; Liebmann et al., 1999). Other studies (Nogués-Paegle and Mo, 1997; Schneider, 2004) also identified the influence of sub-monthly scale signals in the southeast of South America during the austral summer. In general, the sub-monthly scale is considered to play an important role in South America.

The intra-seasonal OLR scale displays high values (Fig. 4) in northeastern and southeastern Brazil extending towards the ITCZ in the North Atlantic and towards the southwest Atlantic along the SACZ (Carvalho et al., 2004). On the other hand, over the western Pacific and the Maritime Continent along the SPCZ, intra-seasonal OLR variance ranges from 50 to 66 $W^2\ m^{-4}$ and is associated to the MJO (Madden and Julian, 1971, 1972), which impacts the southeast and northeast of Brazil (Valadão et al., 2017). These results are similar to those presented by Hirata (2013), who analyzed intra-seasonal variability associated with summer convection in South America.

3.2 Case analysis

3.2.1 Case 1: January 11-12, 2011

The first half of January 2011 is acknowledged as the time of the major natural disaster (Infoclima, 2011) in Rio de Janeiro, Brazil. This event, known as the mega-disaster of the mountains of Rio de Janeiro, is still widely studied by researchers from different disciplines. Although the coast of the states of Rio de Janeiro and Sao Paulo is prone to heavy rainfall and landslides because of its topography, the amount of precipitation that fell during that event was outstanding. The event developed when the SACZ channeled moisture from the Amazon region onto the southeast of Brazil where it rained about 250 mm. As a consequence, downslope floods, mudslides and mudflows left thousands of people homeless, caused power and communication systems to collapse, and destroyed numerous highways and bridges.

Accumulated rainfall in January 2011 in the municipality of Nova Friburgo (state of Rio de Janeiro) was 432.8 mm of which 250.8 mm fell in only 48 h (January 11-12, 2011). On these two days it rained more than the average for the whole month of January, which according to INMET (2009), is 220-260 mm (average from 1961 to 1990). On that occasion, heavy rainfall also occurred in the states of São Paulo, Minas Gerais, Goiás, and Mato Grosso.

Figure 5 shows the average OLR spectral power on the synoptic, sub-monthly and intra-seasonal scales during the event under analysis (January 5 to 11, 2011). A wide range of high values of OLR spectral power extends from the northwest to the southeast of Brazil. The synoptic scale has the greatest amplitudes, followed by the sub-monthly and intra-seasonal scales. On the first days of January 2011, the SACZ was associated to an upper-level cyclonic vortex (Kousky and Gan, 1981), causing precipitation in the northeast of Brazil. During the period of analysis, convective activity developed along the

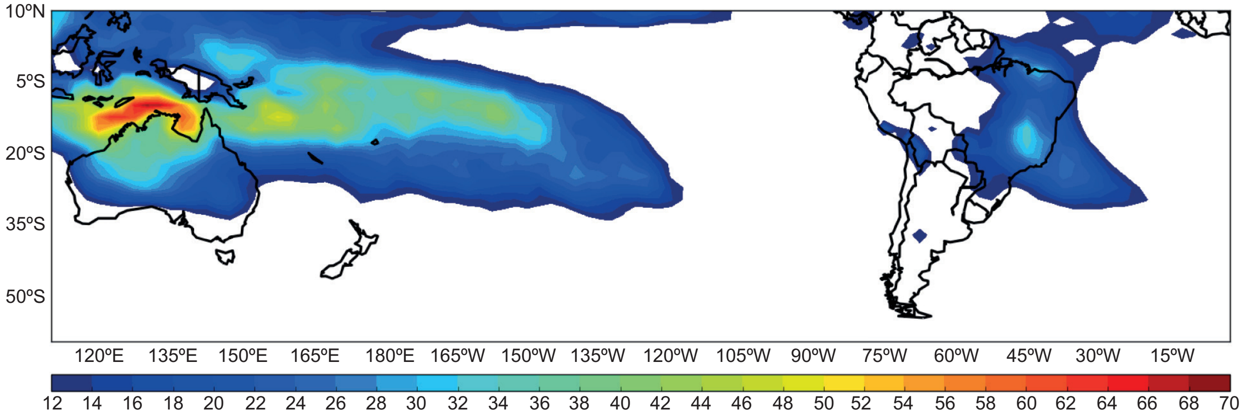

Fig. 4. Spectral OLR variance ($W^2\ m^{-4}$) on the intra-seasonal scale (30 to 60 days) obtained through wavelet transform for austral summers (DJF) in the period 1979-2016.

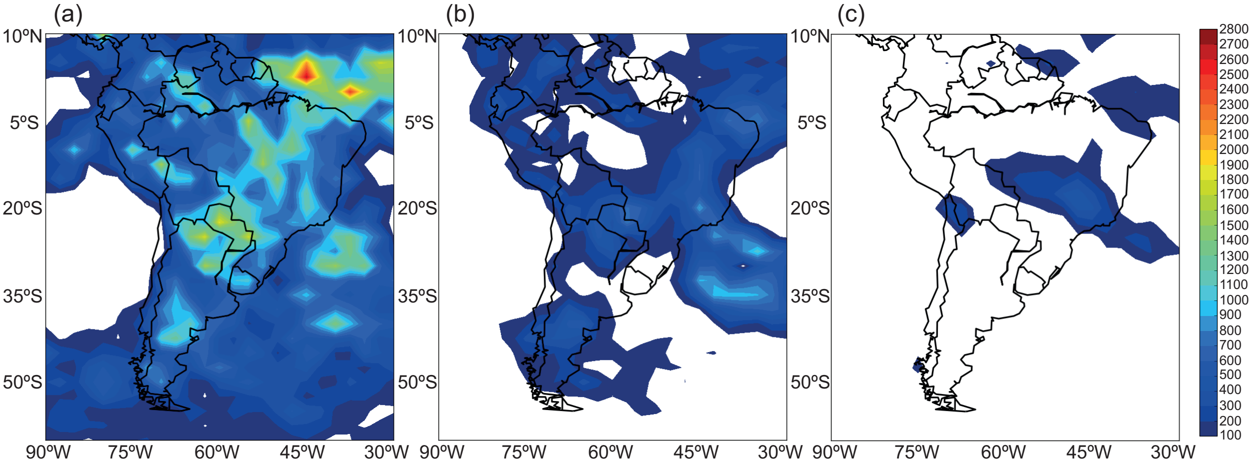

Fig. 5. Mean OLR variance ($W^2 m^{-4}$) of: (a) synoptic, (b) sub-monthly, and (c) intra-seasonal scales from January 5 to 11, 2011.

SACZ. Simultaneously, a convection suppression phase was observed in much of northeastern Argentina and southern Brazil. Such enhancement-suppression of convection forms the well-known rainfall seesaw pattern that prevails during the summer in South America (Nogués-Paegle and Mo, 1997; Carvalho et al., 2004; Schneider, 2004).

Figure 6a shows a contour map calculated with the Global Wavelet Spectrum along 17.5º SW, between 7.5º and 180º W. The longitudinal cross-section at 17.5º S coincides with the mean latitudinal position of the ZCAS event during the summer period December 2010 to February 2011. A longitudinal band that extends from 130º to 75º W shows minimum power values for the selected intra-seasonal and synoptic harmonics. There is also a small region where the annual and inter-annual (two years) cycles are relatively intense. Harmonics power grows

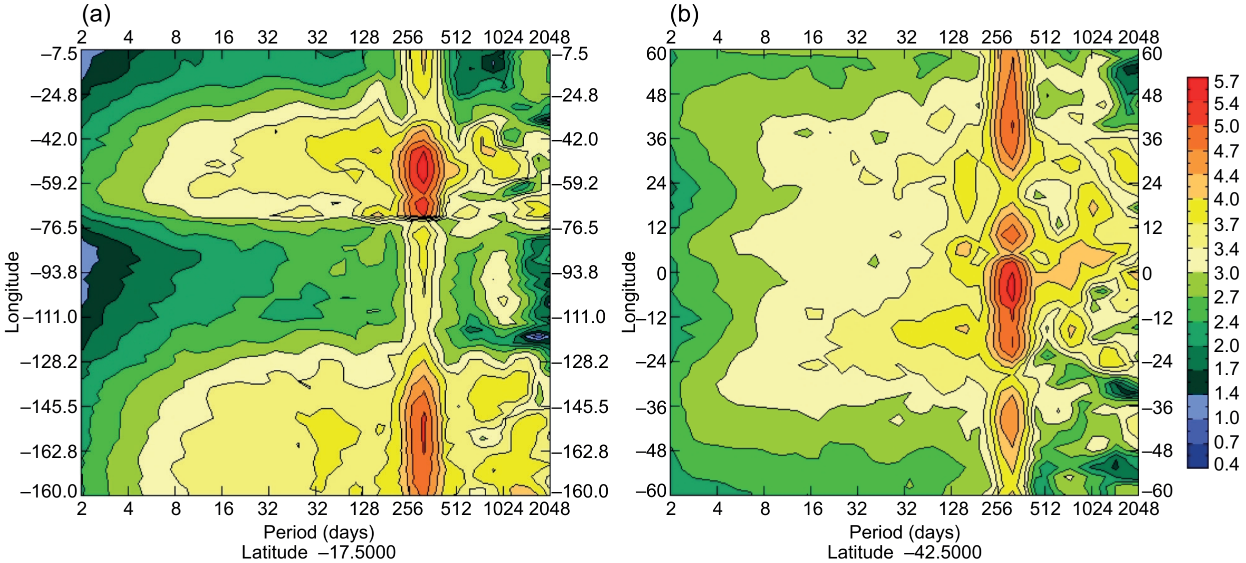

Fig. 6. Harmonic values of OLR global wavelet spectrum as a function of: (a) longitude (along 17.5º S) and (b) latitude (along 42.5º W). Spectral power is represented by the color scale. The period is in logarithmic scale. See text for details.

from this band towards the east and west, so that several scales (annual, intra-seasonal, sub-monthly and synoptic) are present in the South Pacific Ocean (180º to 125º W). The signal of the power spectrum weakens over the south-eastern Pacific (125º to 75º W). On the other hand, the signals of different scales strengthen again from 75º W over the South Pacific to 43º W over South America and weaken again over the South Atlantic Ocean. It is worth highlighting that convection along 17.5º S is attenuated by the relatively cold waters of the eastern Pacific Ocean, the eastern Atlantic Ocean and the Andes mountains. However, over the western Pacific Ocean and South America, convection can be modulated by transient systems, convergence zones, and other sub-monthly and intra-seasonal scale systems.

The longitudinal section (60º N to 60º S) along 42.5º W, which coincides with the mean longitudinal position of the ZCAS event during the summer period from December 2010 to February 2011 (Fig. 6b), shows a remarkable annual cycle along South America, the ITCZ and part of the equatorial North Atlantic Ocean. In the tropical and subtropical areas of South America, a wide band is observed with scales ranging from the synoptic, sub-monthly, intra-seasonal, and semi-annual scales, whose simultaneous presence, in coincidence with the establishment of persistent weather systems such as the SACZ, provides evidence for scale interaction.

Considering the 95% confidence level for the global wavelet spectrum of OLR, a noticeable interaction of intra-seasonal spectral components stands out around January 11. Components were divided into wave groups with periods of 88, 73, 58 and 31 days (intra-seasonal); sub-monthly, with periods of 17 days, and harmonics, with periods of 10 days (synoptic scale). The large volume of rainfall that fell on January 11 and 12 is associated to great power spectrum OLR amplitudes. This is indicative of strong convective activity due to a favorable phase of the intra-seasonal oscillation in the region.

Figure 7 shows the OLR time series for the 2010 and 2011 austral summers on the synoptic (blue), sub-monthly (red), and intra-seasonal (green) scales. The sub-monthly scale presents seven minimum and eight maximum values. Minimum values are associated with negative OLR anomalies, indicative of intense convective activity in the region. On January 14, 2011 sub-monthly-scale OLR values were lower (around –16) than the intra-seasonal and synoptic scales (around –2 and –10, respectively). These negative OLR anomalies on the three scales would indicate phenomena favoring precipitation were active on that day. In this sense, the three scales can be assumed to be interacting from January 11 to 15, 2011 with energy transfer among scales.

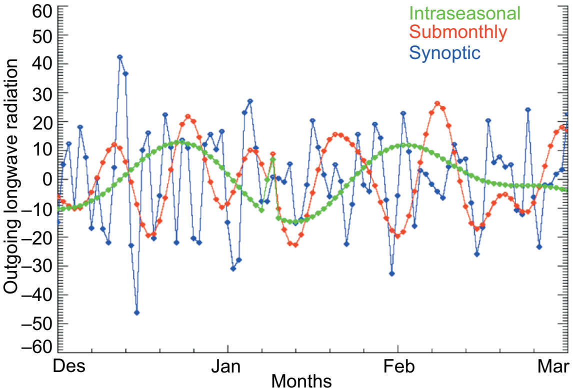

Fig. 7. Time series of OLR for the synoptic scale (blue), sub-monthly (red) and intra-seasonal scale (green) during austral summers (DJF) of 2010 and 2011 in southeast South America.

Based on this analysis, it can be inferred that when the spatial pattern of the negative phase of intra-seasonal oscillation (which favors convection) over southeastern Brazil coincides with the corresponding sub-monthly and synoptic disturbance pattern (SACZ), strong scale interaction occurs which enhances the SACZ and causes more rainfall. In this type of situations, advection of cyclonic vorticity on the synoptic scale and associated divergence in the upper troposphere become more effective in maintaining upward air motion and instability over the region.

In relation to the circulation field associated with the event, Figure 8 shows the streamlines at high (200 hPa) and low (850 hPa) levels. Figure 8a shows an anticyclonic circulation over a large part of South America. To the east of the anticyclone, there is a high-level cyclonic vortex. Figure 8b shows the SACZ crossing the South American continent from the southwest Atlantic to the south of the Amazon region. The SACZ has an associated extratropical

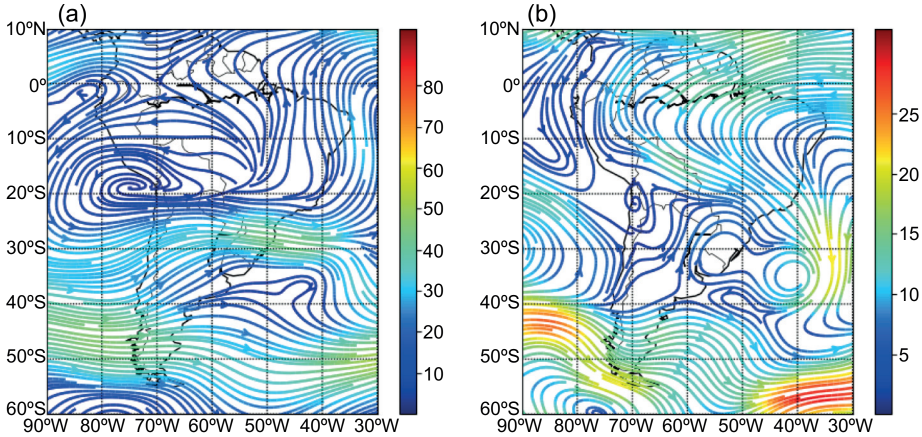

Fig. 8. Streamline (m s^{-1}) in (a) 200 hPa and (b) 850 hPa levels on January 12, 2011.

cyclone over the South Atlantic Ocean at around 35º S. Moisture and heat are transported from the southeast, center-west and north, where the SACZ is active (Fig. 8b), towards the southeast of Brazil (figure not shown).

3.2.2 Case 2: December 22-25, 2014

The second case was a heavy precipitation event associated with the SACZ that occurred in the southeastern region of Brazil from December 22 to 25, 2014. This event was selected after analyzing OLR power spectra of a series of precipitation events because it presented a strong sub-monthly OLR negative anomaly. During those days, intense precipitation was observed in the south, center-west, southeast, and north of the southern region of Brazil. In addition to the SACZ, other systems such as cyclonic circulation at 850 hPa, vertical motion at 500 hPa, and mass divergence at 200 hPa contributed to the rainfall events in these regions.

Figure 9 shows the average behavior of the spectral power of OLR on the synoptic, sub-monthly and intra-seasonal scales, from December 22 to 25, 2014 associated to the occurrence of the SACZ event (Climanálise boletim, 2014). A wide range of high OLR spectral power values extends from the northwest to the southeast of Brazil, coinciding with the establishment of a period of active convection

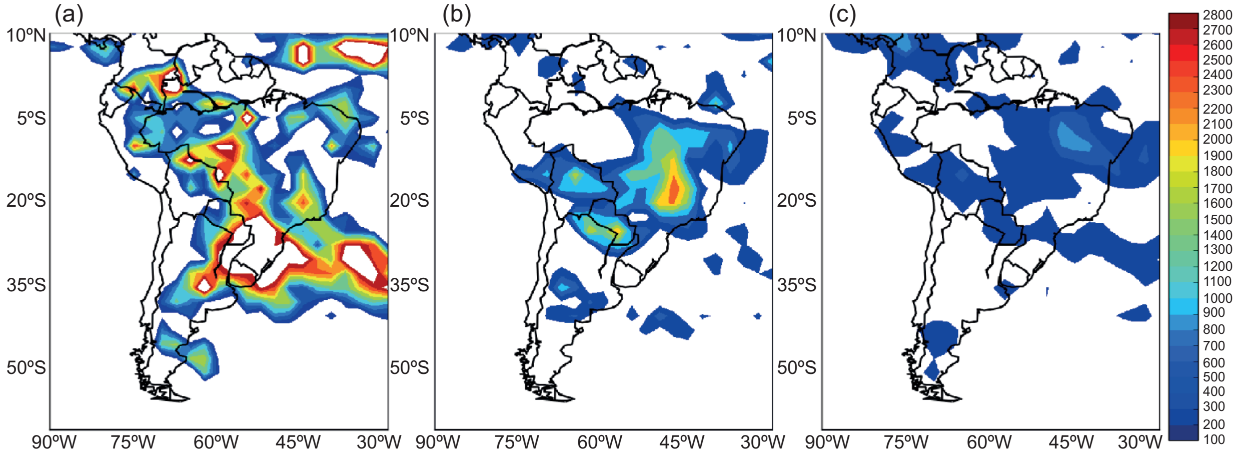

Fig. 9. Mean OLR variance (W^2 m^{-4}) of: (a) synoptic, (b) sub-monthly, and (c) intra-seasonal scales from December 22 to 25, 2014.

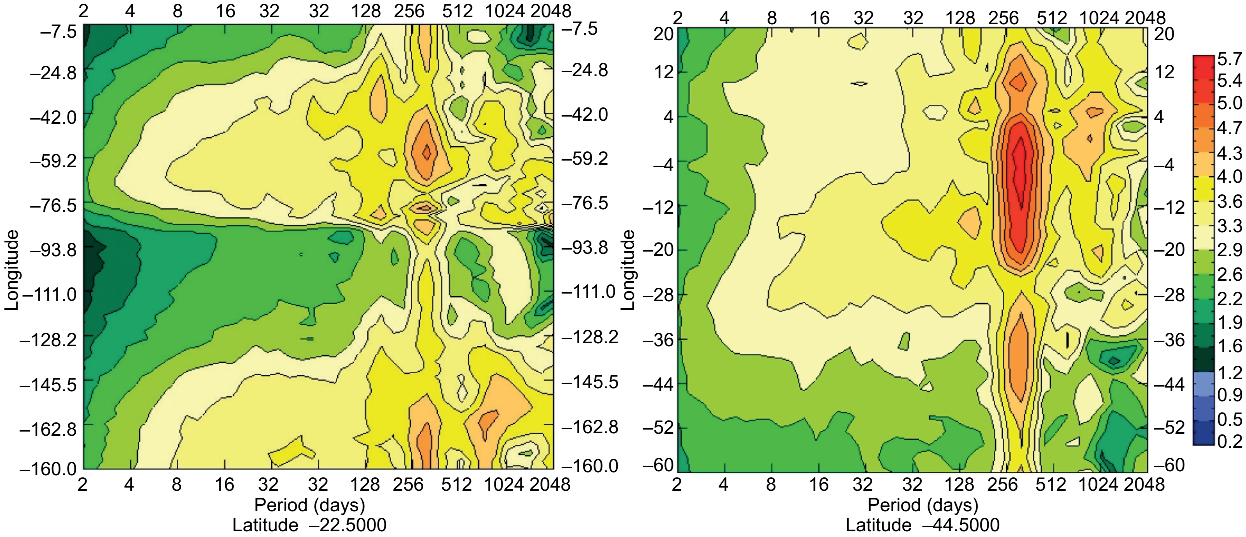

Fig. 10. Harmonic values of OLR global wavelet spectrum as a function of: (a) longitude (along 22.5º S) and (b) latitude (along 44.0º W). Spectral power is represented by the color scale. The period is in logarithmic scale. See text for details.

in the SACZ. The greatest amplitudes are on the sub-monthly scale, followed by the synoptic and intra-seasonal scales. During this event, the most intense precipitation occurred in the central-western and southeastern regions of Brazil.

Contour maps with cross sections at 22.5 S (Fig. 10a) and 44.5º W (Fig. 10b) were calculated with Global Wavelet Spectrum. The longitudinal cross-section along 22.5º S (7.5º to 150º W) coincides with the mean latitudinal position of the ZCAS event during the summer period from December 2014 to February 2015. Within the longitudinal band (60º to 21º W) several scales stand out, i.e., annual, intra-seasonal, sub-monthly, and synoptic. The signals of the different scales strengthen again in the band from 107º to 150º W. It is worth highlighting that along parallel 22.5º S convective activity is attenuated by the relatively cold waters in the eastern Pacific Ocean, the eastern Atlantic Ocean and by the Andes mountains. On the other hand, convection can be modulated by transient systems, convergence zones, and other sub-monthly and intra-seasonal systems over the western Pacific Ocean and South America.

The longitudinal section (20º N to 60º S) along 44.5º W (Fig. 10b), that coincides with the mean longitudinal position of the ZCAS event during the summer period from December 2014 to February 2015, shows a remarkable annual cycle along South America, the ITCZ, and part of the equatorial North Atlantic Ocean. On the other hand, a wide band is observed with scales ranging from sub-monthly to intra-seasonal and semi-annual, mainly in the tropics and subtropics of South America. The simultaneous presence of the sub-monthly and intra-seasonal scales, coinciding with the establishment of persistent weather systems such as the SACZ provides further evidence of scale interaction.

Figure 11 shows the OLR time series for the austral summers of 2014 and 2015 on the synoptic (blue), sub-monthly (red) and intra-seasonal (green) scales. The sub-monthly scale presents five minimum and six maximum values. Minimum values are associated with negative OLR anomalies and are an indication of intense convective activity in the region. On December 22, 2014 the sub-monthly scale presents smaller OLR (around –24) than the intra-seasonal and synoptic scales, which have around –10 and 4, respectively. These values indicate the dominance of the sub-monthly scale on this day. On December 23, 2014 OLR dropped on the synoptic and sub-monthly scales to around –12 and –24, respectively. Although OLR on the intra-seasonal scale showed a slight increase to –9, it remained negative. Negative OLR anomalies on the three scales of variability are indicative of convective activity. In this sense, the three scales can be assumed to be interacting on

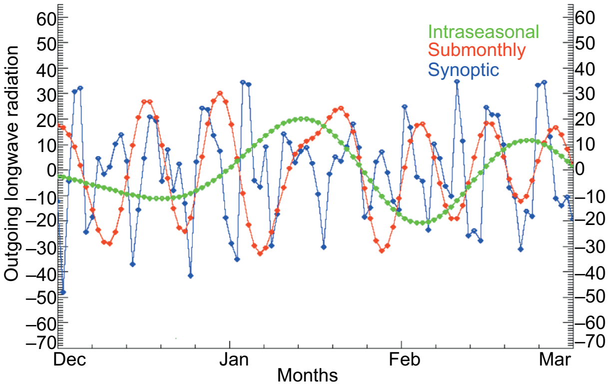

Fig. 11. Time series of OLR for the synoptic scale (blue), sub-monthly (red) and intra-seasonal scale (green) during austral summers (DJF) of 2014 and 2015 in the southeast of South America.

December 23, 2014 with energy transfer among scales. According to Cai and Mak (1990), low frequency planetary scale waves and high frequency synoptic scale waves within a balanced state of the atmosphere are symbiotically dependent on one another. In the context of scale interaction, Cuff and Cai (1995) were able to determine a transfer of energy between low and high frequency modes in an observational study on the interaction between low and high frequency transient systems. These authors argue that low-frequency transients organize high-frequency transients (Schneider, 2004).

Figure 12 shows streamlines at high (200 hPa) and low levels (850 hPa). At high levels (Fig. 12a), anticyclonic circulation is observed over a large part of South America and a high-level cyclonic vortex is observed east of the anticyclone. The subtropical jet is intense in the southern region of Brazil. In addition, a trough is seen to the west of the jet in the south of South America. In the southeast of Brazil, wind convergence is observed at low levels (Fig. 12b), and the South Atlantic Subtropical Anticyclone can be seen entering the continent. The winds associated with the anticyclones coming from the Atlantic Ocean towards the Amazon region change direction to the southeast of Brazil, which indicates that there is transport of moisture and heat into this region. There is a trough in the south, which indicates unstable weather east of this trough.

4. Conclusions

We analyzed the variability modes of the synoptic, sub-monthly, and intra-seasonal scales that modulate rainfall events over South America and adjacent oceans during the austral summers of the period 1979-2016. To do so, we examined OLR power spectrum fields (variance). The results obtained for South America indicate that the sub-monthly scale has influence on the SACZ. Also as observed in the southeastern region of Brazil, the sub-monthly scale presents greater amplitude compared to the intra-seasonal scale.

Based on this analysis, the influence of the synoptic, sub-monthly, and intra-seasonal scales on two

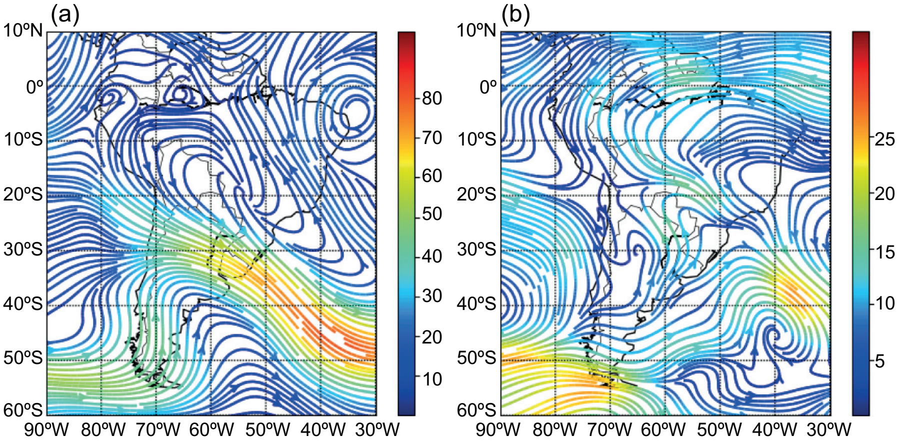

Fig. 12. Streamline (m s^{-1}) in (a) 200 hPa and (b) 850 hPa levels on December 24, 2014.

heavy precipitation events over southeastern Brazil, during an active SACZ, was examined. The analysis of the January 2011 case suggests that when the spatial pattern of the negative phase of intra-seasonal oscillation (which favors convection) in southeastern Brazil concurs with sub-monthly (SACZ) and synoptic scale disturbance patterns, the three scales interact strongly, such that the SACZ becomes more active and rainfall increases. In such situations, synoptic-scale advection of cyclonic vorticity and associated upper-troposphere divergence become more effective in sustaining upward motion and instability over the region. The sub-monthly scale was dominant in the development of the second event of December 22, 2014. On that day, a moisture channel was active, which later turned into the SACZ (December 22 to 25, 2014). In synthesis, the sub-monthly scale is observed to have had the greatest intensity and major importance with respect to the other scales. In addition, the interaction among synoptic, sub-monthly and intra-seasonal variability was observed to decay simultaneously.

Acknowledgments

The authors thank Dr. Nelson Ferreira for his helpful discussions and suggestions. The authors are also grateful for the comments of the reviewers.

References

Álvarez MS, Vera CS, Kiladis GN, Liebmann B. 2016. Influence of the Madden-Julian oscillation on precipitation and surface air temperature in South America. Climate Dynamics 46: 245-262. https://doi.org/10.1007/s00382-015-2581-6

Cai M, Mak M. 1990. Symbiotic relation between planetary and synoptic-scale waves. Journal of the Atmospheric Sciences 47: 2953-2968. https://doi.org/10.1175/1520-0469(1990)047<2953:SRBPAS>2.0.CO;2

Calvello M, D'Orsi Neiva R, Piciullo L, Paes N, Magalhaes M, Alvarenga Lacerda W. 2015. The Rio de Janeiro early warning system for rainfall-induced landslides: Analysis of performance for the years 2010-2013. International Journal of Disaster Risk Reduction 12: 3-15. https://doi.org/10.1016/j.ijdrr.2014.10.005

Carvalho LMV, Jones C, Liebmann B. 2002. Extreme precipitation events in southeastern South America and large-scale convective patterns in the South Atlantic convergence zone. Journal of Climate 15: 2377-2394. https://doi.org/10.1175/1520-0442(2002)015<2377:EPEISS>2.0.CO;2

Carvalho LMV, Jones C, Liebmann B. 2004. The South Atlantic convergence zone: Intensity, form, persistence, and relationships with intraseasonal to interannual activity and extreme rainfall. Journal of Climate 17: 88-108. https://doi.org/10.1175/1520-0442(2004)017<0088:TSACZI>2.0.CO;2

Casarin DP, Kousky VE. 1986. Anomalias de precipitação no sul do Brasil e variações na circulação atmosférica. Revista Brasileira de Meteorologia 1: 83-90.

Cavalcante MRG, Barcellos PCL, Cataldi M. 2020. Flash flood in the mountainous region of Rio de Janeiro state (Brazil) in 2011. Part I: Calibration watershed through hydrological SMAP model. Natural Hazards 102: 1117-1134. https://doi.org/10.1007/s11069-020-03948-3

Cavalcanti IFA, Ferreira NJ, Justi da Silva MGA, Silva Dias MAF. 2009. Tempo e clima no Brasil. Vol. 1. 1a ed. Oficina de Textos, São Paulo, 463 pp.

Climánalise boletim. 2014. Available at: http://climanalise.cptec.inpe.br/~rclimanl/boletim/ (accessed on February 7, 2019).

Cuff TJ, Cai M. 1995. Interaction between the low and high frequency transients in the Southern Hemisphere winter circulation. Tellus 47: 331-350. https://doi.org/10.3402/tellusa.v47i3.11521

Cunningham CC, Cavalcanti IFA. 2006. Intraseasonal modes of variability affecting the South Atlantic convergence zone. International Journal of Climatology 26: 1165-1180. https://doi.org/10.1002/joc.1309

Daubechies I. 1992. Ten lectures on wavelets. Society for Industrial and Applied Mathematics, Philadelphia, 357 pp.

Escobar GCJ. 2014. Síntese sinótica dezembro de 2014. CPTEC/INPE. Available at: https://s3.cptec.inpe.br/admingpt/tempo/pdf/sintese_mensal_1214.pdf (accessed on February 17, 2019).

Foufoula-Georgiou E, Kumar P. Eds. 1995. Wavelets in geophysics. Academic Press, San Diego.

González PLM, Vera CS. 2013. Summer precipitation variability over South America on long and short intraseasonal timescales. Climate Dynamics 43: 1993-2007. https://doi.org/10.1007/s00382-013-2023-2

Gu D, Philander SGH. 1995. Secular changes of annual and interannual variability in the tropics during the past century. Journal of Climate 8: 864-876. https://doi.org/10.1175/1520-0442(1995)008<0864:SCOAAI>2.0.CO;2

Hirata F. 2013. Intraseasonal variability of summer convection over South America. Ph.D. thesis. Georgia Institute of Technology.

Infoclima. 2011. Sistemas meteorológicos e eventos de destaque no Brasil em janeiro de 2011. Infoclima. Boletim de Informações Climáticas do CPTEC/INPE 18: 2. Available at: http://infoclima1.cptec

INMET. 2009. Normais climatológicas do Brazil, 1961-1990. Instituto Nacional de Meteorologia, Brasília, DF. Available at: https://clima.inmet.gov.br/NormaisClimatologicas/1961-1990/precipitacao_acumulada_mensal_anual (accessed in June 2022).

Kodama YM. 1992. Large-scale common features of subtropical precipitation zones (the Baiu frontal zone, the SPCZ, and the SACZ). Part I: Characteristics of subtropical frontal zones. Journal of the Meteorological Society of Japan 70: 813-835. https://doi.org/10.2151/jmsj1965.70.4_813

Kousky VE, Gan MA. 1981. Upper tropospheric cyclonic vortices in the tropical South Atlantic. Tellus 33: 538-551. https://doi.org/10.3402/tellusa.v33i6.10775

Liebmann B, Smith C. 1996. Description of a complete (interpolated) outgoing longwave radiation. Bulletin of the American Meteorological Society 77: 1275-1277. https://doi.org/10.1175/1520-0477-77.6.1274

Liebmann B, Kiladis GN, Marengo JA, Ambrizzi T. 1999. Submonthly convective variability over South America and the South Atlantic convergence zone. Journal of Climate 12: 1877-1891. https://doi.org/10.1175/1520-0442(1999)012<1877:SCVOSA>2.0.CO;2

Madden RA, Julian PR. 1971. Detection of a 40-50-day oscillation in the zonal wind in the tropical Pacific. Journal of the Atmospheric Sciences 28): 702-708. https://doi.org/10.1175/1520-0469(1971)028<0702:DOADOI>2.0.CO;2

Madden RA, Julian PR. 1972. Description of global-scale circulation cells in the tropics with a 40-50-day period. Journal of the Atmospheric Sciences 29: 1109-1123. https://doi.org/10.1175/1520-0469(1972)029<1109:DOGSCC>2.0.CO;2

Netto ALC, Sato AM, Avelar AS, Vianna LGG, Araújo IS, Ferreira DLC, Lima PH, Silva APA, Silva RP. 2013. January 2011: The Extreme Landslide Disaster in Brazil. In: Landslide science and practice (Margottini C, Canuti P, Sassa K, Eds.). Springer, Berlin-Heidelberg. https://doi.org/10.1007/978-3-642-31319-6_51

Nogués-Paegle J, Mo KC. 1997. Alternating wet and dry conditions over South America during summer. Monthly Weather Review 125: 279-291. https://doi.org/10.1175/1520-0493(1997)125<0279:AWADCO>2.0.CO;2

Ottero CR, Chargel LT, Massera da Hora MAG. 2018. Análise de frequência dos dados pluviométricos observados em 2011 e 2013 na Região Serrana, Estado do Rio de Janeiro. Revista Brasileira de Meteorologia 33: 131-139. https://doi.org/10.1590/0102-7786331007

Pezzi LP, Kayano MT. 2009. An analysis of the seasonal precipitation forecasts in South America using wavelets. International Journal of Climatology 29: 1560-1573. https://doi.org/10.1002/joc.1813

Quadro MFL. 1994. Estudo de episódios de Zona de Convergência do Atlântico Sul (ZCAS) sobre a América do Sul. M.Sc. thesis. Instituto Nacional de Pesquisas Espaciais, Brazil.

Reboita MS, Gan MA, Rocha RP, Ambrizzi T. 2010. Precipitation regimes in South America: A bibliographic review. Brazilian Journal of Meteorology 25: 185-200. https://doi.org/10.1590/S0102-77862010000200004

Rodrigues-Alcantara C, Souza EP, Silva Dias MAF, Biezato B. 2014. Influência dos jatos em médios e baixos níveis nos processos de nuvem: estudo numérico de uma linha de instabilidade amazônica. Revista Brasileira de Meteorologia 29: 29-46. https://doi.org/10.1590/S0102-77862014000100004

Salio P, Nicolini M, Saulo AC. 2002. Chaco low-level jet events characterization during the austral summer season. Journal of Geophysical Research 107: 4816. https://doi.org/10.1029/2001JD001315

Salio P, Nicolini M, Zipser J. 2007. Mesoscale convective systems over southeastern South American low-level jet. Monthly Weather Review 135: 1290-1309. https://doi.org/10.1175/MWR3305.1

Saha S, Moorthi S, Pan H, Wu X, Wang J, Nadiga S, Tripp P, Kistler R, Woollen J, Behringer D, Liu H, Stokes D, Grumbine R, Gayno G, Wang, J, Hou, Y, Chuang H, Juang HH, Sela J, Iredell M, Treadon R, Kleist D, Van Delst P, Keyser D, Derber J, Ek M, Meng J, Wei H, Yang R, Lord S, van den Dool H, Kumar A, Wang W, Long C, Chelliah M, Xue Y, Huang B, Schemm J, Ebisuzaki W, Lin R, Xie P, Chen M, Zhou S, Higgins W, Zou C, Liu Q, Chen Y, Han Y, Cucurull L, Reynolds RW, Rutledge G, Goldberg M. 2010. The NCEP

Climate Forecast System Reanalysis. Bulletin of the American Meteorological Society 91: 1015-1058. https:/doi.org//10.1175/2010BAMS3001.1

Saha S, Moorthi S, Wu X, Wang J, Nadiga S, Tripp P, Behringer D, Hou Y, Chuang H, Iredell M, Ek M, Meng J, Yang R, Mendez MP, van den Dool H, Zhang, Q, Wang W, Chen M, Becker E. 2014. The NCEP Climate Forecast System version 2. Journal of Climate 27: 2185-2208. https://doi.org/10.1175/JCLI-D-12-00823.1

Sandeep S, Stordal F. 2013. Use of daily outgoing long wave radiation (OLR) data in detecting precipitation extremes in the tropics. Remote Sensing Letters 4: 570-578. https://doi.org/10.1080/2150704X.2013.769284

Sanches MB. 2002. Análise sinótica da Zona de Convergência do Atlântico Sul (ZCAS) utilizando-se a técnica de composição. M.Sc. thesis. Instituto Nacional de Pesquisas Espaciais, Brazil.

Seluchi ME, Saulo AC. 2012. Baixa do noroeste argentino e baixa do Chaco: Características, diferenças e semelhanças. Brazilian Journal of Meteorology 27: 49-60. https://doi.org/10.1590/S0102-77862012000100006

Schneider MA. 2004. Intra-seasonality in the south, southeast and midwest regions of Brazil during the winter months. M.Sc. thesis. University of São Paulo.

Shimizu MH, Ambrizzi T. 2017. MJO influence on ENSO effects in precipitation and temperature over South America. Theoretical and Applied Climatology 35: 1-20. https://doi.org/10.1007/s00704-015-1421-2

Torrence C, Compo GP. 1998. A practical guide to wavelet analysis. Bulletin of the American Meteorological Society. 79: 61-78. https://doi.org/10.1175/1520-0477(1998)079<0061:APGTWA>2.0.CO;2

Valadão CE, Carvalho LMV, Lucio PS, Chaves R R. 2017. Impacts of the Madden-Julian oscillation on intraseasonal precipitation over Northeast Brazil. International Journal of Climatology 37: 1859-1884. https://doi.org/10.1002/joc.4818

Vasconcelos FC, Cavalcanti IFA. 2010. Evaluation of the eta regional model forecasts for two cases of intense rainfall over the Serra do Mar region. Revista Brasileira de Meteorologia 25: 501-512. https://doi.org/10.1590/S0102-77862010000400009

Vera CS, Álvarez MS, González PLM, Liebmann B, Kiladis. 2018. Seasonal cycle of precipitation variability in South America on intraseasonal timescales. Climate Dynamics 51: 1991-2001. https://doi.org/10.1007/s00382-017-3994-1

Vincent DG. 1994. The South Pacific Convergence Zone (SPCZ): A review. Monthly Weather Review 122: 1949-1970. https://doi.org/10.1175/1520-0493(1994)122<1949:TSPCZA>2.0.CO;2

Vitorino MI. 2002. Análise das oscilações intrasazonais sobre a América do Sul e oceanos adjacentes utilizando a análise de ondaletas. Ph.D. thesis. Instituto Nacional de Pesquisas Espaciais, Brazil.

Weng H, Lau KM. 1994. Wavelets, period doubling, and time frequency localization with application to organization of convection over the Tropical Western Pacific. Journal of the Atmospheric Sciences 51: 2523-2541. https://doi.org/10.1175/1520-0469(1994)051<2523:WPDATL>2.0.CO;2

Atmósfera 36(1), 91-122 (2023)
https://doi.org/10.20937/ATM.53026

CONTENTS

Regional patterns of vegetation, temperature, and rainfall trends in the coastal mountain range of Chiapas, Mexico

Allen WOOTTON[1]*, Paula L. ENRÍQUEZ[1] and Darío NAVARRETE-GUTIÉRREZ[2]

[1] *Departamento de Conservación de la Biodiversidad, El Colegio de la Frontera Sur, 29290 San Cristóbal de las Casas, Chiapas, México.*
[2] *Departamento de Observación y Estudio de la Tierra, la Atmósfera y el Océano, El Colegio de la Frontera Sur, 29290 San Cristóbal de las Casas, Chiapas, México.*
*Corresponding author; email: allen.wootton@estudianteposgrado.ecosur.mx

Received: January 11, 2021; accepted: May 31, 2021

RESUMEN

Los cambios en el CO_2 atmosférico, la temperatura del océano y las condiciones de la vegetación regional en Mesoamérica indican posibles tendencias significativas en la temperatura y lluvias en la Sierra Madre de Chiapas, México. Ésta es una región importante para la flora la fauna que podría verse afectada por las tendencias climáticas. Nuestro objetivo fue determinar si se habían producido tendencias climáticas en un periodo de 27 años en la Sierra Madre y las regiones de menor elevación entre 1990 y 2016, si estas tendencias son parte de cambios a más largo plazo (1960-2016 [57 años]) y la manera en que los cambios en las condiciones de gran escala y regionales/locales pueden influir en estas tendencias. En la Sierra Madre, las temperaturas diarias mínimas generales aumentaron, las temperaturas máximas disminuyeron y la mayoría de las tendencias significativas de temperatura media fueron más frías durante el periodo de 27 años. Tanto el inicio como el final de la temporada húmeda mostraron una tendencia a principios de año, y las lluvias de esta temporada aumentaron significativamente. Las tendencias no fueron significativas durante el periodo de 57 años en la Sierra Madre; sin embargo, en la región adyacente de la costa del Pacífico, continuaron las tendencias significativas de temperaturas más cálidas durante este periodo. Hubo una gran variación en los cambios de temperatura y precipitación entre regiones, y algunas tendencias locales fueron opuestas a los promedios regionales. Es posible que los procesos a gran escala de calentamiento en las temperaturas de la superficie del mar en la costa este de México, un cambio de la fase positiva a negativa en la Oscilación Decenal del Pacífico y los aumentos en el CO_2 atmosférico influyan en estas tendencias. A escala regional, los aumentos en la vegetación densa y la evapotranspiración desde 1990 pueden haber creado condiciones que favorezcan una retroalimentación positiva de mayor humedad oceánica y un ciclo de precipitación basado en la vegetación.

ABSTRACT

Changes in atmospheric CO_2, ocean temperature, and regional vegetation conditions in Mesoamerica indicate that significant trends in temperature and rainfall may have occurred in the Sierra Madre de Chiapas, Mexico. This is an important region for flora and fauna which could be affected by climate trends. We aimed to determine if and where climate trends had occurred in the Sierra Madre and lower elevation regions between 1990 and 2016 (27 years), if these trends were part of longer term (1960-2016 [57 years]) changes, and how changes in large-scale and regional/local conditions may be influencing these trends. In the Sierra Madre, overall minimum daily temperatures increased, maximum temperatures decreased, and the most significant mean temperature trends were cooler during the 27-yr period. Both the start and end of the wet season trended earlier in the year, and wet season rainfall increased significantly. Trends were not significant during the 57-yr period in the Sierra Madre; however, in the adjacent Pacific coast region, significant warmer temperature trends continued during this period. Within regions, there was large variation in temperature and rainfall changes and some local trends were opposite to the regional averages. Large-scale processes of warming sea surface temperatures in the east coast of Mexico, a change from the positive to negative phase of the Pacific Decadal Oscillation and increases in atmospheric CO_2 may be influencing these trends. At the regional scale, increases in dense vegetation and evapotranspiration since 1990 may have created characteristics favoring a positive feedback of higher ocean-based moisture and vegetation-based precipitation cycling.

Key words: climate trends, evapotranspiration, remote sensing, Sierra Madre, vegetation changes.

1. Introduction

Changes since 1990 in influences on the climate of Mesoamerica, including atmospheric (Liverman and O'Brien, 1991; NOAA, 2020a), ocean temperature (Méndez-González et al., 2010) and land cover (Bray, 2009) indicate that significant regional climate trends may have occurred. Predictions or explanations of the causes of climate trends or changes in these regions has often been done based on modeling of global atmospheric conditions (Karmalkar et al., 2008), ocean temperature patterns (Pounds et al., 1999), or regional land use changes (Ray et al., 2006a; Barradas et al., 2010). However, as each tropical region has its own particular topographical characteristics, oceanic influence and land cover change circumstances, the use of local data is also necessary to determine spatial details in actual regional trends and validate models.

The three physiographical regions of the Mexican state of Chiapas closest to the Pacific Ocean (subsequently referred to as Pacific Chiapas) are the Central Depression, Pacific coastal plains (Coast) and Sierra Madre de Chiapas (Sierra Madre) (Fig. 1). The climate of this area is largely influenced by large scale circulation patterns, which determine the direction of airflow, onset and length of the wet season, and frequency and intensity of rainfall events (Hewitson and Crane, 1992). The influence of these large-scale processes on regional climates may depend on trends in sea surface temperatures (SST) (Aguilar et al., 2005), which have been increasing in the Gulf of Mexico and Caribbean Sea since 1965 and 1975, respectively, in the regions closest to the east coast of Mexico (Lluch-Cota et al., 2013).

Short term variations in temperature and precipitation patterns in Chiapas have been found to be weakly correlated with cycles of El Niño Southern Oscillation in the Pacific Ocean, although regional climate patterns varied in relation to this phenomenon (Golicher et al., 2006). Changes between the positive and negative phase of the Pacific Decadal Oscillation (PDO) could also affect climate trends during a longer time period (Méndez-González et al., 2010).

In addition to ocean temperature trends, changes in amounts of atmospheric CO_2 may be influencing the climate of the region. Based on CO_2 modeling, Liverman and O'Brien (1991) predicted that if CO_2 doubled from the 1990 amount of 350 ppm, it would cause increases in air temperature and late dry season and summer precipitation, and decreases in precipitation at the end of the wet season and beginning of the dry season in parts of Chiapas. Since that time, atmospheric CO_2 has increased to 415 ppm in 2020 (NOAA, 2020a).

Regional changes to land vegetation characteristics within Pacific Chiapas may also be influencing the mountain climate of the Sierra Madre. Modeling done on the effect of forest cover change on cloud formation in Costa Rica found that scenarios with large amounts of lower elevation deforestation resulted in lower amounts of cloud cover and higher base cloud heights in mountain forests (Lawton et al., 2001; Ray et al., 2006a). These climatic changes were largely attributed to increases in sensible heat flux from cleared land and reductions in latent heat flux due to vegetation losses (Lawton et al., 2001; Ray et al., 2006a).

Forests and dense vegetation contribute large amounts of water vapor to the atmosphere through evapotranspiration (ET) and can affect regional rainfall through recycling of ocean-source moisture (Durán-Quesada et al., 2012). Changes in vegetation can affect this process (Sheil, 2018) with reductions in tropical forest cover, generally leading to reductions in regional rainfall (Chambers and Artaxo, 2017; Casagrande et al., 2018). The main factors which control ET in an environment are vegetation density and leaf production, and climatic variables such as temperature, irradiance, wind, soil water availability, and vapor pressure (Zhang et al., 2015).

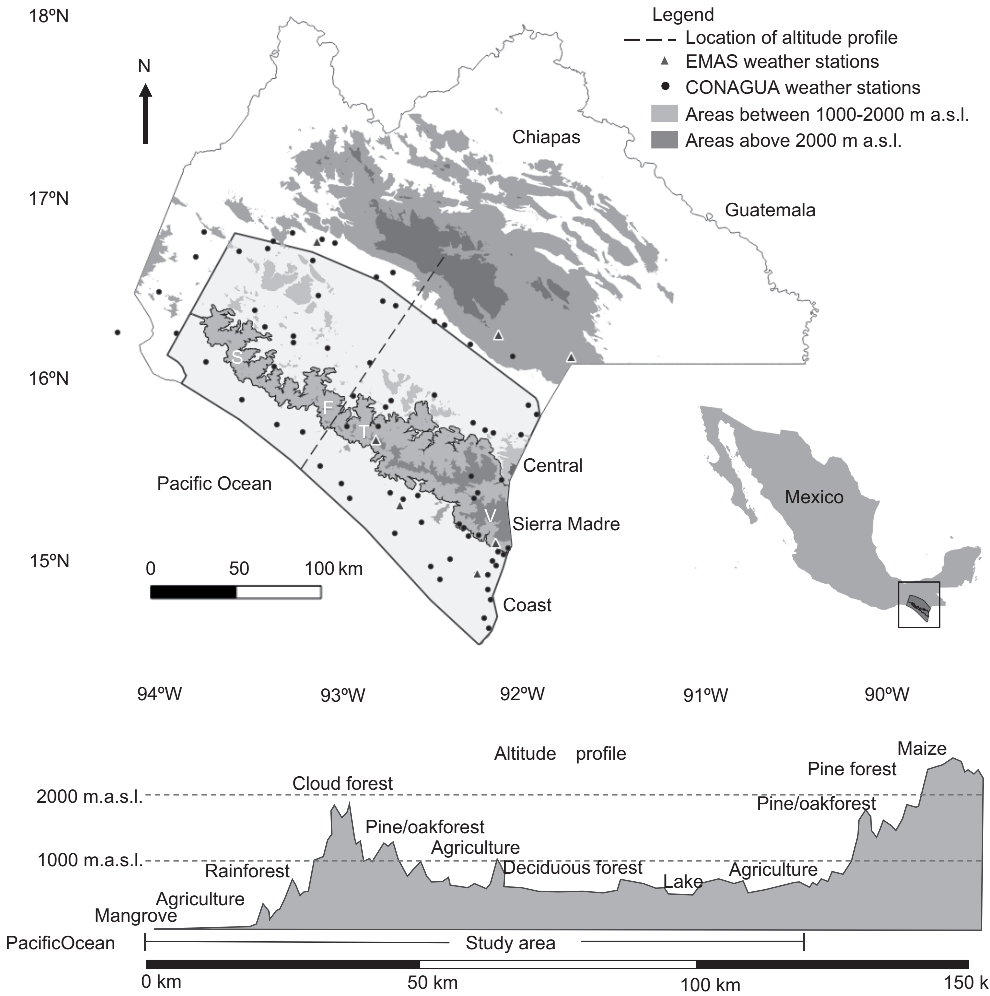

Fig. 1. Study area of the central depression, Sierra Madre, and coast regions of Chiapas, Mexico, locations of the weather stations, and an elevation profile from the Pacific Ocean to the central highlands of Chiapas. Letters S, F, T, and V indicate locations of the biosphere reserves La Sepultura (S), Frailescana (F), El Triunfo (T), and Volcán Tacaná (V).

In regions which are mainly covered in vegetation, such as the study area, the process of transpiration contributes to the greatest portion of ET (Ramón-Reinozo et al., 2019), although evaporation from leaf surfaces can contribute to a significant portion (Ballinas et al., 2015). In a watershed in the Sierra Madre, Castro-Mendoza et al. (2016) estimated that up to 64% of precipitation may be re-cycled to the atmosphere through ET.

Changes in vegetation cover may also affect local trends in temperature and rainfall, however the effects of this in tropical regions is still unclear. In the Lacandon rainforest in eastern Chiapas, maximum daily temperatures generally decreased in areas where there has been deforestation, but there was no relation between local rainfall and forest cover changes (O'Brien, 1998). In Guatemala, areas with greater deforestation within similar forest types had lower amounts of rainfall during the dry season (Ray et al., 2006b). The determination of links between vegetation changes and climate trends are especially important in tropical regions such as Chiapas, where land use change has been occurring rapidly (Solórzano et al., 2003).

These measured or potential changes in oceanic, atmospheric, and regional land cover conditions indicate the potential for climatic change in Pacific Chiapas. Therefore, this study examines the actual effects of these changes in large-scale and regional climatic influences on temperature and rainfall trends in this area, especially the Sierra Madre mountain range, from 1990 to 2016.

The Sierra Madre is the main source of water which flows into the Grijalva River system to produce a large quantity of Mexico's power from dams and is an important source of freshwater resources (Jones et al., 2018). It is also a major coffee-producing region, which may be affected by changes in climate (Schroth et al., 2009). Its ecological importance has been recognized through the establishment of the biosphere reserves El Triunfo, La Sepultura and Volcán Tacaná. These reserves contain populations of flora and fauna which may be affected by long term changes (Rojas-Soto et al., 2012), or cyclical (~30-yr) trends in the mountain climate (Pounds et al., 1999; Lister and García, 2018). Various ecological studies were conducted during the establishment of the reserves in the early 1990's (e.g., Long and Heath, 1991; Solórzano et al., 2000), and a better understanding of climatic trends since 1990 may provide a useful reference to help explain longer term ecological trends in this region (González-García et al., 2017).

The aims of this study were to determine if and where significant climate trends have occurred from 1990-2016 in Pacific Chiapas, if these were cyclical (~30-yr) or part of longer-term (~60-yr) climate changes, and how regional and larger scale processes may be influencing these trends or changes. Specifically, the first objective was to determine spatial patterns of temperature and rainfall changes and locations of significant trends from 1990-2016 in the Sierra Madre to compare with those of the adjacent lowland regions. The second objective was to determine if significant trends during the 27-yr period were part of a longer-term (1960-2016) trend in locations where data were available. The third objective was to relate climate trends to larger scale and regional climatic influence changes during similar time periods.

As mentioned, various studies have described how large-scale oceanic (Hewitson and Crane, 1992) and atmospheric processes (Liverman and O'Brien, 1991) may influence the climate of Pacific Chiapas, and we incorporated these findings into the discussion of the determined climate trends. However, to our knowledge, there have been no previous studies which have included vegetation characteristics and changes in relation to climate trends in this region. Therefore, our third objective was focused on the determination of local and regional changes in vegetation and ET from 1990-2020, which may also be influencing climate trends in Pacific Chiapas and particularly in the mountain regions.

2. Methods

2.1 Study area and time period

Pacific Chiapas (Fig. 1) is a topographically and ecologically complex region where mountainous and coastal terrain create conditions for the growth of many different forest types including mangroves, rainforests, tropical deciduous, oak-pine, cypress, fir, and cloud forests (INEGI, 2017; Fig. 1). Leaf presence is especially seasonal in the tropical deciduous forests (Gómez-Mendoza et al., 2008; Table I), but also in the more evergreen mountain forests where ET can change greatly throughout the year (Ballinas et al., 2015).

Similar to other regions of southern Mexico, the majority of rainfall falls between June and September (Brito-Castillo, 2012). The timing of the onset of the wet season depends strongly on the northward movement of the Intertropical Convergence Zone (ITCZ), which causes trade winds to increase in intensity and bring moist air from the Caribbean and Gulf of Mexico (Brito-Castillo, 2012). During the summer and early fall, tropical cyclones originating from the Caribbean Sea and the Pacific Ocean can bring large amounts of rainfall (García, 1974). Winter rainfall is less and is affected by cold winds originating in central North America which travel over the Gulf of Mexico, collecting humidity (García, 1974). Low pressure systems in northern Mexico also bring in moist air from the Pacific during winter (Brito-Castillo, 2012). Amounts of yearly rainfall (1990-2016 averages) are greatest in the Sierra Madre (Finca A. Prusia weather station: 2860 mm yr^{-1}, with 85% of rainfall during the wet period from June until October), followed by the Coast (Tapachula: 2076 mm yr^{-1}, 78% during the wet period), and lower amounts in the Central Depression (Villaflores: 1222 mm yr^{-1}, 86% during the wet period) (Fig. 2).

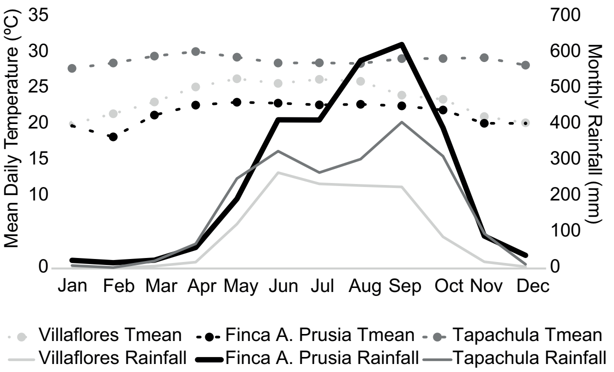

Fig. 2. Monthly averages of mean daily temperature (T_{mean}) and rainfall during the 1990-2016 period in the central depression (Villaflores weather station), Sierra Madre (Finca A. Prusia), and coast (Tapachula) regions.

Daytime (maximum) temperatures are highest in this region just before the wet season due to higher latent heat transfer and radiative forcing (Aguilar et al., 2005). July is often the month with the highest nighttime (minimum) temperatures due to the insulation caused by higher cloud cover (Aguilar et al., 2005). Mean daily temperatures (1990-2016 averages) are highest in the coast (Tapachula, 29 ºC), and lower at higher elevations in the Central Depression (Villaflores, 24 ºC) and the Sierra Madre (Finca A. Prusia, 22 ºC) (Fig. 2). In addition to ocean moisture sources, temperature and rainfall patterns in Pacific Chiapas are also influenced by topography and vegetation characteristics (Hewitson and Crane, 1994; Ray et al., 2006b).

Analysis of data began from 1990 to include greater spatial detail of climate trends with the inclusion of larger numbers of weather stations, which began collecting data around this year; and to provide a climatic reference for comparing ecological changes in the Sierra Madre. Comparisons of 1990-2016 trends were also done for a longer-term (57-yr) period using data from weather stations where significant 1990-2016 trends were determined and data were available since 1960.

Temperature and rainfall data were obtained from weather stations of the Comisión Nacional del Agua (National Water Commission) located within the study area (Conagua, 2018) (Fig. 1 and Table S-I in the supplementary material). Because of a lack of complete data in some weather stations and years with large amounts of cloud cover in Landsat satellite images, the analysis of land cover, NDVI, and potential ET was done using data from a range of years. Satellite images from 1987-1993 were used to represent the year 1990 and images and data from 2015-2020 to represent 2020. Rainfall and temperature trend analysis was done from 1990 to 2016 for most stations, or to 2012 or 2015 where more recent data were not available (Table S-II).

2.2 Temperature and rainfall trends

Trends and changes in average minimum (T_{min}), mean (T_{mean}), and maximum (T_{max}) daily temperature between 1990-2016 were determined using data from 55 weather stations located within the study area (Table S-I). Months were grouped into three seasons representing the main yearly changes in temperature: dry-cool (November-February), dry-hot (March-May), and wet (June-October). Temperature data for each season were obtained by averaging data of the months within each group. Differences in temperature were generally greater between months within a season than between adjacent years of the same month. Therefore, if data for a month was missing, they were estimated by calculating the average of the closest years (for up to one or two years) where data were available. This was done to avoid cooler or warmer month biases within the seasonal monthly averages where some monthly data were missing. If a station was missing more than 15% of monthly data between 1990-2016, or errors were evident (e.g., sudden breaks between temperature trend lines), it was not included in the analysis.

A graph of temperature data was done for each month and weather station and a least squares regression line was applied from 1990 to 2016. The average daily temperature value of the regression line value in 2016 was subtracted from that of 1990 to determine the change between these years. These data were uploaded into the GIS software QGIS v. 3.14 as vector points, and a spatial analysis of temperature changes was done using the Triangulated Irregular Network (TIN) method (Mitas and Mitasova, 1999) in QGIS for each season. This was chosen as the method to best represent the interpolation of the spatial changes in data which were largely influenced by topography (Velásquez et al., 2011).

Using climatic records with gaps in time series creates some uncertainty when assessing trends

(Mardero et al., 2019). To correct for this, Mardero et al. (2019) interpolated data from nearby weather stations in the low elevation Yucatan Peninsula to complete rainfall records. Interpolation was also attempted in our study for stations in the Sierra Madre with missing data (Table S-II). However, results of this interpolation were inaccurate due to the large variation in rainfall between stations in the topographically complex mountain range. Therefore, the analysis of rainfall trends was done using only available data (Tables S-II and S-III).

Monthly rainfall changes between 1990 and 2016 were determined using the same method to calculate temperature changes, with data from 76 weather stations. Significant trends ($p < 0.05$) in temperature and rainfall were determined for three periods: 1960-1989, 1960-2016 and 1990-2016 (where data was available) using the Mann-Kendall test in the Excel extension program XLSTAT 2019. This test has commonly been used to detect significant trends in climate data. It has the assumption that data records are independent, but these data do not need to be normally distributed. As it is non-parametric, results of the test are not influenced by outlier values (Ahmad et al., 2015). Another advantage of using the Mann-Kendall test is that trends can still be determined even if a time series has missing data.

The start, end, and length of the wet season was calculated locally (rather than with regional averages) using daily rainfall data from 65 weather stations. Specifications of the start of the wet season were modified from a similar study done for the Yucatan Peninsula (Mardero et al., 2019). These were: (1) the first day of the year with measurable rainfall (≥ 1mm) followed by at least another day of rainfall within the next five days for a total of at least 20 mm of rainfall; and (2) that within the 30 days following this first day of rainfall, there was no dry spell of seven or more consecutive days without rainfall. The end of the wet season was calculated using these specifications in reverse, and the length of the wet season was calculated as the number of days between the start and the end of the wet season. Changes in the start and end of the wet season were determined by applying a regression line to a graph of the start and end dates and subtracting the values at the years 2016 and 1990 from the regression line.

2.3 Vegetation classification

Analysis of the spatial extent of forest and other vegetation cover in the years 1990 and 2020 was done to determine vegetation changes which could partially explain changes in ET, temperature, and rainfall in the study time period. The spatial extent of vegetation types was determined within the study area from the classification of Landsat level-2 atmospherically corrected images (Table S-IV). Classification was done from images captured during the dry season in order to determine vegetation types based on their density and leaf seasonality characteristics which could affect seasonal ET (Glenn et al., 2011; Ballinas et al., 2015). Images covering the study area, captured during 1987-1993 (Landsat 5) and 2017-2020 (Landsat 8) and which had less than 10% cloud cover, were downloaded from the USGS Earth Explorer website (USGS, 2020). The green, red and infrared bands (bands 2, 3, and 4 of Landsat 5, and bands 3, 4, and 5 of Landsat 8) were combined in QGIS, and these resulting images were uploaded into the land classification software Multispec v. 3.4.

Supervised classification of the image was done in this program to determine the land cover classes: evergreen forest (primary and secondary coniferous, cloud, and rainforest), mangrove, palm plantations, semi-deciduous forest (oak, pine-oak, fruit tree), deciduous forest, scrub, irrigated agriculture or short vegetation (often wetlands), grassland or seasonal agriculture, areas without vegetation (bare soil, rock, urban areas), water (lakes, rivers, coastal waters within the study area), and cloud cover (Table II). Evergreen forests, mangroves and palm plantations were determined as separate classes for areas dominated with tree cover which appeared as darker red in the combination of satellite images. As these evergreen forest types had similar spectral characteristics, images covering the coast and coastal plains were classified separately from the mountain and inland areas to avoid an erroneous classification of mangroves or palm plantations within the entire study area.

Semi-deciduous forest appeared as fainter dark red, deciduous forest as darker brown and scrub as lighter brown. Irrigated agriculture or wetlands appeared as lighter red or darker pink, and non-irrigated fields or soil as light grey (Fig. 3). Coastal wetland and coffee plantation subclasses were difficult to distinguish from the irrigated agriculture/

Table I. Elevation range of vegetation types within the study area according to INEGI* (2017) classification, which were included in the classification of the general vegetation type.

General vegetation type	INEGI classification	Elevation range (masl)
Evergreen forest (higher elevation)	Fir (*Abies* sp.) forest	2000-2900
	Cloud forest	700-4000
	Pine forest	500-2500
Evergreen forest (lower elevation)	Secondary tall rainforest	200-1400
	Riparian forest	600-700
	Riparian rainforest	0-700
Shade coffee plantation	Permanent agriculture	300-2000
Semi-deciduous forest	Pine-oak forest	800-2500
	Oak-pine forest	400-1900
	Semi-deciduous forest	400-1500
	Oak forest	600-1200
	Fruit tree plantations	10-25
	Palm forest	0-5
Deciduous forest	Deciduous tropical forest	300-1700
	Low spiny forest	0-10
Mangrove	Mangrove	Sea level
Palm plantations	Permanent agriculture	10-50
Scrub	High mountain vegetation	3500-4000
	Temporary agriculture	400-2500
	Herbaceous vegetation	550-850
	Savannah	30-800
	Cleared vegetation	50-250
Short vegetation	Irrigated agriculture	5-700
	Coastal dune vegetation	Sea level
	Coastal wetland (Tular)	Sea level
	Coastal wetland (Popal)	Sea level
Grassland/seasonal agriculture	Grassland	0-1000
	Temporary agriculture	0-900

*Instituto Nacional de Estadística y Geografía.

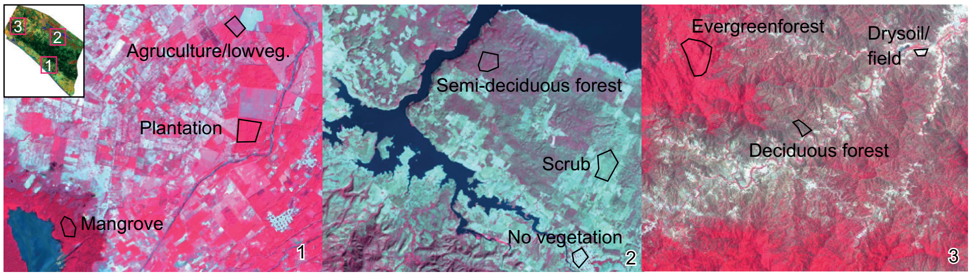

Fig. 3. Examples of vegetation types used for classification in the combination of the green, red, and infrared bands of the satellite images in the (1) coast, (2) central depression, and (3) Sierra Madre regions of Chiapas, Mexico.

short vegetation and evergreen forest classes in the satellite images. Therefore, INEGI series 6 vegetation classifications (INEGI, 2017) corresponding to these vegetation types were used to determine the spatial extent of these subclasses (Table I). Validation of the 2020 vegetation classes was done using 967 reference points randomly placed within the study area. The vegetation classification corresponding to each of these points was compared with vegetation types in higher resolution Google Earth images captured during the dry season from 2017 to 2020. Errors of commission and omission were calculated in a confusion matrix of these validation points (Table III).

2.4 Estimation of evapotranspiration

Various methods have been developed to estimate ET from specific vegetation types to ET at a regional scale (Fisher et al., 2011). The purpose of estimating ET in this study was not to determine the most accurate values for each vegetation type, but rather to determine the processes that have occurred in the study region which may be influencing ET, and as a result, atmospheric water vapor and orographic precipitation in the Sierra Madre. These included changes in temperature, vegetation types and cover, and seasonal changes in leaf cover which is largely influenced by rainfall patterns (Gómez-Mendoza et al., 2008).

Table II. Areas of vegetation types in 1990 and 2020 within the three physiographic regions of the study area (central depression, Sierra Madre, coast), and these three regions together (Pacific Chiapas). The percent of regional area of each land cover is shown next to the area values.

Vegetation type	Year	Area (in ha) and percent (between parentheses) of each vegetation type			
		Central depression	Sierra Madre	Coast	Pacific Chiapas
Evergreen forest	1990	43 663 (3)	328 565 (60)	152 917 (17)	525 145 (19)
	2020	708 66 (6)	351 099 (64)	172 090 (19)	594 055 (22)
Semi-deciduous forest	1990	238 366 (19)	128 683 (24)	144 230 (16)	511 279 (19)
	2020	251 561 (20)	121 921 (22)	187 219 (21)	560 701 (21)
Mangrove	1990	0	0	28 549 (3)	28 549 (1)
	2020	0	0	36 958 (4)	36 958 (1)
Palm plantations	1990	0	0	0	0
	2020	0	0	7152 (1)	7152 (<1)
Deciduous forest	1990	331 660 (26)	29 575 (5)	15 932 (2)	377 167 (14)
	2020	258 537 (20)	15 275 (3)	21 178 (2)	294 990 (11)
Scrub	1990	413 594 (32)	13 193 (2)	73 593 (8)	500 380 (18)
	2020	453 043 (35)	36 996 (7)	144 389 (16)	634 428 (23)
Agriculture/short vegetation/wetland	1990	31 898 (2)	23 136 (4)	214 166 (24)	269 200 (10)
	2020	13 837 (1)	6155 (1)	116 486 (13)	136 478 (5)
Grassland/seasonal agriculture	1990	168 002 (13)	15 914 (3)	222 593 (25)	406 509 (15)
	2020	185 263 (14)	10 137 (2)	149 174 (17)	344 574 (13)
No vegetation	1990	5062 (<1)	897 (<1)	6458 (1)	12 417 (<1)
	2020	5828 (<1)	928 (<1)	16 321 (2)	23 077 (1)
Water	1990	50 753 (4)	0	27 839 (3)	78 592 (3)
	2020	43 723 (3)	0	30 129 (3)	73 852 (3)

Table III. Confusion matrix of 967 points comparing the vegetation types classified from the 2020 Landsat images (Classification) with the validation in Google Earth (Reference).

Classification	Reference										
	E	SD	D	Scrub	SV	Grass	No-V	Man	Palm	Total	Error of commission (%)
E	159	5	0	5	4	0	0	0	17	190	16.3
SD	11	120	0	11	8	1	0	7	8	166	27.7
D	0	11	61	12	0	2	0	0	0	86	29.1
Scrub	0	8	3	170	1	24	2	1	1	210	19.1
SV	2	2	0	3	93	1	0	3	2	106	12.3
Grass	0	1	0	8	1	126	1	0	0	137	8.0
No-V	0	0	0	0	2	0	9	3	0	14	35.7
Man	0	0	0	0	0	0	0	40	0	40	0
Palm	0	0	0	0	0	0	0	0	18	18	0
Total	172	147	64	209	109	154	12	54	46	967	
Error of omission (%)	7.6	18.4	4.7	18.7	14.7	18.2	25.0	25.9	60.9		

E: evergreen forest; SD: semi-deciduous forest; D: deciduous forest; SV: irrigated agriculture/short vegetation; Grass: grassland or seasonal agriculture ; No-V: no vegetation; Man: mangrove; Palm: palm plantation.

Potential ET (PET) is a calculation of the potential amount of water vapor re-entering the atmosphere through ET from the land surface and plants (Xiang et al., 2020). This is based on mainly climatic variables, whereas actual ET is also influenced by vegetation characteristics (Allen et al., 1998). To estimate actual ET in the study area, a method incorporating PET calculations with regional vegetation index values was used (Glenn et al., 2011). This method has been used in other tropical mountain environments (Ramón-Reinozo et al., 2019).

2.4.1 Step 1

We first determined the most appropriate PET calculation method to use. The Penman Monteith (PM) method is often used as the standard to calculate PET but this requires a larger number of environmental data inputs which are not available in most weather stations in Chiapas. Previous analysis comparing the results of PET methods requiring data which are available from all stations in Chiapas with the PM method was done using data from seven weather stations of the automatic weather stations (EMAS, for their acronym in Spanish) located within or near the study area (Table S-V) (Conagua, 2020). These stations collected all the variables required for the comparisons of methods. On average, the Turc method (Turc, 1961) produced values closest to the PM value, especially in the mountain areas (Table S-V), therefore this method was chosen to calculate regional PET.

2.4.2 Step 2

PET was calculated with data from 49 weather stations within the study area. Estimations of temperature at three additional locations, based on temperatures or interpolations of temperatures recorded at nearby weather stations at similar elevations in the Sierra Madre (El Triunfo, El Porvenir; Table S-I) were also included to produce a more accurate interpolation of PET at higher elevation areas (Sierra Madre 1, 2, and 3; Table S-I). The average long-term values of T_{min}, T_{mean}, and T_{max} were calculated for each station using the value of the least squares regression line at the years 1990, 2005, and 2020. Values were calculated for these years for the same seasons as the temperature trend data: dry-cool representing the wet to dry transition season, dry-hot representing the dry season, and the wet season. PET values calculated for these years and seasons corresponded with the vegetation image layers created (described in the next steps). Raster layers of PET were created using the TIN method in QGIS.

2.4.3 Step 3

The Normalized Difference Vegetation Index (NDVI) was used as vegetation index to include vegetation characteristics in the ET estimation. Satellite images from the transition, dry, and wet seasons captured within three years of 1990, 2005, and 2020 were used to create the NDVI images (Table S-IV).

2.4.4 Step 4

A second VI formula was used to standardize the images. In the NDVI images, the most similar vegetation cover to the reference vegetation used to represent conditions where PET would be equal to actual ET was irrigated agriculture (mainly sugar cane in the Coast region) (Aguilar-Rivera et al., 2012), which had an average NDVI value of 0.82. Therefore, this value was used as the NDVI reference value ($NDVI_{ref}$) so that PET would be representative of the estimation of ET in this vegetation type. Denser vegetation types such as evergreen forest would have a higher estimate of ET and seasonal leaf producing vegetation types such as scrub, fields or deciduous forest during the dry season would have a lower estimate. This is representative of the natural conditions in similar mountain regions (Holwerda et al., 2013). $NDVI_{min}$ is the lowest NDVI value in the image. Zero was used for this value.

$$VI = 1-\left(NDVI_{ref}-NDVI\right)/\left(NDVI_{ref}-NDVI_{min}\right) \quad (1)$$

2.4.5 Step 5

Estimation of daily ET was then done by multiplying the PET layer obtained from the Turc calculation (step 2) and the Vegetation Index (VI) layer (step 4), which replaces the standard crop coefficient in agricultural ET estimations in order to represent natural vegetation types (Glenn et al., 2011).

$$ET = PET \times VI \quad (2)$$

INEGI series 6 polygons corresponding to the vegetation classes in this study (Table I) were used to separate ET estimations by vegetation type from the raster layers of the regional ET estimations. These raster cuts were used to estimate the mean and standard deviation of ET for each vegetation type (Table IV).

2.5 Local climate and vegetation change relations

O'Brien (1998) determined that local temperature trends were related to a higher degree with forest cover change within a radius of between 0.5 and 3 km from weather stations in the Lacandon rainforest in Chiapas, with the relationship less evident as radius sizes increased or decreased from this range. Therefore, in our study, changes in forest cover and NDVI between 1990 and 2020 during the dry season were calculated within a 2 km radius of each station where there was a significant T_{mean} trend. At these locations, the correlation between forest cover

Table IV. Estimations and standard deviations of evapotranspiration (ET) (mm/day) from land cover types in 1990 and 2020 during the transition from wet to dry, dry, and wet seasons.

Land cover types	1990 transition	1990 dry	1990 wet	2020 transition	2020 dry	2020 wet
High elevation evergreen	3.22 ± 0.52	3.86 ± 0.87	3.97 ± 0.92	3.04 ± 0.54	3.87 ± 0.77	3.54 ± 1.05
Low elevation evergreen	3.24 ± 0.55	3.69 ± 0.92	4.10 ± 0.75	3.12 ± 0.51	3.84 ± 0.84	3.89 ± 0.88
Semi-evergreen forest	2.88 ± 0.59	3.02 ± 0.77	4.05 ± 0.86	3.02 ± 0.55	3.39 ± 0.85	4.05 ± 0.88
Shade coffee plantation	3.52 ± 0.47	4.10 ± 0.72	4.01 ± 0.62	3.48 ± 0.43	4.26 ± 0.58	3.95 ± 0.94
Mangrove	3.67 ± 0.74	3.93 ± 0.94	4.05 ± 1.01	3.75 ± 0.66	4.50 ± 0.93	4.12 ± 0.75
Deciduous forest	2.36 ± 0.60	2.26 ± 0.56	4.02 ± 0.82	2.84 ± 0.59	2.95 ± 0.76	4.33 ± 0.80
Scrub	2.53 ± 0.68	2.63 ± 0.86	3.93 ± 0.75	2.65 ± 0.62	2.91 ± 0.86	3.99 ± 0.84
Coastal wetland	3.48 ± 0.51	3.43 ± 1.06	3.93 ± 0.66	3.27 ± 0.58	4.36 ± 0.77	4.29 ± 0.78
Irrigated agriculture	3.12 ± 0.84	2.94 ± 1.03	4.03 ± 0.57	3.12 ± 0.74	3.45 ± 1.10	3.98 ± 0.89
Grassland or seasonal agriculture	2.28 ± 0.61	1.99 ± 0.51	3.71 ± 0.84	2.28 ± 0.61	2.39 ± 0.72	4.01 ± 0.78
Oil palm plantation				3.76 ± 0.60	4.38 ± 0.92	4.76 ± 0.68

(evergreen, semi-deciduous, and deciduous) and NDVI changes with temperature change was tested using Spearman's correlation test.

3. Results

3.1 Temperature trends and changes

The average T_{min} in the Sierra Madre increased from 1990 to 2016 in all three seasons. In the dry-cool season T_{min} increased by 0.2 ± 2.2 ºC, in the dry-hot season by 0.4 ± 1.7 ºC, and in the wet season by 0.5 ± 1.9 ºC. During the same period, T_{max} decreased during the dry-cool season by 1.8 ± 1.2 ºC, in the dry-hot season by 1.2 ± 1.3 ºC, and in the wet season by 1.9 ± 1.3 ºC. The average T_{mean} also decreased during the dry-cool season by 0.8 ± 1.4 ºC, 0.2 ± 1.3 ºC during the dry-hot season, and 1.9 ± 1.3 ºC during the wet season.

In the lower elevation regions, there was a similar pattern with increases in T_{min} during the dry-cool (coast: 1.1 ± 1.23 ^{o} C), dry-hot (coast 1.3 ± 1.1 ºC; central depression: 0.6 ± 1.6 ºC), and wet seasons (coast: 1.5 ± 1.1 ^{o} C; central depression: 0.7 ± 1.8 ºC). The exception was the 0.5 ± 1.6 ^{o} C decrease in T_{min} during the dry-cool season in the central depression. There was also a similar pattern to the Sierra Madre in average T_{max} change with decreases in the lower elevation regions during the dry-cool (central depression: 1.6 ± 1.6 ºC), dry-hot (coast: 0.3 ± 1.1 ºC; central depression: 0.4 ± 1.9 ºC), and wet seasons (coast: 0.4 ± 1.1 ºC; central depression: 1.0 ± 1.4 ºC). There was no change in average T_{max} during the dry-cool period in the coast region.

Within Pacific Chiapas, there were 48 significant trends (Mann-Kendall $p < 0.05$) determined for T_{mean} between 1990 and 2016 during the three seasons. Of these, 25 were positive (warmer) trends and 23 were negative (cooler) trends (Fig. 4, Table S-VI). Seventeen of these significant trends in temperature were from changes of 2.5 ºC or greater. Of these, five were cooler trends and 12 were warmer. Of the 10 significant temperature trends shown in the Sierra Madre, only one was warmer during the dry-hot season.

Where data were available between 1960 and 2016, five significant earlier-period (1960-1989) trends contrasted in direction (cooler/warmer or reverse) with later- period (1990-2016) trends at the same weather station. All significant 1990-2016 temperature trends (almost all warmer) in the coast were also significant during the longer 1960-2016 period, whereas significant cooler 1990-2016 trends in the Sierra Madre were not significant during the period since 1960 (Table S-VII).

3.2 Rainfall trends and changes

There was little change in monthly rainfall in the Sierra Madre during most of the dry season from January until April. In May, which is typically at the end of the dry season, rainfall increased greatly, and this trend continued during the wet months from June until September. At the end of the wet season in October, areas within the El Triunfo and Volcán Tacaná biosphere reserves in the Sierra Madre showed dryer trends and La Sepultura, Frailescana, and the southeast region of El Triunfo, wetter trends. The months of the early dry season in November and December had average rainfall decreases between 1990 and 2016 (Fig. 5). There was a similar, but less extreme pattern of regional averages of monthly rainfall changes in the lower elevation regions, however the largest increases in rainfall occurred at the end of the wet season during the month of October (104 ± 117 mm) in the coast region (Figs. 5 and S-1).

Twenty-one significant monthly rainfall trends (Mann-Kendall $p < 0.05$) were determined within Pacific Chiapas. All were positive (wetter) and occurred during the months from the end of the dry season/beginning of the wet season in May until the end of the wet season in October. There were negative (dryer) trends recorded at some of the weather stations within the study area, however these were non-significant. Many of the significant trends were registered within the Sierra Madre or coastal foothills of the Sierra below 1000 m, and values of changes in monthly rainfall ranged from 110 to 650 mm. The greatest increases in monthly rainfall occurred in some of the coastal areas during the months of June and September, and in the Sierra Madre each month from June to October (Table S-III). Of these, only one significant rainfall trend was also significant during the 57-yr period from 1960-2016 at the Metapa de Domínguez weather station in the coast region, with a wetter trend for the month of September (Fig. 6, Table S-VII).

The average wet season began 7.5 ± 10.6 days earlier between 1990 and 2016 in the Sierra Madre,

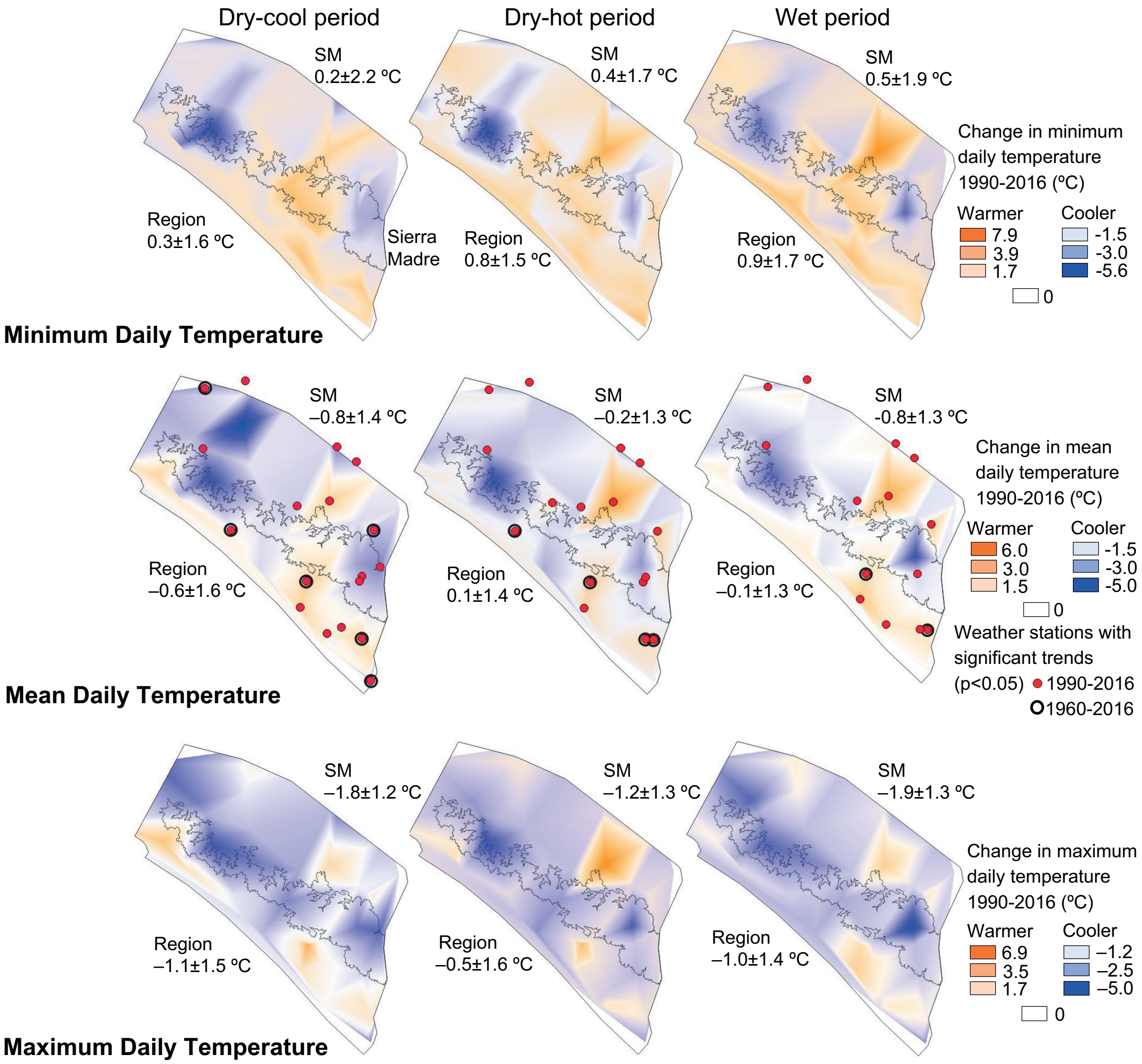

Fig. 4. Average daily temperature change between 1990 and 2016 in the central depression, Sierra Madre, and coast regions of Chiapas, Mexico. Cooler temperature changes are shown in blue and warmer changes in orange. Red points indicate locations of weather stations with significant trends in average daily temperature. The mean and standard deviation of temperature changes within the study area are written below "Region" on the map. Mean and standard deviation within the Sierra Madre (SM) region are written below "SM".

which corresponds to the wetter trend in rainfall during May. The average end of the wet season was also earlier by 4.9 ± 8.4 days, due to dryer trends in October in some parts of the Sierra Madre. On average, the length of the wet season increased by 2.7 ± 13.6 days, although this varied greatly with the central portion of the Sierra Madre increasing, and the southeast portion near to Volcán Tacaná decreasing in length (Fig. 7). The average wet season also began earlier in the lower elevation regions (coast: 6.2 ± 13.2 days; central depression: 7.8 ± 15.1 days) but, in contrast to the Sierra Madre, ended later (coast: 1.1 ± 9.4 days; central depression: 4.2 ± 10.5 days).

3.3 Changes in vegetation types and evapotranspiration

The difficulty in determining boundaries between vegetation types with similar characteristics is

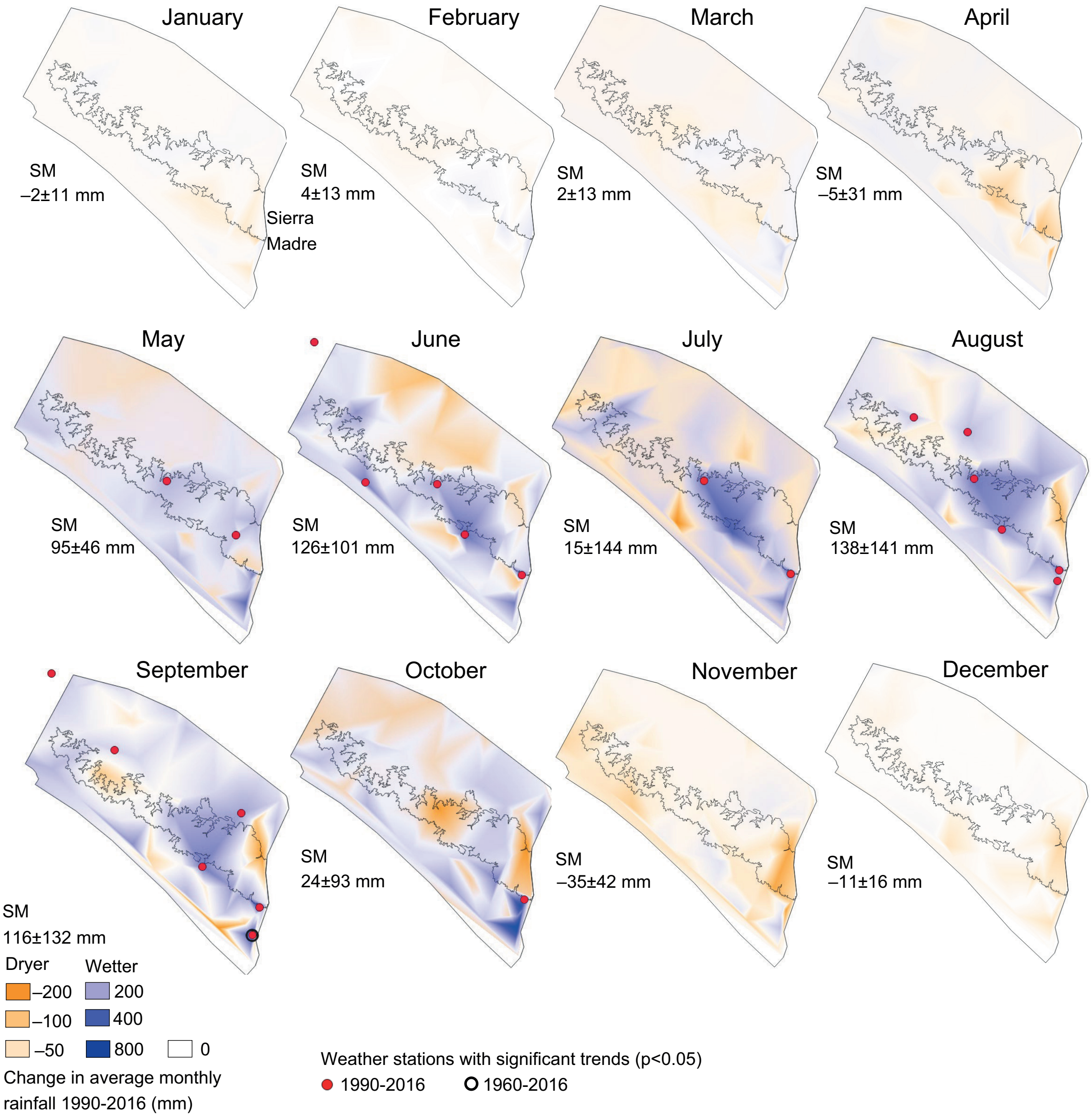

Fig. 5. Changes in monthly rainfall between 1990 and 2016 in the central depression, Sierra Madre, and coast regions of Chiapas, Mexico. Wetter changes are shown in blue and dryer changes in orange. Red points indicate locations of weather stations with significant trends in monthly rainfall. The mean and standard deviation of monthly rainfall changes within the Sierra Madre (SM) region are written below "SM" on the map.

shown in the results of the confusion matrix of the vegetation classification validation (Table III). There was an overclassification of evergreen forest within the palm plantations and mangrove types due to the similarities of these forests, especially with the 30 m^2 resolution of Landsat images. There was also a higher overlap in classification of deciduous vegetation with gradients between types. The overall accuracy of the 2020 vegetation classification was 82%.

Between 1990 and 2020, the combined area of evergreen and semi-evergreen forest types (cloud forest, rainforest, oak, pine and other coniferous forests, fruit tree, palm plantations, and mangroves) increased in all three regions. In the central depression, these

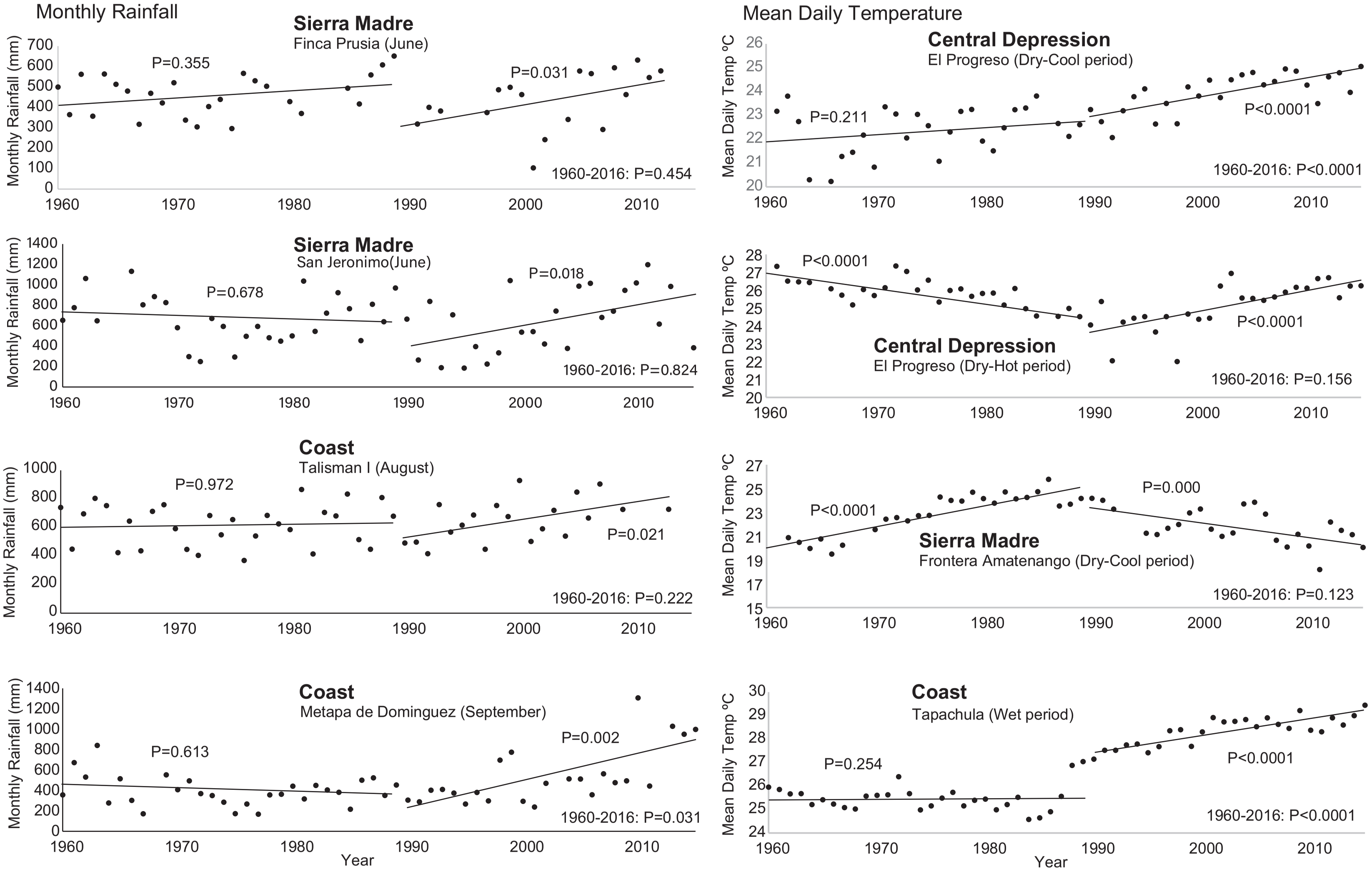

Fig. 6. Trends in monthly rainfall and mean daily temperature during the periods 1960-1989 and 1990-2016 for select weather stations in the central depression, Sierra Madre, and coast regions of Chiapas, Mexico.

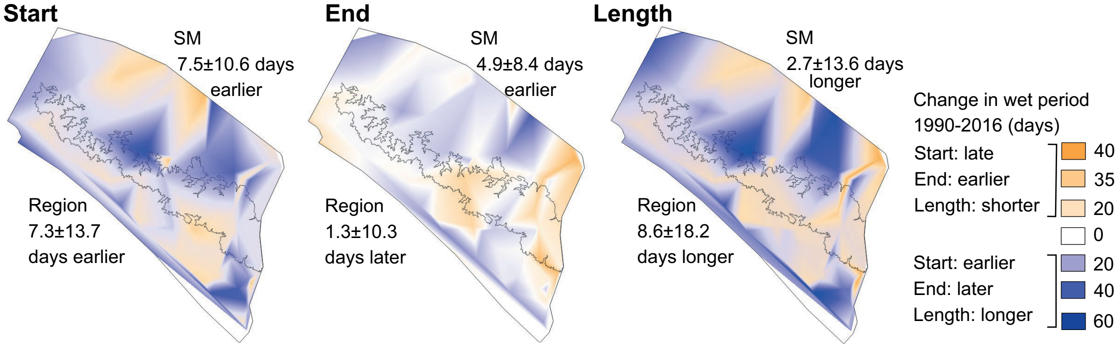

Fig. 7. Changes in the number of days between 1990 and 2016 in the start, end and course of the wet season. The mean and standard deviation of changes in days of the start, end, and course of the wet season within the entire study area (Pacific Chiapas) are written below "Region" on the map. The mean and standard deviation within the Sierra Madre (SM) region are written below "SM".

forest types increased by 14%, in the Sierra Madre by 3%, and in the coast by 22%; however, with the inclusion of deciduous forest as part of the overall forest areas, forest cover decreased from 1990 to 2020 in the central depression. Deciduous forest has similar characteristics than the scrub type and the boundary is not always clear in the satellite images or in the field, as there can be a gradient between deciduous tree cover and shrubby savanna. The area of scrub vegetation and grassland/temporary agriculture can also change throughout the year, as large areas of land which had grown to become scrublands are burned each year to clear land for cultivation. The combined land cover of deciduous forest or scrub decreased by 5% in the central depression but increased by 22% in the Sierra Madre and 85% in the coast (Fig. 8, Table II).

These changes in vegetation types created conditions for larger areas of leaf-covered forests in the transition and dry seasons in all regions. Leaf producing forest cover also increased in the Sierra Madre and coast regions during the wet season, but not in the central depression, where the inclusion of deciduous forests (which produce leaves in the wet season) reduced the overall area of leaf-producing forest (Fig. 9). These seasonal and long-term changes can also be seen in the average values of the NDVI (Table S-VIII), which increased in all regions for all three seasons between the 1990 and 2020 images. These increases during the wet season in the central depression could be due to denser growth of the scrub vegetation type or a lower NDVI value at the end of the wet season (November) in the 1990 image compared to the earlier date of the image captured in the 2020 wet season (August). Most of the comparisons in the period 1990-2020 (30 years) were done between similar times of the year, but there were no Landsat images during the 1987-1993 wet

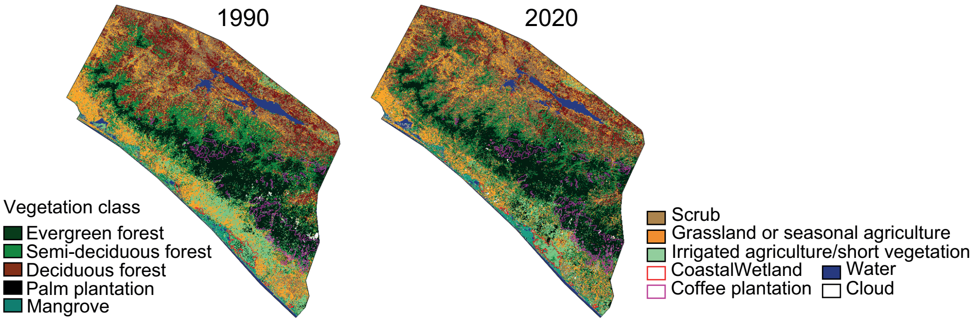

Fig. 8. Land cover in 1990 and 2020 in the Pacific regions of Chiapas, Mexico.

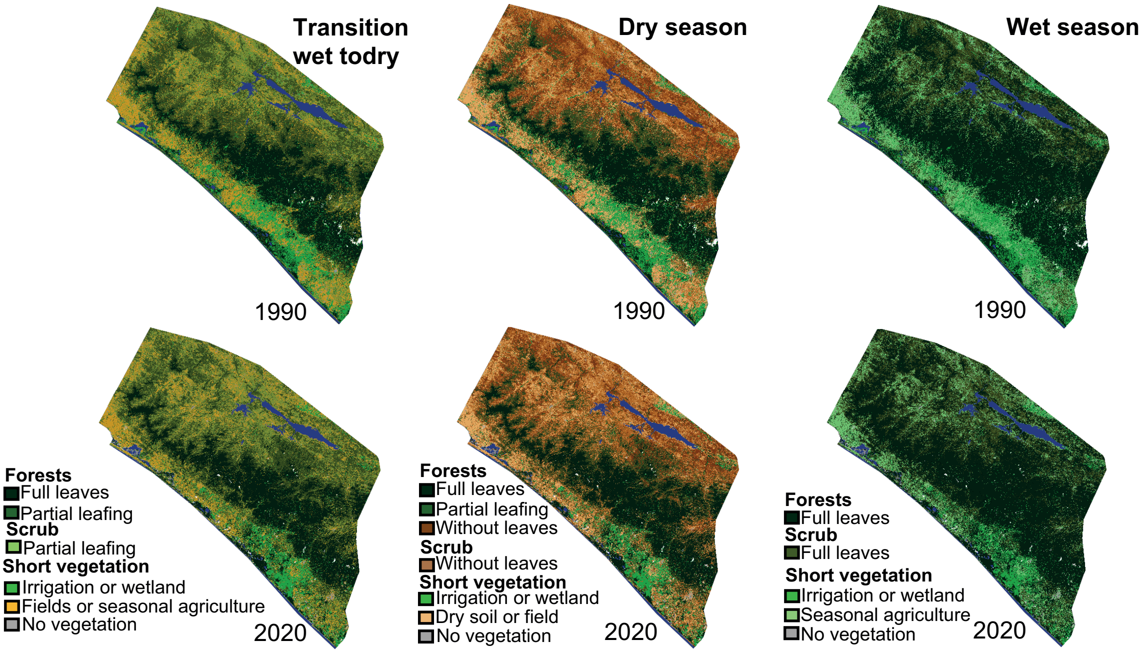

Fig. 9. Seasonal vegetation characteristics of the transition from wet to dry, dry, and wet seasons in 1990 and 2020.

season without large amounts of cloud cover, so the use of an image captured in November was the best option available.

This vegetation index (live green vegetation density) increases, which theoretically would create conditions for greater ET, were offset by decreases in PET between 1990 and 2016, during all three seasons. These decreases were due to the overall regional temperature changes, which were on average warming T_{min} and cooling T_{max}. Overall decreases in PET were outweighed by the increases in vegetation index and estimated ET increased between 1990 and 2020 from 2.70 to 2.83 mm/day in the transition season, 2.83 to 3.16 mm/day in the dry season, and without change in the wet season. However, there was variation in the direction of changes between these years with an increase in estimated ET between 1990 and 2005 and a decrease between 2005 and 2020, during the transition season. ET decreased slightly between 1990 and 2005 and then increased between 2005 and 2020 during the dry and wet seasons (Fig. 10).

During the 2020 dry season, the highest amounts of ET were estimated for the coastal low-elevation evergreen vegetation types: mangrove, palm plantation, and coastal wetland (Table IV). These were followed by mountain evergreen vegetation types: shade coffee, high elevation evergreen forest, low elevation evergreen forest, and lower elevation irrigated agriculture. Lower ET were estimated for deciduous or dry vegetation types: deciduous forest, scrub, and non-irrigated land. During the wet season, when all vegetation types produce green leaves, the denser, low-elevation vegetation, including deciduous forest had the highest estimation of ET. ET decreased with vegetation types at higher, cooler elevations in the Sierra Madre. During the transition season, the highest amounts of ET were observed in the lower-elevation evergreen vegetation types, with ET decreasing in the higher-elevation evergreen types and the lowest amounts in the deciduous vegetation types as leaves dry and fall.

During the dry season, estimates of ET increased from 1990 to 2020 in all vegetation types, except the high-elevation evergreen forest where there was no change (Table IV). During the wet season, ET only increased in the lower-elevation vegetation types between 1990 and 2020 and decreased in the mid- to higher-elevation forest and coffee plantation vegetation. There was little change in the scrub type. Lower-elevation vegetation types also had increases in ET

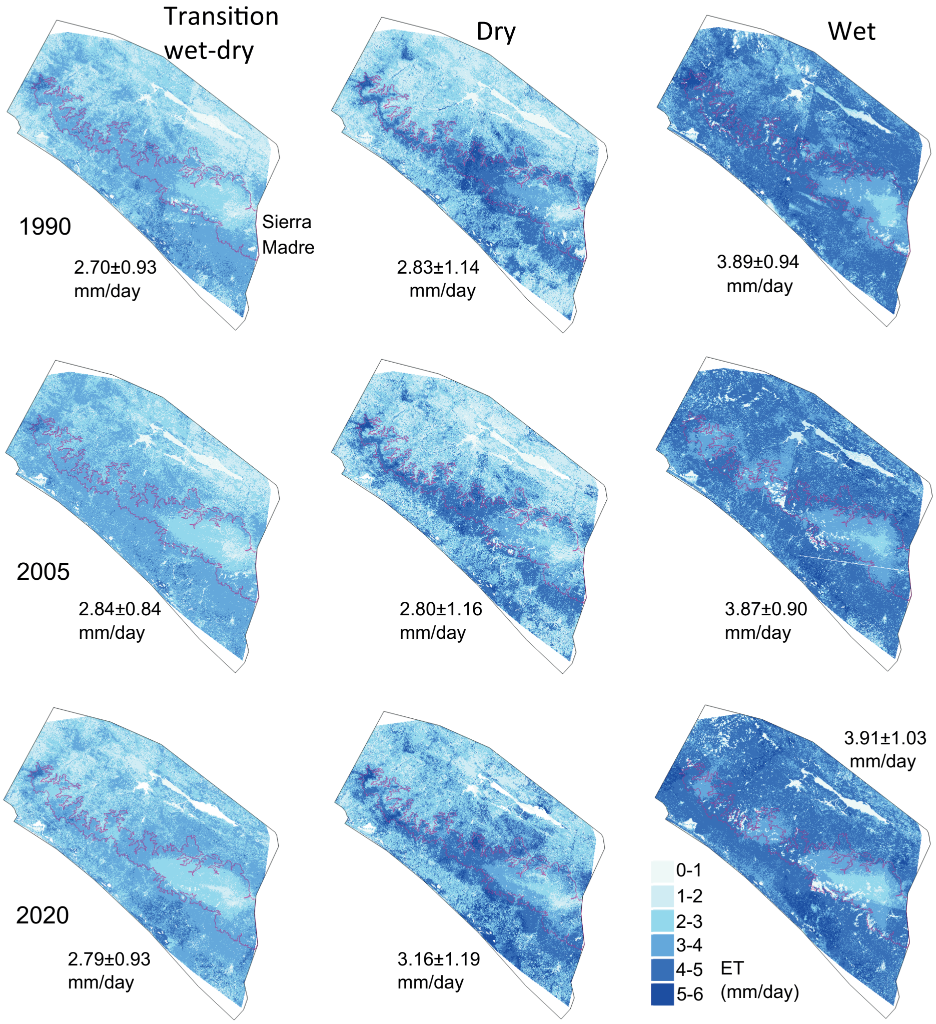

Fig. 10. Estimates of evapotranspiration in the transition from wet to dry, dry, and wet seasons of 1990, 2005, and 2020 in the Pacific regions of Chiapas, Mexico. The mean and standard deviation of evapotranspiration within the study area is written next to each image.

during the transition season, except for the coastal wetland which had a decrease. ET also increased in the mid-elevation semi-evergreen forest during this season. The evergreen forest types and coffee plantations in the Sierra Madre had decreases in ET.

3.4 Relation between local climate trends and vegetation changes

There was no clear correlation between vegetation changes within a 2-km radius of weather stations where there was a significant trend in T_{mean}, and changes in T_{mean} at these locations. This was the case for both changes in NDVI ($p = 0.88$), and percent change in forest cover ($p = 0.85$). Some areas which had experienced reductions in forest cover between 1990 and 2020 had positive trends of T_{mean}, whereas others had negative trends. Likewise, areas that experienced gains in forest cover had either positive or negative T_{mean} trends.

4. Discussion

4.1 Comparisons between 1960-2016, 1990-2016 trends and large-scale climatic influences

The generally wetter wet seasons and dryer dry seasons during the 1990-2016 period in all three regions were consistent with global trends in precipitation (Murray-Tortarolo et al., 2017) during a similar time period (1980-2005). Murray-Tortarolo et al. (2017) discussed that these trends may have been the result of global oceanic (La Niña years) and atmospheric (1991 Mt. Pinatubo eruption) conditions during the late 1980s and early 1990s, which lowered global precipitation during these years, and the beginning of global warming influences. However, the relation between rainfall and La Niña are variable within Mexico and are generally associated with higher rainfall in Southern Mexico (Bravo-Cabrera et al., 2017). The lack of significant trends in rainfall in Pacific Chiapas during a longer time period (1960-2016) at most weather stations where there was a wetter trend during the 1990-2016 period, was also consistent with global trends (Murray-Tortarolo et al., 2017), except for an area of the Coast (Metapa de Domínguez during September; Fig. 5, Table S-VII) where there was an extended 57-yr significant wetter trend.

Significant cooler trends between 1990-2016 in the Sierra Madre were not significant since 1960, which contrasted with the longer continuation of significant warmer trends in the coast. Increasing trends in rainfall since 1990 in the mountain region may be related to the cooler trends during 1990-2016 (mostly due to decreases in T_{max}; Fig. 4) at higher elevations because of greater cloud cover.

Regional climatic trends between 1990 and 2016 in Pacific Chiapas were consistent with those attributed to the effects of long-term trends in the Pacific Decadal Oscillation (PDO) in southern Mexico (Méndez-González et al., 2010). During this period, the PDO index showed a negative trend from a positive phase in the 1990s to a negative phase in the 2000s (NOAA, 2020b). Méndez-González et al. (2010) determined that from 1950-2007, negative periods of the PDO have been associated with higher summer precipitation, cooler summer T_{max}, and warmer T_{min} in southern Mexico. These trends were determined on average for the study region, although not consistently for all weather stations, especially in some parts of the coast, which had increases in both T_{min} and T_{max} (Fig. 4).

Summer rainfall in Chiapas is also strongly influenced by the ITCZ bringing moisture from the Caribbean Sea and Gulf of Mexico. SSTs have increased both in the Gulf of Mexico and the Caribbean since 1975 (Lluch-Cota et al., 2013), and higher amounts of evaporation from a warmer surface may increase atmospheric moisture and intensify downwind rainfall (Brito-Castillo, 2012). Increases in rainfall often indicate cloudier conditions and this can affect regional temperatures (Englehart and Douglas, 2005), effects consistent with the determined regional trends. Increased cloud cover blocks incoming day time solar radiation, lowering T_{max}, whereas nighttime T_{min} are increased by the insulation of cloud cover, which reemits longwave radiation back to the ground. The predicted climate effects of increases in global atmospheric CO_2 from 1990 amounts described by Liverman and O'Brien (1991) for the southern Pacific region of Mexico were also consistent with those determined by this study for rainfall patterns, although the predicted temperature increases were only determined on average for T_{min}.

4.2 Relations between land use change, vegetation and climate trends

Between 1970 and 2000, Chiapas experienced large amounts of deforestation (Richter, 2000; Solórzano et al., 2003). However, reviews published in the years after 2000 began to discuss a possible change in the rate of deforestation and beginning of reforestation in parts of Mesoamerica (Bray, 2009). Evidence supporting this prediction may be shown by Vaca et al. (2012), who reported a decreased annual rate of deforestation between the periods of 1990-2000 and 2000-2006 in the dry tropical forests of the central depression of Chiapas. Bonilla-Moheno and Aide (2020) also reported an increase in forest cover in the lower elevation, inland portion of the Sierra Madre between 2001-2014, which was consistent with what was determined in this study.

The abandonment of agricultural areas during increased urban migration, and the large scale of land which had already been deforested by 1990 may have contributed to increased forest cover in the areas adjacent to the Sierra Madre between 1990 and 2020 (Bonilla-Moheno and Aide, 2020). Trends of increasing rainfall in these regions may also have been influential for regeneration of forests in abandoned agricultural areas, even when there were large variations in rainfall between years (Martínez-Ramos et al., 2018). The steep and less accessible Sierra Madre region was by far the most forested of the study area, with very little overall change in forest cover. The establishment of biosphere reserves beginning in 1990, and programs such as Payment for Hydrological Environmental Services within communities of the Sierra Madre influenced the slower changes in this region (Cano-Díaz et al., 2015).

Large differences in species composition can exist between vegetation types which are difficult to distinguish remotely, such as regenerating deciduous forests and native scrub ecosystems (Gordillo-Ruiz et al., 2020). Species composition, diversity and succession stage can influence differences in vegetation responses to climate trends and ET (Ballinas et al., 2015; Sakschewski et al., 2016). Additionally, topography, vegetation cover, and soil characteristics of landscapes can influence water availability from rainfall (Ponette-González et al., 2010; Schwartz et al., 2019); and vegetation can have physiological responses to changes in climate allowing them to regulate ET (Massmann et al., 2019). These physiographic and physiological characteristics indicate a limitation of the modeling we used to estimate ET. We hope our regional focus inspires further field-based studies of ET in the specific vegetation types we have included. However, the use of local climatic data and remote sensing, which showed increases in dense vegetation cover and regional estimations of ET between 1990 and 2020, were useful to understand the contribution of vegetation changes to the climate of Pacific Chiapas, in particular the coastal mountains.

Regional increases in forest vegetation and ET may have contributed to positive climatic feedback, which combined with the influences of increasing SST in the east coast of Mexico, a negative phase of the PDO in the west coast, and increasing atmospheric CO_2, produced larger positive trends in rainfall during the late dry and wet seasons. Estimates of ET mainly decreased in the mountain evergreen forests between 1990 and 2020 (Table IV) due to decreasing trends in temperature (Fig. 4). However, there were overall increases in estimated regional ET, due to increases in the density of leaf producing vegetation cover and some regional temperature increases, especially in the lower elevation regions (Fig. 10, Table S-VIII). There is also a strong relationship between the onset of the wet season and the production of leaves in deciduous and semi-deciduous vegetation in Mexico (Gómez-Mendoza et al., 2008). The earlier trend in the start of the wet season in this region may indicate that leaf production is beginning earlier in the year; also that, along with increases of available soil moisture, it could result in earlier increases in ET, contributing to higher atmospheric moisture and higher orographic rainfall in the Sierra Madre.

Increases in semi-deciduous and evergreen forest cover between 1990 and 2020 may cause greater regional latent heat flux, decreases in sensible heat flux (Ray et al., 2006a, b), and increases in surface roughness (Spracklen et al., 2018). This may affect heights of orographic cloud cover, which potentially could decrease with these land cover change conditions (Lawton et al., 2001; Fairman et al., 2011), and affect the altitudinal distribution of rainfall (Barradas et al., 2010). The constant burning of regenerating deciduous forest and savannahs for seasonal agriculture in the central depression creates conditions of higher surface albedo, which can negatively affect rainfall (Fuller and Ottke, 2002). This may be another reason for the lower regional increases in rainfall in the central depression in comparison with the much greater forested Sierra Madre region.

At various locations, significant climate trends differed from the overall average regional changes (Figs. 4 and 5; Tables S-III and S- VI). There were no clear relations between local significant temperature or rainfall changes and vegetation changes (forest cover or NDVI). This suggests that the regional climate changes determined were influenced to a greater extent by long term atmospheric and oceanic processes and regional vegetation changes. Local differences in temperature and rainfall patterns may be due to topography, air flow patterns, and the orographic nature of precipitation in this mountainous region, as in other parts of Mesoamerica (Barradas et al., 2010; Maldonado et al., 2018).

Many of the ocean influence patterns are cyclical at a time scale greater than the study period of 27 years (Fuentes-Franco et al., 2015). Therefore, the climate trends and patterns determined in this study may change as trends change in the large-scale climatic influences which affect Chiapas (Aguilar et al., 2005). However, if increasing vegetation cover trends continue in this region, they may moderate future climate cycles in the Sierra Madre (Lawton et al., 2001; Bonan, 2008).

5. Conclusion

Regional 1990-2016 climate trends within Pacific Chiapas included increases in T_{min}, decreases in T_{max}, an earlier shift in the wet season, and greater amounts of rainfall within this season. All significant temperature trends continued from 1960-2016 in the coast region but less so in the central depression and did not in the Sierra Madre. Only one significant rainfall (wetter) trend continued during this 57-yr period, in an area of the coast. The more recent (1990-2016) trends occurred during a period of change in ocean and atmospheric climatic influences in the region, including a negative trend in the PDO index, warming SST in the Gulf of Mexico and the Caribbean, and rising amounts of atmospheric CO_2. During the same time period, regional extents of evergreen and semi-evergreen forest types, NDVI values, and estimates of ET increased. These changes may have enhanced the climatic patterns influenced by large-scale processes.

Acknowledgments

We thank the two anonymous reviewers for their helpful comments to improve the article.

The first author received a doctoral scholarship from Conacyt (No. 884660).

References

Aguilar E, Peterson TC, Obando PR, Frutos R, Retana JA, Solera M, Soley J, González-García I, Araujo RM, Rosa-Santos A, Valle VE, Brunet M, Aguilar L, Álvarez L, Bautista M, Castañón C, Herrera L, Ruano E, Sinay JJ, Sánchez E, Hernández-Oviedo GI, Obed F, Salgado JE, Vázquez JL, Baca M, Gutiérrez M, Centella C, Espinosa J, Martínez D, Olmedo B, Ojeda-Espinoza CE, Núñez R, Haylock M, Benavides H, Mayorga R. 2005. Changes in precipitation and temperature extremes in Central America and northern South America, 1961-2003. Journal of Geophysical Research: Atmospheres 110: D23107. https://doi.org/10.1029/2005JD006119

Aguilar-Rivera N, Rodríguez DA, Enríquez V, Castillo A, Herrera S. 2012. The Mexican sugarcane industry: Overview, constraints, current status and long-term trends. Sugar Tech 14: 207-222. https://doi.org/10.1007/s12355-012-0151-3

Ahmad I, Tang D, Wang T, Wang M, Wagan B. 2015. Precipitation trends over time using Mann-Kendall and spearman's rho tests in swat river basin, Pakistan. Advances in Meteorology 2015: 1-15. http://doi.org/10.1155/2015/431860

Allen RG, Pereira LS, Raes D, Smith M. 1998. Crop evapotranspiration. Guidelines for computing crop water requirements. FAO Irrigation and drainage paper 56. Food and Agriculture Organization of the United Nations, Rome, 327 pp. Available at: http://www.fao.org/docrep/X0490E/X0490E00.htm

Ballinas M, Esperón-Rodríguez M, Barradas VL. 2015. Estimating evapotranspiration in the central mountain region of Veracruz, Mexico. Bosque 36: 445-455.

Barradas VL, Cervantes-Pérez J, Ramos-Palacios R, Puchet-Anyul C, Vázquez-Rodríguez P, Granados-Ramírez R. 2010. Meso-scale climate change in the central mountain region of Veracruz State, Mexico. In: Tropical montane cloud forests: Science for conservation and management (Bruijnzeel LA, Scatena FN, Hamilton LS, Eds.). Cambridge University Press, 549-556.

Bonan GB. 2008. Forests and climate change: forcings, feedbacks, and the climate benefits of forests. Science 320: 1444-1449. https://doi:10.1126/science.1155121

Bonilla-Moheno M, Aide TM. 2020. Beyond deforestation: Land cover transitions in Mexico. Agricultural Systems 178: 102734. https://doi.org/10.1016/j.agsy.2019.102734

Bravo-Cabrera JL, Azpra-Romero E, Zarraluqui-Such V, Gay-García C. 2017. Effects of El Niño in Mexico during rainy and dry seasons: An extended treatment. Atmósfera 30: 221-232. https://doi.org/10.20937/atm.2017.30.03.03

Bray DB. 2009. Forest cover dynamics and forest transitions in Mexico and Central America: Towards a "great restoration"? In: Reforesting landscapes: Linking patterns and process (Nagendra H, Southworth J., Eds.). Springer, Dordrecht, 85-120. https://doi.org/10.1007/978-1-4020-9656-3_5

Brito-Castillo L. 2012. Regional pattern of trends in long-term precipitation and stream flow observations: singularities in a changing climate in Mexico. In: Greenhouse gases: Emission, measurement and management (Liu G. Ed.). BoD Books on Demand, Norderstedt, 387-412.

Cano-Díaz VC, Cortina-Villar S, Soto-Pinto L. 2015. La construcción de la acción colectiva en una comunidad del área natural protegida La Frailescana, Chiapas, México. Argumentos 28: 79-96.

Casagrande E, Recanati F, Melià P. 2018. Assessing the influence of vegetation on the water budget of tropical areas. IFAC-PapersOnLine 51: 1-6. https://doi.org/10.1016/j.ifacol.2018.06.190

Castro-Mendoza I, Magdaleno-González R, Cruz-Salinas E, Reynoso-Santos R, López-Báez W. 2016. Balance hídrico de la cuenca Pijijiapan en Chiapas, México. Ingeniería Hidráulica y Ambiental 37: 18-28. http://scielo.sld.cu/pdf/riha/v37n2/riha02216.pdf

Chambers JQ, Artaxo P. 2017. Deforestation size influences rainfall. Nature Climate Change 7: 175-176. https://doi.org/10.1038/nclimate3238

Conagua. 2018. Comisión Nacional del Agua. Available at: https://smn.conagua.gob.mx/es/climatologia/informacion-climatologica/informacion-estadistica-climatologica (accessed on October 22, 2018).

Conagua. 2020. Estaciones meteorológicas automáticas (EMAS). Comisión Nacional del Agua. Available at: https://smn.conagua.gob.mx/es/observando-el-tiempo/estaciones-meteorologicas-automaticas-ema-s (accessed on July 20, 2020).

Durán-Quesada AM, Reboita M, Gimeno L. 2012. Precipitation in tropical America and the associated sources of moisture: A short review. Hydrological Sciences Journal 57: 612-624. https://doi.org/10.1080/02626667.2012.673723

Englehart PJ, Douglas AV. 2005. Changing behavior in the diurnal range of surface air temperatures over Mexico. Geophysical Research Letters 32: L01701. https://doi.org/10.1029/2004GL021139

Fairman JG, Nair US, Christopher SA, Mölg T. 2011. Land use change impacts on regional climate over Kilimanjaro. Journal of Geophysical Research: Atmospheres 116: DO3110. https://doi.org/10.1029/2010JD014712

Fisher JB, Whittaker RJ, Malhi Y. 2011. ET come home: Potential evapotranspiration in geographical ecology. Global Ecology and Biogeography 20: 1-18. https://doi.org/10.1111/j.1466-8238.2010.00578.x

Fuentes-Franco R, Coppola E, Giorgi F, Pavia EG, Diro GT, Graef F. 2015. Inter-annual variability of precipitation over Southern Mexico and Central America and its relationship to sea surface temperature from a set of future projections from CMIP5 GCMs and RegCM4 CORDEX simulations. Climate Dynamics 45: 425-440. https://doi.org/10.1007/s00382-014-2258-6

Fuller DO, Ottke C. 2002. Land cover, rainfall and land-surface albedo in West Africa. Climatic Change 54: 181-204. https://doi.org/10.1023/A:1015730900622

García E. 1974. Distribución de la precipitación en la República Mexicana. Investigaciones Geográficas 5: 7-20.

Glenn EP, Neale CM, Hunsaker DJ, Nagler PL. 2011. Vegetation index-based crop coefficients to estimate evapotranspiration by remote sensing in agricultural and natural ecosystems. Hydrological Processes 25: 4050-4062. https://doi.org/10.1002/hyp.8392

Golicher JD, Ramírez-Marcial N, Levy-Tacher SI. 2006. Correlations between precipitation patterns in southern Mexico and the El Niño sea surface temperature index. Interciencia 31: 80-86.

Gómez-Mendoza L, Galicia L, Cuevas-Fernández ML, Magana V, Gómez G, Palacio-Prieto JL. 2008. Assessing onset and length of greening period in six vegetation types in Oaxaca, Mexico, using NDVI-precipitation relationships. International Journal of Biometeorology 52: 511-520. https://doi:10.1007/s00484-008-0147-6

González-García F, Santana-C E., Barbudo PDJ, Rico-Gray V, Moliner VU. 2017. Diet and feeding behavior of the Horned Guan (*Oreophasis derbianus*) in Mexico. The Wilson Journal of Ornithology 129: 771-782. https://doi.org/10.1676/16-041.1

Gordillo-Ruiz MC, Pérez-Farrera, MÁ, Castillo-Santiago MÁ. 2020. Estructura y composición arbórea del bosque tropical caducifolio secundario en la Depresión Central, Chiapas, México. Madera y Bosques 26: e2632055. https://doi.org/10.21829/myb.2020.2632055

Hewitson BC, Crane RG. 1992. Large-scale atmospheric controls on local precipitation in tropical Mexico. Geophysical Research Letters 19: 1835-1838. https://doi.org/10.1029/92GL01423

Hewitson BC, Crane RG. 1994. Precipitation controls in southern Mexico. In: Neural nets: Applications in geography (Hewitson BC, Crane RG, Eds.). Springer, Dordrecht, 121-143.

Holwerda F, Bruijnzeel LA, Barradas VL, Cervantes J. 2013. The water and energy exchange of a shaded coffee plantation in the lower montane cloud forest zone of central Veracruz, Mexico. Agricultural and Forest Meteorology 173: 1-13. https://doi.org/10.1016/j.agrformet.2012.12.015

INEGI. 2017. Conjunto de datos vectoriales de uso del suelo y vegetación escala 1:250 000, Serie VI. Instituto

Nacional de Estadística y Geografía. Available at: https://www.inegi.org.mx/app/biblioteca/ficha.html?upc=889463173359 (accessed on August 27, 2020).

Jones KW, Brenes CLM, Shinbrot XA, López-Báez W, Rivera-Castañeda A. 2018. The influence of cash and technical assistance on household-level outcomes in payments for hydrological services programs in Chiapas, Mexico. Ecosystem Services 31: 208-218. https://doi.org/10.1016/j.ecoser.2018.04.008

Karmalkar AV, Bradley RS, Diaz HF. 2008. Climate change scenario for Costa Rican montane forests. Geophysical Research Letters 35: 1-5. https://doi.org/10.1029/2008GL033940

Lawton RO, Nair US, Pielke RA, Welch RM. 2001. Climatic impact of tropical lowland deforestation on nearby montane cloud forests. Science 294: 584-587. https://doi.org/10.1126/science.1062459

Lister BC, Garcia A. 2018. Climate-driven declines in arthropod abundance restructure a rainforest food web. Proceedings of the National Academy of Sciences 115: E10397-E10406. https://doi.org/10.1073/pnas.1722477115

Liverman DM, O'Brien KL. 1991. Global warming and climate change in Mexico. Global Environmental Change 1: 351-364. https://doi.org/10.1016/0959-3780(91)90002-B

Lluch-Cota SE, Tripp-Valdéz M, Lluch-Cota DB, Lluch-Belda D, Verbesselt J, Herrera-Cervantes H, Bautista-Romero JJ. 2013. Recent trends in sea surface temperature off Mexico. Atmósfera 26: 537-546. https://doi.org/10.1016/S0187-6236(13)71094-4

Long A, Heath M. 1991. Flora of the El Triunfo biosphere reserve, Chiapas, Mexico. A preliminary floristic inventory and the plant communities of Polygon 1. Anales del Instituto de Biología de la Universidad Nacional Autónoma de México. Serie Botánica 62: 133-172

Maldonado T, Alfaro EJ, Hidalgo HG. 2018. A review of the main drivers and variability of Central America's Climate and seasonal forecast systems. Revista de Biología Tropical 66: S153-S175. https://doi.org/10.15517/RBT.V66I1.33294

Mardero S, Schmook B, Christman Z, Metcalfe SE, de la Barreda-Bautista B. 2019. Recent disruptions in the timing and intensity of precipitation in Calakmul, Mexico. Theoretical and Applied Climatology 140: 129-144. https://doi.org/10.1007/s00704-019-03068-4

Martínez-Ramos M, Balvanera P, Villa FA, Mora F, Maass JM, Méndez SMV. 2018. Effects of long-term inter-annual rainfall variation on the dynamics of regenerative communities during the old-field succession of a neotropical dry forest. Forest Ecology and Management 426: 91-100. https://doi.org/10.1016/j.foreco.2018.04.048

Massmann A, Gentine P, Lin C. 2019. When does vapor pressure deficit drive or reduce evapotranspiration? Journal of Advances in Modeling Earth Systems 11: 3305-3320. https://doi.org/10.1029/2019MS001790

Méndez-González J, Ramírez-Leyva A, Cornejo-Oviedo E, Zárate Lupercio A, Cavazos-Pérez T. 2010. Teleconexiones de la Oscilación Decadal del Pacífico (PDO) a la precipitación y temperatura en México. Investigaciones Geográficas 73: 57-70.

Mitas L, Mitasova H. 1999. Spatial interpolation. In: Geographical information systems: Principles, techniques, management and applications (Longley PA, Goodchild MF, Maguire DJ, Rhind DW, Eds.). John Wiley & Sons, New York, 481-492.

Murray-Tortarolo G, Jaramillo VJ, Maass M, Friedlingstein P, Sitch S. 2017. The decreasing range between dry-and wet-season precipitation over land and its effect on vegetation primary productivity. PLoS ONE 12: e0190304. https://doi.org/10.1371/journal.pone.0190304

NOAA. 2020a. Global Monitoring Laboratory. National Oceanic and Atmospheric Administration. Available at: https://www.esrl.noaa.gov/gmd/ccgg/trends/global.html (accessed on October 12, 2020).

NOAA. 2020b. Physical Science Laboratory. National Oceanic and Atmospheric Administration. Available at: https://psl.noaa.gov/pdo/ (accessed on October 12, 2020).

O'Brien KL. 1998. Tropical deforestation and climate change: What does the record reveal? The Professional Geographer 50: 140-153. https://doi.org/10.1111/0033-0124.00110

Ponette-González, AG, Weathers KC, Curran LM. 2010. Water inputs across a tropical montane landscape in Veracruz, Mexico: Synergistic effects of land cover, rain and fog seasonality, and interannual precipitation variability. Global Change Biology 16: 946-963. https://doi.org/10.1111/j.1365-2486.2009.01985.x

Pounds JA, Fogden MP, Campbell JH. 1999. Biological response to climate change on a tropical mountain. Nature 398: 611-615. https://doi.org/10.1038/19297

Ramón-Reinozo M, Ballari D, Cabrera JJ, Crespo P, Carrillo-Rojas G. 2019. Altitudinal and temporal evapotranspiration dynamics via remote sensing and vegetation index-based modelling over a scarce-monitored, high-altitudinal Andean paramo ecosystem of Southern Ecuador. Environmental Earth Sciences 78: 340. https://doi.org/10.1007/s12665-019-8337-6

Ray DK, Nair US, Lawton RO, Welch RM, Pielke Sr RA. 2006a. Impact of land use on Costa Rican tropical montane cloud forests: Sensitivity of orographic cloud formation to deforestation in the plains. Journal of Geophysical Research: Atmospheres 111: D02108. https://doi.org/10.1029/2005JD006096

Ray DK, Welch RM, Lawton RO, Nair US. 2006b. Dry season clouds and rainfall in northern Central America: Implications for the Mesoamerican Biological Corridor. Global and Planetary Change 54: 150-162. https://doi.org/10.1016/j.gloplacha.2005.09.004

Richter M. 2000. The ecological crisis in Chiapas: Acase study from Central America. Mountain Research and Development 20: 332-339. https://doi.org/10.1659/0276-4741(2000)020[0332:TECICA]2.0.CO;2

Rojas-Soto OR, Sosa V, Ornelas JF. 2012. Forecasting cloud forest in eastern and southern Mexico: conservation insights under future climate change scenarios. Biodiversity and Conservation 21: 2671-2690. https://doi.org/10.1007/s10531-012-0327-x

Sakschewski B, von Bloh W, Boit A, Poorter L, Peña-Claros M, Heinke J, Joshi J, Thonicke K. 2016. Resilience of Amazon forests emerges from plant trait diversity. Nature Climate Change 6: 1032-1036. https://doi.org/10.1038/nclimate3109

Schroth G, Laderach P, Dempewolf J, Philpott S, Haggar J, Eakin H, Castillejos T, García-Moreno J, Soto-Pinto L, Hernández R, Eitzinger A. Ramírez-Villegas J. 2009. Towards a climate change adaptation strategy for coffee communities and ecosystems in the Sierra Madre de Chiapas, Mexico. Mitigation and Adaptation Strategies for Global Change 14: 605-625. https://doi.org/10.1007/s11027-009-9186-5

Schwartz NB, Budsock AM, Uriarte M. 2019. Fragmentation, forest structure, and topography modulate impacts of drought in a tropical forest landscape. Ecology 100: e02677. https://doi.org/10.1002/ecy.2677

Sheil D. 2018. Forests, atmospheric water and an uncertain future: the new biology of the global water cycle. Forest Ecosystems 5: 1-22. https://doi.org/10.1186/s40663-018-0138-y

Solórzano S, Castillo S, Valverde T, Ávila L. 2000. Quetzal abundance in relation to fruit availability in a cloud forest in southeastern Mexico. Biotropica 32: 523-532.

Solórzano S, Castillo-Santiago MA, Navarrete-Gutiérrez DA, Oyama K. 2003. Impacts of the loss of neotropical highland forests on the species distribution: A case study using resplendent quetzal an endangered bird species. Biological Conservation 114: 341-349. https://doi.org/10.1016/S0006-3207(03)00054-5

Spracklen DV, Baker JCA, García-Carreras L, Marsham JH. 2018. The effects of tropical vegetation on rainfall. Annual Review of Environment and Resources 43: 193-218. https://doi.org/10.1146/annurev-environ-102017-030136

Turc L. 1961. Estimation of irrigation water requirements, potential evapotranspiration: A simple climatic formula evolved up to date. Annales Agronomiques 12: 13-49.

USGS. 2020. Earth Explorer. United States Geological Survey. Available at: https://earthexplorer.usgs.gov/ (accessed on July 2, 2020).

Vaca RA, Golicher DJ, Cayuela L, Hewson J, Steininger M. 2012. Evidence of incipient forest transition in Southern Mexico. PLoS ONE 7: e42309. https://doi.org/10.1371/journal.pone.0042309

Velásquez N, Liverman, Botero V, Vélez JI. 2011. Rainfall distribution based on a Delaunay triangulation method. In: Transactions on Computational Science XIV (Gavrilova M, Tan CJK, Mostafavi M, Eds.). Springer, Berlin, Heidelberg, 173-187. https://doi.org/10.1007/978-3-642-25249-5_7

Xiang K, Li Y, Horton R, Feng H. 2020. Similarity and difference of potential evapotranspiration and reference crop evapotranspiration. A review. Agricultural Water Management 232: 1-16. https://doi.org/10.1016/j.agwat.2020.106043

Zhang K, Kimball JS, Nemani RR, Running SW, Hong Y, Gourley JJ, Yu Z. 2015. Vegetation greening and climate change promote multidecadal rises of global land evapotranspiration. Scientific Reports 5: 15956. https://doi.org/10.1038/srep15956

SUPPLEMENTARY MATERIAL

Table S-I. Coordinates and elevations of the weather stations with data used for the analysis of temperature, potential evapotranspiration, and monthly rainfall.

Weather Station	Analysis variable	Latitude	Longitude	Elevation (masl)	Region
Adolfo Ruiz Cortínez	T/PET	14.875000	–92.537500	4	Coast
Arriaga	T/PET/R	16.241667	–93.908333	64	Coast
Cacahoatán	R	14.988333	–92.164444	480	Coast
Cacaluta	T/PET/R	15.365	–92.731111	80	Coast
Chahuites	T/PET/R	16.25	–94.233056	23	Coast
Despoblado	T/PET/R	15.2025	–92.558056	63	Coast
Ejido Ibarra	R	15.333889	–92.952222	9	Coast
El Dorado	T/PET/R	14.672778	–92.212778	35	Coast
Escuintla (DGE)	T/PET/R	15.330833	–92.655833	92	Coast
Finca Argovia	R	15.126667	–92.299167	620	Coast
Francisco Sarabia	T/PET/R	15.417778	–92.998333	25	Coast
Frontera Hidalgo	T/PET/R	14.777222	–92.176111	60	Coast
Horcones	T/PET	15.955278	–93.605556	130	Coast
Huehuetán	T/R	15.002222	–92.400278	65	Coast
Independencia	T/PET/R	15.348333	–92.578333	112	Coast
Ingacio López Rayón	T/PET/R	14.617778	–92.184722	7	Coast
Las Brisas	T/PET/R	15.514444	–93.116944	10	Coast
Mazatán	T/PET/R	14.886389	–92.453889	15	Coast
Medio Monte	T/PET/R	14.915278	–92.190556	245	Coast
Metapa de Domínguez	R	14.831111	–92.191667	98	Coast
Pijijiapan	T/PET/R	15.697778	–93.211389	57	Coast
Plan de Iguala	T/PET/R	14.958889	–92.504167	18	Coast
Salvación	T/PET/R	15.143889	–92.701389	8	Coast
San Isidro	R	15.742778	–93.351389	45	Coast
San Jerónimo	T/R	15.039722	–92.136389	750	Coast
Santo Domingo	T/R	15.0275	–92.104167	859	Coast
Talismán I	R	14.963056	–92.147222	340	Coast
Tapachula	T/PET/R	14.920833	–92.25	193	Coast
Tonalá	T/PET/R	16.084167	–93.743889	55	Coast
Tres Picos	T/PET/R	15.875	–93.545833	20	Coast
Buenos Aires	T/PET/R	15.3325	–92.2675	1820	Sierra Madre
El Porvenir	T/PET/R	15.457222	–92.281111	2847	Sierra Madre
Finca A. Prusia	R	15.731944	–92.794167	1040	Sierra Madre
Finca Chicharras	T/PET/R	15.133056	–92.242222	1328	Sierra Madre
Finca Cuxtepeques	T/PET/R	15.728611	–92.968889	1550	Sierra Madre
Finca Germania	R	15.194444	–92.345833	1214	Sierra Madre
Finca Hamburgo	R	15.173089	–92.325278	1200	Sierra Madre
Frontera Amatenango	T/PET/R	15.433611	–92.114167	900	Sierra Madre
Monterrey	PET/R	16.058889	–93.368889	700	Sierra Madre
Motozintla	T/R	15.364167	–92.248056	1260	Sierra Madre
Reforma II	T/PET/R	15.9	–92.933333	700	Sierra Madre
Unión Juárez	T/PET/R	15.0625	–92.080556	1300	Sierra Madre
Úrsulo Galván	T/PET/R	16.278611	–93.418611	700	Sierra Madre
El Triunfo	PET	15.6566	–92.8081	1973	Sierra Madre
Sierra Madre 1	PET	15.5497	–92.6268	1898	Sierra Madre
Sierra Madre 2	PET	15.8709	–93.1338	1896	Sierra Madre
Sierra Madre 3	PET	16.1977	–93.6121	2366	Sierra Madre
Acala	T/PET/R	16.552778	–92.804167	420	Central Depression

T: temperature; PET: potential evapotranspiration; R: monthly rainfall.

Table S-I. Coordinates and elevations of the weather stations with data used for the analysis of temperature, potential evapotranspiration, and monthly rainfall.

Weather Station	Analysis variable	Latitude	Longitude	Elevation (masl)	Region
Aquespala	R	15.794167	–91.920278	617	Central Depression
Benito Juárez	R	16.082778	–92.840556	580	Central Depression
Berriozábal	T/R	16.796944	–93.265278	890	Central Depression
Cascajal	T/PET/R	16.308889	–92.486111	650	Central Depression
Catarinitas	T/PET/R	15.9025	–92.482778	945	Central Depression
Chicomuselo	T/PET/R	15.751667	–92.273611	550	Central Depression
El Boquerón	T/PET/R	16.644167	–93.157222	500	Central Depression
El Progreso	T/R	16.708889	–93.4025	781	Central Depression
Finca Ocotlán	T/PET/R	16.369444	–93.477222	650	Central Depression
Flores Magón	R	16.393333	–92.696111	482	Central Depression
Francisco I. Madero	R	16.802778	–93.755278	736	Central Depression
Guadalupe Grijalva	T/PET/R	15.693611	–92.161111	630	Central Depression
Jaltenango	T/PET/R	15.870833	–92.723889	640	Central Depression
La Angostura (CFE)	T/R	16.419722	–92.767778	500	Central Depression
La Mesilla	T/R	16.184167	–92.2875	1210	Central Depression
La Unión	T/PET/R	16.665	–93.800833	580	Central Depression
Las Flores	T/R	16.691944	–93.563056	480	Central Depression
Ocozocoautla	R	16.750883	–93.373889	838	Central Depression
Paso Hondo	R	15.684444	–92.006944	660	Central Depression
Portaceli	PET/R	16.449167	–93.125278	780	Central Depression
Puente Colgante	T/PET/R	16.740556	–93.031111	418	Central Depression
Puente Concordia (CFE)	T/PET/R	15.848611	–91.968056	582	Central Depression
Querétaro	R	15.838611	–92.755556	665	Central Depression
Revolucion Mexicana	T/PET/R	16.163056	–93.076389	540	Central Depression
Rosendo Salazar	R	16.471111	–94.003889	721	Central Depression
San Miguel	T/PET/R	15.708611	–92.208611	600	Central Depression
Soyatitán	T/PET/R	16.288889	–92.428333	832	Central Depression
Tuxtla Gutiérrez (CFE)	T/PET/R	16.761667	–93.102778	532	Central Depression
Villa Corso	R	16.194444	–93.2625	600	Central Depression
Villa de Chiapilla	R	16.5775	–92.715278	550	Central Depression
Villaflores	T/PET/R	16.228889	–93.2625	554	Central Depression
Abelardo L. Rodríguez	R	16.379167	–92.2375	1920	Central Highlands
La Cabaña	R	16.714167	–92.628889	2113	Central Highlands
La Trinitaria (CFE)	T/PET/R	16.117778	–92.051667	1540	Central Highlands

T: temperature; PET: potential evapotranspiration; R: monthly rainfall.

Table S-II. Years with data used to determine significant rainfall trends.*

	Years with data where significant rainfall trends were determined																				
	Central Depression					Sierra Madre													Coast		
Year	1	2	3	4	5	6	7	8	9	10	11	12	13	14	15	16	17	18	19	20	21
1990	■		■		■					■	■	■	■	■	■	■	■	■	■	■	■
1991		■	■	■	■	■	■	■	■		■	■	■	■	■	■	■	■	■	■	■
1992	■		■	■	■	■	■	■	■	■	■	■	■	■	■	■	■	■	■	■	■
1993	■	■	■		■	■	■	■	■	■	■	■	■	■	■	■	■	■	■	■	■
1994	■	■	■	■	■					■	■	■		■	■	■	■	■	■	■	■
1995	■	■	■	■	■	■	■	■	■	■	■	■	■	■	■	■	■	■	■	■	■
1996	■	■	■	■	■	■	■	■	■	■	■	■	■	■	■	■	■	■	■	■	■
1997	■	■	■	■	■	■	■	■	■	■	■	■	■	■	■	■	■	■	■	■	■
1998	■	■		■	■	■	■	■	■	■	■	■	■	■	■	■	■	■	■	■	■
1999	■	■		■	■	■	■	■	■	■	■	■	■	■	■	■	■	■	■	■	■
2000	■	■		■	■	■	■	■	■		■	■	■	■	■	■	■	■	■	■	■
2001	■	■	■		■	■	■	■	■			■	■	■	■	■	■	■	■	■	■
2002	■	■	■	■	■	■	■	■	■	■	■	■	■	■	■	■	■	■		■	■
2003	■	■	■	■	■						■	■	■	■	■	■	■	■	■	■	■
2004	■	■		■	■	■	■	■	■	■	■	■	■	■	■	■	■	■	■	■	■
2005	■	■	■	■	■	■	■	■	■	■	■	■	■	■	■	■		■	■	■	■
2006	■	■	■	■	■	■	■	■	■	■	■	■	■	■	■	■	■	■	■	■	■
2007	■	■	■	■	■	■	■	■	■	■	■	■	■	■	■	■	■	■	■	■	■
2008	■	■	■	■	■	■	■	■	■	■	■	■	■	■	■	■	■	■	■		■
2009	■	■	■	■	■	■	■	■	■	■	■	■	■	■	■	■	■	■	■	■	■
2010	■	■	■	■	■	■	■	■	■	■	■	■	■	■	■	■	■	■	■		■
2011	■	■	■	■	■	■	■	■	■	■	■	■	■	■	■	■	■	■	■		■
2012	■	■		■	■	■	■	■	■	■	■			■				■	■		
2013	■	■		■						■	■	■	■	■	■	■	■		■	■	■
2014	■	■		■	■					■	■	■	■					■			■
2015				■										■	■	■	■	■	■		■
2016				■																	

*Central depression: 1) Francisco I. Madero (June), 2) Francisco I. Madero (Sept), 3) Villa Corzo (Aug), 4) Chicomuselo (Sept), 5) Benito Juárez (Aug); Sierra Madre: 6) Finca A. Prusia (May), 7) Finca A. Prusia (June), 8) Finca A. Prusia (July), 9) Finca A. Prusia (Aug), 10) Buenos Aires (May), 11) Independencia (June), 12) Independencia (Aug), 13) Independencia (Sept), 14) San Jerónimo (June), 15) San Jerónimo (July), (16) San Jerónimo (Aug), (17) San Jerónimo (Sept), (18) San Jerónimo (Oct); and coast: (19) San Isidro (June), (20) Talismán (Aug), (21) Metapa de Domínguez (Sept).

Table S-III. Changes in monthly rainfall between 1990 and 2016 in the Sierra Madre, central depression (CD) and coast areas of Chiapas, Mexico. Only weather stations with significant ($p < 0.05$) rainfall trends are included. Significant rainfall trends during the longer 1960-2016 period at the same stations are indicated in the far-right column (trend since 1960), where data are available since 1960. Details of these trends are shown in Table S-VII.

Area	Weather station	Month	No. of data	Regression value	P-value	Change (mm)	Trend since 1960
CD	Francisco I. Madero	June	26	0.4036	0.002	200	
CD	Villa Corzo	Aug	17	0.4004	0.002	160	
CD	Francisco I. Madero	Sept	25	0.3475	0.002	220	
CD	Chicomuselo	Sept	24	0.2314	0.018	260	
CD	Benito Juárez	Aug	25	0.1852	0.021	180	
Sierra	Finca A. Prusia	May	18	0.277	0.003	200	No
Sierra	Buenos Aires	May	21	0.2848	0.010	150	
Sierra	Finca A. Prusia	June	18	0.2232	0.031	230	No
Sierra	Independencia	June	23	0.4194	0.000	440	
Sierra	San Jerónimo	June	25	0.2243	0.018	500	No
Sierra	Finca A. Prusia	July	18	0.2692	0.023	400	No
Sierra	San Jerónimo	July	24	0.2778	0.004	500	No
Sierra	Finca A. Prusia	Aug	18	0.1242	0.041	400	No
Sierra	Independencia	Aug	24	0.2366	0.031	320	
Sierra	San Jerónimo	Aug	24	0.2286	0.035	400	No
Sierra	Independencia	Sept	23	0.2495	0.002	400	
Sierra	San Jerónimo	Sept	23	0.3234	0.006	650	No
Sierra	San Jerónimo	Oct	25	0.2541	0.012	470	No
Coast	San Isidro	June	23	0.3693	0.001	400	
Coast	Talismán	Aug	20	0.2549	0.021	250	No
Coast	Metapa de Domínguez	Sept	24	0.4361	0.002	600	Yes

Table S-IV. Landsat satellite images used for classification of vegetation types and estimation of evapotranspiration.

Path	Row	Season	Date	Landsat	Bands used for classification	Bands used for NDVI
1990 (1987-1992)						
22	49	Transition	19 December 1987	5	2,3,4	3,4
21	49	Transition	3 February 1990	5	2,3,4	3,4
21	50	Transition	1 December 1989	5	2,3,4	3,4
22	49	Dry	19 March 1992	5	2,3,4	3,4
21	49	Dry	19 April 1991	5	2,3,4	3,4
21	50	Dry	19 April 1991	5	2,3,4	3,4
22	49	Wet	19 November 1988	5	2,3,4	3,4
21	49	Wet	14 August 1987	5	2,3,4	3,4
21	50	Wet	8 July 1991	5	2,3,4	3,4
2005 (1997-2011)						
22	49	Transition	22 December 1997	5	2,3,4	3,4
21	49	Transition	1 February 1998	5	2,3,4	3,4
21	50	Transition	16 November 1998	5	2,3,4	3,4
22	49	Dry	1 April 2011	5	2,3,4	3,4
21	49	Dry	9 April 1999	5	2,3,4	3,4
21	50	Dry	8 March 1999	5	2,3,4	3,4
22	49	Wet	24 August 2000	5	2,3,4	3,4
21	49	Wet	16 July 2000	5	2,3,4	3,4
21	50	Wet	24 July 1997	5	2,3,4	3,4
2020 (2017-2020)						
22	49	Transition	11 January 2017	8	3,4,5	4,5
21	49	Transition	28 December 2019	8	3,4,5	4,5
21	50	Transition	28 December 2019	8	3,4,5	4,5
22	49	Dry	23 April 2019	8	3,4,5	4,5
21	49	Dry	26 April 2017	8	3,4,5	4,5
21	49	Dry	29 January 2020	8	3,4,5	4,5
21	50	Dry	11 February 2019	8	3,4,5	4,5
22	49	Wet	29 August 2019	8	3,4,5	4,5
21	49	Wet	5 July 2019	8	3,4,5	4,5
21	50	Wet	16 August 2017	8	3,4,5	4,5

Table S-V. Comparison of potential evapotranspiration (PET) methods for seven weather stations located within or near to the study area for days representing the dry (1 May 2020), and wet (25 July 2020) seasons. Percent Errors between each of the simpler PET methods used in comparison with the Penman Monteith (PM) method are shown between parenthesis.

Weather station	Season	Potential evapotranspiration values (mm/day)			
		PM	Thornthwaite	Hargreaves	Turc
Coast					
Tapachula	Dry	5.44	5.45 (0.2)	5.98 (9.9)	5.04 (–7.4)
	Wet	4.79	5.30 (10.6)	5.96 (24.4)	5.10 (6.4)
Escuintla	Dry	4.34	5.07 (16.9)	6.42 (48.0)	5.52 (27.3)
	Wet	4.73	5.04 (6.6)	5.80 (22.7)	5.06 (7.0)
Sierra Madre					
El Triunfo	Dry	4.35	4.09 (-5.9)	4.19 (–3.7)	3.92 (–9.8)
	Wet	3.83	4.13 (7.8)	3.45 (–9.8)	3.29 (–13.9)
Volcán Tacaná	Dry	2.91	4.29 (47.4)	4.36 (50.0)	4.06 (39.7)
	Wet	1.36	4.19 (208.5)	3.35 (146.6)	3.21 (136.6)
Central depression/highlands					
Comitán	Dry	4.98	4.60 (–7.6)	4.55 (–8.6)	4.16 (–16.5)
	Wet	4.74	4.72 (–0.5)	4.78 (0.7)	4.33 (–8.7)
Tuxtla	Dry	5.28	4.92 (-6.7)	5.08 (–3.7)	4.51 (–14.5)
	Wet	4.90	4.99 (1.9)	5.65 (15.3)	4.96 (1.3)
Lagunas de Montebello	Dry	2.32	4.24 (82.5)	3.58 (54.1)	3.41 (46.7)
	Wet	3.34	4.42 (32.3)	4.72 (41.4)	4.35 (30.5)

Table S-VI. Changes in average daily temperature between 1990 and 2016 in the Central Depression (CD), Sierra Madre, and Coast regions of Chiapas, Mexico. Only weather stations with significant ($p<0.05$) temperature trends are included. Significant temperature trends during the longer 1960-2016 period at the same stations are indicated in the far-right column (Trend since 1960), where data are available since 1960. Details of these trends are shown in Table S-VII.

Area	Weather station	Season	No. of data	Regression value	P-value	Change (^{o}C)	Trend	Trend since 1960
CD	Catarinitas	Dry-cool	24	0.2336	0.018	2.7	Warm	
CD	Guadalupe Grijalva	Dry-cool	25	0.2009	0.047	–1.4	Cool	Yes
CD	Jaltenango	Dry-cool	27	0.3876	0.000	–1.1	Cool	
CD	Soyatitán	Dry-cool	27	0.646	<0.0001	–3.5	Cool	
CD	La Mesilla	Dry-cool	27	0.7258	0.05	–5.0	Cool	
CD	Tuxtla Gutiérrez (CFE)	Dry-cool	26	0.6112	<0.0001	–2.9	Cool	
CD	El Progreso	Dry-cool	27	0.558	<0.0001	2.0	Warm	Yes
CD	Catarinitas	Dry-hot	24	0.6103	0.001	6.0	Warm	
CD	Guadalupe Grijalva	Dry-hot	25	0.2772	0.003	2.5	Warm	No
CD	Jaltenango	Dry-hot	27	0.2017	0.033	–1.0	Cool	
CD	Soyatitán	Dry-hot	27	0.318	<0.0001	–1.5	Cool	
CD	La Mesilla	Dry-hot	27	0.4293	0.000	–3.1	Cool	
CD	Tuxtla Gutiérrez (CFE)	Dry-hot	26	0.3435	0.005	–2.2	Cool	
CD	El Progreso	Dry-hot	27	0.5245	<0.0001	2.5	Warm	No
CD	Catarinitas	Wet	24	0.5763	0.002	5.2	Warm	
CD	Guadalupe Grijalva	Wet	25	0.2547	0.023	3.1	Warm	No
CD	Jaltenango	Wet	27	0.3518	0.001	–1.4	Cool	
CD	Soyatitán	Wet	27	0.2293	<0.0001	–1.2	Cool	
CD	La Mesilla	Wet	27	0.28	0.009	–2.3	Cool	
CD	Tuxtla Gutiérrez (CFE)	Wet	26	0.3517	0.009	–1.8	Cool	
CD	El Progreso	Wet	27	0.6608	<0.0001	3.3	Warm	No
Sierra	Buenos Aires	Dry-cool	27	0.3447	0.003	–1.8	Cool	
Sierra	Frontera Amatenango	Dry-cool	26	0.4652	0.000	–3.5	Cool	No
Sierra	Motozintla	Dry-cool	26	0.3686	0.011	–1.9	Cool	No
Sierra	Ursulo Galvan	Dry-cool	23	0.3038	0.023	–1.8	Cool	
Sierra	Buenos Aires	Dry-hot	27	0.236	0.010	–0.9	Cool	
Sierra	Reforma II	Dry-hot	27	0.3049	0.008	1.2	Warm	
Sierra	Motozintla	Dry-hot	26	0.2678	0.025	–2.0	Cool	No
Sierra	Ursulo Galván	Dry-hot	23	0.2135	0.039	–1.3	Cool	
Sierra	Buenos Aires	Wet	27	0.108	0.023	–1.0	Cool	
Sierra	Ursulo Galván	Wet	23	0.5223	0.001	–2.2	Cool	
Coast	Pijijiapan	Dry-cool	27	0.2785	0.010	0.9	Warm	Yes
Coast	Tapachula	Dry-cool	27	0.878	<0.0001	2.5	Warm	Yes
Coast	Escuintla	Dry-cool	27	0.6687	<0.0001	2.8	Warm	Yes
Coast	Plan de Iguala	Dry-cool	26	0.1355	0.029	0.9	Warm	
Coast	Huehuetán	Dry-cool	27	0.5034	0.021	1.3	Warm	
Coast	Salvación	Dry-cool	27	0.5077	0.000	2.7	Warm	
Coast	Ignacio López Rayón	Dry-cool	26	0.5177	0.000	–1.8	Cool	Yes
Coast	Pijijiapan	Dry-hot	27	0.1376	0.05	0.7	Warm	Yes
Coast	Medio Monte	Dry-hot	26	0.2626	0.028	1.2	Warm	Yes
Coast	Tapachula	Dry-hot	27	0.6059	<0.0001	1.9	Warm	Yes
Coast	Escuintla	Dry-hot	27	0.5386	0.000	3.3	Warm	Yes
Coast	Salvacion	Dry-hot	25	0.3778	0.001	2.3	Warm	
Coast	Medio Monte	Wet	26	0.5173	0.000	1.1	Warm	Yes
Coast	Tapachula	Wet	27	0.7001	<0.0001	1.2	Warm	Yes
Coast	Escuintla	Wet	27	0.4543	0.003	2.1	Warm	Yes
Coast	Plan de Iguala	Wet	26	0.4562	0.001	1.5	Warm	
Coast	Salvación	Wet	26	0.6964	<0.0001	3.6	Warm	

Table S-VII. Significant ($p < 0.05$) trends in mean daily temperature and monthly rainfall during the periods of 1960-1989 and 1960-2016 at climate stations with significant trends during the 1990-2016 period, where data are available since 1960 in the regions of Pacific Chiapas.

Mean daily temperature Trends 1960-1989/1960-2016

Weather station	Season/ month	Period	No. of data	Reg. value	P-value	Change (^{o}C)	Trend
Guadalupe Grijalva	Dry-cool	1960–2016	54	0.1925	0.001	–1.6	Cool
Guadalupe Grijalva	Dry-hot	1960–1989	29	0.2994	0.001	–1.9	Cool
El Progreso	Dry-cool	1960–2016	57	0.0687	<0.0001	1.8	Warm
El Progreso	Dry-hot	1960–1989	30	0.4865	<0.0001	–1.9	Cool
Frontera Amatenango	Dry-cool	1960–1989	30	0.7776	<0.0001	5.3	Warm
Tapachula	Dry-cool	1960–2016	57	0.7538	<0.0001	5.2	Warm
Tapachula	Dry-hot	1960–2016	57	0.6872	<0.0001	4.8	Warm
Tapachula	Wet	1960–2016	57	0.773	<0.0001	4.6	Warm
Escuintla	Dry-cool	1960–1989	30	0.2315	0.011	1.5	Warm
Escuintla	Dry-cool	1960–2016	57	0.1313	0.002	1.3	Warm
Escuintla	Dry-hot	1960–2016	57	0.0544	0.040	0.9	Warm
Escuintla	Wet	1960–2016	57	0.1029	0.008	1.0	Warm
Ignacio López Rayón	Dry-cool	1960–1989	29	0.414	0.001	1.2	Warm
Ignacio López Rayón	Dry-cool	1960–2016	56	0.1284	0.027	–0.9	Cool
Ignacio López Rayón	Dry-hot	1960–2016	56	0.5215	<0.0001	–2.3	Cool
Ignacio López Rayón	Wet	1960–2016	56	0.4717	<0.0001	–1.5	Cool
Pijijiapan	Dry-cool	1960–1989	30	0.2979	0.017	1.3	Warm
Pijijiapan	Dry-cool	1960–2016	57	0.482	<0.0001	1.7	Warm
Pijijiapan	Dry-hot	1960–2016	57	0.0942	0.020	0.6	Warm
Medio Monte	Dry-cool	1960–1989	30	0.3287	0.001	0.8	Warm
Medio Monte	Dry-cool	1960–2016	57	0.4819	<0.0001	1.2	Warm
Medio Monte	Dry-hot	1960–1989	30	0.2458	0.006	–0.9	Cool
Medio Monte	Dry-hot	1960–2016	57	0.3215	0.000	1.7	Warm
Medio Monte	Wet	1960–2016	57	0.6236	<0.0001	1.6	Warm
Monthly rainfall trends 1960-1989/1960-2016						(mm)	
Metapa de Domínguez	September	1960–2016	53	0.031	0.1527	310	Wet

Table S-VIII. Mean and standard deviations of the Normalized Difference Vegetation Index (NDVI), Potential evapotranspiration (PET), and estimation of evapotranspiration (ET) values within the central depression, Sierra Madre, and coast regions of Chiapas, Mexico, during the transition from wet to dry, dry, and wet season of 1990, 2005, and 2020.

Region	Season	NDVI	PET (mm/day)	ET estimation (mm/day)
Central Depression	1990 transition	0.49 ± 0.19	3.80 ± 0.15	2.33 ± 0.92
	1990 dry	0.35 ± 0.14	5.39 ± 0.26	2.31 ± 0.94
	1990 wet	0.65 ± 0.16	4.81 ± 0.20	3.87 ± 0.97
	2005 transition	0.56 ± 0.19	3.66 ± 0.16	2.54 ± 0.83
	2005 dry	0.35 ± 0.16	5.30 ± 0.25	2.27 ± 1.00
	2005 wet	0.68 ± 0.16	4.63 ± 0.16	3.89 ± 0.91
	2020 transition	0.59 ± 0.22	3.49 ± 0.21	2.52 ± 0.95
	2020 dry	0.42 ± 0.17	5.20 ± 0.33	2.69 ± 1.11
	2020 wet	0.72 ± 0.19	4.42 ± 0.26	3.93 ± 1.03
Sierra Madre	1990 transition	0.72 ± 0.14	3.30 ± 0.36	2.94 ± 0.69
	1990 dry	0.64 ± 0.17	4.51 ± 0.51	3.58 ± 0.99
	1990 wet	0.71 ± 0.15	4.27 ± 0.39	3.75 ± 0.89
	2005 transition	0.75 ± 0.12	3.10 ± 0.40	2.89 ± 0.62
	2005 dry	0.63 ± 0.16	4.30 ± 0.55	3.36 ± 0.97
	2005 wet	0.74 ± 0.15	4.62 ± 0.16	3.59 ± 0.82
	2020 transition	0.81 ± 0.12	2.88 ± 0.45	2.89 ± 0.62
	2020 dry	0.71 ± 0.15	4.08 ± 0.60	3.57 ± 0.91
	2020 wet	0.77 ± 0.19	3.60 ± 0.57	3.43 ± 1.01
Coast	1990 transition	0.64 ± 0.21	3.09 ± 0.21	3.09 ± 0.88
	1990 dry	0.49 ± 0.20	5.07 ± 0.28	3.11 ± 1.15
	1990 wet	0.68 ± 0.17	4.76 ± 0.27	4.03 ± 0.92
	2005 transition	0.70 ± 0.19	3.76 ± 0.20	3.27 ± 0.79
	2005 dry	0.52 ± 0.21	4.93 ± 0.26	3.24 ± 1.14
	2005 wet	0.70 ± 0.18	4.57 ± 0.27	4.01 ± 0.90
	2020 transition	0.68 ± 0.23	3.68 ± 0.25	3.14 ± 0.95
	2020 dry	0.60 ± 0.23	4.78 ± 0.31	3.58 ± 1.21
	2020 wet	0.77 ± 0.19	4.36 ± 0.36	4.19 ± 0.93

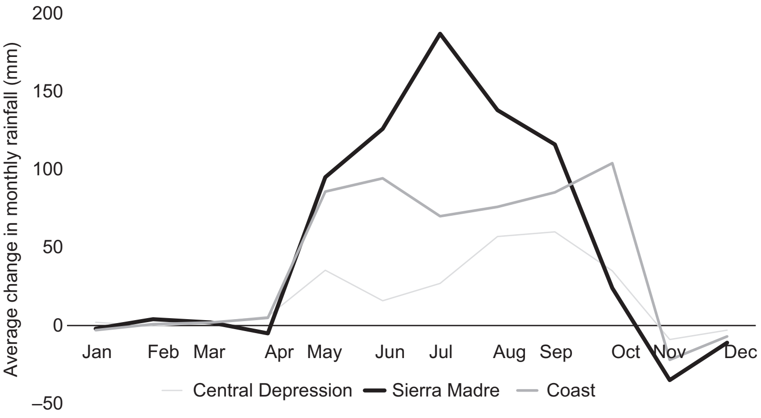

Fig. S-1. Regional averages of changes in monthly rainfall (mm) between 1990-2016 in the central depression, Sierra Madre and coast regions of Chiapas Mexico.

Atmósfera 36(1), 123-142 (2023)
https://doi.org/10.20937/ATM.53002

CONTENTS

Agroclimatic zoning of the state of Nayarit, Mexico

Mayra MENDOZA-CARIÑO[1], Ana Laura BAUTISTA-OLIVAS[2]*, Daniel MENDOZA-CARIÑO[3],
Carlos Alberto ORTIZ-SOLORIO[4], Héctor DUARTE-TAGLES[2] and Gerardo CRUZ-FLORES[1]

[1] *Facultad de Estudios Superiores Zaragoza, Universidad Nacional Autónoma de México, 09230 Ciudad de México, México.*
[2] *Universidad de Sonora, Hermosillo, Apartado Postal 305, Sonora, México.*
[3] *Universidad Tecnológica de Tecamachalco, 75483 Tecamachalco, Puebla, México.*
[4] *Colegio de Postgraduados, 56230 Texcoco, Estado de México, México.*
*Author for correspondence: abautistaolivas@gmail.com

Received: October 31, 2020; accepted: June 10, 2021

RESUMEN

La productividad agrícola del estado de Nayarit ha disminuido desde 1998. El objetivo de este estudio fue realizar la zonificación agroclimática del estado y determinar los cultivos que se pueden producir con mayores beneficios, según el sistema de clasificación climática de Papadakis. Para ello, se utilizaron características hídricas y térmicas, e índices derivados de valores meteorológicos de 25 estaciones climatológicas que limitan la distribución geográfica de los cultivos. Los grupos climáticos establecidos fueron tres: tropical, subtropical y tierra fría con cuatro, tres y dos subgrupos cada uno, respectivamente. Los dos primeros favorecen los cultivos de cereales de invierno como avena (*Avena sativa* L.), cebada (*Hordeum vulgare* L.), centeno (*Secale cereale* L.) y trigo (*Triticum aestivum* L.); y de verano como arroz (*Oryza sativa* L.), maíz (*Zea mays* L.), mijo (*Panicum italicum* L.) y sorgo (*Sorghum bicolor* (L.) Moench), además de banana (*Musa paradisiaca* L.), caña de azúcar (*Saccharum officinarum* L.), cítricos y papa (*Solanum tuberosum* L.). En el grupo climático de tierra fría, se encontraron maíz y papa. Con base en el método Papadakis, para cada subgrupo climático identificado se indicaron los cuidados necesarios para obtener buenos rendimientos (tipo de cultivo; épocas de siembra; aplicación de riego, fertilizantes y agroquímicos) y para evitar problemas fitosanitarios y de almacenamiento después de la cosecha. El mapa de zonificación agroclimática se generó con el método de interpolación de la distancia inversa ponderada. Este estudio puede ser la base para planificar con éxito los cultivos en la región y mejorar la economía del estado.

ABSTRACT

Agriculture productivity in the state of Nayarit has decreased since 1998. The aim of this study was to undertake the agroclimatic zoning across the state in order to determine the type of crops more convenient to render the highest yields, based on the Papadakis climate classification system. Hydric and thermal characteristics pertaining to the geographic distribution of crops were used, as well as indexes derived from meteorological data provided by 25 climate stations. There were three climatic groups identified: tropical, subtropical and cold land, having four, three and two subgroups each, respectively. The first two climatic groups support winter cereals such as oat (*Avena sativa* L.), barley (*Hordeum vulgare* L.), rye (*Secale cereale* L.) and wheat (*Triticum aestivum* L.); and summer cereals such as corn (*Zea mays* L.), millet (*Panicum italicum* L.), rice (*Oryza sativa* L.) and sorghum (*Sorghum bicolor* [L.] Moench), in addition to banana (*Musa paradisiaca* L.), citrus, potato (*Solanum tuberosum* L.) and sugar cane (*Saccharum officinarum* L.). On the other hand, corn and potato were found in the cold land climatic group. Based on the methodology of Papadakis, for each climatic sub-group identified, a set of recommendation managements were given to improve yields (crop type, sowing season, irrigation, fertilizing and other agrochemicals application) and to avoid crop damage. An agroclimatic-zoning map was generated by using the inverse distance weighted interpolation method. This study may contribute to the successful planning of crops across the region and thus to improve the state's economy.

Keywords: agroecological zoning, humidity pattern, Papadakis' climate classification system.

1. Introduction

Mexico's geography entails a diversity of climates, which gives an agricultural potential for the yield of a vast range of crops. However, there is a lack of studies suggesting the best suitable crops in Mexico for different environments. Regularly, the choice of a crop in the country relies on the market, governmental subsidies and the farmer's own interests.

Agriculture is the main economic activity in the state of Nayarit, using 602 407 ha (22% of the total state's area), whereof 110 895 ha are irrigated and 491 512 ha are for non-irrigated farming (INEGI, 2011). There are three crop seasons: fall-winter (from October to January), encompassing over 39.1% of the farmland; spring-summer (from March to August), covering over 10.7%, and perennial (from January to December), involving 50.2% (SIAP, 2021). The irrigated and non-irrigated surface areas during the fall-winter season are 42.3 and 57.7%; 18.9 and 81.1% during spring-summer, and 11.2 to 88.8% for perennials (SIAP, 2021). The irrigated and non-irrigated surface areas during the fall-winter season are 41.6 and 58.4% of the total farmland; 16.9 and 83.1% during spring-summer, and 11.5 to 88.5% for perennials (SIAP, 2020). Main crops per cultivated surface area are: sorghum, corn, beans (*Phaseolus vulgaris* L.), sugar cane (*Saccharum officinarum* L.), and mango (*Mangifera indica* L.) (Gobierno del Estado de Nayarit-INEGI, 2017).

During 1995-2006, the state's total production was less than 60 000 000 t per year and it has been decreasing since 1998. Despite the widest spread of agriculture in 2005 (a little more than 380 000 ha), the total crop yields were some of the lowest ever (20 000 000 t) (Zamudio and Méndez, 2011). The total crop surface during the 2016-2017 farming year was 61 213.62 ha and yielded 1 365 619.16 t per year, with an economic value of MXN 2 739 139 310 (Conagua, 2018). Such an agricultural productivity is low, despite the increase of agricultural surface in 2019 to 182 105.71 ha that yielded earnings of MXN 5 065 591 410 (SIAP, 2019).

This situation has a negative impact on the state's economy. According to the state's GDP (Gobierno del estado de Nayarit-SAGARPA, 2010), Nayarit has a low 11% contribution of the primary sector (23% secondary, and 66% tertiary), due to economic transformations that took place during the decade of 2010, when contributions of the primary sector began to decline (50%). At the national level, Nayarit contributed in 2018 with 0.7% of the GDP: 1.3, 0.4 and 0.8% of the primary, secondary and tertiary sectors, respectively (IIEG-Gobierno del Estado de Jalisco, 2020).

In the state of Nayarit, agriculture has two production systems: technology-based (with irrigation infrastructure, acceptable yields and sufficient profit margins), and dryland farming (with non-irrigated agriculture and low productivity), both co-existing in the same territory (included the only irrigation district within the state, DR-043) and even used in the same crops. DR-043 has an extension of 51 329 ha, whereof 29 864.8 ha were irrigated (99.3% using surface water and 0.7% with groundwater) during the 2018-2019 farm season (CONAGUA, 2021). Farmers in DR-043 have access to credits and technical assistance, allowing the use of agricultural technology for a better commercial performance.

Crop zoning encompasses a study aiming to limit areas for the adequate growing of one or more species of plants; therefore, ensuring good crop yields. Agroclimatic studies assess the climate with respect to the needs of a crop, whereas an agroecological study also takes into account limiting soil factors such as texture and depth, as well as the type of technology used for production.

Climate is key in agriculture (Villa et al., 2001) and allows for the correct management of crops (White et al., 2001). Environmental temperature is one of the most important climatic and meteorological factors for plant growth, determining spatial distribution of natural vegetation and the suitability of crops (Lozada and Sentelhes, 2008). Temperature directly influences the physiological processes of the plant such as respiration, mineral absorption, photosynthesis, growth, flowering and water balance (Aguilar et al.*,* 2010).

Cold and heat intensity and duration affect metabolic activity, plant growth and viability, thus, limiting the geographic distribution of crops. Temperature and precipitation are the most relevant indicators, since the former closely determines biological processes, while the latter determines vegetation cover and crop productivity (Allen et al.*,* 1989). It is important, however, to include solar radiation since it sets the conditions of insolation, photoperiod, photosynthesis and the real and potential evapotranspiration (Velasco and Pimentel, 2010). The long and slow process of adaptation of crop plants to natural environments in the sake of better yields, turn them more susceptible to climate than wild plant communities. The decline in resistance counteracts the gain in productivity, with serious impact on agriculture.

The aim of this study was to undertake the agroclimatic zoning of the state of Nayarit, based on Papadakis' climate classification system (PCCS) (Papadakis, 1970), in order to determine the most convenient crops to obtain highest yields. The zoning system used for this purpose, which is also used in Spain (Lozano et al., 2000), is probably the best known and most applied worldwide (Velasco and Pimentel, 2010).

2. Materials and methods

2.1 Study area

Nayarit (23º 05'-20º 36' N; 103º 43'-105º 46' W) is a state in central Mexico with an extension of 27 621 km^2, limiting to the north with Sinaloa and Durango, to the east with Durango, Zacatecas and Jalisco, to the south with Jalisco and the Pacific Ocean, and to the west with the Pacific Ocean and Sinaloa. Twenty-five weather stations (WS) distributed across Nayarit and bordering states (whose geographical locations are listed in Table I) were selected for this study.

The types of climate in Nayarit and the percentages of the state area they encompass are: hot humid with heavy rainfall in summer (Am), 0.56%; hot sub-humid with summer rainfall (A[w]), 60.63%; warm sub-humid with summer rainfall (ACw), 30.96%; temperate sub-humid with summer rainfall (C[w]), 6.15%, and semi-arid very hot and hot (BS1[h']), 1.7% (INEGI, 2018) (Fig. 1). The average annual temperature is 25 ºC, the minimum average temperature is 10 ºC in January, whereas the maximum average temperature is about 35 ºC in May and June. The raining season is in summer (May through September), averaging an annual precipitation of 1100 mm (García, 2004) (see Table I for greater detail).

Nayarit has a wide range of soil types (Table II): Acrisol, Andosol, Arenosol, Cambisol, Fluvisol, Gleysol, Leptosol, Luvisol, Nitisol, Phaeozem, Regosol, Solonchak, Umbrisol and Vertisol (INEGI, 2018). The type of land is distributed within the state as follows: agriculture (15.9 %), grassland (14.6 %), livestock (61.2 %), woodland (4.9 %), and non-productive (3.4 %) (Bojórquez et al.*,* 2006). Nayarit is divided into four hydrological regions: Presidio San Pedro, Lerma-Santiago, Huicicila and Ameca. The main rivers across the state are Acaponeta, San Pedro, Santiago, Huicicila and Ameca. Freshwater bodies and salty ponds are the Aguamilpa, San Rafael and Amado Nervo dams, and the Agua Brava lake.

2.2 Methodology

The agroclimatic zoning was based on PCCS (Papadakis, 1970), which relies on climate variables such as average, maximum and minimum temperatures, annual and monthly rainfall, and potential evapotranspiration. The information from the 25 WS was gathered from data records (1951 to 2010) provided by Mexico's National Weather Service (SMN, 2019).

PCCS classifies geographic regions into 10 climatic groups, according to three dimensions: winter and summer types, and humidity patterns. These groups are cold land, desert, Mediterranean, Pampean and tropical (nine subdivisions each); polar alpine and subtropical (five subdivisions each); marine and steppe (eight subdivisions each); and continental humid (three subdivisions). PCCS includes a list of 186 special diagnostics used to define each group's subdivisions.

PCCS underlines the concept of monthly climate based on thermic and hydric characteristics, identifying 29 monthly thermic climates according to the average temperatures and extremes (maximum and minimum); and seven monthly hydric climates, composed by monthly precipitation plus the volume of water stored in soil due to previous rainfalls.

Table I. Geographical location and climate conditions of the weather stations (WS) in Nayarit and surrounding states (1951-2010).

	Weather stations	Code	Latitude	Longitude	Altitude (masl)	AT_{mean} (˚C)	AT_{max} (˚C)	AT_{min} (˚C)	AP_{mean} (mm)	ATE (mm)
Durango	Las Bayas	10040	23º 30' 16"	104º 49' 28"	2643	11.1	20.2	2.1	1040.1	NA
Jalisco	Bolaños	14023	21º 49' 30"	103º 47' 00"	963	24.4	33.6	15.2	593.3	1902.3
	Hostotipaquillo	14068	21º 03' 52"	104º 03' 05"	1300	21.7	30.1	13.2	838.5	1958.7
	San Gregorio	14125	20º 37' 15"	104º 34' 05"	1640	15.4	23.9	6.9	1305.1	1365.6
	Tenzompa	14306	22º 22' 34"	103º 55' 29"	1770	16.8	26.2	7.3	698.7	2124.4
Nayarit	Acaponeta	18001	22º 29' 24"	105º 21' 15"	24	25.9	33.3	18.5	1325	1896.7
	Amatlán de las Cañas	18003	20º 48' 00"	104º 24' 00"	798	24.9	34.1	15.6	800.3	NA
	Capomal	18004	21º 50'2 2"	105º 07' 16"	35	26.1	33.3	18.9	1529	1821.1
	Despeñadero	18008	21º 50' 29"	104º 43' 21"	315	26.7	33.7	19.8	846.5	2409.9
	El Carrizal	00018045 E	21º 49' 38"	104º 34' 30"	632	28.3	35.2	21.4	1155	2086.5
	El Naranjo	18085	22º 02' 03"	104º 51' 43"	239	27.2	34.3	20.1	1378.6	1799.6
	Huaynamota	18014	21º 55' 11"	104º 30' 49"	670	25.2	33.9	16.4	853.5	NA
	Jumatan (CFE)	18019	21º39'00"	105º 02' 00"	359	23.9	30.4	17.5	1443.7	1443.9
	La Yesca	18020	21º 19' 28"	104º 00' 45"	1357	27.5	36.2	18.8	743	2437.1
	Las Gaviotas	18021	20º 53' 23"	105º 08' 12"	56	26.1	33.4	18.9	1577.6	1699
	Pajaritos	18068	22º 22' 40"	105º 15' 15"	76	25.2	32.6	17.8	1349.4	1898.2
	Paso de Arocha	18025	21º 16' 31"	105º 04' 52"	84	25	31.3	18.7	1685.4	1558.8
	Rosamorada	18028	22º 07' 20"	105º 12' 14"	30	25.7	33.2	18.2	1361.1	1707.4
	San José Valle	18030	20º 44' 38"	105º 13' 46"	20	27.4	33.8	21.1	1071.3	1810
	San Juan Peyotán	18031	22º 21' 40"	104º 25' 54"	639	25.1	35	15.1	848.2	1963.3
	San Marcos	18080	20º 57' 25"	105º 21' 12"	7	25.9	33.3	18.6	1051.3	
	Tecuala	18036	22º 24' 20"	105º 27' 30"	10	25	32.4	17.7	993.8	1609.6
	Tepic	18038	21º 30' 00"	104º 53' 00"	935	20.3	27.5	13.1	1239.9	1807.5
	Zacualpan	18043	21º 15' 00"	105º 10' 00"	29	25	30.8	19.1	1375.7	NA
Sinaloa	Ototitán	25186	23º 00' 50"	105º 40' 00"	93	26.3	35	17.5	913.7	NA

ATE: annual total evaporation; AP_{mean}: annual average precipitation; AT_{mean}: annual average temperature; AT_{max}: annual maximum temperature; AT_{min}: annual minimum temperature; NA: non-available.

Source: SMN, 2019.

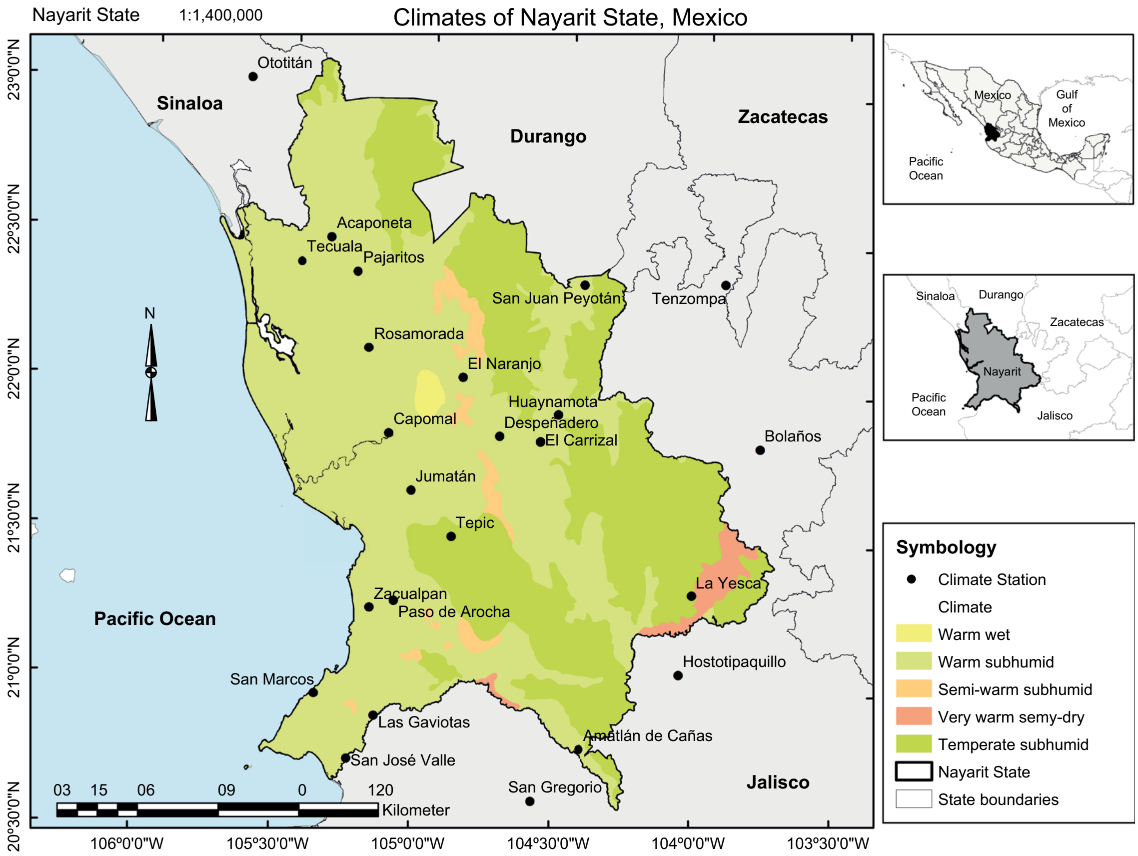

Fig. 1. Climates of the state of Nayarit, Mexico.

Arid climate (a) is defined when a set of climate variables entails less than 25% of the potential evapotranspiration; dry (s), between 25 to 50%; dry hydric intermediate (i), 50 to 75%; humid hydric intermediate (y), 75 to 100%; post-humid (p), more than 100%; humid (h), if rainfall denotes more than 100%; hyper-humid (w), when precipitation plus the soil moisture stored from previous rainfalls account for more than 200% of the potential evapotranspiration (Papadakis, 1970). PCCS computes evapotranspiration based on mid-day saturation deficit. The three PCCS dimensions were calculated using the climatic information from each WS.

2.2.1 Calculation of winter climate types

Data used correspond to the coldest month based on the average of absolute minimum temperatures (T_{pb}), the average of minimum temperatures (T_{min}), and the average of maximum temperatures (T_{max}). T_{pb} was calculated as follows:

$$\mathrm{T_{pb}} = 1.0891*(\mathrm{T_{min}}) - 4.7689 \qquad (1)$$

From these values, the types of winter climate were determined for each WS according to criteria shown in Table III.

2.2.2 Calculation of summer climate types

This process included the frost-free period (FFP) and T_{max} from different months. FFP was calculated using T_{pb} in two forms: minimum FFP (FFP_{min}), where monthly $T_{pb} > 7.0$ ºC; and available FFP (FFP_{avail}), when monthly $T_{pb} > 2.0$ ºC. Hence, it was necessary to know the T_{pb} of every month of the year.

T_{max} was used in four ways: (1) T_{max} of the month whose average temperature (T_{mean}) was the highest along the year; (2) average temperature of the six hottest months of the year ($T \times 6$), according to T_{mean}; (3) average temperature of the four hottest months ($T \times 4$) based on T_{mean}, and (4) average of maximum temperatures for all months in a year. Then, the types

Table II. Soil types in the state of Nayarit, Mexico.

Name/code	Characteristics	Surface (%)
Acrisol (AC)	Low-activity clay soil, acid and infertile for agriculture, common in rainy areas, red tone or light yellow with red spots, susceptible to erosion if logging and root removal.	1.91
Andosol (AN)	Andosols accommodate soils that develop in glass-rich volcanic ejecta under almost any climate. Andosols have a high potential for agricultural production, they are generally fertile soils. The strong phosphate fixation of Andosols (caused by active Al and Fe) is a problem.	0.57
Arenosol (AR)	Arenosols have high permeability and low water and nutrient storage capacity. Arenosols offer ease of cultivation, rooting and harvesting of root and tuber crops.	0.78
Cambisol (CM)	Cambisols combine soils with at least an incipient subsurface soil formation. Transformation of parent material is evident from structure formation and mostly brownish discoloration, increasing clay percentage, and/or carbonate removal. Cambisols make good agricultural land and are used intensively.	21.46
Fluvisol (FL)	Soils developed in fluvial, lacustrine and marine deposits, no groundwater and no high salt contents in the topsoil. Good natural fertility.	1.90
Gleysol (GL)	Gleysols comprise soils saturated with groundwater for long enough periods to develop reducing conditions resulting in gleyic properties. Redox processes are caused by ascending gases (CO_2, CH_4).	0.11
Leptosol (LP)	Leptosols comprise very thin soils over continuous rock and soils that are extremely rich in coarse fragments. Thin soils with various kinds of continuous rock or of unconsolidated materials with less than 20% (by volume) fine earth.	15.49
Luvisol (LV)	Luvisols have a higher clay content in the subsoil than in the topsoil, as a result of pedogenetic processes (especially clay migration) leading to an argic subsoil horizon. Luvisols have high-activity clays throughout the argic horizon and a high base saturation in the 50-100 cm depth.	16.11
Nitisol (NT)	Nitisols are deep, well-drained, red tropical soils with diffuse horizon boundaries and a subsurface horizon with at least 30 percent clay and moderate to strong. The deep and porous solum and the stable soil structure of Nitisols permit deep rooting and make them quite resistant to erosion.	0.94
Phaeozem (PH)	Phaeozems accommodate soils of relatively wet grassland and forest regions in moderately continental climates. Dark soils rich in organic matter. Phaeozems are porous, fertile soils and make excellent farmland.	12.13
Regosol (RG)	Regosols are very weakly developed mineral soils in unconsolidated materials. Not very thin, unconsolidated, generally fine-grained material. Regosols in desert areas have minimal agricultural significance.	15.92
Solonchak (SC)	Solonchaks have a high concentration of soluble salts at some time in the year. Arid and semi-arid regions, notably in areas where ascending groundwater reaches the upper soil or where some surface water is present, with vegetation of grasses and/or halophytic herbs, and in inadequately managed irrigation areas.	5.38
Umbrisol (UM)	Umbrisols have a significant accumulation of organic matter in the mineral surface soil and a low base saturation somewhere within the first meter (in most cases in the mineral surface soil). Soils with dark topsoil. Weathering material of siliceous rock or of strongly leached basic rock.	2.59
Vertisol (VM)	Vertisols are heavy clay soils with a high proportion of swelling clays. These soils form deep wide cracks from the surface downward when they dry out, which happens in most years. Sediments that contain swelling clays, or swelling clays produced by neoformation from rock weathering.	1.21
Others	Different types of soils with minimal non-mappable areas.	3.5

Source: INEGI, 2018; IUSS Working Group WRB, 2015.

Table III. Winter and summer climate types in Mexico according to Papadakis (1970).

Winter type*/ characteristics	T_{pb}	$T_{mín}$	$T_{máx}$	Summer type/ Characteristics	$FFP_{mín}$	FFP_{avail}	T_{Max}	Tx6	Tx4
		(ºC)			(months)			(ºC)	
Equatorial (Ec)		>18		Cotton (G)	>4.5		>33.5	>25	
Tropical (Tp)	> 7	13-18		Cotton (g)	>4.5		<33.5	>25	
Tropical (tP)	> 7	8-13	>21	Coffee (c)**	12		<33.5	>21	
Tropical (tp)	> 7	8-13	<21	Rice (O)	>3.5		>25.0	>21	
Citrus (Ct)	–2.5 a 7	>8	>21	Maize (M)		>4.5		>21	
Citrus (Ci)	–2.5 a 7	>8	10-21	Triguera cálida (T)		>4.5			>17
		<8	>21						
Oat (Av)	–10 a –2.5	>4	>10	Wheat (t)		2.5-4.5			>17
Oat (av)	–10 a –2.5	>4	5-10	Andine-alpine (A)		>1			>10
		<4	>10						
Triticum (Tv)	–29 a –10		> 5						
Triticum (Ti)	–29 a –10		0 y 5						

*Based on coldest month of the year; **all months with $T_{max} < 33.5$ and $T_{mín} < 20$ ºC.
T_{pb}: average of absolute minimum temperatures; T_{min}: average of minimum temperatures; T_{max}: average of maximum temperatures; FFP_{min}: minimum frost-free period; FFP_{avail}: available FFP; T_{max}: highest temperature registered for the month with the highest average temperature; T × 6: average temperature of the six hottest months of the year according to T_{mean}; T × 4: average temperature of the four hottest months based on T_{mean}.
Source: authors' self-preparation based on Papadakis (1970) information.

of summer climate could be determined for each WS according to criteria shown in Table III.

2.2.3 Humidity pattern

The humidity pattern refers to the natural availability of water for plants, based on three indices calculated from the water balance in soil (Thornwaite, 1948) to store up to 100 mm of water: annual humidity, monthly humidity and lixiviated rainfall. Monthly hydric characteristics were calculated using precipitation data, monthly potential evapotranspiration (PET) and the amount of water stored in the soil from previous rainfalls. Water balance facilitated the estimation of PET (Elías et al., 2001):

$$PET = 5.625 \ \left(e_a - e_{mi-2}\right) \tag{2}$$

where PET is the potential evapotranspiration (mm); e_a the vapor pressure to saturation (mbar) computed with the highest average temperature; e_{mi-2} the vapor pressure to saturation (mbar) computed with the lowest average temperature minus two Celsius degrees. Both vapor pressure variables were calculated as follows:

$$e_a = 6.1078 \ exp^{\left[\frac{17.27 \ *Tmáx}{Tmáx \ + \ 237.3}\right]} \tag{3}$$

$$e_{mi\_2} = 6.1078 \ exp^{\left[\frac{17.27 \ *\left(Tmín-2\right)}{\left(Tmín-2\right) \ + \ 237.3}\right]} \tag{4}$$

Water balance was performed using Excel software. The months of the year were listed on the spreadsheet followed by data in columns about precipitation (P), PET and P-PET. This latter column allowed the identification of the month in which water balance began, i.e., setting the first month when P > PET, since a positive value indicates water excess.

From that month on, the positive value filled in the column named "exceeding" in the worksheet, adding the P-PET value of the following month as long as it was also positive. The process was repeated until a negative value was obtained, indicating the end of water excess, and thus, a zero value was registered in the column. PCCS deems the water storage capacity of the soil to 100 mm, the highest value possible, although the sum could be even higher.

The positive value of the excess column was subtracted from the column named "water used" (water amount to meet the PET requirements), repeating the process every month until depletion or negative values were obtained. Water balance allowed for the calculation of monthly and annual humidity indices, and the lixiviated rainfall as well, for the wet season.

2.2.3.1 Annual humidity index (HI_A)

The HI_A was calculated according to the following equation:

$$HI_A = \frac{P_{annual}}{PET_{annual}} \quad (5)$$

where P is precipitation (mm) and PET evapotranspiration (mm), both annually. HI_A determined the hydric pattern of the CS.

2.2.3.2 Monthly humidity index (HI_m)

The HI_m allowed differentiating wet months (H; with $HI_m > 1.0$) from intermediate (I; $0.5 < HI_m < 1.0$) and dry (S; with $HI_m < 0.5$). This index was estimated using water consumption data:

$$HI_m = \frac{\mathrm{P_m + water\ used_m}}{\mathrm{PET_m}} \quad (6)$$

where P_m is the monthly precipitation (mm), *water used*$_m$ is water used in the month (mm) and PET_m is the monthly evapotranspiration (mm). In cases where there was no water consumption, HI_m was calculated as follows:

$$HI_m = \frac{P_m}{PET_m} \quad (7)$$

2.2.3.3 Lixiviated rainfall (L_n)

L_n is composed by the sum of differences of P-PET from the wet months, expressed as mm (Eq. [8]) and in percentage (Eq. [9])

$$\mathrm{L_n} = \sum\left(\mathrm{P - PET}\right) \text{ of wet months} \quad (8)$$

$$\mathrm{L_n} = \left[\frac{\sum\left(\mathrm{P - PET}\right)_{\text{of wet months}}}{\mathrm{PET_{annual}}}\right]*100 \quad (9)$$

where P is precipitation (mm), PET potential evapotranspiration (mm), and the wet months were those whose P-PET value was positive, confirmed by HI_m. The humidity pattern was determined for all WS using HI_A and HI_m L_n data calculated from a list of 186 PCCS special diagnostics (Table IV).

2.2.4 Agroclimatic zoning map

The software ArcMap v. 10.5 was used to make the agroclimatic zoning map based on the shape files of geographic metadata provided by the National Commission for the Knowledge and Use of Biodiversity (CONABIO, 2008) and the National Water Commission (CONAGUA, 2021), using the cross-sectional Mercator projection system, datum WGS 1984. For the calculation of climatic variables, the inverse-distance weighted (IDW) interpolation method was appropriate since they depend on the geographical location.

The map combines regions with similar climate, first dividing them into small units (cells) with similar climatological conditions. Then, the IDW computes each cell values through a weighted lineal combination from a set of sample points, which is a function of the inverse distance. Surface interpolation is a dependent variable of the geographical site (ESRI, 2016), which for this study was the climatic groups and subgroups of the PCCS.

3. Results and discussion

3.1 Determination of winter climate types

Temperature data from 1951 through 2010 of almost all CS records, identified January as the coldest month of the year, except in La Yesca (December), San Marcos and Zacualpan (both in February). The lowest T_{pb}, T_{min} and T_{max} on that month were measured in Las Bayas (–6.6, –1.7 and 17.7 ºC) and Tenzompa (–3.9, 0.8 and 22.1 ºC) (Fig. 2); the highest, in El Carrizal (14.5, 17.7 and 32.4 ºC).

CS were assigned to the following type of winter climates: 17 stations in tropical zone (Tp [hot], tP [warm]); five in the citric zone (Ct [tropical], Ci [typical]); and three in the oat zone (av) (Table V).

3.2 Determination of summer climate types

All of the CS recorded $T_{pb} > 2.0$ ºC all year round (i.e., frost free), except for Amatlán de Cañas (11 months of FFP_{min}); Bolaños, Hostotipaquillo and San Juan Peyotán (nine months); Tepic (five months); San Gregorio and Tenzompa, (four months); and Las Bayas (none). Also, all WS recorded a 12-month FFP_{avail} except Las Bayas, San Gregorio and Tenzompa, which registered FFP_{avail} during one, six and seven months, respectively.

Table IV. Climate patterns of Mexico according to Papadakis (1970).

Humidity pattern	Characteristics
Humid	$HI_A > 1$, Ln (%) > 0.20 of PET
	HU: all months wet
	Hu: at least one month dry
Monsoon	Humid monsoon (MO): Ln (%) > 0.20 of PET and $HI_A > 0.88$
	Dry monsoon (Mo): Ln (%) < 0.20 of PET; $0.44 < HI_A < 0.88$
	Semiarid monsoon (mo): $HI_A < 0.44$
Desert	Desert: all months with T > 15 ºC are dry; $HI_A < 0.22$
	Absolut desert (da): $HI_m < 0.25$, for all months with $T_{max} > 15$ ºC, $HI_A < 0,09$
	Mediterranean desert (de): not dry enough for da; winter rainfall greater than summer
	Monsoon desert (do): not dry enough for da; July-August less dry than April-May
	Isohigro desert (di): not da, nor de or do

PET: potential evapotranspiration; HIA: annual humidity index; HIm: monthly humidity index; Ln: lixiviated rainfall; Tmax: average of maximum temperatures.
Special diagnostics: the complete list of 186 diagnostics is not included in this document. For more information refer to Papadakis (1970).

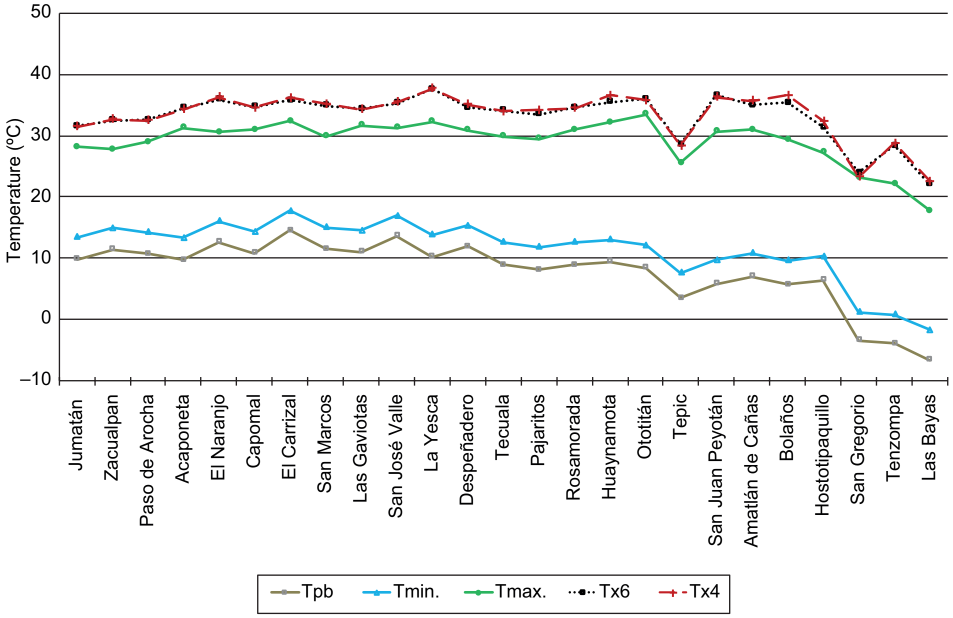

Fig. 2. Temperature records for coldest months (December-February) in participating climate stations (1951 to 2010).

Table V. Climatic groups of the study zone based on Papadaki’s Climate Classification System (PCCS) (1970).

Weather station	Groupand subgroup	SD*	Climatic Group	Climatic Subgroup	Winter type	Summer ype	Humidity Pattern	Area (ha)**
Jumatán	1.32	4, 63	Tropical	Marine savanna tropical	Tp	g	Mo	72 603.56
Zacualpan	1.32	4, 63	Tropical	Marine savanna tropical	Tp	g	Mo	
Paso de Arocha	1.37	4, 63, 95	Tropical	Marine savanna tropical	Tp	g	MO	
Acaponeta	1.42	64	Tropical	Continental savanna tropical	Tp	G	Mo	504 856.40
El Naranjo	1.42	64	Tropical	Continental savanna tropical	Tp	G	Mo	
Capomal	1.42	64	Tropical	Continental savanna tropical	Tp	G	Mo	
El Carrizal	1.42	64	Tropical	Continental savanna tropical	Tp	G	Mo	
San Marcos	1.42	64	Tropical	Continental savanna tropical	Tp	G	Mo	
Las Gaviotas	1.42	64	Tropical	Continental savanna tropical	Tp	G	Mo	
San José Valle	1.42	64	Tropical	Continental savanna tropical	Tp	G	Mo	
Despeñadero	1.533	35	Tropical	Semiarid tropical	Tp	G	mo	1010 722.42
La Yesca	1.534	0	Tropical	Semiarid tropical	Tp	G	mo	
Tecuala	1.915	36	Tropical	Cool-winter tropical	tP	G	Mo	893 481.53
Pajaritos	1.915	36	Tropical	Cool-winter tropical	tP	G	Mo	
Rosamorada	1.915	36	Tropical	Cool-winter tropical	tP	G	Mo	
Ototitán	1.916	35	Tropical	Cool-winter tropical	tP	G	mo	
Huaynamota	1.917	33	Tropical	Cool-winter tropical	tP	G	mo	
San Gregorio	2.4	1	Cold land	High cold land $^{\beta}$	av	t	Hu	
Tenzompa	2.44	1	Cold land	High cold land $^{\beta}$	av	t	mo	
Las Bayas	2.6	1	Cold land	High Andine $^{\beta}$	av	a	Mo	
Tepic	4.24	0	Subtropical	Continental subtropical	Ci	g	Mo	191 950.46
Bolaños	4.31	32	Subtropical	Continental semitropical	Ct	G	mo	88 485.63
San Juan Peyotán	4.321	33	Subtropical	Continental semitropical	Ct	G	mo	
Amatlán Cañas	4.321	35	Subtropical	Continental semitropical	Ct	G	mo	
Hostotipaquillo	4.4	106	Subtropical	Marine semitropical $^{\beta}$	Ct	g	mo	

Winter types: av: *Avena* (oats) zone; Ct: citrus zone (average daily maximum of the coldest month > 21 ºC); Ci: citrus zone (average daily maximum of the coldest month between 10-21 ºC), Tp: tropical zone (average of the lowest coldest month > 7 ºC, average daily minimum of the coldest month between

13-18 ºC); tP: tropical zone (as for Tp, but average daily minimum of the coldest month between 8-13 ºC, average daily maximum of the coldest month >21 ºC).

Spring types: a: Andine-Alpine zone; G: *Gossypium* (cotton) zone (average daily maximum of the warmest month > 33.5 ºC); g$^{\text{Þ}}$: *Gossypium* (cotton) zone (as for G, but average daily maximum of the warmest month < 33.5 ºC); t: *Triticum* (wheat) zone.

Humidity regimen: MO: rainy monsoon; Mo: dry monsoon; mo: semiarid monsoon; Hu: humid.

*Special diagnostics: the complete list of 186 diagnostics is not included in this document (or more information refer to Papadakis, 1970); **climatic subgroups determined by PCCS, however WS located outside the state of Nayarit.

La Yesca (40.6 ºC) was the WS with the highest T_{max} value, whereas Las Bayas (23.4 ºC) had the lowest; T × 6 of La Yesca was 37.6 ºC and for Las Bayas 22 ºC; T × 4 for the same WS was 37.6 and 22.55 ºC, respectively (Fig. 2). According to the data obtained, the number of CS assigned to types of summer climates were as follows: 23 to the cotton zone (17 to the hottest [G]; five to the mild hot or warm [g]); one to an alpine zone (a), and two to the wheat zone (t) (Table V).

3.3 Humidity pattern determination

According to the humidity patterns, CS with extreme rainfall values were Paso de Arocha (1685.4 mm) and Bolaños (593.3 mm); extreme PET values were observed in San Juan Peyotán (2797.68 mm) and Las Bayas (1188.32 mm); in the rest of the CS, intermediate amounts were recorded (Fig. 3). However, all CS had higher PET values than P, which indicates an important water flow across the soil-plant-atmosphere system. As for the water balance, the highest PET value was recorded at La Yesca (–2028.16 mm). The WS with lowest P-PET values were San Gregorio (–89.2 mm) and Paso de Arocha (–106.59 mm).

The number of CS that exhibited a particular hydric pattern were: one humid (Hu) ($HI_A > 1$ and $L_n > 20\%$) and 24 monsoon (14 dry monsoon [Mo; $0.44 < HI_A < 0.88$ and $L_n < 20\%$]; 9 semi-arid monsoon [mo; $HI_A < 0.44$]; and one rainy monsoon [MO; $HI_A > 0.88$]) (Table IV). CS were associated with three climate groups, according to the winter and summer types, hydric patterns and special diagnostics (Table V). Nevertheless, subtropical and tropical climatic groups are found only in Nayarit. The cold land group was registered in WS located in surrounding states (Table V).

3.4 Agroclimatic zoning and recommended crops

Figure 4 shows the agroclimatic zoning of the state of Nayarit, followed by the analysis based on the three climatic groups and the respective subgroups identified.

3.4.1 Tropical climate group

3.4.1.1 Cool-winter tropical subgroup

Non-irrigated winter potato (*Solanum tuberosum* L.) and rice (*Oryza sativa* L.) render high yields. Olives and grapes also grow well; however, since the summer is long and humid, they require fungicides and growth regulators for pest control and the use of irrigation during the dry season as well. Marginal progress is observed on winter cereals such as oat (*Avena sativa* L.), barley (*Hordeum vulgare* L.), rye (*Secale cereale* L.) and wheat (*Triticum aestivum* L.);

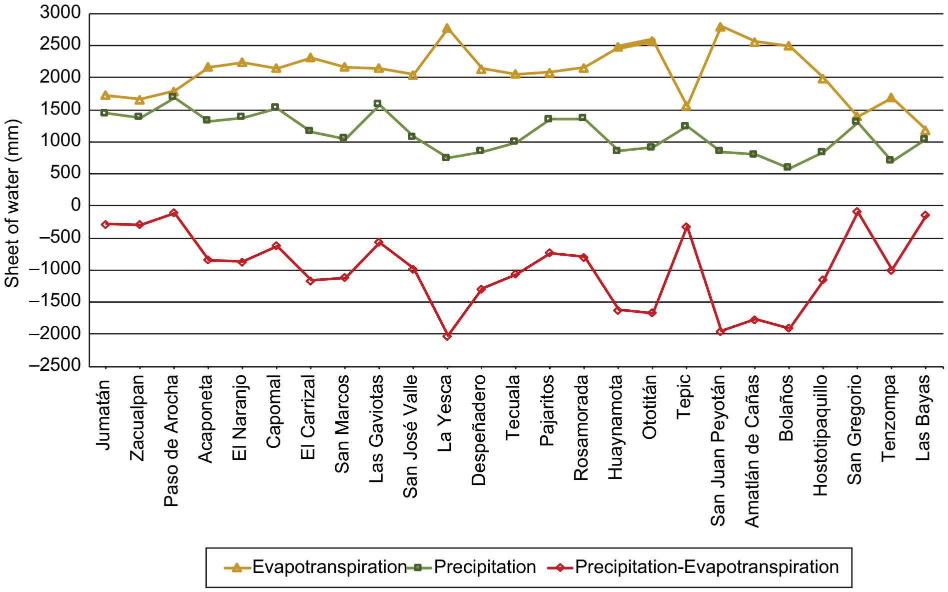

Fig. 3. Annual hydric pattern of the climate stations in the study (1951 to 2010).

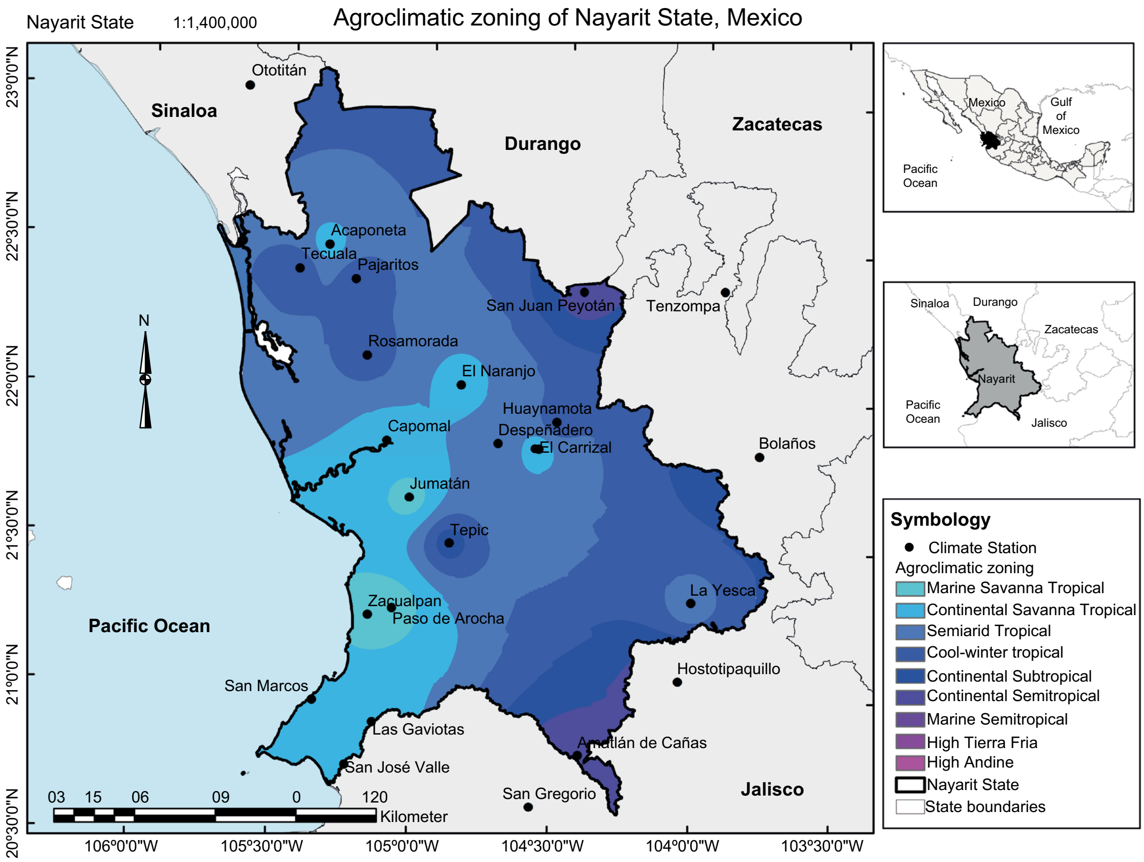

Fig. 4. Agroclimatic zoning of the state of Nayarit, Mexico.

and summer cereals such as rice, corn (*Zea mays* L.), temperate millet (*Panicum miliaceum* L.), pearl millet (*Pennisetum cinereum* Stapf & C.E. Hubbard) and sorghum (*Sorghum bicolor* [L.] Moench). All of them need irrigation, fertilizers and growth regulators, and require close attention to sowing dates: grains are hard to store when harvested during the wet season, whereas in the dry season, they could be damaged.

Therefore, it is recommended to sow at the beginning of the wet period, even though the harvest will take place under rainy weather. For instance, corn is sowed at the start the wet season, whereas sorghum and millet are sowed afterwards in order to be harvested and stored in the dry period. Non-irrigated rice is planted if the dry season is longer than five months, but the storage may turn difficult when it is harvested during rainfall. In all cases, there is a need of fertilizers, growth regulators and grain driers. Table VI shows recommended crops for Nayarit according to PCCS groups and subgroups identified.

3.4.1.2 Continental tropical savanna subgroup

The continental savannah subgroup is excellent for irrigated banana and citric. Coconuts (*Cocos nucifera* L.) grow in high water-retention capacity soils; cotton has low yields and may develop sanitary problems; and forages may grow with low quality. This type of climate has the same features as the cool-winter tropical for winter and summer cereals described before. Sugar cane and forages grow with poor sugar content and nutrients, hence the need for growth regulators and nitrogen-based fertilizers, respectively.

3.4.1.3 Marine tropical savanna subgroup

Summer cereals are planted in regions with tropical marine savannah climate, using growth and respiratory regulators to control the effect of warm nighttime, as well as fertilizers to increase crop yields. Corn yields an optimal production if harvested during the dry season, and cotton, banana, sugar cane and citric require irrigation. This type of climate is too hot for

Table VI. Crops with improved yields, according to climate groups in Papadakis' (1970) system.

Climate group	Subgroup	Winter cereal				Summer cereal				Other crops									
		Oats	Rye	Barley	Wheat	Rice	Corn	Millet	Sorghum	Olives	Cotton	Banana	Sugarcane	Citric	Forage	Potato	Beetroot	Tea	Grapes
Tropical	Cool-winter tropical	-	-	-	-	✓	✓	✓	✓	✓	-	-	✓	✓	-	✓	-	-	✓
	Continental savanna tropical	-	-	-	-	✓	✓	✓	✓	-	✓	✓	✓	✓	-	-	-	-	-
	Marine savanna tropical	-	-	-	-	✓	✓	✓	✓	-	✓	✓	✓	✓	-	-	-	-	-
	Semiarid tropical	-	-	-	-	✓	✓	✓	✓	-	✓	✓	✓	✓	✓	-	-	-	-
Subtropical	Marine semitropical	✓	✓	✓	✓	✓	✓	-	-	-	-	-	✓	✓	-	✓	-	-	-
	Continental semitropical	✓	✓	✓	✓	✓	✓	-	✓	✓	✓	✓	✓	✓	✓	✓	✓	-	✓
	Subtropical continental	✓	✓	✓	✓	✓	✓	✓	✓	✓	✓	✓	✓	✓	✓	✓	✓	-	✓
Cold land	High Andine	-	-	-	-	-	✓	-	-	-	-	-	-	-	-	✓	-	-	-
	High cold land	✓	✓	✓	✓	✓	✓	✓	✓	-	-	-	✓	-	-	✓	-	-	-

coffee (*Coffea* spp.) and beet crops (i.e., very low yields). Forages produce low-protein levels.

3.4.1.4 Semiarid tropical subgroup

Semiarid tropical climate is good for irrigated summer cereals, and renders good yields if growth regulators and fertilizers are used and harvesting takes place during the dry season. Protein content in forage grains is usually low. Banana (with irrigation), sugar cane, and non-irrigated cotton and citric grow efficiently. According to Díaz-Padilla et al. (2012), Nayarit exhibits excellent agroclimatic conditions to increase the cropland for Persian lime (*Citrus latifolia* Tan.) production. These authors identified 418 000 ha with high potential productivity for this crop.

3.4.2 Subtropical climate group

3.4.2.1 Marine semitropical subgroup

Winter cereals are produced properly by irrigation or in rainwater storing soils. Potato is an autumn or spring crop, whereas sugar cane corresponds to winter season. Summer cereals need no irrigation; however, rice grows better when is irrigated. On the other hand, millet and sorghum are more affected than corn due to warmer nights. This climate is humid, therefore, inadequate for cotton. Citrus may grow well without irrigation, whereas banana and sugar cane thrive in FFP regions. Fertilizers and growth regulators in winter and summer cereals increase crop yields.

3.4.2.2 Continental semitropical subgroup

Winter and summer cereals such as non-irrigated sorghum, irrigated corn and rice grow well in the absence of low temperatures. Warm nights in summer enhance crops growth. In some cases, accelerated growth affects sugar storage and nutrition of plants, hence, growth regulators and nitrogen-based fertilizers are needed to overcome the problem and still obtain good yields. The warmer nights of summer time foster the growth of all crops; therefore, the use of nitrogen-based fertilizers in addition to grow regulators is recommended to obtain better yields.

Other irrigated crops for this type of climate with FFP are cotton, alfalfa (*Medicago sativa* L.), banana and citric (favors orange's color); sugar cane is recommended where winter presents few freezing events; olives and grapes grow well where one or more months are humid, but it is possible to face disease problems in plants and excessive root grow. Spring and autumn potato are good for short winters, and beet for winter.

3.4.2.3 Continental subtropical subgroup

In zones with continental subtropical climate, recommended crops are irrigated alfalfa, banana and citric (in FFP), winter cereals, beet and spring or autumn potato where winter cold gets mild. Fertilizers and growth regulators are necessary in order to render good yields, since summer nights tend to be warmer. Olives and grapes grow well without irrigation in zones where one or two months of summer are humid; however, only some types of summer cereals are appropriate.

3.4.3 Cold land climate group

3.4.3.1 High Andean subgroup

This climate is too cold for winter crops, such as sugar cane and potato (except wild potato [*S. acaule* Bitter]). As for winter cereals, only corn grows but with restrictions, due to low temperatures reached at night. Lowest temperatures recorded in this type of climate are also inconvenient for cotton, banana, coffee, citrus and tea.

Winter cereals may be planted in spring or autumn, but irrigation and fertilizer applications are necessary. For middle-term crops, such as sugar cane and potato, irrigation is compulsory, although it could be expensive for the farmer. This climate is rather cold-fresh for summer cereals, but corn may grow with the limitations imposed by cold nights. It is not recommended for cotton, banana, coffee, citrus and tea.

3.5 Agroclimatic zoning of PCCS and its relation to the climatic conditions of Nayarit

Based on García's classification system (García, 2004), the main climate types distributed across the state's surface are hot subhumid with summer rainfall (60.63%), and warm subhumid with summer rainfall (30.96%) (INEGI, 2018). Comparing this information with our study results, we found similar characteristics matching the tropical and subtropical climatic groups of the PCCS. respectively, where most of the WS are located (Fig. 1).

The largest surface area when zoning with the PCCS corresponded to semiarid tropical climate (1 010 722.42 ha), whereas the marine tropical savanna subgroup had the least (72 603.56 ha) (Table V). Irrigated farmland area (219 817.95 ha) was smaller than dryland agriculture area (299 361.56 ha) (Fig. 5).

Hernández et al. (2018) compared the Köppen Climate Classification (modified by García, 1964) with the Worldwide Bioclimatic Classification System (Rivas-Martínez et al., 2011) in Mexico, identifying coincidences regarding humid conditions. For Nayarit, Hernández et al. (2018) determined tropical macrobioclimate, tropical-season rain bioclimate, and tropical xeric, as the three highest ranking units according to summer climates and intermediate humidity patterns (in both systems). These results have also similar features than the tropical and subtropical climate groups of the present study.

3.6 PCCS applications versus other agroclimatic zoning methods

PCCS is a useful tool for adequate crop planning, based on the main climatic factors of a particular area. Halabian et al. (2014) used this methodology in Iran (East-Azerbaijan province), where they identified the climate types across the province and determined the best crops for each. The study also recommended sowing months for sugar beet, which is a very important crop for the country's economy. On the other hand, Alonso et al. (2012) analyzed the impact of climate change on the agriculture potential of 17 municipalities in Cantabria (Spain), using agroclimatic zoning by means of the PCCS. Their study disclosed the ecological requirements for 14 crops, as well as the agricultural boost of cranberries (*Vaccinium uliginosum* L.) and grapevines (*Vitis vinifera* L.) in the territory.

In Venezuela, Colotti (1997) evaluated different classifications of common use in agroclimatology, among others the Thornthwaite (1948) method and PCCS, in order to identify convenient applications related to PET. Velasco and Pimentel (2010) used the same methodology for the zoning of the state of Sinaloa (northwest coast of Mexico), highlighting that PET estimation varies according to the method being used: underestimation by the Makkink method (53% of the registered evaporation) or very high

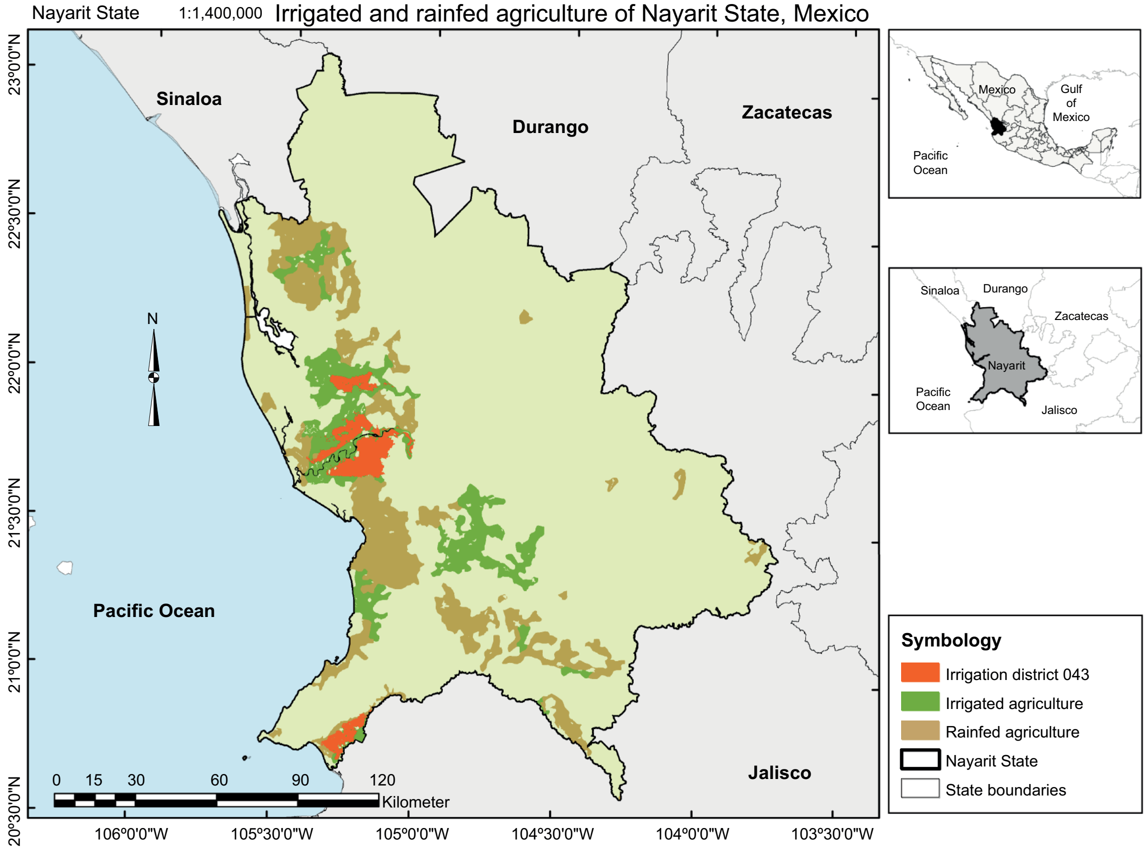

Fig. 5. Irrigated and non-irrigated agricultural zones in the state of Nayarit, Mexico.

values with the PCCS (96%). These authors recommend adapting the evaporimeter tank method and the use of monthly coefficients of evaporation (higher for dry months).

González et al. (2009) found significant differences between measured PET and calculated PET when tracing the bioclimatic map of the Mendoza grasslands (Argentina): –27.6% using the Thornthwaite method, 7.2% with PCCS, 6.7% using the Penman-Monteith method, and –6.4% with the Penman standard method. The investigations of Ortiz and Chile (2020) in the Tumbaco Valley (Ecuador) also showed fluctuations in evapotranspiration values of the reference crop (ET_0): based on FAO-56, the Makkink and evaporimeter tank methods generated lower values (11.59 and 7.29%, respectively), whilst the Hargreaves, modified Thornthwaite, FAO Radiation, Priestley and Taylor, Turcun, and Jensen and Haise methods produced higher values (41.59, 26, 11.87, 3.92. 1.46, and 0.18%, respectively).

Temporal and spatial variability of climate forced the use of different methodologies for PET estimation. Although based on meteorological data, some of these were empirically obtained through field experiments while others were theoretical approaches (Landon, 2004), such as the evaporimeter tank and the Penman-Monteith model, respectively. Some others are based on temperatures, such as the Thornthwaite and Turc method, or in temperature and solar radiation, such as the Hargreaves, Jensen & Haise, Makkink, Priestley & Taylor, FAO Radiation models (Bhabagrahi et al., 2012). Thus, model complexity, climatic variables diversity, and the varying conditions from which different models were designed, influence the fluctuating PET estimation.

It is important to bear in mind that PET implies a set of a simultaneous process of water loss: soil evaporation and plant transpiration. Apart from water availability in the surface horizon, soil evaporation depends on the solar energy it receives, which decreases along the crop cycle: at the beginning, water is lost through the former mechanism; later, as the crop progresses and the water layer covers up, the latter mechanism takes place. These are features taken into consideration by the FAO method for PET calculation, in addition to soil moisture, soil fertility and use of fertilizers, soil management practices, presence of hard breaking horizons and salinity, regarding soil-related variables; and plant cover and density, disease control and parasite presence regarding plant-related variables (Allen et al., 1998, 2006).

For this reason, FAO (Allen et al., 2006) suggests the FAO Penman-Monteith (FAO-56 PM) as the most precise method for PET calculation based on climatic parameters, suitable for arid and humid climate estimations, which incorporates physiological and aerodynamic parameters as well: (i) aerodynamic resistance (atmospheric evaporative demand according to climate variables such as temperature, relative humidity, sunlight hours, wind, altitude and latitude); (ii) crop surface resistance (water flood diffusion from roots to plant stomata and direct water evaporation from soil), and (iii) albedo (solar radiation reflected by the crop), using a reference crop (grass height of 0.12 m, irrigated with a total cover of soil surface) with surface resistance of 70 s m^{-1} and 0.23 of albedo (Allen et al., 2006).

From this standpoint, PCCS is an empirical method that uses equations with a minimum of meteorological variables ($T_{\max}$ and $T_{\min}$) for PET calculation, regardless of crop characteristics and soil factors; hence, calculated values may differ from those estimated by other methods. When computing water balance and analyzing historical monthly PET, this study found that all WS recorded the highest PET in May, except for La Yesca and San Gregorio (both in April), San Marcos (August) and Zacualpan (November).

There were five periods of six months each, where PET was highest: from January to June (Acaponeta, Amatlán de Cañas, Despeñadero, El Carrizal, Jumatán, Las Gaviotas, La Yesca, Ototitán, Pajaritos, Paso de Arocha, Rosamorada, San Gregorio and Tepic), February to July (Bolaños, Capomal, El Naranjo, Hostotipaquillo, Huaynamota, Las Bayas, San Juan Peyotán and Tecuala), March to August (San José Valle and Tenzompa), June to November (San Marcos), and July to December (Zacualpan). This allowed to identify that in the first two periods (January-June and February-July) PET records were the highest in 52 and 36% of WS, respectively.

Seven periods of different duration were also identified where PET was greater than P for all months: 56% of WS from October to June, and all-year round in Bolaños (Table VII). PET estimations with the PCCS method were conclusive to determine the humidity pattern of the WS in this study, and thus for the agroclimatic zoning of Nayarit. Results indicate that crop selection across the state must be done according to the water deficit of those months, in order to ensure optimal yields.

Jiménez et al. (2004) state that, undoubtedly, climate is one of the main factors a farmer should always take into account, providing its influence over plants' growth and maturation. Nevertheless, these authors outlined the importance of analyzing the soil and the crop as an integrated system, otherwise, there is a risk of an incomplete and unreliable zoning. For instance, in their study to determine potentially agricultural zones for sugar cane production in the south of Tamaulipas (northeast Mexico), they realized that if only climate was analyzed (agroclimate zoning), 86.9% of the territory was set as very suitable for that crop and 13.1% only suitable. However, when they included soil characteristics (such as units, phases, textures and slopes), only 40% of the territory was set as suitable for sugar cane (Jiménez et al., 2004).

Díaz et al. (2000) concluded that crop adaptability analysis is insufficient if no other information is taken into account, especially soil characteristics. In an agroecological zoning study of coffee (*Coffea arabica* L.) and camedor palm (*Chamaedorea elegans* Mart.) agroforestry systems conducted in Veracruz, Mexico, Pérez-Portilla and Geissert-Kientz (2006) found that temperature and water availability explain 70% of crop distribution within the study area, and soil characteristics only account for 45%. In other words, the distribution of agroforestry systems is defined in low temperatures by a less cold-weather tolerance of coffee plants, but not for fertility and stone content of the soil. Hence, the corresponding analysis between crop suitability and the presence of the agroforestry system only matched regarding climate. Ohmann and Spies (1998) support the findings when they assert the secondary role of soil in the distribution of species at low-level scale.

Table VII. Historical monthly evapotranspiration of WS from Nayarit (Mexico) and its surroundings (1951-2010).

Weather stations	Months with PET > P (mm)	Months with P > PET (mm)
Acaponeta, Capomal, El Carrizal, El Naranjo, Jumatán, La Bayas, Las Gaviotas, Ototitán, Pajaritos, Paso de Arocha, Rosamorada, San Marcos, San José Valle and Tecuala	October to June	July to September
Despeñadero, Hostotipaquillo, Huaynamota y Tenzompa	September to June	July and August
Tepic and Zacualpan	October to May	June to September
Amatlán de las Cañas and La Yesca	August to June	July
Bolaños	All-year round	-
San Gregorio	November to May	June to October
San Juan Peyotán	September to July	August

PET: potential evapotranspiration; P: precipitation.

In similar studies, Medina and Aldana (2019) compared the Caldas-Lang & Holdridge climate classification method to the climate soil zoning in Valle del Cauca (Colombia). The outcomes of the study provided valuable knowledge about climate conditions associated with soil formation and enhanced the assessments over soil use and management in the basin. For this reason, FAO (1997) insists that by integrating soil components into zoning methodologies, the agroecological approach (as opposed to only climatic) has the advantage of evaluating suitability and land potential productivity as well. This underpins more advanced studies focusing on potential crop projection areas, harvest and production, which in turn allows for the evaluation of land degradation and sustainability capacity, as well as generating optimization models for land use in cattle farming.

All aforementioned highlights PCCS limitations: (i) PET estimations may differ from other methods, as PET is computed with a minimum of meteorological variables, however, this could become an advantage if data availability from WS is rather scarce (climatic, soil-related and of the crops themselves); (ii) overlook of crop characteristics and soil factors; (iii) few crops inclusion and, in the case of Mexico, very few fruit trees, and (iv) loose precision in crops of tea types.

In Mexico, agroclimatic zoning studies are scarce, and even more those comparing methodologies for the same zone aiming to suggest the most suitable crops to render optimal yields. Therefore, as a result of recurrent limited information available and its less complex construction, PCCS arise as a useful tool for crop planning according to the climatic variables of a region.

4. Conclusions

In the agroclimatic zoning of the state of Nayarit by means of the Papadakis' climate classification system, three climatic groups and nine sub-groups were identified. Sugar cane, winter and summer cereals, and citrus, are suitable for tropical and subtropical climatic groups. For cold land, the recommended crops are corn and potato. In most cases, the crops may require irrigation, fertilizers and other supplies to increase yields. This productivity framework may be implemented by agreements with the farmworkers and sustained by cost-quality studies for the decisions on crop selection.

Zoning studies are strategies to increase agricultural productivity by an adequate crop management, and the proper use of modern technology, pest and plant diseases control, or even to introduce new crops or varieties in areas with clearly defined environmental characteristics. In addition, they become an excellent tool for economic and social analysis of deficit produces, national and international farm market balances and export perspectives as well. The importance of this type of studies lies in the definition of crops with the best ecological perspectives, according to the available resources within a specific area. Among PCCS limitations are: PET estimations may differ from other methods, as PET is computed with a minimum of meteorological variables; overlook of crop and soil characteristics; few crops inclusion and, in the case of Mexico, very few fruit trees and loose precision in crops of tea types.

References

Aguilar RN, Galindo M, Fortanelli M, Contreras SC. 2010. Evaluación multicriterio y aptitud agroclimática del cultivo de caña de azúcar en la región de Huasteca (México). Revista Corpoica-Ciencia y Tecnología Agropecuaria 11: 144-154.

Allen RG, Jensen ME, Wright JL, Burman RD. 1989. Operational estimates of reference evapotranspiration. Agronomy Journal 81: 650-662. https://doi.org/10.2134/agronj1989.00021962008100040019x

Allen RG, Pereira LS, Raes D, Smith M. 1998. Crop evapotranspiration: Guidelines for computing crop water requirements. FAO Irrigation and Drainage Paper 56. Food and Agriculture Organization of the United Nations, Rome, 328 pp.

Allen RG, Pereira L, Raes D, Smith M. 2006. Evapotranspiración del cultivo. Guías para la determinación de los requerimientos de agua de los cultivos. FAO Riego y Drenaje 56. Food and Agriculture Organization of the United Nations, Rome, 322 pp.

Alonso FJ, Bedia J, Bruschi V, Fernández JM, Ferrer F, Francés E, Gutiérrez JM, Herrera S. 2012. Impacto del cambio climático en el territorio de la mancomunidad de municipios sostenibles de Cantabria: Resultados aplicables a la gestión del territorio. In: VIII Congreso Internacional Asociación Española de Climatología: Cambio climático. Salamanca.

Bhabagrahi S, Imtisenla W, Bidyut D, Bhagwati B. 2012. Standardization of reference evapotranspiration models for a subhumid valley rangeland in the eastern Himalayas. Journal of Irrigation and Drainage Engineering 138: 880-895. https://doi.org/10.1061/(ASCE)IR.1943-4774.0000476

Bojórquez I, Nájera O, Hernández A, Flores F, González A, García D, Madueño A. 2006. Particularidades de formación y principales suelos de la llanura costera norte del estado de Nayarit, México. Cultivos Tropicales 27: 19-26.

Colotti BE. 1997. Evaluación de algunas clasificaciones agroclimáticas. Revista Terra 13: 189-201.

Conabio. 2008. Catálogo de metadatos geográficos. Available at: http://www.conabio.gob.mx/informacion/metadata/gis/destdv250k_2gw.xml?_httpcache=yes&_xsl=/db/metadata/xsl/fgdc_html.xsl&_indent=no (accessed on October 19, 2018).

Conagua. 2018. Estadísticas agrícolas de las unidades de riego. Año agrícola 2016-2017. Comisión Nacional del Agua, Mexico. Available at: https://files.conagua.gob.mx/conagua/publicaciones/Publicaciones/SGIH-3-18.pdf (accessed on April 16, 2021).

Conagua. 2021. Distritos y unidades de riego. Comisión Nacional del Agua, Mexico. Available at: http://sina.conagua.gob.mx/sina/tema.php?tema=distritosriego&ver=mapa (accessed on April 16, 2021).

Díaz HB, Plascencia V, Arteaga R, Vázquez P. 2000. Estudio y zonificación agroclimáticos en la región Altos de Chiapas, México. Investigaciones Geográficas 42: 7-27.

Díaz-Padilla G, Guajardo-Panes RA, Medina-García G, Sánchez-Cohen I, Soria-Ruíz J, Vázquez-Alvarado JMP, Quijano-Carranza JA, Legorreta-Padilla F, Ruíz-Corral JA. 2012. Potencial productivo de especies agrícolas de importancia socioeconómica en México. Instituto Nacional de Investigaciones Forestales, Agrícolas y Pecuarias, Mexico.

Elías C, Castelli SF, Bosh A. 2001. Clasificaciones climáticas. Agrometeorología. Ediciones Mundi-Prensa, Madrid.

ESRI. 2016. Cómo funciona IDW. Available at: https://desktop.arcgis.com/es/arcmap/10.3/tools/spatial-analyst-toolbox/how-idw-works.htm (accessed on October 19, 2018).

FAO. 1997. Zonificación agro-ecológica. Guía general. Boletín de Suelos 73. Food and Agriculture Organization of the United Nations, Rome. Available at: http://www.fao.org/3/W2962S/w2962s04.htm (accessed on March 20, 2021).

García E. 1964. Modificaciones al sistema de clasificación climática de Köppen (para adaptarlo a las condiciones de la República Mexicana). 5a. ed. Instituto de Geografía, UNAM, Mexico.

García E. 2004. Modificaciones al sistema de clasificación climática de Köppen. Instituto de Geografía, UNAM, Mexico.

Gobierno del Estado de Nayarit-SAGARPA. 2010. Diagnóstico sectorial en el estado de Nayarit. Asesoría Técnica Investigación y Servicios Agropecuarios, Nayarit, Mexico.

Gobierno del Estado de Nayarit-INEGI. 2017. Anuario estadístico y geográfico de Nayarit 2017. Instituto Nacional de Estadística y Geografía Nayarit, Mexico.

González LM, Menenti M, Diblasi MA. 2009. Mapa bioclimático para las travesías de Mendoza (Argentina) basado en la fenología foliar. Revista de la Facultad de Ciencias Agrarias XLI: 105-122.

Halabian AH, Dehghanpoor FA, Azizi M, Ganjali J. 2014. Disclosing the effect of climatic factors on the growth and yield of sugar beet in province Azerbaijan East. Journal of Biodiversity and Environmental Sciences 5: 431-441.

Hernández ME, Ordóñez MJ, Giménez J. 2018. Análisis comparativo de dos sistemas de clasificación bioclimática aplicados en México. Investigaciones Geográficas 95: 1-14. https://doi.org/10.14350/rig.57451

IIEG. 2020. Boletín económico anual 2019. Instituto de Información Estadística y Geográfica, Gobierno del Estado de Jalisco, México, 37 pp.

INEGI. 2011. Anuario estadístico de Nayarit 2011. Instituto Nacional de Estadística y Geografía, Mexico.

INEGI. 2018. Aspectos geográficos. Nayarit. Instituto Nacional de Estadística y Geografía, Mexico.

IUSS Working Group WRB. 2015. World reference base for soil resources 2014, update 2015. International soil classification system for naming soils and creating legends for soil maps. World Soil Resources Reports No. 106. Food and Agriculture Organization of the United Nations, Rome, 203 pp.

Jiménez CA, Vargas TV, Salinas C, Aguirre B, Rodríguez C. 2004. Aptitud agroecológica para el cultivo de la caña de azúcar en el sur de Tamaulipas, México. Investigaciones Geográficas, 53: 58-74.

Landon R. 2004. An evaluation of reference evapotranspiration models in Louisiana. Louisiana State University, USA.

Lozada G, Sentelhes P. 2008. Modelos de estimación de las temperaturas promedio de la mínima, máxima y media diaria para la región Andina de Venezuela. Agronomía Tropical 58:141-153.

Lozano J, Delgado H, Ortega E, Pérez-Blanco E, Asensio C. 2000. Uso de suelos para el cultivo de cereales en el término de Cuevas del Becerro (Málaga). Edafología 7: 105-112.

Medina AE, Aldana OE. 2019. Análisis comparativo de las zonificaciones climáticas de Caldas-Lang y Holdridge, con la zonificación del clima edáfico del estudio semidetallado de suelos, en la cuenca del río Cauca, departamento del Valle del Cauca. M. Sc. thesis. Universidad Santo Tomás, Bogotá, Colombia.

Ohmann JL, Spies TA. 1998. Regional gradient analysis and spatial pattern of woody plant communities of Oregon forest. Ecological Monographs 2: 151-182.

Ortiz C, Chile A. 2020. Métodos de cálculo para estimar la evapotranspiración de referencia para el Valle de Tumbaco. Siembra 7: 70-79. https://doi.org/10.29166/siembra.v7i1.1450

Papadakis J. 1970. Climates of the world: Their classification, similitudes, differences and geographic distribution. Edited by the author, Buenos Aires, Argentina.

Pérez-Portilla E, Geissert-Kientz D. 2006. Zonificación agroecológica de sistemas agroforestales: el caso café (*Coffe aarabica* L.)-Palma Camedor (*Chamaedor eaelegans* Mart.). Interciencia 31: 556-562.

Rivas-Martínez S, Rivas-Sáenz S, Penas A. 2011. Worldwide bioclimatic classification system. Global Geobotany 1: 1-634. https://doi.org/10.5616/gg110001

SIAP. 2019. Anuario estadístico de la producción agrícola. Servicio de Información Agroalimentaria y Pesquera, Mexico. Available at: https://nube.siap.gob.mx/cierreagricola/ (accessed on August 04, 2020).

SIAP. 2021. Nayarit. Infografía agroalimentaria 2021. Servicio de Información Agroalimentaria y Pesquera, Mexico. Available at: https://nube.siap.gob.mx/infografias_siap/pag/2021/Nayarit-Infografia-Agroalimentaria-2021

SMN. 2019. Normales climatológicas por estado. Available at: https://smn.conagua.gob.mx/es/climatologia/informacion-climatologica/normales-climatologicas-por-estado (accessed on January 20, 2019).

Thornthwaite CW. 1948. An approach towards a rational classification of climate. Geographical Review 38: 55-94. https://doi.org/10.2307/210739

Velasco I, Pimentel E. 2010. Zonificación agroclimática de Papadakis aplicada al estado de Sinaloa, México. Investigaciones Geográficas 73: 86-102.

Villa CM, Inzunza I, Catalán V. 2001. Zonificación agroecológica de hortalizas involucrando grados de riesgo. Terra Latinoamericana 19: 1-7.

White DH, Lubulwa G, Menz K, Zuo H, Wint W, Slingenbergh J. 2001. Agro-climatic classification systems for estimating the global distribution of livestock numbers and commodities. Environment International 27: 181-187. https://doi.org/10.1016/S0160-4120(01)00080-0

Zamudio V, Méndez E. 2011. La vulnerabilidad de erosión de suelos agrícolas en la región centro-sur del estado de Nayarit, México. Ambiente y Desarrollo XV: 12-40.

Atmósfera 36(1), 143-154 (2023)
https://doi.org/10.20937/ATM.53027

Partial COVID-19 lockdown effect in atmospheric pollutants and indirect impact in UV radiation in Rio Grande do Sul, Brazil

Adriana BECERRA-RONDÓN[1]*, Jorge DUCATI[1] and Rafael HAAG[2]

[1] *Centro Estadual de Pesquisas em Sensoriamento Remoto e Meteorologia, Universidade Federal do Rio Grande do Sul, Av. Bento Gonçalves, 9500, Porto Alegre, RS, Brazil.*
[2] *Universidade Estadual do Rio Grande do Sul, Av. Bento Gonçalves, 8855, Porto Alegre, RS, Brazil.*
*Corresponding author; email: abecerrarondon@gmail.com

Received: January 11, 2021; accepted: May 27, 2021

RESUMEN

La pandemia de COVID-19 redujo notablemente las actividades industriales y otras intervenciones antrópicas sobre el ambiente, lo cual disminuyó la emisión de gases contaminantes y aerosoles. El monitoreo de la calidad del aire comúnmente es desempeñado por estaciones automatizadas, las cuales proporcionan información precisa casi en tiempo real; no obstante, están sujetas a problemas de mantenimiento y no permiten alcanzar una cobertura total de grandes áreas geográficas. Alternativamente, los sensores orbitales proporcionan información detallada de grandes áreas a bajo costo. En consecuencia, este estudio tuvo por objeto analizar el efecto del cese parcial de actividades por la COVID-19 sobre los contaminantes atmosféricos y su impacto indirecto sobre la radiación UV en Rio Grande do Sul, Brasil. Analizamos la concentración de dióxido de nitrógeno (NO_2), ozono total (O_3) e índice ultravioleta (UVI) adquiridos por el sensor OMI (a bordo del satélite Aura), durante mayo, para los periodos de 2010 a 2018, 2019 y 2020. Calculamos las diferencias durante estas tres series temporales. Los resultados mostraron reducciones de hasta 33.9% del NO_2 en la mayor parte del área de estudio, acompañadas de incrementos de hasta 3.5% en el ozono total y hasta 4.8% en el UVI. Aunque el NO_2 desempeña un papel fundamental en la química estratosférica, nuestros resultados sugieren que su disminución en 2020 no tuvo incidencia directa en el incremento de O_3; sin embargo, el NO_2 fue en parte responsable del incremento en el UVI, que a su vez provocó calentamiento en la estratosfera y aumento del O_3.

ABSTRACT

The COVID-19 pandemic introduced a significant decrease in industrial activities and other anthropogenic interventions on the environment, followed by a reduction of the emission of pollutant gases and aerosols. Monitoring of air quality is commonly performed through automatic stations, which can provide nearly real-time, accurate information. However, stations located in urban areas are subject to maintenance problems and extensive coverage for large areas is not feasible. As an alternative approach, data from orbital sensors can provide useful information for large areas at a low cost. Consequently, this study aimed to analyze the partial COVID-19 lockdown effect in atmospheric pollutants and its indirect impact in UV radiation in Rio Grande do Sul, Brazil. Data on concentrations of nitrogen dioxide (NO_2), total ozone (O_3), and ultraviolet index (UVI) acquired by the OMI sensor aboard the Aura satellite were accessed for May, for the entire period 2010 to 2018, 2019, and 2020. Differences between these time series were calculated. Results showed significant reductions in NO_2 in most of the study area by as much as 33.9%, followed by increases in total ozone of up to 3.5% and the UVI by up to 4.8%. Although NO_2 plays a fundamental role in stratospheric chemistry, our results suggest that its decrease in 2020 was not directly responsible for the increase in total O_3; however, NO_2 was partially the cause for the increase in UVI, which in turn led to the heating of the stratosphere, generating an increase in O_3.

Keywords: OMI sensor, ultraviolet index, total ozone, nitrogen dioxide, southern Brazil.

1. Introduction

Ultraviolet (UV) radiation from 100 to 400 nm constitutes about 8% of the electromagnetic radiation emitted by the Sun (Robinson, 1966; de Andrade and Tiba, 2016), whereas the proportion which reaches the ground at Earth is reduced to 4% due to physical processes in the atmosphere and to additional—geographical, temporal, astronomical and others—factors (Iqbal, 1983; Huffman, 1992; Guarnieri et al., 2004; Silva et al., 2008; Fountoulakis et al., 2020). Its intensity is frequently expressed on a time basis by the Ultraviolet Index (UVI) through a dimensionless numerical scale (WHO, 2002; WMO, 2011). Despite this sharp reduction, the UV radiation reaching the ground still has the potential to induce significant damages to the primary productivity and aquatic organisms (Cardoso, 2011), in the yield of forest and crops (Caldwell et al., 2003), on the survival of amphibians as environmental indicators (Tiegte et al., 2001), while increasing the degradation of some materials and inducing alterations in photochemical reactions linked to tropospheric urban pollution (Davis and Sims, 1983). UV radiation is also known to have negative impacts on human skin, eyes, and immune system (Coariti, 2017). Therefore, the knowledge of UV spatio-temporal variability has received considerable attention from research projects (Bais et al., 2007; Kerr and Fioletov, 2008).

The main parameter modulating ultraviolet absorption is stratospheric ozone (90% of total O_3), which presents a seasonal pattern due to natural processes of formation, transport, and destruction, thus ozone concentrations are at their lowest levels in fall and highest in spring (Wakamatsu et al., 1989; André et al., 2003). However, this variability is influenced by natural phenomena and anthropogenic activities (Fahey and Hegglin, 2011; Bais et al., 2015), the latter being linked to the industrial production of nitrogen dioxide (NO_2) formed from the oxidation of nitrous oxide (N_2O) coming from the troposphere. NO_2 can attain high concentrations in the stratosphere (90% of all NO_2), where it destroys O_3 through catalytic processes by sequestering active radicals (Seinfeld and Pandis, 1998).

Changes in natural processes and phenomena, amplified or caused by human actions, can generate potential hazards both to human communities and to the environment (Cheval et al., 2020). A notable change started in the end of 2019 with the unexpected outbreak of coronavirus disease (COVID-19), later declared a "global pandemic" by the World Health Organization (WHO) in the first semester of 2020. This disease has been reported in almost all geographic areas and climatic conditions, with a great impact on both economies and environments. Zambrano-Monserrate et al. (2020) mention that the indirect impact of the pandemic on the environment has been little analyzed, and estimate that negative indirect effects would be greater than positive. Thus, studies that evaluate these impacts and how they are linked to infection and death rates are increasingly urgent and necessary to inform decision-makers at all levels (Liu et al., 2021; Paital and Agrawal, 2021; Travaglio et al., 2021; Vásquez-Apestegui et al., 2021).

Against the COVID-19 crisis, global drastic actions were taken by the majority of nations aiming to slow disease propagation. These actions had as collateral effects a significant global reduction of consumption of fossil fuels and decrease of levels of NO_2 and other atmospheric pollutants by 20 to 50%, facts that improved air quality (Tobias et al., 2020; Sharma et al., 2020; Zheng et al., 2020). South America is one of the regions most affected by COVID-19 (Zhu et al., 2020), and restrictions on most activities in Brazil started in March; as a result, drastic reductions in NO (up to 77.3%), NO_2 (up to 54.3%) and CO (up to 64.8%) were reported in São Paulo State, for the five-year monthly mean and the four-week period prior to the restrictions. On the other hand, ozone concentrations increased by 30%, possibly related to the decrease in nitrogen monoxide (Nakada and Urban, 2020; Siciliano et al., 2020).

In the state of Rio Grande do Sul a partial lockdown was declared starting on March 16 and extending for several months, with public and private recreational areas and educational centers, besides commerce in general (except food and medicine) being closed. Land transport had a 40% reduction, air transport 90%, and use of private vehicles was significantly reduced; however, industrial activities, health, and basic services were not suspended (Ubiratan, 2020; Google, 2021). This scenario offers an opportunity to evaluate variations and trends of atmospheric physical processes over an area exposed to high levels of UV radiation for being close to the Antarctic ozone hole (Kirchhoff et al., 2000; Guarnieri et al., 2004).

Remote sensing provides a cost-effective method to estimate many variables from regional to global scales. A large set of data on the atmosphere is continuously acquired and generated by a combination of satellite radiance measurements and radiative transfer models, providing spatial and temporal information under widely different atmospheric conditions. The accuracy of the models is limited mostly by uncertainties in input parameters representing the atmosphere and the Earth's surface, a limitation that is mitigated by the combined use of ground-based monitoring and information of satellite sensors. With the increasing use of satellite images, improvements in algorithms have been implemented to offer expeditious, accurate information over changes in air quality and their human impacts (Bais et al., 2007; Liu et al., 2016; Mostafa et al., 2021).

Catalytic agents like NO_2 have an important role in atmospheric chemistry related to ozone formation and destruction, O_3 being the main vector to absorption of UV reaching the planet's surface. In the recent context of reduction of activities due to the pandemics, emissions of greenhouse gases had fallen to levels not reported since World War II (Global Carbon Project, 2020). Monitoring these changes by conventional ground-level stations provide near-surface information, which however has spatial resolution limited by the surface density of station. This limitation presently can be mitigated by data acquired form satellite remote sensing, which provides data with large spatial cover and capability to detect spatio-temporal changes of several atmospheric pollutants and UV processes (Liu et al., 2016). Given that, presently, a series of sensors in orbit around the Earth display capabilities to detect several atmospheric pollutants and UV processes, the objective of this paper was to analyze the partial COVID-19 lockdown effect on atmospheric pollutants and its indirect impact on UV radiation in Rio Grande do Sul. To this end, our analysis will be based on widely available data on the atmosphere, acquired from orbital sensors.

2. Material and methods

2.1 Study area

Rio Grande do Sul is the Brazilian southernmost state, having international borders with Argentina to the west and with Uruguay to the south. Its area is 281 707 km², and with more than 11 million inhabitants it is the fifth most populated state in the country. The capital is Porto Alegre, whose metropolitan area concentrates an important fraction of the state's population and economic activities. Regarding the consumption of fossil fuels, the state has about 7.1 million vehicles (IBGE, 2019). The region has a humid subtropical climate with a large seasonal variation with hot summers and well-defined cold winters. Mean temperatures vary from 15 to 18 ºC, with lows of as much as –10 ºC (June and July) and highs going up to 40 ºC (December to March) (Livi, 2002).

2.2. Satellite observations

This research was performed from data acquired by the Ozone Monitoring Instrument (OMI) sensor onboard satellite Aura. This instrument is equipped with a spectrometer pointed to the nadir which measures the ultraviolet light (264-504 nm) coming from the Sun and back scattered by the atmosphere. The algorithms Differential Optical Absorption Spectroscopy (DOAS) and Total Ozone Mapping Spectrometer (TOMS) were developed to derive several products (Levelt et al., 2006), of which we used NO_2 (OMNO2d), total O_3 (OMTO3d), and UVI (OMUVBd) (Krotkov et al., 2006; Tanskanen et al., 2006).

For OMNO2d (total column density) data is provided in molecules cm^{-2}, a spatial resolution of 0.25º × 0.25º (Lat/Lon), and daily frequency; also daily, but with 1.0º × 1.0º (Lat/Lon) spatial resolution and Dobson units (where $1\ DU = 2.7 \times 10^{18}$ molecules $O_3\ cm^{-3}$) for product OMTO3d (total column density), and in a non-dimensional scale for product OMUVBd (intensity at local solar noon).

Since restrictions to social mobility started in March and considering that after two months environmental changes would be well established, we selected May as our period of assessment. A time series of 11 years (2010-2020) with 1003 images with daily measurements (97% of the series) was acquired from the data provider GES-DISC (NASA, 2020). Processing was performed using free software RStudio, and the spatial resolution of products OMUVBd and OMTO3d was resampled to 0.25º to have uniformity with product OMNO2d. For this 0.25º resolution, the study area is covered by 420 cells.

2.3. Data analysis

To evaluate the behavior of these variables in this unique scenario, we selected three different periods: 2010 to 2018 (long-term trend), 2019 (period prior to the partial lockdown scenario), and 2020 (partial lockdown scenario). For each product, we calculated the average per cell for all 420 cells of the study area, for May, in these three periods. The averages were calculated using the daily values for each of these periods, as follows:

$$Var_i = \frac{\sum_{t\ end\ date}^{start\ date} Var_{i,t}}{n} \quad (1)$$

where Var_i is the average of the variable in each cell for the respective period; start date and end date correspond to the first and last date of each period, and n is the number of days in the period.

To assess spatio-temporal percentage changes of variables in May 2020 in relation to previous periods, we calculated differences between their means. From these differences, we calculated the percentages of variation by dividing them by the mean of each period prior to the pandemics:

$$P = \frac{(C_2 - C_1)}{C_1} \times 100\% \quad (2)$$

where P is percentage change between different periods, C_1 is the mean concentration of the previous period, and C_2 is the average of the latter period.

Finally, Pearson correlation coefficients were derived to estimate the relation of NO_2 with total O_3 and UVI, taking as values to be compared the measured concentrations or index in the 420 cells covering the state.

3. Results

Table I presents the averages for May in the years 2010 to 2018, 2019, and 2020. Taking 2020 as reference, and for NO_2, a drop of 1.30% was observed with respect to the historical mean derived for the 2010 to 2018 period; compared with 2019, 2020 displays a decrease of 5.03% in NO_2. Considering total O_3, in 2020 a drop of 1.12% was observed with respect to the historical mean for 2010 to 2018, but if compared only with 2019, 2020 shows an increase of 2.32% in total O_3. For the ultraviolet index (UVI), an increase of 10.43% was observed in 2020 compared to the 2010-2018 time series, and of 15.18% compared with 2019.

Figure 1a shows the spatio-temporal distribution of NO_2. For 2010-2018 the largest NO_2 concentrations were found in the metropolitan area of the capital, Porto Alegre (3.92E + 15 molecules cm^{-2}), and the lowest at the hinterland (2.67E + 15 molecules cm^{-2}); these values are of 4.12E + 15 and 2.44E + 15 molecules cm^{-2} for 2019, and of 4.17E + 15 and 2.25E + 15 molecules cm^{-2} for 2020, respectively. Figure 1b presents results for total O_3, where it is possible to observe a gradient in latitude, with this variable decreasing southward. Maximum and minimum averages were 271 and 263 DU for 2010-2018; 262 and 255 for 2019, and 269 and 262 for 2020, respectively. In Figure 1c we present results for the ultraviolet index; again, there is a gradient in latitude, but inversely if compared with O_3, since now UVI decreases northwards. Values for UVI are 4.25 and 3.06 (2010-2018); 3.69 and 3.15 (2019); and 4.64 and 3.55 (2020), respectively.

Table I. May results for the UVI, NO_2 and total O_3 for Rio Grande do Sul State, Brazil, with respect to the historical mean for 2010 to 2018, mean for 2019, and mean for 2020.

	UVI	NO_2 (10^{15} molec./cm^2)	Total O_3 (DU)
Mean 2010 to 2018	3.64	3.06	267
Mean 2019	3.49	3.18	258
Mean 2020	4.02	3.02	264

UVI: Ultraviolet Index.

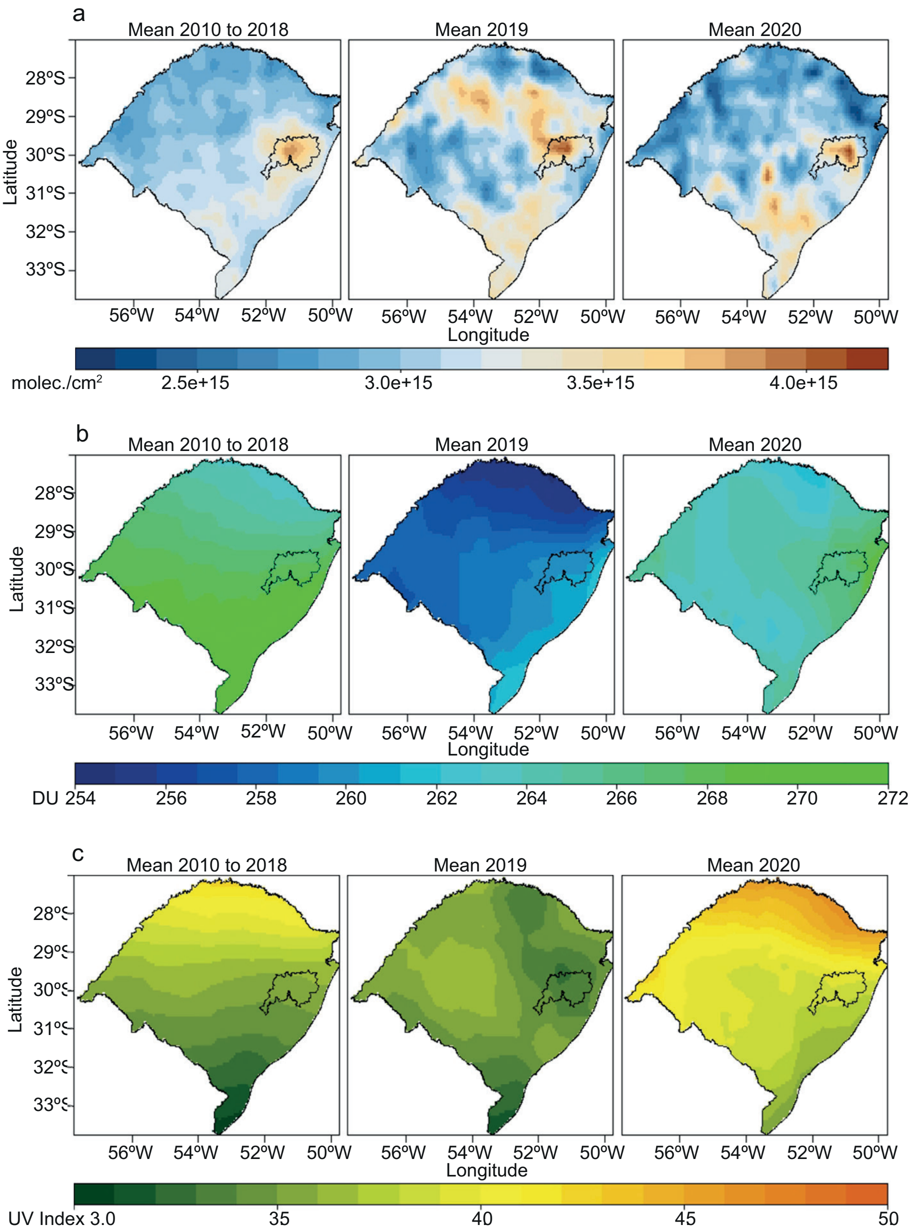

Fig. 1. Spatio-temporal variability of the studied variables for Rio Grande do Sul State, Brazil. (a) NO_2, (b) total O_3, (c) Ultraviolet Index. The metropolitan area of the state capital is highlighted.

Figure 2 presents the variation of the studied variables, taking 2020 as reference. In Figure 2a we can see that, compared with the time series 2010-2018, NO_2 values dropped in 55.5% of the studied area, being lower in amounts up to 28.7%. In the remaining area, the increase of NO_2 was up to 30.9%. However, compared with 2019, 2020 showed decreasing NO_2 in 66.4% of the state area by amounts up to 33.9%, while in the remaining area increases up to 45.4% in NO_2 were observed.

Figure 2b presents results for total O_3. Compared with the time series 2010-2018, in 2020 total O_3 dropped as much as 0.5% in 89.6% of the studied area; in the remaining 10.4% of the state, total O_3

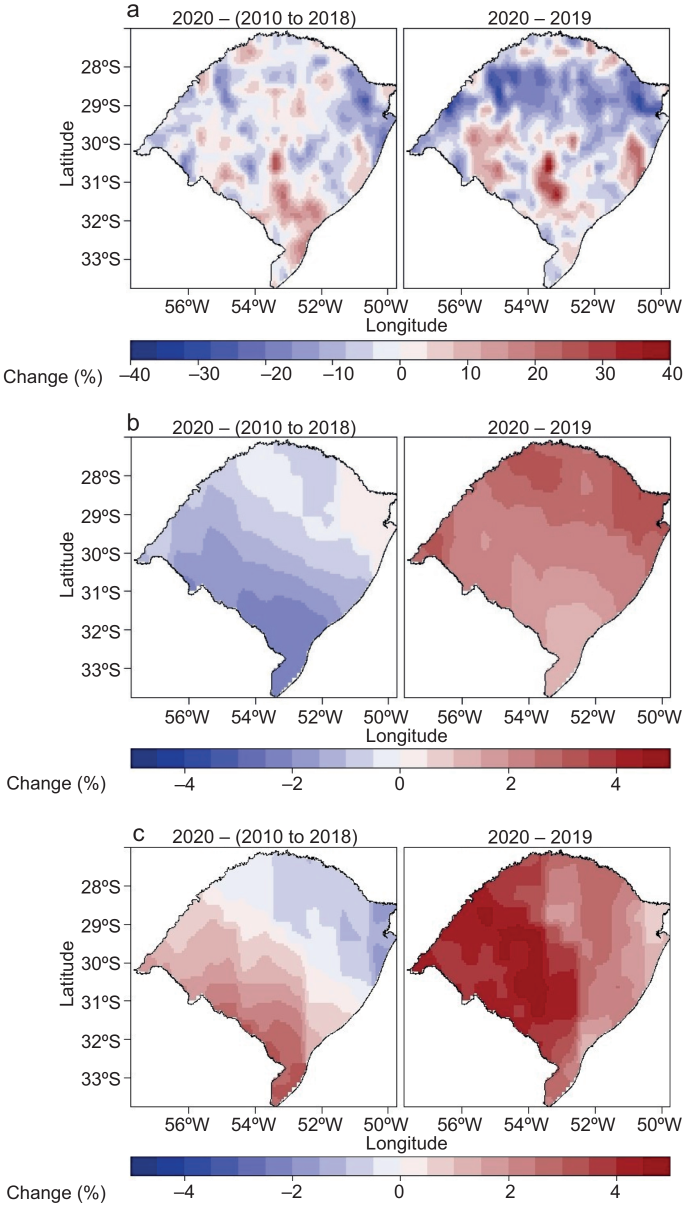

Fig. 2. Spatio-temporal variability of the studied variables for Rio Grande do Sul State, Brazil (2020 minus the indicated period). (a) NO_2, (b) total O_3, (c) Ultraviolet Index.

increased as much as 2.5%. However, when compared with 2019, it was observed that in 2020 total O_3 increased in all studied cells by values up to 3.5%.

Figure 2c presents results for the UVI. Compared with the time series 2010-2018, in 2020 UVI increased in 60.5% of the area, by values up to 3.3%, while in the remaining cells UVI was up to 1.7% smaller. Compared with 2019, in 2020 100% of the cells had increased UVI in values up to 4.8%.

Figure 3 presents correlations of NO_2 with the UVI and total O_3 for the studied periods taking the whole set of 420 cells covering the state.

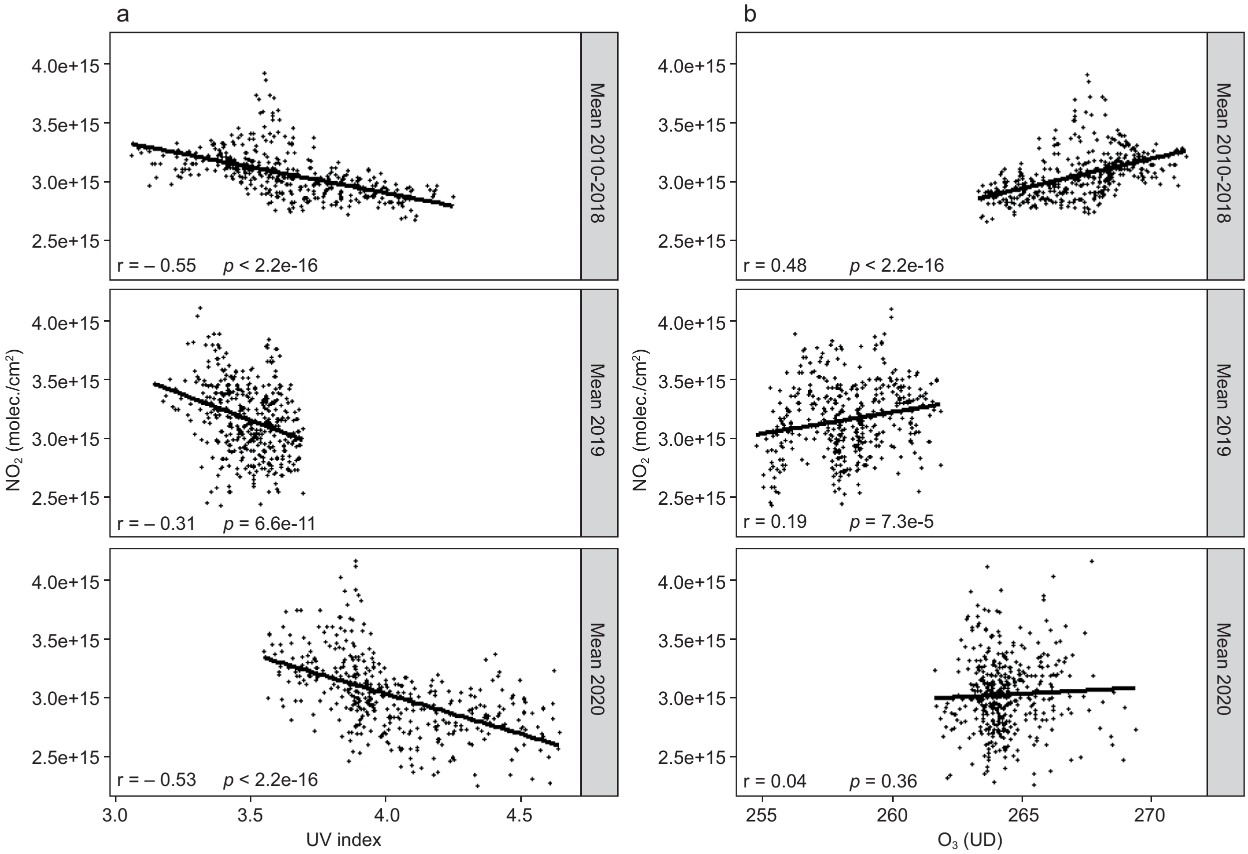

Fig. 3. Correlations of averages of NO_2 to: (a) Ultraviolet Index, (b) total O_3, for Rio Grande do Sul State, Brazil. In each box, the coefficient of correlation r and the p-value are provided.

4. Discussion

Air pollution represents a significant risk both to health and the environment, with NO_2 being one of the key pollutants, reacting with other chemicals to generate acid rain, which is harmful to the ecosystem. Its concentration level is influenced by complex variables such as wind, temperature, burning material, besides policies and other anthropogenic factors of each city (Wang and Su, 2020; Liu et al., 2021). According to WHO, current levels of NO_2 should be 40 µg m^{-3} for the annual mean and 200 µg m^{-3} for the 1-h mean (WHO, 2006). In Brazil, regulated levels are higher, with 60 µg m^{-3} for the annual average and 260 µg m^{-3} for the 1-h average (CONAMA, 2018). However, for the state of Rio Grande do Sul, the recommended levels are equal to those stipulated by WHO (FEPAM, 2019).

During the pandemic, this pollutant received wide attention from the international community, since partial lockdown measures promoted the decrease of the main sources of NO_2. According to the State Environmental Protection Foundation of Rio Grande do Sul, the concentration of NO_2 in the surface during the first months (January to May) of this extreme event was within the recommended limits and did not show a significant reduction or alteration of the levels concerning the previous years; this was due to the location of the stations (in just five cities) outside urban centers and the possible influence of emissions of industrial facilities that could have remained in operation in the places where the monitoring was being carried out (FEPAM, 2020).

Our results from satellite data suggest significant changes in NO_2 emissions by May 2020, which were reduced in more than half of the state area by 28.7 to 33.9%, depending on the considered period, which points to a temporary improvement of air quality. Such decreases in NO_2 emissions are in agreement with recent reports of variations from 20 to 54.3% in several countries (Muhammad et al., 2020; Nakada and Urban, 2020; Sharma et al., 2020; Siciliano et al., 2020; Tobias et al., 2020; Wang and Su, 2020; Zheng et al., 2020). This temporary reduction of NO_2 emissions in a short period is important even when the largest emitter of pollution (diesel transport) has continued to contribute on a smaller scale. However, Wang and Su (2020) mention that in the long run, a rebound in air pollutants is inevitable.

Discrepancies between ground measurements and satellite data do exist, mainly because ground stations, which are few and not evenly distributed, monitor the daily maximum concentrations from 1-h averages near the surface, while satellite data recover the daily density of the NO_2 column measured for the whole area. Therefore, units from these two sources are different and orbital data is not comparable with the recommended national and international levels (Liu et al., 2021. In this context, our work (being carried out from satellite data) only allows to detect changes over time, and to understand the impact of the partial lockdown on air pollution and various related factors in areas that have not yet been quantitatively considered.

Regarding total O_3, which increased from 2.5 to 3.5%, and UVI, which increased from 3.3 to 4.8%, it is to be noted that these increases in May 2020 are in contrast with expected drops in total O_3 in periods corresponding to May due to secondary effects in the Antarctic ozone hole, and a similar decrease in UVI due to a lower zenith solar angle, larger cloudiness and temperature drops between April and August in South America (Kirchhoff et al., 1996; Guarnieri et al., 2004; Kerr and Fioletov, 2008; Salgado et al., 2010; Schmalfuss et al., 2014; Nunes, 2017). These two variables used to have a well-defined pattern in May, but in May 2020, compared to May 2019, increases were observed in 100% of the state area. We note that, although both NO_2 and total O_3 changed in 2020, these alterations were not spatially correlated: as it can be seen in Figure 3b for the year 2020, from a cell-to-cell basis there is no significant correlation between these two variables. Only for a longer time series (2010 to 2018), some significant correlation is suggested.

In contrast with the weak or non-existent correlation between NO_2 and total O_3, Figure 3a shows significant inverse correlations between NO_2 and the UVI, especially for the 2010 to 2018 time series and for 2020.

Atmospheric processes involving ultraviolet radiation act in a complex form. In the stratosphere, UV radiation participates in the Chapman Cycle, being significantly absorbed at 310 nm and with decreasing intensity up to 345 nm (Kirchhoff et al., 2000; Koronakis et al., 2002). Simultaneously, NO_2, generated by oxidation of nitrous oxide (N_2O) transported from the troposphere, acts in a catalytic form destroying O_3 and suppressing its loss through other catalytic mechanisms sequestering free radicals (Seinfeld and Pandis, 1998). However, in the troposphere, UV radiation acts in photochemical reactions of several pollutants, the rates of these reactions being dependent on the concentrations of stratospheric ozone, natural and anthropogenic aerosol particles, and cloudiness (Chubarova, 2006). Even at low concentrations, tropospheric gases and particles have an effect on UV similar to their stratospheric counterparts, which is due to higher absorption in the UV interval at lower altitudes (Chubarova, 2006; Barnard and Wenny, 2010). Particulate material like black carbon is generated in most combustion processes, and its action in light extinction leads to a decrease in transmission of UV radiation (Barnard and Wenny, 2010). Therefore, in polluted-atmosphere conditions, the UV intensity can decrease by up to 15% in areas of anthropogenic activity (Koronakis et al., 2002; Chubarova, 2004; Barnard and Wenny, 2010); low pollutant concentrations lead to higher UVI, which in turn leads to stratospheric warming and an influx from the lower atmosphere of O_3-enriched air (WMO, 2020).

Even though NO_2 has a crucial role in atmospheric chemistry, its decrease in 2020 was not correlated with the total O_3 increase ($r = –0.04$, Fig. 3b). However, NO_2 correlated negatively with UVI ($r = –0.53$, Fig. 3a). This suggests that, in opposition to the well-known adverse effects of atmospheric pollutants, in certain aspects, they have an apparently beneficial effect in reducing the ultraviolet flux on the surface.

5. Conclusions

Air pollutant concentrations are influenced by variables as wind, temperature, burning materials, and other anthropogenic factors. In this paper, we looked for the effects of the slowing of human activities (e.g., vehicular traffic, industrial complex, and mining activities) on atmospheric parameters. This was done by the sole use of remote sensing data, a resource that is widely available and covers large areas. It was shown that the slowing of activities in 2020 lead to a reduction in NO_2 emissions (up to 33.9 %), and increased levels of total O_3 (up to 3.5 %), and the UVI (up to 4.8 %). This simultaneous increase in total O_3 and UVI suggests that O_3 is not the only factor influencing UV radiation at the surface, and future monitoring actions may have to look for other factors. We would cite these findings, which add to the mounting evidence linking NO_2 to total O_3 and UVI, as the main contribution of this research.

This work generated some insights: firstly, about the magnitude of the impact of human activity on the environment, where this impact is extended well beyond urban areas. This impact is not sustainable, but a discussion on its nature (be it positive or negative), was not part of the aims of this work. Secondly, initiatives taken by the authorities, eventually supported by the population, can be effective to change the environmental profile in large areas, being therefore potentially and equally effective in the effort against the disease spread. Finally, we hope that in the medium/long term this assessment can be helpful to decision-makers, in their actions to improve policies that promote a balance between economic growth, air pollution, and health.

Acknowledgments

ABR acknowledges the Brazilian agency Coordenação de Aperfeiçoamento de Pessoal de Nível Superior (CAPES) for the doctoral fellowship.

References

André IRN, Ferreira NJ, Conforte JC. 2003. Análise do comportamento do ozônio estratosférico na América do Sul e vizinhanças utilizando-se imagens do satélite NIMBUS7/TOMS. In: Anais do XI Simpósio Brasileiro de Sensoriamento Remoto. Belo Horizonte, 1117-1124.

Bais AF, Lubin D, Arola A, Bernhard G, Blumthaler M, Chubarova N, Erlick C, Gies HP, Krotkov NA, Lantz K, Mayer B, Mckenzie RL, Piacentini RD, Seckmeyer G, Slusser JR, Zerefos CS. 2007. Surface ultraviolet radiation: Past, present, and future. In: Scientific assessment of ozone depletion: 2006 (Ennis, CA), Ed.). Global Ozone Research and Monitoring Project, Report No. 50. World Meteorological Organization, Geneva.

Bais AF, Mckenzie RL, Bernhard G, Aucamp PJ, Ilyas M, Madronich S, Tourpali K. 2015. Ozone depletion and climate change: impacts on UV radiation. Photochemical & Photobiological Sciences 14: 19-52. https://doi.org/10.1039/C4PP90032D

Barnard WF, Wenny BN. 2010. Ultraviolet radiation and its interaction with air pollution. In: UV radiation in global climate change (Gao W, Slusser JR, Schmoldt DL, Eds.). Springer, Berlin, 291-330. https://doi.org/10.1007/978-3-642-03313-1_11

Caldwell MM, Ballaré CL, Bornman JF, Flint SD, Björn LO, Teramura AH, Kulandaivelu G, Tevini M. 2003. Terrestrial ecosystems, increased solar ultraviolet radiation and interactions with other climatic change factors. Photochemical & Photobiological Sciences 2: 29-38. https://doi.org/10.1039/B211159B

Cardoso VM. 2011. Efeitos da radiação ultravioleta-A e ultravioleta-B sobre os embriões do camarão de água-doce *Macrobrachium olfersii* (Crustacea, Decapoda) e o papel da radiação ultravioleta-A na fotorreativação. M.Sc. thesis. Federal University of Santa Catarina.

Cheval S, Mihai-Adamescu C, Georgiadis T, Herrnegger M, Piticar A, Legates DR. 2020. Observed and potential impacts of the COVID-19 pandemic on the environment. International Journal of Environmental Research and Public Health 17: 4140. https://doi.org/10.3390/ijerph17114140

Chubarova NE. 2004. Influence of aerosol and atmospheric gases on ultraviolet radiation in different optical conditions including smoky mist of 2002. Doklady Earth Sciences 394: 62-67.

Chubarova NE. 2006. Role of tropospheric gases in the absorption of UV radiation. Doklady Earth Sciences 407: 294-297. https://doi.org/10.1134/S1028334X06020322

Coariti JR. 2017. Características da Radiação Ultravioleta Solar e seus efeitos na saúde humana nas cidades de La Paz, Bolívia e Natal, Brasil. Ph.D. thesis. Federal University of Rio Grande do Norte.

CONAMA. 2018. Padrões de Qualidade do Ar (Resolução nº 491/2018). Conselho Nacional do Meio Ambiente. Diário Oficial da União 223: 155-156.

Davis A, Sims D. 1983. Weathering of polymers. Applied Science Publishers, London.

De Andrade RC, Tiba C. 2016. Extreme global solar irradiance due to cloud enhancement in northeastern Brazil. Renewable Energy 86: 1433-1441. https://doi.org/10.1016/j.renene.2015.09.012

Fahey DW, Hegglin MI. 2011. Twenty questions and answers about the ozone layer: 2010 update. In: Scientific assessment of ozone depletion, 2010. Global Ozone Research and Monitoring Project, Report No. 52. World Meteorological Organization, Geneva.

FEPAM. 2019. Rede estadual de monitoramento automático da qualidade do ar. Fundação Estadual de Proteção Ambiental Henrique Luis Roessler. Available at: http://www.fepam.rs.gov.br/qualidade/relatorios.asp (accessed on March 19, 2021).

FEPAM. 2020. Efeito do isolamento Covid−19 na qualidade do ar. Fundação Estadual de Proteção Ambiental Henrique Luis Roessler. Available at: http://www.fepam.rs.gov.br/qualidade/relatorios.asp (accessed on March 19, 2021).

Fountoulakis I, Diémoz H, Siani A-M, Laschewski G, Filippa G, Arola A, Bais AF, De Backer H, Lakkala K, Webb AR, De Bock V, Karppinen T, Garane K, Kapsomenakis J, Koukouli M-E, Zerefos CS. 2020. Solar UV Irradiance in a changing climate: Trends in Europe and the significance of spectral monitoring in Italy. Environments 7, 1. https://doi.org/10.3390/environments7010001

Global Carbon Project. 2020. Carbon budget 2021. Available at: https://www.globalcarbonproject.org/carbonbudget/index.htm (accessed on April 4, 2020).

Google. 2020. COVID-19 community mobility report. Available at: https://www.google.com/covid19/mobility?hl=en (accessed on March 21, 2021).

Guarnieri RA, Guarnieri FL, Contreira DB, Padilha LF, Echer E, Pinheiro DK, Schuch AMP, Makita K, Schuch NJ. 2004. Ozone and UV-B radiation anticorrelations at fixed solar zenith angles in southern Brazil. Geofísica Internacional 43: 17-22. https://doi.org/10.22201/igeof.00167169p.2004.43.1.209

Huffman RE. 1992. Atmospheric ultraviolet remote sensing. Academic Press, California.

IBGE. 2019. Cidades. Rio Grande do Sul. Instituto Brasileiro de Geografia e Estatística. Available at: http://www.cidades.ibge.gov.br (accessed on August 10, 2020).

Iqbal M. 1983. An introduction to solar radiation. Academic Press, Toronto, New York, London.

Kerr JB, Fioletov VE. 2008. Surface ultraviolet radiation. Atmosphere-Ocean 46: 159-184. https://doi.org/10.3137/ao.460108

Kirchhoff VWJH, Schuch NJ, Pinheiro DK, Harris JM. 1996. Evidence for an ozone hole perturbation at 30º South. Atmospheric Environment 30: 1481-1488. https://doi.org/10.1016/1352-2310(95)00362-2

Kirchhoff VWJH, Echer E, Leme NP, Silva AA. 2000. A variação sazonal da radiação ultravioleta solar biologicamente ativa. Revista Brasileira de Geofísica 18: 63-74. https://doi.org/10.1590/S0102-261X2000000100006

Koronakis PS, Sfantos GK, Paliatsos AG, Kaldellis JK, Garofalakis JE, Koronaki IP. 2002. Interrelations of UV-global/global/diffuse solar irradiance components and UV-global attenuation on air pollution episode days in Athens, Greece. Atmospheric Environment 36: 3173-3181. https://doi.org/10.1016/S1352-2310(02)00233-9

Krotkov NA, Carn SA, Krueger AJ, Bhartia PK, Yang K. 2006. Band residual difference algorithm for retrieval of SO_2 from the Aura Ozone Monitoring Instrument (OMI). IEEE Transactions on Geoscience and Remote Sensing 44: 1259-1266. https://doi.org/10.1109/TGRS.2005.861932

Levelt PF, van den Oord GHJ, Dobber MR, Mälkki A, Visser H, de Vries J, Stammes P, Lundell JOV, Saari H. 2006. The Ozone Monitoring Instrument. IEEE Transactions on Geoscience and Remote Sensing 44: 1093-1101. https://doi.org/10.1109/TGRS.2006.872333

Liu F, Zhang Q, van der A RJ, Zheng B, Tong D, Yan L, Zheng Y, He K. 2016. Recent reduction in NOx emissions over China: Synthesis of satellite observations and emission inventories. Environmental Research Letters 11: 114002. https://doi.org/10.1088/1748-9326/11/11/114002

Liu Q, Harris JT, Chiu LS, Sun D, Houser PR, Yu M, Duffy DQ, Little MM, Yang C. 2021. Spatiotemporal impacts of COVID-19 on air pollution in California, USA. Science of the Total Environment 750: 141592. https://doi.org/10.1016/j.scitotenv.2020.141592

Livi FP. 2002. O clima em Porto Alegre no século XX: uma análise de séries temporais. M.Sc. thesis. Federal University of Rio Grande do Sul.

Mostafa MK, Gamal G, Wafiq A. 2021. The impact of COVID 19 on air pollution levels and other environmental indicators. A case study of Egypt. Journal of Environmental Management 277: 111496. https://doi.org/10.1016/j.jenvman.2020.111496

Muhammad S, Lon, X, Salman M. 2020. COVID-19 pandemic and environmental pollution: A blessing in disguise? Science of the Total Environment 728: 138820. https://doi.org/10.1016/j.scitotenv.2020.138820

Nakada LYK, Urban RC. 2020. COVID-19 pandemic: Impacts on the air quality during the partial lockdown in São Paulo state, Brazil. Science of the Total Environment 730: 139087. https://doi.org/10.1016/j.scitotenv.2020.139087

NASA. 2020. Earth Observatory. National Aeronautics and Space Administration. Available at: https://urs.earthdata.nasa.gov (accessed on August 10, 2020).

Nunes M. 2017. Influência da coluna total de ozônio na variabilidade da radiação ultravioleta sobre o sul da América do Sul. M.Sc. thesis. Federal University of Pelotas.

Paital, B, Agrawal PK. 2021. Air pollution by NO_2 and $PM_{2.5}$ explains COVID-19 infection severity by overexpression of angiotensin-converting enzyme 2 in respiratory cells: A review. Environmental Chemistry Letters 19: 25-42. https://doi.org/10.1007/s10311-020-01091-w

Robinson N. 1966. Solar Radiation. Elsevier, New York.

Salgado CAC, Paes Leme NM, Zamorano F, Quel EJ, Viana R. 2010. Influence of the ozone hole on the American South cone 1992-2009. In: Proceedings of the 2010 Meeting of the Americas. Foz do Iguaçu.

Schmalfuss LSM, Mariano GL, Pinheiro DK, Peres LV. 2014. Análise dos dois principais fatores de decaimento da coluna total de Ozônio sobre o sul da América do Sul. Ciência e Natura 36: 415-422. https://doi.org/10.5902/2179460X12812

Seinfeld JH, Pandis SN. 1998. Atmospheric chemistry and physics: From air pollution to climate change. Wiley Interscience, New York.

Sharma S, Zhang M, Anshika, Gao J, Zhang H, Kota SH. 2020. Effect of restricted emissions during COVID-19 on air quality in India. Science of the Total Environment 728: 138878. https://doi.org/10.1016/j.scitotenv.2020.138878

Siciliano B, Dantas G, da Silva CM, Arbilla G. 2020. Increased ozone levels during the COVID-19 lockdown: Analysis for the city of Rio de Janeiro, Brazil. Science of the Total Environment 737: 139765. https://doi.org/10.1016/j.scitotenv.2020.139765

Silva F, Oliveira HSM, Marinho GS. 2008. Variação do índice de radiação solar ultravioleta em Natal-RN entre 2001 e 2007. In: II Congresso Brasileiro de Energia Solar e III Conferência Regional Latino-Americana da ISES, Florianópolis.

Tanskanen A, Krotkov NA, Herman JR, Arola A. 2006. Surface ultraviolet irradiance from OMI. IEEE Transactions on Geoscience and Remote Sensing 44: 1267-1271. https://doi.org/10.1109/TGRS.2005.862203

Tiegte JE, Diamond SA, Ankley GT, DeFoe DL, Holcombe GW, Jensen KM, Degitz SJ, Elonen GE, Hammer E. 2001. Ambient solar UV radiation causes mortality in larvae of three species of *Rana* under controlled exposure conditions. Photochemistry and Photobiology 74: 261-268. https://doi.org/10.1562/0031-8655(2001)0740261ASURCM2.0.CO2

Tobias A, Carnerero C, Reche C, Massagué J, Via M, Minguillón MC, Alastuey A, Querol X. 2020. Changes in air quality during the lockdown in Barcelona (Spain) one month into the SARS-CoV-2 epidemic. Science of the Total Environment 726: 138540. https://doi.org/10.1016/j.scitotenv.2020.138540

Travaglio M, Yu Y, Popovic R, Selley L, Santos-Leal N, Martins LM. 2021. Links between air pollution and COVID-19 in England. Environmental Pollution 268: 115859. https://doi.org/10.1016/j.envpol.2020.115859

Ubiratan E. 2020. No limite a aviação brasileira registra queda de 90%. Aero Magazine. Available at: https://aeromagazine.uol.com.br/artigo/no-limite-aviacao-brasileira-registra-queda-de-90_5420.html (accessed on March 21, 2021).

Vásquez-Apestegui V, Parras-Garrido E, Tapia V, Paz-Aparicio VM, Rojas JP, Sánchez-Ccoyllo OR, Gonzales GF. 2020. Association between air pollution in Lima and the high incidence of COVID-19: Findings from a post hoc analysis. Research Square (preprint). https://doi.org/10.21203/rs.3.rs-39404/v1

Wakamatsu S, Uno I, Ueda H, Uehara K, Tateishi H. 1989. Observational study of stratospheric ozone intrusions into the lower troposphere. Atmospheric Environment 23: 1815-1826. https://doi.org/10.1016/0004-6981(89)90065-6

Wang Q, Su M. 2020. A preliminary assessment of the impact of COVID-19 on environment. A case study of China. Science of the Total Environment 728: 138915. https://doi.org/10.1016/j.scitotenv.2020.138915

WHO. 2002. Global solar UV index: a practical guide. World Health Organization, World Meteorological Organization, United Nations Environment Programme, International Commission on Non-Ionizing Radiation Protection. Available at: https://apps.who.int/iris/handle/10665/42459

WHO. 2006. Air quality guidelines. Global update 2005. Particulate matter, ozone, nitrogen dioxide and sulfur dioxide. World Health Organization, Geneva.

WMO. 2011. Scientific assessment of ozone depletion. Global Ozone Research and Monitoring Project, Report No. 52. World Meteorological Organization, Geneva.

WMO. 2020. Arctic ozone depletion reached record level. World Meteorological Organization, Geneva. Available at: https://public.wmo.int/en/media/news/arctic-ozone-depletion-reached-record-level (accessed on August 10, 2020).

Zambrano-Monserrate MA, Ruano MA, Sánchez-Alcalde L. 2020. Indirect effects of COVID-19 on the environment. Science of the Total Environment 728: 138813. https://doi.org/10.1016/j.scitotenv.2020.138813

Zheng B, Geng G, Ciais P, Davis SJ, Martin RV, Meng J, Wu N, Chevallier F, Broquet G, Boersma F, van der AR, Lin J, Guan D, Lei Y, He K, Zhang Q. 2020. Satellite-based estimates of decline and rebound in China's CO_2 emissions during COVID-19 pandemic. Science Advances 6: 1-10. https://doi.org/10.1126/sciadv.abd4998

Zhu L, Liu X, Huang H, Avellán-Llaguno RD, Llaguno Lazo MM, Gaggero A, Soto-Rifo R, Patiño L, Valencia-Avellan M, Diringer B, Huang Q, Zhu Y-G. 2020. Meteorological impact on the COVID-19 pandemic: A study across eight severely affected regions in South America. Science of the Total Environment 744: 140881. https://doi.org/10.1016/j.scitotenv.2020.140881

Atmósfera 36(1), 155-169 (2023)
https://doi.org/10.20937/ATM.52940

CONTENTS

Quantification of greenhouse gas emissions of a steel factory in Brazil

Danielle ALVES DE NOVAES GOMES[1], Janaina DA COSTA PEREIRA TORRES DE OLIVEIRA[2]
and Thiago SIMONATO MOZER[3]*

[1] *Programa de Pós-Graduação em Tecnologia Ambiental, Escola de Engenharia Industrial e Metalúrgica de Volta Redonda, Universidade Federal Fluminense, Avenida dos Trabalhadores, 420, Sala D44, Vila Santa Cecília, Volta Redonda – RJ, Brasil, CEP 27255-250.*
[2] *Centro Universitário de Volta Redonda, Avenida Paulo Erlei Alves Abrantes, 1325, Três Poços, Volta Redonda – RJ, Brasil, CEP 27240-560.*
[3] *Departamento de Química, Instituto de Ciências Exatas, Universidade Federal Fluminense, Rua Desembargador Ellis Hermídio Figueira, 783, Bloco C, sala 306C, Aterrado, Volta Redonda – RJ, Brasil, CEP 27213-145.*
*Corresponding author: thiagomozer@id.uff.br

Received: July 2, 2020; accepted: April 21, 2021

RESUMEN

Este trabajo tuvo como objetivo identificar y cuantificar las emisiones de gases de efecto invernadero (GEI) de una fábrica del sector siderúrgico, considerando la importancia de estos datos en el contexto de grandes emisiones globales de GEI. Como resultado, se identificó que las emisiones del Ámbito 1 eran las más altas de la industria, representando más de 89% de las emisiones totales en CO_2eq. Este escenario se identifica principalmente por la configuración de la matriz energética brasileña, que contribuye a reducir las emisiones del Ámbito 2. La metodología abordada (GHG Protocol v. 2018.1.4) resultó adecuada para el cálculo de emisiones destinado un informe más amplio (cantidad anual). Sin embargo, con el fin de desarrollar un indicador para la organización, con datos detallados mensuales, fue necesario adecuar la herramienta, que la contribuciónl de este trabajo.

ABSTRACT

This work aimed to identify and quantify greenhouse gases (GHG) emissions of a steel factory, considering the importance of these data in the context of large global GHG emissions. As a result, Scope 1 emissions were identified as the highest in the industry, representing more than 89% of total emissions in CO_2eq. This scenario is mainly identified a result of the Brazilian energy matrix configuration, which contributes to reduce Scope 2 emissions. The used methodology (GHG Protocol v. 2018.1.4) proved to be appropriate for calculating emissions within a broader report (annual amount). However, in order to develop an indicator for the organization, with monthly detailed data, it was necessary to adapt the tool, which is the differential of this work.

Keywords: global warming, CO_2 emissions, industrial emissions, greenhouse gases, atmospheric pollution, steel industry.

1. Introduction

Capitalism is the production system that has generated the highest material wealth. Before the Industrial Revolution, the rate of economic growth and the amount of produced goods and services were meager. In this way, fossil fuels have been essential to economic evolution during the last two centuries but they have also produced negative effects: they increased the concentration of greenhouse gases (GHG) as a result of their combustion to generate energy in the industrial processes. These gases, in excess, cause pollution, respiratory diseases, changes in the atmospheric chemistry and accelerate the global warming phenomenon (Alves, 2014).

GHG, whose emissions have grown about 60% from 1990 to 2017, are gaseous constituents that absorb and re-emit infrared radiation into the atmosphere. The main causes associated with this increase are related to the planet's energy production infrastructure and emissions associated with deforestation of tropical forests (CEBDS, 2018). Due to the energy consumption generated from fossil fuels burning and emissions from transformation processes of their inputs to products, industrial activity also contributes significantly to the increase in GHG concentration (MDIC, 2013).

Within the industrial sector, the steel industry stands out for being a basic industry that plays an essential role in economic growth. It supplies inputs for several market segments. Likewise, the industrial sector is a major consumer of energy and materials. It is also responsible for a significant negative environmental impact due to the extensive physical and chemical reactions involved in the steelmaking process (Carvalho et al., 2016).

In 2019, Brazil ranked 9th in world's steel production, with 32.5×10^6 t of crude steel, which corresponds to 1.7% of thw global production. China is at the top of this ranking, with a production of 996.3×10^6 tons, equivalent to more than 50% of the world production. India, Japan, the USA, Russia, South Korea, Germany and Turkey occupy positions 2 to 8, respectively (Instituto Aço Brasil, 2020).

According to the results of GHG estimates for the Brazilian industrial sector, the steel industry is below the world's average with emissions per ton of steel decreasing from 1.547 t CO_2eq per ton of crude steel in 2015 to 1.457 in 2050. These values are observed, mainly, by the introduction of charcoal in the production of steel in integrated plants and the better use of process gases, generating a lower demand for metallurgical coke (Santos et al., 2010).

Brazil emitted 2.2 billion tons of GHG in 2019 (total emissions). The Industrial Processes and Product Use sector was responsible for 5% of the total. The highlight is given to the Land Use Change and Agricultural sectors, which accounted for 72% of Brazilian emissions that year (SEEG, 2019).

Anthropogenic activities in general have already increased the Earth's average temperature by about 1 ºC, with a probability to reach 1.5 º C between 2030 and 2052. If no global changes are assumed to limit this warming, global temperature may still reach 2 ºC above pre-industrial levels. Allowing this increase means assuming loss of natural habitats and species, reduction of polar ice caps and sea levels rise, with serious consequences for human health, security and economic growth (IPCC, 2018).

Fourteen countries in the G20 (Argentina, Brazil, Canada, France, Germany, India, USA States) were responsible for more than 80% of global carbon emissions between 1991 and 2017 (Erdoğan et al., 2020). If GHG emissions remain at current rates, countries will suffer serious consequences, mainly the poorest, as they are less prepared to deal with these fast changes. Habitats will change so sharply that many species will be unable to adapt, causing the extinction of animals and vegetables. In addition, diseases such as malaria and malnutrition will become more common, threatening the health of millions of people (Watts et al., 2015).

The international community has been struggling to combat global warming, as well as its consequences . Voluntary agreements between nations have been developed as an alternative to solve the problem (Mok et al., 2014). According to Cifci and Oliver (2018), international climate agreements such as the 1997 Kyoto Protocol and, more recently, the Paris Climate Agreement, mention that climate change is the most urgent challenge of our time and report that international cooperation to reduce GHG emissions plays a key role in this challenge.

The meetings of the Conference of the Parties (COP) held in Paris (2015) and Marrakesh (2016) for international climate negotiations, presented some promising results. However, it is noteworthy that efforts are few and the way to avoid dangerous climate change is still far off (Rockström et al., 2016; Hickmann, 2017).

The demand for adapting production to new practices that comply with environmental legislation, which imposes certain limits, and the current ecological thinking of society, lead industries to use clean technologies and, necessarily, to adopt pollution control systems and appropriate equipment (Novaes and Souza, 2018). Thus, industries need to absorb their negative externalities and use clean technology in order to retain the market.

Countries are looking for technologies and alternatives to reduce carbon emissions without negatively affecting economic development. Industrial progress is important, but it needs adjusting to the protection of environment in order to guarantee environmental quality. Through innovation, sustainable economic growth strategies have emerged (Erdoğan et al., 2020). Companies first need to appraise their emissions through quantitative data so they can evaluate the best mitigation strategies for their corporate GHG emissions and search for innovations.

In China, for example, the national progress of CO_2 emissions decrease can be attributed to high efficiency projects established by energy service companies. Population, consumption of coal, and research and development inputs have a positive influence on the decrease of CO_2 emissions (Zheng et al., 2018). In mining areas, the use of solar water heating systems is an alternative for reducing average annual CO_2 emissions. The problem is the high cost of the new energy source, such as solar energy (Xue, 2020). Within European telecommunications companies, the largest contributor to GHG emissions was the consumption of purchased electricity (Radonjič and Tompa, 2018).

In fact, a growing number of private companies have begun to contribute to climate change mitigation voluntarily. However, only when this sector receives a clear political signal, the companies will make substantial efforts to calculate and report their emissions accurately. This attitude requires the use of stringent GHG control regulations and the adoption of appropriate policy instruments (Hickmann, 2017).

Thereby, this work aimed to carry out a complete inventory of GHG emissions from a steel factory, using the tool provide by the Brazilian GHG Protocol Program. The factory under study aimed to understand and quantify its GHG emissions in order to mitigate them later. This is a significant step, in which the organization is committed to the community, fulfilling its social responsibility. Then, an adaptation of the tool was made for a monthly report, allowing companies to carry out a more precise control and monitoring their emissions in a shorter time, something that has not been reported until now. The results can be used as reference and basis for other industries, enabling them to use the knowledge and results presented.

2. Material and methods

This work was carried out in a steel factory located in the state of Rio de Janeiro, Brazil. Only data related to the number of employees, consumption of raw materials and fuels applicable to the production process, electricity consumption, vehicle handling and final disposal of waste were authorized for disclosure in this work. All data used in this research refer to 2017 and were obtained through technical visits and information collected on site, informed by employees from the Health, Safety and Environment (HSE) sector.

This work consists of a qualitative and a quantitative research, followed by a descriptive and exploratory case study, based on the specifications of the Brazilian GHG Protocol Program. GHG emissions of the steel factory were quantified through the bottom-up approach (sectorial approach), which allows knowing the emissions through specific consumption and emission factors, as well as an analysis of these emissions.

The bottom-up approach uses information directly related to the source. It is used for point sources, requiring more resources to collect information from the specific location. The organization has operational control and measurement of this data (Ugaya et al., 2013). This approach allows to know the emissions through specific consumption and also specific emission factors, which are used for the elaboration of corporate inventories (sectorial approach).

A single element was examined in this research, a steel factory. According to Yin (2015), a single case study is recommended when the access to multiple cases is difficult. This methodology can be used to find out if the propositions are correct or if a group of explanations is more relevant. This research can be a significant contribution to knowledge building and even support direct future research in this field.

2.1 Quantification of GHG emissions with the GHG Protocol method

Among the different methodologies for quantifying, analyzing and managing corporate GHG emissions, the GHG Protocol Corporate Accounting and Reporting Standard is the most used tool worldwide by companies and governments (WBCSD, 2014).

The GHG Protocol is a management method, compatible with the International Organization for Standardization (ISO) and the Intergovernmental Panel on Climate Change (IPCC) quantification methodologies. Its application in Brazil is adapted to the national context. It was developed by the World Resources Institute in association with the World Business Council for Sustainable Development in 1998, and it is periodically updated (FGV/WRI, 2009). In addition to its wide use, this tool stands because it offers a structure to account GHG with a modular and flexible way. Its policy neutrality and the fact that it is based on a wide public consultation process were also decisive factors for choosing this methodology and using it in this work.

According to this method, companies need to assess their responsibility for GHG emissions from (*a*) their internal operations, (*b*) the purchase of energy from sources outside the corporation and internal use, and (*c*) emissions from products upstream and downstream of the value chain. These responsibilities are referred as Scope 1, Scope 2, and Scope 3, respectively (Patchell, 2018).

All the potential sources of GHG emissions into the atmosphere from the industrial establishment were identified. All activities and operational routines were verified. The studied plant is integrated with the transformation cycle starting at iron ore. The pig iron is manufactured in a blast furnace, with charcoal as its main reducing agent.

The identified emission sources were based on the amount of fuel used by the fleet, internal industrial processes, total consumed energy and generated effluents. These sources were classified as direct (Scope 1) or indirect (Scope 2), as established in the GHG Protocol methodology. Due to insufficient data to report Scope 3 emissions, only the mandatory reports (Scopes 1 and 2) were chosen.

Quantification of emissions was performed using the methodology of the Brazilian GHG Protocol Program v. 2018.1.4 (EAESP/FGV , 2021). The methodology of this research followed the guidelines and information contained in this method.

Three limits were defined: the temporal range (reference period), the organizational limits, and the operational limits. The reference period was the time frame for quantification of emissions (from January until December 2018) and served as the basis for the analysis of emissions data. The organizational limits physically delimit where the work will be performed. The Brazilian GHG Protocol Program considers two approaches to consolidate emissions: operational control (when the company has the authority to define and implement operating policies, including 100% of its emissions in the inventory) and equity participation (inclusion of emissions according to equity interests, reflecting its participation percentage in the operation). The operational limit refers to all activities within the organizational limits that emit GHG. Identification of emission sources is required, as well as distinguishing between direct and indirect emissions in order to associate them with the corresponding scopes.

The GHG Protocol includes calculations based on specific emission factors for the analyzed components. The approach used to calculate GHG emissions is the application of documented emission factors. The emission factor is a mathematical indicator of the amount of GHG emitted to the atmosphere in relation to a given emission source.

Each spreadsheet of the tool was programmed using the formula and the emission factor to quantify the emission, presenting, in the end, the scope emission and its condensation. The tool has a model of source transformation into CO_2 equivalent (CO_2eq), considering the global warming potential (GWP) of each GHG.

Emission factors determine how much of a GHG was emitted by the activity. It corresponds to a representative value reporting the amount of GHG emissions or removals to an associated activity. A practical example is how much CO_2 is emitted when one liter of fuel is consumed (SEBRAE, 2015).

The agents that publish factors used as reference by the Brazilian GHG Protocol calculation tool are (*a*) the IPCC (scientific basis that presents standard values), (*b*) the National Energy Balance (BEN), (*c*) the Brazilian Ministry of Science, Technology, Innovations and Communications (MCTIC), (d) the Brazilian Ministry of Environment (MMA), and (*e*) the Department for Environment Food and Rural Affairs (DEFRA).

The Brazilian GHG Protocol tool uses the emission estimation method (estimation approach), which consists of emission data (such as data on electricity consumption and gasoline burning in vehicles) multiplied by appropriate emission factors (used to determine the quantity emitted by a given source, depending on some parameters). Thus, to calculate emissions or removals of different GHG, in general, the tool performs the calculation according to Eq. (1) below:

$$E_{GHG} = C \times EF \quad (1)$$

where E_{GHG} GHG emissions or removals, C is the combination of activity information (activity data), and EF is the emission factor.

Subsequently, emissions or removals are converted to identify the amount of CO_2eq in tons (tCO_2eq). This calculation is made considering the global warming potential of each GHG (Eq. [2]):

$$E = E_{GHG} \times GWP \quad (2)$$

where E are GHG emissions or removals in CO_{2eq}, E_{GHG} are emissions or removals from GHG, and GWP is the global warming potential of GHG.

GWP values used as a reference and emission factors used in the inventory were provided by the GHG Protocol estimation tool. The simplified method presented above represents the quantification of emissions by the Brazilian GHG Protocol tool for the following categories: stationary combustion, mobile combustion, fugitive emissions (Scope 1) and energy (Scope 2). The calculation of industrial processes and effluents categories (Scope 1) was performed with alternative data that will be discussed below.

2.2 Industrial processes category

The Industrial Processes category requires the value already calculated by Eq. (1). It is a more complex and particular category to be calculated (it will depend on the operation of each organization). There is a reporting space in the tool to enter these values.

According to Eq. (1), the data of each activity are multiplied by their respective emission factors to obtain the corresponding value for GHG emissions or removals. Thus, when the equivalent emission factors are not found in the literature, it is possible to calculate them by mass balance, since the amount of carbon present in a ton of precursor (supervised item) is known (IPCC, 2006).

This work adopted the methodology used by the Guidelines for national greenhouse gas inventories (IPCC, 2006). The calculation was made using the carbon content and the mass balance. The emission factor is the carbon content in tons multiplied by the CO_2 molecular weight: 44 t of CO_2 correspond to 12 t of C (3.6667 t of C).

The equivalent emission is obtained with Eq. (3):

$$EF = CC \times 44/12 \quad (3)$$

where EF is the emission factor, CC is the carbon content in tons, and 44/12 is the molecular mass to carbon atomic mass ratio.

The values equivalent to carbon content of each item were obtained through laboratory analyzes of the carbon amount of each element, performed by the company itself. The values obtained after these calculations (emissions in tons of CO_2) were introduced in the Brazilian GHG Protocol tool to follow the calculation of CO_2eq emissions.

2.3 Effluent category

For the calculation of this category, the type of treatment performed and the amount of waste or effluent produced based on the number of active persons in the plant were recorded. There are two different ways to account these emissions: (*a*) as Scope 1 direct emissions if the company performs any treatment of effluents or solid waste generated within the established organizational limit; (*b*) as Scope 3 indirect emissions when the company collects all wastes and effluents and gives them a different destination, where another company is responsible for their treatment (SEBRAE, 2015).

The studied company has a sewage treatment station equipped with an anaerobic filter, which receives effluents only from the bathrooms located in the upper part of the plant (treatment of sanitary effluents). This area is located in the sector of the company that covers foundry/valves and the parts yard, which is composed of 69 employees.

The GHG Protocol tool follows five steps for this quantification:

Step 1. Sequential treatments applied to effluents. It is necessary to identify if two types of anaerobic

Table I. Per capita contribution of sewage and unit of organic load contribution, in industrial, commercial and construction site activities.

Pattern	Sewage per capita contribution (L day^{-1})	Unit of organic load contribution (g BOD day^{-1})
General non-residential activity	70	25
Non-residential activity with dining hall with kitchen	95	50

Source: INEA (2007).

treatment are applied sequentially to the generated effluent; in the case of the company under study they were not applied.

Step 2. Estimation of wastewater generation data (amount of wastewater generated in the inventory year in m³ yr^{-1}). This calculation is performed by multiplying the per capita contribution of sewage (data available in the guideline DZ-215 [Table I]) by the number of employees (INEA, 2007). Thus, the calculation was:

$70 \times 69 = 4830$ L day^{-1}
$4830/1000 = 4.830$ m³ day^{-1}
$4.830 \times 365 = 1{,}762.95$ m³ yr^{-1}

Step 3. Effluent organic composition data: the effluent degradable organic load data must be filled, choosing whether the data unit corresponds to biological oxygen demand (BOD) or chemical oxygen demand (COD). The following calculation was made based on the DZ-215 guideline (Table I):

$25 \times 69 = 1725$ g BOD day^{-1}
$1725/1000 = 1.725$ kg BOD day^{-1}
$1.725 \times 365 = 629.625$ kg BOD yr^{-1}

The value inserted in the Brazilian GHG Protocol tool was the degradable organic component of the effluent, which was obtained by dividing the value found in the amount of liquid effluent generated by the value of the unit of organic load contribution:

$629.625/1{,}762.95 = 0.357$ kg BOD m^{-3}

Then, data regarding the amount of nitrogen present in the effluent and the N_2O emission factor of the effluent needed to be filled. If there is no specific N_2O emission factor, this data may not be filled and remain as a blank field. In this case, the tool will use the default suggested by the IPCC (2006). Nitrogen data entered in the quantification tool were obtained through monthly reports issued by the National Service for Industrial Learning (SENAI). This institution estimated the average value to calculate GHG emissions, which was 45 kg N m^{-3}.

Step 4. Type of treatment applied to the effluent. In this case, the anaerobic reactor option was selected.

Step 5. CH_4 recovery. If applicable, this line shows the amount of methane recovered from the effluent treatment in the inventoried year. No value was inserted.

3. Results and discussion

3.1 Quantification of GHG emissions through the Brazilian GHG Protocol tool

A survey regarding GHG emission sources of the studied company was carried out, corresponding to their operational limits. The data from 2017 (time limit of this work) consisted of the company's operational control approach. Seventeen sources were identified within the following categories: stationary combustion, mobile combustion, fugitive emissions, industrial processes, and effluents and energy.

The stationary combustion category is related to the burning of fuels by fixed equipment, which can be owned by the company or rented to operate under its management. Mobile combustion is related to the burning of fuels by mobile equipment. Emissions resulting from the intentional or accidental release of GHG (generated by air conditioning gas leaks or fire extinguishers, for example) are accounted in fugitive emissions. The industrial processes category includes all sources of industrial processes emissions that transform materials, either chemically or physically, and there may also be GHG sources through the use of products. The effluents category includes the waste produced during industrial processes that is no longer used by the company (SEBRAE, 2015). All of these reported categories refer to Scope 1.

Scope 2 refers to the accounting of GHG emissions from the generation of purchased electricity, heat or steam. These emissions are generated where the energy is produced and subsequently consumed by the inventoried company. It is noteworthy that if the company carrying out the inventory produces any of these types of energy, the emissions generated by this process cannot be reported in Scope 2. In this case, they must be reported in Scope 1, since they will become direct emissions produced by the inventoried company itself (SEBRAE, 2015).

The required data to quantify the emissions were based on documented real data. Requisitions were made to the company's Warehouse and Controlling sectors, weighing reports and vouchers were redirected to the Health, Safety and Environment sector. Then, all information was provided to the authors for further analysis.

For all items, the required information for data entry was collected, as required by the Brazilian GHG Protocol spreadsheet. The quantification was made from the determination of the sources of GHG emission.

GHG emissions (t GHG) inventoried by the GHG Protocol tool, as prescribed by the Kyoto Protocol, are shown in Table II. According to this table, CO_2 is the most representative GHG of the steel factory emissions. The amount of 36 483.01 t CO_2eq corresponds to 99.27% of Scope 1 GHG emissions (36 750.47 CO_2eq) of the analyzed factory. This is mainly due to the transformation of pig iron into steel in converters and electric furnaces of the steel factory. This process always releases CO and CO_2 (Carvalho et al., 2016).

GWP is the GHG contribution to global warming. The GWP of methane and nitrous oxide used by the GHG Protocol tool were 25 and 298, respectively (IPCC, 2007). So, the representative values of these GHG increased and the Scope 1 total emissions reached 44 778.33 t CO_2eq. Scope 2 emissions (considering GWP of CO_2 equal to 1) remained at 5 460.95 t CO_2eq. Figure 1 illustrates the total CO_2eq emissions.

The total GHG emissions reached 50 239.27 t CO_2eq (Fig. 1). Scope 1 emissions (44 778.33 t CO_2eq) were responsible for 89.13% of the total CO_2eq emitted by all sources. The configuration of the Brazilian energy matrix contributed to the reduced Scope 2 emissions (5 460.95 t CO_2eq or 10.87% of the total CO_2eq emitted). According to data from the Energetic Research Company (EPE, 2016), 43.5% of the Brazilian energy consumption comes from renewable sources while in the rest of the world this percentage is 14%. Renewable energy represents 82% of the sources of electric power generation in Brazil. This scenario is very positive for Brazil, because plants generating energy from renewable sources generally emit less GHG and have lower operating costs.

Table II. Total greenhouse gas emissions in tons.

GHG	Scope 1 (t GHG)	Scope 1 (t CO_{2eq})	Scope 2 (t GHG)	Scope 2 (t CO_{2eq})
CO_2	36 483.01	36 483.01	5460.95	5460.95
CH_4	261.568	6539.20	—	—
N_2O	5.893	1756.11	—	—
HFCs	—	—	—	—
PFCs	—	—	—	—
SF_6	—	—	—	—
NF_3	—	—	—	—
Total	36 750.47	44 778.33	5460.95	5460.95

Source: Prepared by the authors based on the calculation performed by the GHG Protocol tool, v. 2018.1.4.

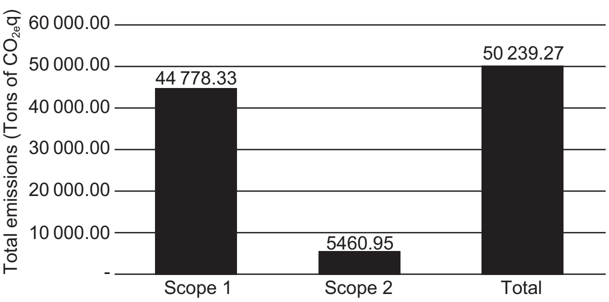

Fig. 1. Total emissions (Scope 1 and Scope 2) in tons of carbon dioxide equivalent (t CO_{2eq}). (Source: Prepared by authors [2019]).

Technological innovation in the industrial sector has a major impact on energy consumption and varies according to the level of technological development of the machinery and equipment used in the production process. The most sophisticated technologies in the industrial sector have high costs. As many countries do not have the opportunity to develop new technologies, they import these products. Scope 2 CO_2 emissions are reduced as new energy-saving technologies are used, rather than machines and equipment with lower energy consumption (Erdoğan et al. 2020).

Table III shows the detailed Scope 1 direct emissions: inputs used for combustion (stationary or mobile) in machinery and processes; fugitive emissions from reloading fire extinguishers; physical and chemical reactions of industrial processes, and treatment of sanitary effluents. It also exhibits the large representation of the stationary combustion category (24 407.88 t, 54.51% of the total GHG emissions of the analyzed factory), followed by the industrial processes category (19 762.50 t, 44.13% of the total GHG emissions of the analyzed factory). Figure 2 shows the percentage of participation of each category.

The stationary combustion category involves the burning of fuels through stationary equipment such as blast furnace, greenhouses and centrifugal machines (Table IV). A representative reduction in GHG emissions from a steel factory necessarily involves blast furnace as an important source of gas greenhouse gases. In a low carbon scenario, oxygen blast furnace with top gas recycling blast furnace (turbine for recovering top gases) is a technological possibility for reducing emissions. In a simplified way, the impact achieved with the mentioned technology is the capture of CO_2 through chemical absorption and reuse of gases (CO) in the blast furnace (CETESB, 2018).

According to Table IV, the most used fuel was natural gas, which contributes to 66.88% of the GHG emissions (16 324.72 t) within the stationary combustion category. Charcoal is the second, with 33.10% of the GHG emissions (8 078.99 t).

Biogenic CO_2 emissions must be reported but not accounted, since they are considered neutral (CO_2 emission equals CO_2 removal). These emissions corresponded to 139 248.92 t (Fig. 3).

Analyzing data in Figure 3, the stationary combustion category has the largest contribution of this type of emission, since 139 216.23 t of biogenic CO_2 (99.98%) are equivalent to the charcoal consumed in the blast furnace of the steel factory (neutral

Table III. Summary of each organization's GHG emissions by scope and category.

GHG	Stationary combustion (t)	Mobile combustion (t)	Fugitive emissions (t)	Industrial Processes (t)	Waste (solid waste + effluent) (t)	Total emissions Scope 1 (t)
CO_2	16 312.97	406.17	1.38	19 762.50	—	36 483.01
CH_4	261.24	0.03	—	—	0.30	261.57
N_2O	5.25	0.02	—	—	0.62	5.89
HFC	—	—	—	—	—	—
PFC	—	—	—	—	—	—
SF_6	—	—	—	—	—	—
NF_3	—	—	—	—	—	—
CO_2eq	24 407.88	413.37	1.381	19 762.50	193.20	44 778.33

Source: Prepared by the authors based on the calculation performed by the GHG Protocol tool, v. 2018.1.4.

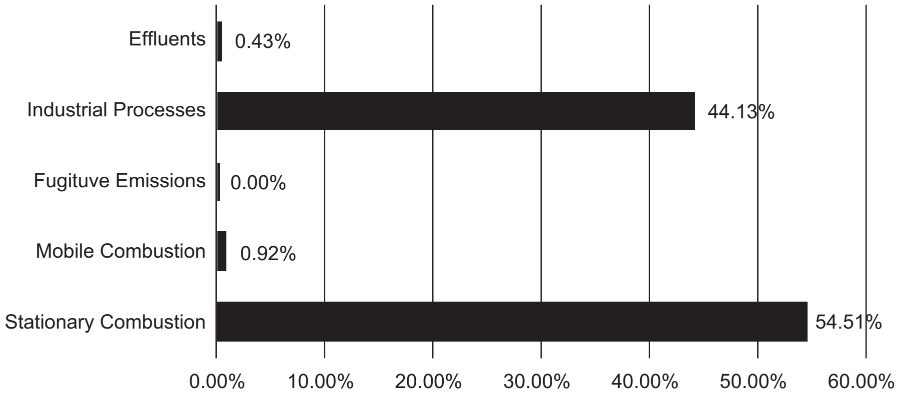

Fig. 2. Scope 1 greenhouse gases emissions by category. (Source: Prepared by authors [2019]).

Table IV. Specification of GHG emissions from the stationary combustion category.

Source	Fuel	Consumed amount	CO_{2eq} emissions (t)
Blast furnace	Charcoal	48 240.38 t	8 078.99
Ore heater, greenhouses, ovens, centrifugal machines, mixer and canteen	Injected dry natural gas	7 890 316.00 m³	16 324.72
Greenhouses and ovens	Liquefied petroleum gas (LPG)	0.36 t	1.06
Laboratory and maintenance (welding and cutting)	Acetylene gas	0.919 t	3.11
Total			24 407.88

Source: Prepared by the authors based on the calculation performed by the GHG Protocol tool, v. 2018.1.4.

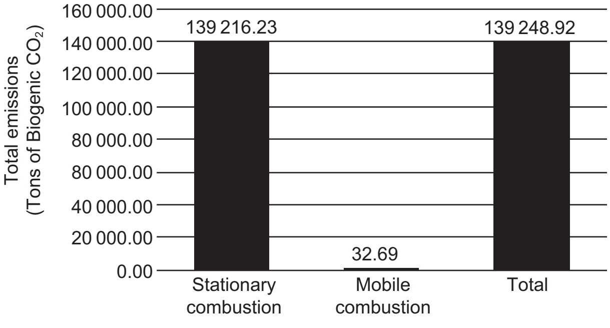

Fig. 3. Emissions in biogenic CO_2 (in metric tons). (Source: Prepared by authors [2019]).

emission). Mobile combustion emitted 32.69 t of biogenic CO_2 (0.023%), due to the fraction of biodiesel and ethanol present in diesel and domestic gasoline.

Scope 1 had the highest emissions from the industry, representing more than 89% of the CO_2eq total emissions. The stationary combustion category was highly representative, mainly due to the use of natural gas and, secondly, charcoal. Emissions accounted as CO_2eq corresponded only to emissions of CH_4 and N_2O, since CO_2 emissions (larger representation of emissions: 139 216.23 t) are not accounted because they are considered neutral.

Biogenic CO_2 emissions represented 7.91% (32.69 t CO_2) of the mobile combustion category (413.37 t CO_{2eq}). This amount is equivalent to the mandatory addition of ethanol in gasoline or biodiesel in diesel, regulated by specific resolutions in Brazil.

The configuration of the Brazilian energy matrix contributes to the reduced Scope 2 emissions, representing 10.87% (5 460.95 t CO_{2eq}) of the total inventoried GHG emissions (50 239.27 t CO_{2eq}).

The replacement of coal by charcoal is an important example of a GHG mitigation step in production processes. The use of renewable charcoal is an alternative way to mitigate GHG emissions, acting directly to improve resource efficiency during the carbonization process for pig iron production, ferroalloys and steel. Renewable biomass resources can be obtained from sustainably planted forests. Charcoal pig iron can be considered a green pig iron (Ministério do Meio Ambiente, 2016).

For the metal production, the studied company melts the iron in blast furnaces using charcoal produced in its own unit. The use of biomass (such as charcoal instead of coal) is a very positive point that can be highlighted. If the company did not use renewable biomass, there would be no neutral emissions and its GHG emissions would be higher, since coal is a fossil and non-renewable source of GHG emissions.

When charcoal is used in the blast furnace, 139 216.23 t of biogenic CO_2 (considered neutral, CO_2 emission being equal to CO_2 removal) are emitted during the stationary combustion category. Total CO_2eq emissions from other fuels used in this category were 24 407.88 t CO_2eq. However, if the company had used national metallurgical coal, instead of charcoal, emissions related to the stationary combustion category would have risen to 139 897.206 t CO_2eq.

A survey was carried out using the public emissions registry on the website of the Brazilian GHG Protocol Program in order to compare GHG emissions from the steel factory under study with other inventoried steelworks during the same period (2017). The public emissions registry is a platform for the disclosure of corporate inventories of GHG emissions from organizations participating in the Brazilian GHG Protocol Program.

Table V shows a comparison between the values of GHG emissions released by three steel companies with the emissions of the steel factory under study.

A direct comparison between steel industries is not possible, since they have different sizes and manufacturing capacities. The largest emissions are related to Scope 1, from the stationary combustion and industrial processes categories. This does not mean that emissions related to energy consumption should be disregarded (Scope 2 emissions). According to Siitonen et al. (2010), the steel industry is one of the industrial sectors with the highest energy consumption. A global reduction of CO_2 emissions requires more energy efficiency of industrial plants, therefore seeking to efficiently apply the use of equipment

Table V. Corporate greenhouse gases emissions (in t CO_2eq) reported by steel companies in the Public Emissions Registry.

GHG emissions by category	Company studied in this work (2017)	Ternium Brasil (2017)	CSN (2017)	ArcelorMittal (2017)
		Scope 1		
Stationary combustion	24 407.88	164 273.54	7 580 902.40	0.00
Mobile combustion	413.37	9675.90	207 915.10	15 552.97
Fugitives	1.38	87.55	109 043.08	0.00
Industrial processes	19 762.50	10 238 562.49	6 677 438.66	18 423 997.32
Effluents	193.20	0.00	1864.41	0.00
Total	44 778.33	10 412 599.48	14 577 163.65	18 439 550.29
		Scope 2		
Energy	5460.95	6049.07	245 959.84	83 394.10

Source: Prepared by authors (2019).

is an important criterion in the CO_2 emissions benchmarking. Other forms of energy efficiency can be considered, such as reducing losses and maximizing the reuse of gases to reduce the demand of fuels.

The cogeneration process aims to stimulate the structuring of the electric energy production with the reuse of heat in synergy with steelmakers, blast furnaces and coke ovens (Santos et al., 2010). Energy consumption during this process, the composition of the fuel and the technologies used, and the efficiency of resources can influence the CO_2 emission in the steel industry (Zhang et al., 2009; Huang et al., 2010; Xu et al., 2016).

Through a brief analysis of the fuel used by the company for its fleets (cars, ambulances, forklifts and locomotive) within the mobile combustion category, it was observed that if the company chooses to use biofuels (replacement of commercial diesel oil by biodiesel and gasoline for ethanol) its emissions would be biogenic, i.e., emissions related to the natural carbon cycle (neutral emissions).

The assessment and control of GHG emissions is a way to revert the scenario of large emissions that has been causing a rise in the planet's average surface temperature. Similar works based their research on the quantification of GHG emissions. Hwang et al. (2017) estimated GHG emissions and emission factors in nine incineration plants in Korea, measuring GHG concentrations in flue gas samples. Kyung et al. (2017) estimated the total GHG emissions generated from all stages of the life cycle of a sewer pipe system. Other works with similar proposals are the following: Carvalho et al. (2017) performed the quantification and analysis of GHG emissions from the Pontifical Catholic University of Rio de Janeiro to contribute with the university's environmental agenda. Almeida et al. (2020) measured the related to GHG emissions of an electricity generation industry and proposed strategies to reduce environmental impacts from the use of natural gas. Both used the GHG Protocol tool.

3.2. Adaptation of the Brazilian GHG Protocol Program Tool for its use in monthly reports

Emission data obtained in a shorter period of time would provide a more efficient control of GHG emissions. This could be accomplished through the development of a monthly indicator. Thus, the GHG Protocol v. 2018.1.4 was adapted for monthly reporting. The methodologies and emission factors proposed by the original tool were not modified. The spreadsheet columns were maintained in order to measure emissions month by month, reorganizing and structuring the tool.

The GHG Protocol tool is flexible, making possible its use for several segments that need to quantify their emissions. Therefore, in this work only the tables applicable to the factory under study have been adapted, while those that were not applicable were disregarded because they were not necessary for the quantification of GHG emissions from the studied steel factory.

The original tool uses, in some calculations, the ARRED function in Excel (which rounds a number to a specified number of digits). The adapted tool did not round the number and used all decimal places so that the value was as real as possible. So, there was a small difference between the values calculated by the original tool and the adapted one. Rounding is a recognized technique and is widely used in mathematics (especially when there is no device for performing numerical calculations), since it makes easier to work with numbers that have a large number of digits. This feature was dismissed because Excel is a spreadsheet editor that auto performs the proposed count.

Tables VI-IX show the values found using the adapted tool for monthly reports and the original tool from the GHG Protocol Program, by category. The company measured nitrogen data by laboratory analysis. The input values for the amount of nitrogen from the generated effluent corresponded to the average provided by the company (45 kgN m^{-3}). This value was repeated for 12 months. Thus, the values of total emissions in CO_2eq were the same for all months.

The adaptation of the tool was simpler in the case of scope 2 (energy category). The tool itself contained the total CO_2 emissions calculated monthly because of the necessary parameters to calculate this category (emission factors). The National Interconnected System (SIN) makes the parameters available monthly.

4. Conclusions

This work aimed to estimaye GHG emissions from a steel company, using the methodology developed

Table VI. Emissions of greenhouse gases found in the tools used from the stationary combustion category.

Stationary combustion (monthly report)		
Month	Total CO_2eq emissions (t)	Total biogenic CO_2 emissions (t)
January	831.797	4985.281
February	2102.317	13 361.276
March	2173.851	12 862.826
April	2194.952	12 337.364
May	2206.462	11 665.905
June	2403.182	14 418.492
July	2229.584	12 218.985
August	1964.285	10 949.109
September	2010.018	11 993.915
October	2056.937	11 899.373
November	2174.286	12 208.365
December	2060.209	10 315.339
Total	24 407.880	139 216.231
Original GHG Protocol data	Total CO_2eq emissions (t) 24 407.875	Total biogenic CO_2 emissions (t) 139 216.231

Source: Prepared by authors (2019).

Table VII. Emissions of greenhouse gases found in the tools used from the category mobile combustion.

Mobile combustion (monthly report)		
Month	Total CO_2eq emissions (t)	Total biogenic CO_2 emissions (t)
January	17.598	1.240
February	37.246	2.594
March	45.558	3.650
April	36.816	2.967
May	34.535	2.786
June	32.721	2.635
July	39.301	3.164
August	29.407	2.374
September	33.368	2.691
October	22.136	1.790
November	48.245	3.879
December	36.377	2.922
Total	413.307	32.693
Original GHG Protocol data	Total CO_2eq emissions (t) 413.371	Total biogenic CO_2 emissions (t) 32.693

Source: Prepared by authors (2019).

Table VIII. Emissions of greenhouse gases found in the tools used from the fugitive emissions and industrial processes categories.

Fugitive emissions (monthly reporting)		Industrial processes (monthly reporting)	
Month	Total CO_2eq emissions (t)	Month	Total CO_2eq emissions (t)
January	0.000	January	548.866
February	0.048	February	1759.425
March	0.268	March	2070.978
April	0.112	April	1749.116
May	0.000	May	1641.895
June	0.000	June	1638.765
July	0.000	July	1714.951
August	0.000	August	1528.520
September	0.370	September	1771.463
October	0.503	October	1909.887
November	0.080	November	1936.694
December	0.000	December	1491.944
Total	1.381	Total	19 762.503
Original GHG Protocol data	Total CO_2eq emissions (t) 1.381	Original GHG Protocol data	Total CO_2eq emissions (t) 19 762.515

Source: Prepared by authors (2019).

by the Brazilian GHG Protocol Program. Then, an adaptation of the tool was carried out to enable a monthly monitoring of GHG emissions.

Scope 1 emissions, which are GHG emissions from the company's internal operations, were the highest: 44 778.33 t CO_2eq (89.13% of the total CO_2eq). The other 10.87% of the total CO_2eq emitted refers to Scope 2 (energy category). This lower participation of the energy category was possible because a large part of Brazil's energy is produced from renewable sources, which generally have lower GHG emissions.

Among the calculated categories, stationary combustion accounted for 54.51% of CO_2eq emissions. Biogenic CO_2 emissions corresponded to 139 248.92 t. This value is very representative: if the company did not use biomass, CO_2eq emissions would not be considered neutral; consequently, they would increase significantly.

Table IX. Emissions of greenhouse gases found in the tools used from the effluents and energy categories.

Effluents (monthly report)		Energy (monthly report)	
Month	Total CO_2eq emissions (t)	Month	Total CO_2eq emissions (t)
January	16.109	January	133.722
February	16.109	February	258.351
March	16.109	March	448.166
April	16.109	April	452.851
May	16.109	May	441.832
June	16.109	June	347.275
July	16.109	July	394.314
August	16.109	August	576.123
September	16.109	September	633.310
October	16.109	October	707.425
November	16.109	November	649.225
December	16.109	December	418.354
Total	**193.304**	**Total**	**5460.947**
Original GHG Protocol data	Total CO_2eq emissions (t) 193.204	Original GHG Protocol data	Total CO_2eq emissions (t) 5460.947

Source: Prepared by authors (2019).

There is no predefined ideal quantitative GHG value for each organization. Thus, institutions always need to search for continuous improvement in their production processes.

The company's interest in global warming issues is tangible, since, as observed, it already has targets to reduce its energy consumption. Practical actions such as the use of charcoal were reported and the monitoring of its emissions was possible through the monthly indicator developed in this work.

The results obtained with the adaptation of the Brazilian GHG Protocol Program tool are a differential of this work about carbon emissions. A recommendation to the industry is to expand its transparency policy, giving all shareholders and employees an important role in the process of climate change mitigation.

Summarizing, the continuous improvement of energy efficiency is an option for mitigating GHG emissions. If the studied company had used national metallurgical coal, instead of charcoal, emissions related to the stationary combustion category would have risen from 24 407.875 to 139 897.206 t CO_2eq. Thus, actions to improve operational control and replace old equipment with more efficient ones are required. The strategy to be adopted will depend on the cost/benefit ratio of each action and its significance.

Acknowledgments

We are grateful for the financial support provided by the Brazilian Coordination of Improvement of Higher-Level Personnel (Coordenação de Aperfeiçoamento de Pessoal de Nível Superior, CAPES) (finance code 001).

References

Almeida FTR, Guimarães CS, Serra EG. 2020. Estimativa das emissões de gases de efeito estufa e proposta de mitigação dos impactos ambientais gerados por um empreendimento de geração de energia elétrica: um estudo de caso. Brazilian Journal of Development 6: 41175-41189. https://doi.org/10.34117/bjdv6n6-599

Alves JED. 2014. Aquecimento global e o decrescimento demo-econômico. Revista Espinhaço 3: 4-16. https://doi.org/10.5281/zenodo.3966040

Carvalho PSL, Mesquita PPD, Araújo EDG. 2016. Sustentabilidade da siderurgia brasileira: eficiência energética e competitividade. BNDES Setorial 41: 181-236. Available at: https://web.bndes.gov.br/bib/jspui/handle/1408/4287 (accessed in April 2021).

Carvalho JPAF, Van Elk AGHP, Romanel C. 2017. Inventário de emissões e gases de efeito estufa no campus Gávea da PUC-RIO. Engenharia Sanitária e Ambiental 22: 591-595. https://doi.org/10.1590/s1413-41522017155865

CEBDS. 2018. Diálogo talanoa, Relatório 1. Conselho Empresarial Brasileiro para o Desenvolvimento Sustentável. Available at: https://d335luupugsy2.cloudfront.net/cms/files/14773/1542124839Relatrio_Talanoa_final.pdf (accessed in February 2019).

CETESB. 2018. Estudo de baixo carbono para a indústria siderúrgica no Estado de São Paulo de 2014 a 2030. Companhia Ambiental do Estado de São Paulo. Available at: https://cetesb.sp.gov.br/proclima/wp-content/uploads/sites/36/2018/09/SINTESE-PUBLICA%C3%87%C3%83O_on-line.pdf (accessed in April 2021).

Cifci E, Oliver ME. 2018. Reassessing the links between GHG emissions, economic growth, and the UNFCCC:

A difference-in-differences approach. Sustainability 10: 334. https://doi.org/10.3390/su10020334

EAESP-FGV. 2021. Programa Brasileiro GHG Protocol. Escola de Administração de Empresas de São Paulo da Fundação Getulio Vargas. Available at: https://eaesp.fgv.br/centros/centro-estudos-sustentabilidade/projetos/programa-brasileiro-ghg-protocol (accessed in April 2021).

EPE. 2016. Matriz energética. Empresa de Pesquisa Energética. Available at: http://www.epe.gov.br/pt/abcdenergia/matriz-energetica-e-eletrica (accessed in April 2019).

Erdoğan S, Yıldırım S, Yıldırım DÇ, Gedikli A. 2020. The effects of innovation on sectoral carbon emissions: Evidence from G20 countries. Journal of Environmental Management 267: 110637. https://doi.org/10.1016/j.jenvman.2020.110637

FGV/WRI. 2009. Especificações do Programa Brasileiro GHG Protocol. Cartilha 76. Fundação Getulio Vargas/World Resources Institute. Available at: https://s3-sa-east-1.amazonaws.com/arquivos.gvces.com.br/arquivos_ghg/152/especificacoes_pb_ghgprotocol.pdf (accessed in April 2021).

Hickmann T. 2017. Voluntary global business initiatives and the international climate negotiations: A case study of the Greenhouse Gas Protocol. Journal of Cleaner Production 169: 94-104. https://doi.org/10.1016/j.jclepro.2017.06.183

Huang Z, Ding X, Sun H, Liu S. 2010. Identification of main influencing factors of life cycle CO_2 emissions from the integrated steelworks using sensitivity analysis. Journal of Cleaner Production 18: 1052-1058. https://doi.org/10.1016/j.jclepro.2010.02.010

Hwang K, Choi S, Kim M, Heo J, Zoh K. 2017. Emission of greenhouse gases from waste incineration in Korea. Journal of Environmental Management 196: 710-718. https://doi.org/10.1016/j.jenvman.2017.03.071

INEA. 2007. DZ-215.R-4 - Diretriz de controle de carga orgânica biodegradável em efluentes líquidos de origem sanitária. Instituto Estadual do Ambiente. Available at: http://www.inea.rj.gov.br/cs/groups/public/documents/document/zwew/mde0/~edisp/inea0014059.pdf (accessed in May 2020).

Instituto Aço Brasil. 2020. A siderurgia em números. Available at: https://acobrasil.org.br/site/wp-content/uploads/2020/04/Mini_anuario_2020_completo.pdf (accessed in February 2021).

IPCC. 2006. 2006 IPCC Guidelines for national greenhouse gas inventories (Eggleston HS, Buendia L, Miwa K, Ngara T and Tanabe K, Eds.). National Greenhouse Gas Inventories Programme, Intergovernmental Panel on Climate Change. Available at: https://www.ipcc-nggip.iges.or.jp/public/2006gl/vol3.html (accessed in June 2018).

IPCC. 2007. Fourth Assessment Report: Climate Change 2007 (AR4). Intergovernmental Panel on Climate Change, Geneva. Available at: https://www.ipcc.ch/assessment-report/ar4/ (accessed in November 2018).

IPCC. 2018. Global Warming of 1.5 °C. Intergovernmental Panel on Climate Change, Geneva. Available at: https://www.ipcc.ch/sr15/ (accessed in January 2019).

Kyung D, Dongwook K, Sora Y, Wonyong C, Woojin L. 2017. Estimation of greenhouse gas emissions from sewer pipeline system. Carbon Footprinting 22: 1901-1911. https://doi.org/10.1007/s11367-017-1288-9

MDIC. 2013. Plano setorial de mitigação e adaptação à mudança do clima para a consolidação de uma economia de baixa emissão de carbono na indústria de transformação. Ministério do Desenvolvimento, Indústria e Comércio Exterior. Available at: http://extwprlegs1.fao.org/docs/pdf/bra167310.pdf (accessed 2021 April)

Ministério do Meio Ambiente. 2016. Siderurgia sustentável. Available at https://antigo.mma.gov.br/clima/politica-nacional-sobre-mudanca-do-clima/siderurgia-sustentavel.html (accessed in April 2019).

Mok KL, Han SH, Choi S. 2014. The implementation of clean development mechanism (CDM) in the construction and built environment industry. Energy Policy 65: 512-523. https://doi.org/10.1016/j.enpol.2013.10.039

Novaes DA de, Souza PS da S. 2018. Análise do desenvolvimento sustentável no balanço social da empresa eletronuclear. Episteme Transversalis 9: 166-180. Available at: http://revista.ugb.edu.br/ojs302/index.php/episteme/article/view/890 (accessed in April 2021).

Patchell J. 2018. Can the implications of the GHG Protocol's scope 3 standard be realized? Journal of Cleaner Production 185: 941-958. https://doi.org/10.1016/j.jclepro.2018.03.003

Radonjič G, Tompa S. 2018. Carbon footprint calculation in telecommunications companies – The importance and relevance of scope 3 greenhouse gases emissions. Renewable and Sustainable Energy Reviews 98: 361-375. https://doi.org/10.1016/j.rser.2018.09.018

Rockström J, Schellnhuber HJ, Hoskins B, Ramanathan V, Brasseur G, Gaffney O, Nobre C, Meinshausen M, Lucht W. 2016. The world's biggest gamble. Earth's Future 4: 465-470. https://doi.org/10.1002/2016EF000392

Santos FCB, Dubeux CBS, Pereira Jr. AO. 2010. Emissão de gases de efeito estufa – 2050: Implicações econômicas e sociais do cenário de plano governamental. Available at http://www.centroclima.coppe.ufrj.br/images/documentos/ies-brasil-2050/4_-_Cenario_de_Emiss%C3%B5es_de_GEE_-_Setor_Industrial_Demanda_de_Energia_e_Emissoes_de_Processos_Industriais_-_IES_Brasil_2050.pdf (accessed in February 2021).

SEBRAE. 2015. Guia de implementação: Gestão de emissões e remoções de gases de efeito estufa (GEE). Serviço Brasileiro de Apoio às Micro e Pequenas Empresas.SEEG. 2019. Sistema de Estimativas de Emissões e Remoções de Gases de Efeito Estufa. Available at: http://seeg.eco.br/ (accessed in February 2021).

Siitonen S, Tuomaala M, Ahtila P. 2010. Variables affecting energy efficiency and CO_2 emissions in the steel industry. Energy Policy. 38: 2477-2485. https://doi.org/10.1016/j.enpol.2009.12.042

Ugaya CML, Lora EES, Silva ER da, Freires FGM, Lima GBA, Neto JAA de, Neto JV, Xavier LH, Junior LCM de, Oliveira LB de, Meiriño MJ, Leme MMV, Quelhas OLG, Gouvinhas RP, Câmara RPB de, Silva RM da, Braga RCS de, Motta RS da, Matos RMB, Curi RC, França SLB, Almeida TAN das, Mattos UAO de, Curi WF. 2013. Gestão Ambiental de Unidades Produtivas. Elsevier, Rio de Janeiro.Watts N, Adger WN, Agnolucci P. 2015. Health and climate change: Policy responses to protect public health. Environnement, Risques et Sante 386: 1861-1914. https://doi.org/10.1016/S0140-6736(15)60854-6

WBSCD. 2014. The greenhouse gas protocol: A corporate accounting and reporting standard. World Business Council for Sustainable Development. Available at: https://www.wri.org/publication/greenhouse-gas-protocol (accessed in February 2021).

Xu W, Wan B, Zhu T, Shao M. 2016. CO_2 emissions from China's iron and steel industry. Journal of Cleaner Production139: 1504-1511. https://doi.org/10.1016/j.jclepro.2016.08.107

Xue Y. 2020. Empirical research on household carbon emissions characteristics and key impact factors in mining areas. Journal of Cleaner Production 256: 120470. https://doi.org/10.1016/j.jclepro.2020.120470

Yin RK. 2015. Estudo de caso: Planejamento e métodos. Bookman Editora, Porto Alegre.

Zhang M, Mu H, Ning Y. 2009. Accounting for energy-related CO_2 emission in China, 1991-2006. Energy Policy 37: 767-773. https://doi.org/10.1016/j.enpol.2008.11.025

Zheng S, Alvarado V, Xu P, Leu S, Hsu S. 2018. Exploring spatial patterns of carbon dioxide emission abatement via energy service companies in China. Resources, Conservation and Recycling 137: 145-155. https://doi.org/10.1016/j.resconrec.2018.06.004

Atmósfera 36(1), 171-182 (2023)
https://doi.org/10.20937/ATM.52966

Prediction of atmospheric corrosion from meteorological parameters: Case of the atmospheric basin of the Costa Rican Western Central Valley

Javier E. RODRÍGUEZ-YÁÑEZ[1]*, Erick RIVERA-FERNÁNDEZ[2], Daniel ALVARADO-GONZÁLEZ[3],
Mariela ABDALAH-HERNÁNDEZ[3] and Rafael QUIRÓS-QUIRÓS[4]

[1]*Urban Ecology Research Laboratory, Costa Rica Distance University, 474-2050, Mercedes de Montes de Oca, San José, Costa Rica.*
[2]*School of Physics and Center for Geophysical Research, University of Costa Rica, 11501-2060, San Pedro de Montes de Oca, San José, Costa Rica.*
[3]*Advanced Computing Laboratory, National High Technology Center, 1174-1200, Pavas, San José, Costa Rica.*
[4]*School of Geography, University of Costa Rica, 11501-2060, San Pedro de Montes de Oca, San José, Costa Rica.*
*Corresponding author; email: jrodriguezy@uned.ac.cr

Received: August 26, 2020; accepted: April 20, 2021

RESUMEN

La evaluación de la corrosión atmosférica se basa actualmente en el estudio de las cuencas atmosféricas (AB, por sus siglas en inglés). La modelización de la corrosión atmosférica implica en muchos casos la medición de varios parámetros meteorológicos y de contaminación atmosférica, concretamente la temperatura, la humedad relativa, el cloruro y el dióxido de azufre, lo que hace más complejo el proceso de estimación. Sin embargo, para el Valle Central Occidental (WCV, por sus siglas en inglés) de Costa Rica, un AB de baja contaminación, es posible desarrollar modelos simplificados de corrosión atmosférica, basados en un pequeño número de parámetros atmosféricos. En este trabajo se analizaron las variables meteorológicas de la región de estudio en cuanto a su dependencia de la altitud y su aplicabilidad en el desarrollo de un modelo simplificado para predecir la tasa de corrosión (Vcorr). El resultado del modelo de predicción se comparó con el modelo estándar de la norma ISO 9223:2012, mostrando una mayor habilidad y dando resultados fiables para un amplio intervalo de altitudes.

ABSTRACT

The assessment of atmospheric corrosion is currently based on the study of atmospheric basins (AB). Modeling atmospheric corrosion in many cases involves the measurement of several meteorological and atmospheric pollution parameters, specifically temperature, relative humidity, chloride, and sulfur dioxide, making the estimation process more complex. However, for the Western Central Valley (WCV) in Costa Rica, a low-pollution AB, it is possible to develop simplified atmospheric corrosion models based on a small number of atmospheric parameters. In this paper, the meteorological variables of the study region were analyzed in terms of their dependency on altitude and their applicability in the development of a simplified model to predict the corrosion rate (Vcorr). The output of the predictive model was compared with the standard model of ISO 9223:2012, showing a higher skill and giving reliable results for a wide interval of altitudes.

Keywords: atmospheric basin, corrosion, meteorological parameters, basic modeling.

1. Introduction

The Costa Rican Western Central Valley (WCV) is limited to the northwest by the Central Volcanic mountain range, to the east by the hills of Ochomogo, and to the southwest by the foothills of the Talamanca mountain range. The average altitude of the WCV is about 1000 m above sea level (m.a.s.l.), with values up to 2000 m.a.s.l. in some places (IMN, 2008).

The region's average annual precipitation is 2300 mm, with two clearly marked seasons: a rainy season from May to November and a dry season from December to April. During the rainy season, a relative minimum of precipitation occurs in July-August, known as the *veranillo* or mid-summer drought (Magaña et al., 1999). Temperature and relative humidity show small changes, with average values of 20 ºC and 75 %, respectively, varying with altitude and the time of the year (Solano and Villalobos, 2000; IMN, 2008). The predominant winds are the trade winds that blow from the northeast to the southwest. The Central Volcanic mountain range allows the passage of trade winds over the mountains or through mountain passes (mainly the gaps of La Palma and Desengaño). The seasonal variation of wind intensity, associated with the Caribbean low-level jet, determines most of the climatic changes in the WCV (Muñoz et al., 2002; Amador, 2008). Another characteristic pattern of the wind in the WCV is related to mountain-valley circulations. These are generated by temperature differences between both geographic landforms during the day, causing the wind to move from the mountain to the valley in the morning and in the opposite direction in the afternoon (Zárate, 1978; Barrantes et al., 1985). Due to the climatic and orographic conditions of the WCV, this area can be considered an Atmospheric Basin (AB). Here the climatic variability, circulation, and dispersion of air pollutants are driven mainly by the prevailing direction of winds and orography (Zárate, 1980; Muñoz et al., 2002; Caetano and Iniestra, 2008; García-Reynoso et al., 2009; Herrera et al., 2012; SEMARNAT-INECC, 2016).

Metallic materials are thermodynamically unstable under atmospheric conditions, which causes their deterioration, giving rise to the atmospheric corrosion phenomenon. A usual way to evaluate this process is by obtaining the loss of material in a fundamental state with respect to the time of exposure to the environment. This way allows the corrosion rate estimation as a loss of mass per unit area (mg $m^{-2} y^{-1}$) or as a loss of sheet thickness (µm y^{-1}) during the exposure time. Low carbon steel is the most common material for visualizing corrosión, similar to ASTM A36/A36M-19 (ASTM International, 2019).

Previous research by Morcillo et al. (2011) and the guidelines of the ISO 9223:2012 standard state that temperature (T), relative humidity (RH), chlorides (Cl^-), and sulfur oxides (SO_2) are the primary agents that contribute to corrosion. Temperature and relative humidity provide enough conditions for the material oxidation process, while pollutants modify the oxides formed on steel surfaces, producing distortion in the crystalline network and structural weakness. Consequently, materials turn more labile and porous, becoming more susceptible to corrosive attacks (Feliu et al., 1993; Morcillo et al., 2013; Díaz et al., 2018).

Temperature and relative humidity variables are obtained from meteorological data, and the deposition of both chlorides and sulfur oxides is measured or estimated by air pollution evaluation methods. These parameters permit the characterization of the effects of pollution variation on the corrosion rate in the WCV (Morcillo et al., 1998; Roberge et al., 2002; Morcillo et al., 2012; Robles, 2013; Garita-Arce et al., 2014; Rodríguez-Yáñez et al., 2015; Alcántara et al., 2015; Morcillo, 2017).

Garita-Arce et al. (2014) proposed a series of models for obtaining corrosion rates depending on the available information. For Costa Rica, maps of applicability of the corrosion models are based on the work of Rodríguez-Yáñez et al. (2015). These maps present an increasing complexity, starting from the Brooks deterioration index to the ISO 9223 (ISO, 1992) standard and using linear equations to model corrosion rate. The updated ISO 9223:2012 (ISO, 2012a) standard includes a new model for estimating corrosion. It considers the annual corrosion as a function of climatic and pollution variables.

2. Data and methods

Hourly meteorological data for several stations within the WCV were provided by the National Meteorological Institute and the Costa Rican Electricity Institute (IMN and ICE, respectively, by their Spanish acronyms). Figure 1 shows the location of the area

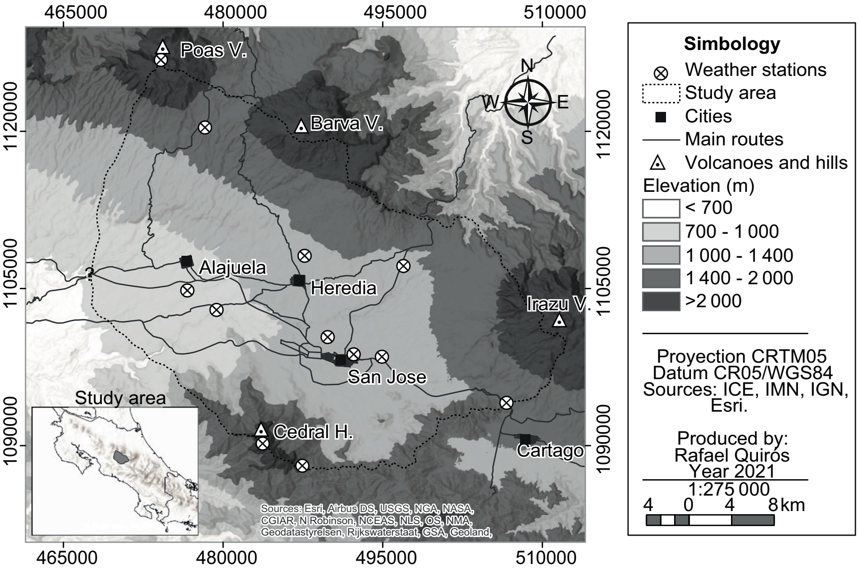

Fig. 1. Location of the WCV and the weather stations used for data collection.

of study. The analysis period was from 2010 to 2019 (see Table I). Only meteorological stations with less than 5 % of missing data were considered. From these data, the variables of interest were T and RH. The time of wetness (TOW), defined as the fraction of hours per year where T is greater than 0 ºC and RH is greater than or equal to 80 %, was also obtained.

2.1 Atmospheric conditions and air pollution

Within the studied period, the number of both warm (El Niño) and cold (La Niña) phases of the El Niño-Southern Oscillation (ENSO) is similar (NOAA, 2019). ENSO episodes are linked to inter-annual variations in circulation and precipitation patterns over Costa Rica (Fernández et al. 2013).

On the other hand, the volcanic activity was low and spaced in time. It was mainly associated with eruptions of the Poás and Turrialba volcanoes in 2015. During most of these eruptive events, winds were not blowing toward the WCV (OVSICORI, 2015). Under these conditions, several authors have shown that pollution levels of chlorides and sulfur oxides in the WCV are about 5 mg m^{-2} d^{-1} and 10 mg m^{-2} d^{-1}, respectively (Robles, 2013; Herrera-Murillo et al., 2014). These levels correspond to a low polluted atmosphere.

2.2 Corrosion models

According to the results of Garita-Arce et al. (2014) for the low carbon steel, an estimation curve of the corrosion rate at the WCV can be derived from meteorological parameters, specifically RH and TOW. Corrosion rate (Vcorr) for the WCV is a linear function of TOW or RH, as given by the following equations:

$$\mathrm{Vcorr} = 0.949RH - 56.65 \quad \mathrm{R}^2 = 0.930, \tag{1}$$

$$\mathrm{Vcorr} = 22.87TOW + 7.85 \quad \mathrm{R}^2 = 0.953, \tag{2}$$

where,
Vcorr: corrosion rate, µm y^{-1},
TOW: fraction average annual hours of wetness, dimensionless,
RH: average annual relative humidity, %.

The above equations were determined for an altitude of 1108 m.a.s.l. in the La Sabana sector of San José, Costa Rica.

The ISO 9223:2012 standard contains guidelines to determine Vcorr. One of them is to utilize the corrosion categories listed in Table II. A second alternative is to obtain it by employing model equations.

Table I. Location of the meteorological stations available in the WCV.

Name	North latitude	West longitude	Altitude (m.a.s.l)	Start date	End date
RECOPE, Ochomogo	09º 53’ 40.2”	83º 56’ 19.4”	1546	01/01/2010	31/01/2018
CIGEFI	09º 56’ 11.0”	84º 02’ 43.0”	1210	01/01/2010	31/01/2018
IMN, Aranjuez	09º 56’ 16.6”	84º 04’ 10.8”	1181	01/01/2010	31/01/2018
Juan Santamaría International airport	09º 59’ 26.5”	84º 12’ 52.9”	913	01/01/2010	15/02/2018
Fraijanes lake	10º 08’ 14.4”	84º 11’ 36.6”	1720	01/01/2010	31/01/2018
RECOPE, La Garita	10º 00’ 19.0”	84º 17’ 45.0”	740	12/01/2010	31/01/2018
West Pavas, near to airport	09º 57’ 26.3”	84º 08’ 51.6”	997	01/01/2010	05/03/2015
Santa Bárbara	10º 02’ 00.0”	84º 09’ 57.0”	1070	01/01/2010	31/01/2018
Belén	09º 58’ 30.0”	84º 11’ 08.0”	926	01/01/2010	02/11/2017
Burio hill, Aserrí	09º 50’ 25.3”	84º 06’ 45.6”	1811	14/11/2012	12/10/2017
Altos Tablazo, Higuito	09º 50’ 12.4”	84º 03’ 18.1”	1660	28/06/2012	31/05/2017
Chitaria hill, Santa Ana	09º 53’ 30.1”	84º 11’ 37.3”	1717	01/03/2011	11/10/2017
Poás volcano lake	10º 11’ 21.0”	84º 13’ 55.2”	2598	05/09/2011	12/02/2018
Cedral hill, Escazú	09º 51’ 41.1”	84º 08’ 45.2”	2255	29/08/2012	12/10/2017
School of Agricultural Sciences, Santa Lucía, Heredia	10º 01’ 22.8”	84º 06’ 42.4”	1257	19/11/2013	31/01/2018
West Tobías Bolaños airport, Pavas	09º 57’ 26.3”	84º 08’ 51.6”	981	05/03/2015	10/10/2017
San Luis	10º 00’ 54.0”	84º 01’ 36.0”	1341	01/09/2018	31/9/2019
Colima	09º 57’ 09.0”	84º 05’ 24.2”	1145	01/01/2010	12/31/2017

Table II. Corrosion rate for different corrosivity categories for low carbon steel.

Corrosion category	Corrosion rate (μm y^{-1})	Corrosivity level
C1	≤ 1.3	Very low
C2	1.3 to 25	Low
C3	25 to 50	Medium
C4	50 to 80	High
C5	80 to 200	Very High
CX	200 to 700	Extreme

In this standard, the set of equations to calculate the corrosion of carbon steel is:

$$\begin{aligned} &\mathrm{Vcorr} = 1.77\ \mathrm{P_d^{0.52}} \exp\left(0.020\ \mathrm{RH} + \mathrm{f_{St}}\right) + \\ &0.102\ \mathrm{S_d^{0.62}} \exp\left(0.033\ \mathrm{RH} + 0.040\ \mathrm{T}\right), \\ &\mathrm{f_{St}} = 0.150\left(\mathrm{T\text{-}10}\right),\ \ \mathrm{T} \leq 10 \text{ or} \\ &f_{St} = -0.054\left(\mathrm{T\text{-}10}\right),\ \mathrm{T} > 10 \\ &N = 128 \qquad \mathrm{R^2} = 0.85 \end{aligned} \tag{3}$$

where,
f_{st}: factor of Steel
Vcorr: corrosion rate in the first year, μm y^{-1},
T: annual average temperature, ºC,
RH: annual average relative humidity, %,
P_d: annual average SO_2 deposition, mg m^{-2} d^{-1},
S_d: annual average Cl$^-$ deposition, mg m^{-2} d^{-1}.

2.3. Data processing

Annual averages of RH, T, and TOW were obtained for each location with the corresponding standard deviation. A relatively high correlation between these parameters and altitude (A), in m.a.s.l., was found. The determination correlation coefficient (R^2) is a useful statistic for testing linearity. An acceptable value of R^2 must be higher than 0.75 (Wilks, 2011).

General data analysis was performed with Python. The corrosion rate was determined and represented in two maps. One was generated with a simplified model, and the other with the new method formulated by the ISO 9223:2012 standard. Contour lines for the WCV were taken from the Atlas of Costa Rica with a spatial resolution of 10 m (Ortiz-Malavasi, 2015), and the maps were created with ArcGIS software.

The simplified and the ISO 9223:2012 models were compared between them and against experimental measurements. The latter were obtained according to the procedures in the ISO 9223:2012, ISO 9225:2012, and ASTM G1-03 (ISO, 2012a; ISO, 2012b; ASTM International, 2017) standards.

3. Results and discussion

3.1. Meteorological parameters

Most stations were located below 1500 m.a.s.l. and inside the valley. There were less data points in medium-altitude locations a (1500 m.a.s.l. to 2000 m.a.s.l.), and only three in the most elevated parts (above 2000 m.a.s.l.). The geographical distribution of the meteorological observations was not homogeneous. Data points were scarce in the northern section of the WCV, particularly around the foothills of the Barva volcano.

Figures 2, 3, and 4 represent the relations between temperature, relative humidity, and time of wetness with altitude and their standard deviation.

Based on the information presented in figure 2, the equation that describes the temperature variation between 700 m.a.s.l. and 2600 m.a.s.l. is:

$$T = -0.00680A + 28.61 \qquad \mathrm{R}^2 = 0.971, \tag{4}$$

where,
T: annual average temperature, ºC,
A: altitude, m.a.s.l.

The value of the vertical temperature gradient in the WCV from equation (4) is remarkably similar to the global mean value of –6.5 ºC km^{-1} in the lower atmosphere Sendiña-Nadal and Pérez-Muñuzuri, 2006). The standard deviation tends to increase with altitude at a rate of 2 % for every 1000 m. This behavior is possibly related to a more significant seasonal variability of temperatures in mountainous regions of the WCV (Solano and Villalobos, 2000). Usually, the standard deviation of temperature in the WCV is less than 0.5ºC.

In figure 3, it can be observed that relative humidity increases linearly with an altitude between 700 m.a.s.l. and 2600 m.a.s.l. This relation is expressed as:

$$RH = 0.0129A + 61.54 \qquad \mathrm{R}^2 = 0.951, \tag{5}$$

where,
RH: annual average relative humidity, %,
A: altitude, m.a.s.l.

At higher elevations, the air usually reaches the saturation point, and clouds may form. In the WCV, relative humidity was near the 100 % value at 2600 m.a.s.l. (Murphy and Hurtado, 2013). Above this altitude, equation (5) is not applicable.

The standard deviation of RH is usually less than 5 %, with a slight tendency to decrease with altitude. In the lowest areas of the valley, the seasonal

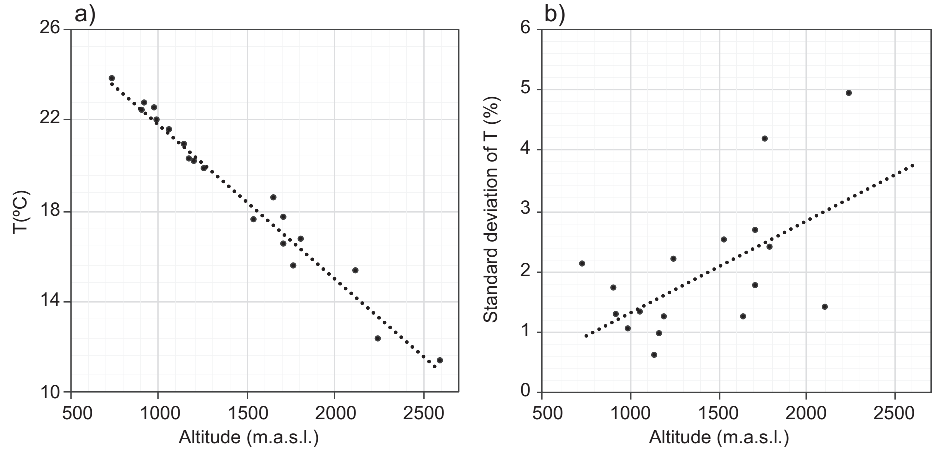

Fig. 2. Variation of (a) annual average and (b) standard deviation of temperature with altitude.

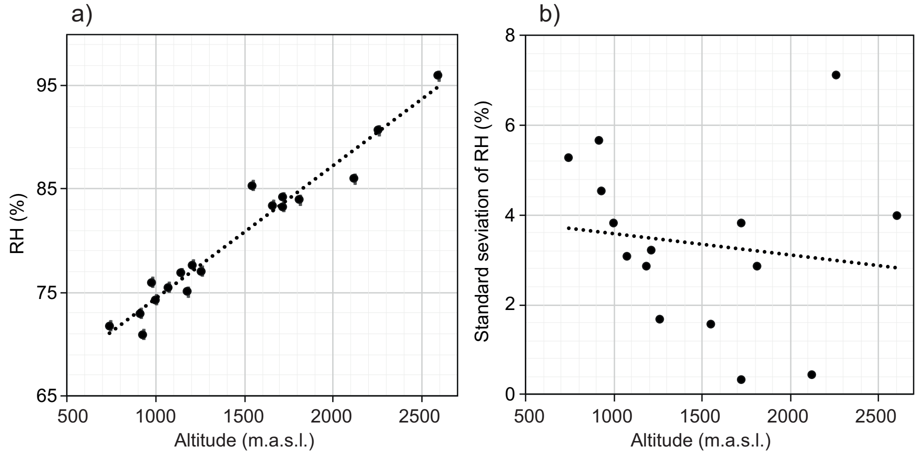

Fig. 3. Variation of (a) annual average and (b) standard deviation of RH with altitude.

variability of RH is usually determined by the differences between dry and rainy seasons (Abdalah-Hernández et al., 2019).

Campos and Castro (1992) explained that RH could quickly vary from 20 % to 100 % at higher elevations of the eastern part of the WCV. This variation is due to dry upper troposphere air and the transport of humid air masses through the mountain pass from the Caribbean region. According to these authors, RH fluctuations decrease at lower elevations.

The relation between time of wetness and altitude from 700 m.a.s.l. to 2600 m.a.s.l., as shown in figure 4, is as follows

$$TOW = 0.000362A + 0.0261 \quad R^2 = 0.900, \tag{6}$$

where,

TOW: average fraction of annual hours of wetness per year, dimensionless,

A: altitude, m.a.s.l.

The TOW increases while the deviation standard decreases with altitude (Rodríguez-Yáñez et al., 2015). This proportionality is due to more saturated air at higher elevations, where RH increases and gets close to 100 %.

The variance of the TOW in the lower valley is associated with changes between the dry and rainy seasons. There is also greater homogeneity in the

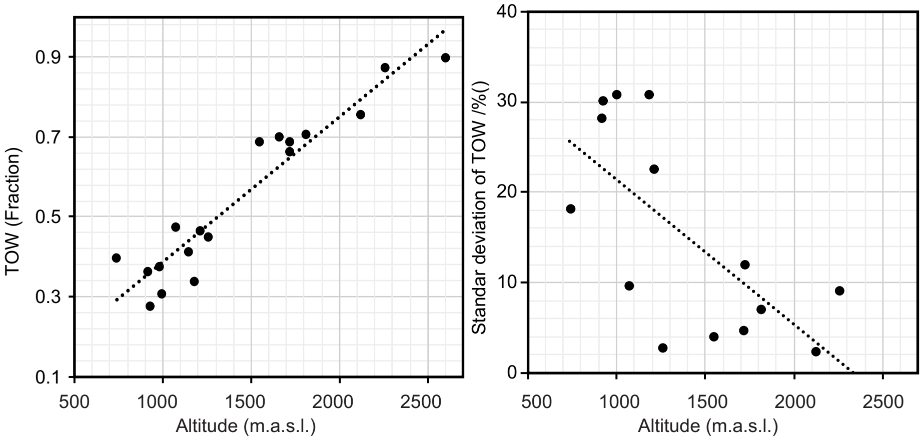

Fig. 4. Variation of (a) annual accumulated average and (b) standard deviation of time of wetness with altitude.

TOW at higher elevations since the RH values tend to be above 80 % for extended periods.

3.2. Estimation of Vcorr using the linear and ISO models

Using the linear relationships from the previous section (equations 4 to 6) is possible to calculate the variation of Vcorr with altitude by only considering meteorological variables (equations 1 and 2). The derived equations for corrosion rate, based on RH and TOW, are:

$$\mathrm{Vcorr} = 0.0083\ A+8.44 \quad R^2 = 0.884, \tag{7}$$

$$\mathrm{Vcorr} = 0.0123\ A+1.73 \quad R^2 = 0.857 \tag{8}$$

In both cases, the estimated R^2 values are greater than 0.75 and therefore acceptable.

A similar process is applied to the ISO 9223:2012 equation (equation 3). The factors P_d and S_d are estimated by Herrera et al. (2012) approximation. In this case:

$$\mathrm{Vcorr} = 5.861\exp(0.0006252\ A+0.22586) +0.277\exp(0.000154\ A+3.175). \tag{9}$$
$$R^2 = 0.807$$

The simplified equation of ISO 9223:2012 is governed by the effect of RH and increases exponentially with the altitude.

3.3. Model output comparison

Field corrosion data was collected from September 2018 to September 2019. Table III shows the location and altitude of the measurement sites, as well as the annual average of the atmospheric variables and pollutants at each point. Atmospheric corrosion, from observations and models (equations 1 to 3 and 7 to 9), is shown in Table IV.

Pollutant levels were similar to those utilized for the approximations with equations 7 to 9; however, RH and TOW did not follow the expected tendency with altitude. The reason for this behavior is probably the position of the stations in the WCV since they were located under the influence of different climatic conditions. Particularly, the station in San Luis is constantly influenced by humid air masses transported from the Caribbean region (Campos and Castro, 1992).

Figure 5 illustrates the predicted corrosion from equations 7 to 9 and their comparison with actual measurements.

The Vcorr values from the simple linear models based on RH and TOW (equations 7 and 8,

Table III. Annual mean atmospheric parameters and levels of pollutants in three different sites.

Site	North latitude	West longitude	A (m.a.s.l.)	RH (%)	TOW (fraction)	T (ºC)	Cl^- ($mg\ m^{-2}\ d^{-1}$)	SO_2 ($mg\ m^{-2}\ d^{-1}$)
CIGEFI	09º 56’ 11”	84º 02’ 43”	1210	79.92	0.5701	20.29	3.82	6.06
San Luis	10º 00’ 54”	84º 01’ 36”	1341	90.19	0.8126	18.36	3.52	8.58
Santa Ana	09º 52’ 54”	84º 11’ 14”	1772	83.46	0.6643	17.41	4.00	7.02

Table IV. Atmospheric corrosion in three different sites, using equations 1 to 3, 7 to 9, and actual values, in $\mu m\ y^{-1}$. Values in *italics* correspond to overestimations of the corrosion rate compared to actual measurements (bold black quantities). Other modeled corrosion rates showing small differences (less than 5 %) with respect to observations are underlined.

Site	Vcorr model *RH* (eq. 1)	Vcorr model *TOW* (eq. 2)	Vcorr ISO 9223 (eq. 3)	Vcorr Observed	Vcorr model *RH* (eq. 7)	Vcorr model *TOW* (eq. 8)	Vcorr ISO 9223 (eq. 9)
CIGEFI	*19.2*	*20.8*	*20.8*	**17.4**	16.7	*18.6*	*23.8*
San Luis	*28.9*	*26.5*	*30.0*	**17.3**	18.2	*19.6*	*25.2*
Santa Ana	*22.5*	*22.9*	*24.9*	**16.6**	*23.4*	*23.2*	*31.0*

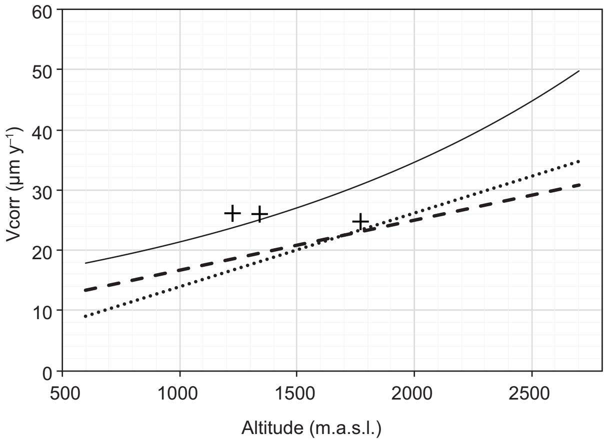

Fig. 5. Vcorr vs. Altitude, for a model using a) equation 7 (RH, dotted line), b) equation 8 (TOW, dashed line), c) equation 9 (ISO 9223, solid line). Actual measurements are represented by cross markers (+).

respectively) increased rapidly with altitude and corresponded to C2 and C3 corrosivity categories, according to the ISO 9223:2012 standard (Table II). The corrosion in the ISO 9223:2012 model shows a more significant increase with altitude. This increase is due to the exponential behavior of equation 9, governed by the RH variable. The difference between observed values and the ISO 9223:2012 equation is around 20 % at medium altitudes. In the mountain (Santa Ana), this contrast reaches the order of 100 %.

Model outputs in comparison with observations presented notable differences. When the atmospheric parameters are used (equations 1 and 2), the deviations are greater in places with high values of *RH* (RH > 80 %) or *TOW* (TOW > 0.6), for example, in San Luis. When considering the simple models with altitude dependency (equations 7 and 8), there is generally a good estimation of Vcorr in the region between 1000 m.a.s.l. and 1400 m.a.s.l. Overestimation greater than 10% occurs at altitudes higher than 1500 m.a.s.l. It is important to consider that most of the population of the WCV lives within the 900 m.a.s.l to 1400 m.a.s.l altitude range (INEC, 2011).

The model-based of ISO 9223:2012 (equations 3 and 9) presented higher values with respect to observations. This problem was already pointed out in some studies carried out in the tropical atmosphere (Correa-Bedoya et al., 2007; Corvo et al., 2008, Morcillo et al., 2012; Morcillo et al., 2013, Garita-Arce et al., 2014; Rios et al., 2017; Vera et al., 2017).

In figure 6, the shown maps complement each other. It is possible to apply both the RH- and the TOW-based models (Fig. 6a or 6b, respectively) in the central region of the WCV (from 900 m.a.s.l to 1400 m.a.s.l.) and the ISO 9223:2012 model (Fig. 6c) overestimated the corrosion in all altitudes.

4. Conclusions

Simple models based on RH, TOW, and the ISO standard were used to determine Vcorr in the WCV. The measurements indicated intermediate (C2) levels of Vcorr in the region, with values ranging from 16.6 to 17.4 μm y^{-1}. Almost all the proposed models presented a level of Vcorr within the C2 category.

The linear equations dependent on atmospheric parameters only (equations 1 and 2) always overestimated the value of Vcorr with differences between 10 % and 70 %. Conversely, the altitude-dependent models (equations 7 and 8), presented a more realistic estimation, between 1000 m.a.s.l and 1400 m.a.s.l.

The equation of the ISO 9223:2012 standard (equation 3) and its simplified form based on the altitude (equation 9) showed an exponential behavior governed by the increase of RH with altitude.

The results demonstrated that linear equations with regular parameters, such as RH, are more practical for determining Vcorr at low altitudes in the WCV, specifically in the range of 1000 m.a.s.l to 1400 m.a.s.l., where most of the population of the WCV lives. Vcorr calculations out of this range showed larger discrepancies with respect to observations (more than 10 %).

The ISO model overestimated the Vcorr values in the WCV for all altitudes. In some cases, the differences were greater than 20 %.

The WCV is not a climatically uniform region, as it shows significant spatial and temporal variations. This variability suggests the need for more assessments considering these factors, given the dependency of corrosion with RH. Future analyses should encompass mountain profiles, climatic sub-regions, and climatic periods (for example, dry and rainy seasons).

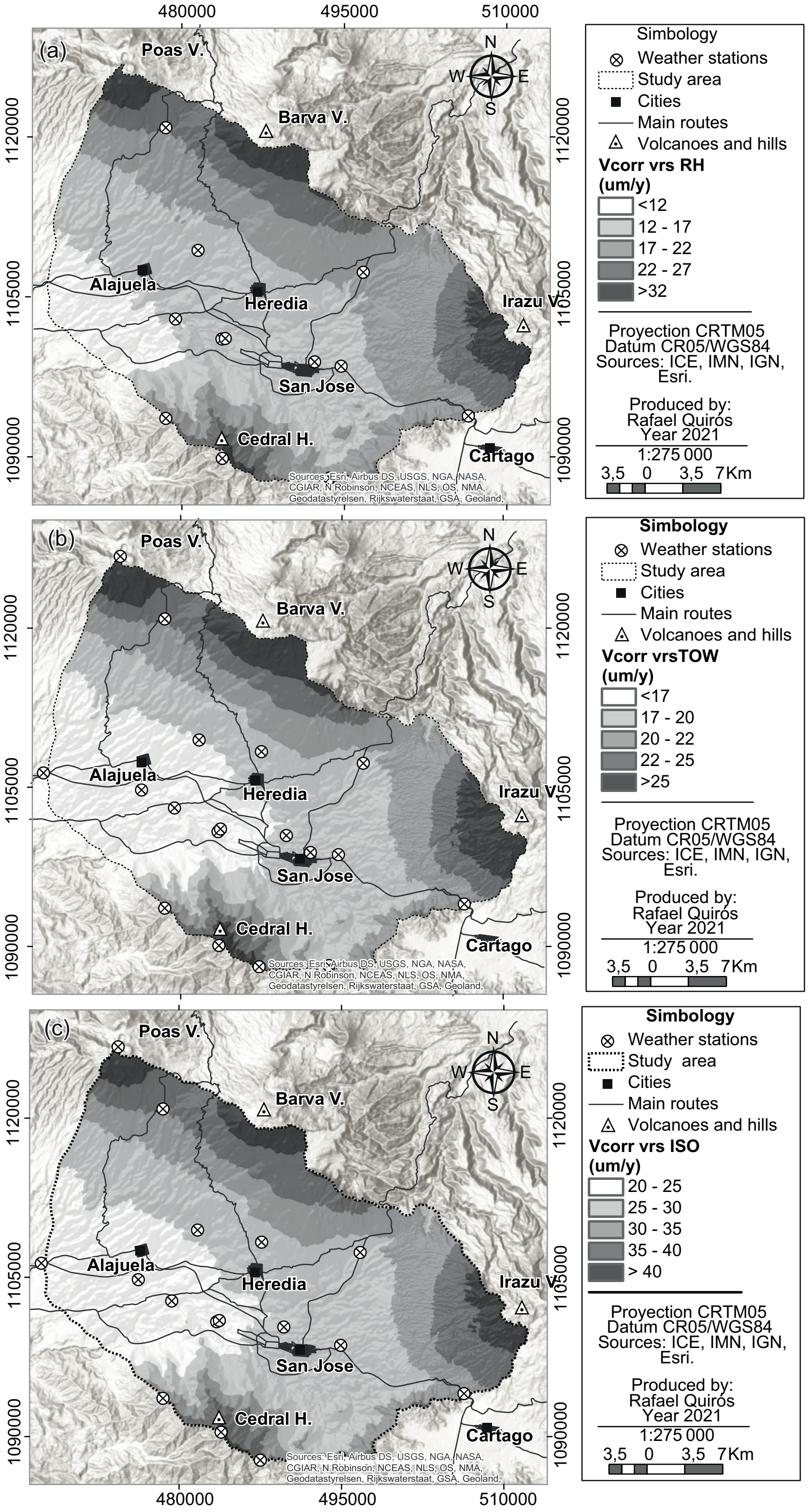

Fig. 6. Map of Vcorr using the a) RH, b) TOW, and c) ISO models.

Acknowledgments

Special thanks to the National Meteorological Institute and the Costa Rican Electricity Institute for providing the meteorological data of the Western Central Valley. The actual corrosion data was obtained from measuring sites located at facilities of the National Power and Light Company and the Ministry of Security. This study was funded by the National Council of University Presidents (CONARE) of Costa Rica as part of a collaborative project among the State Distance University (UNED-VINVES-6-10-50), the University of Costa (UCR-VI-805-B8-650), the National High Technology Center (CeNAT-VI-269-2017), the National University (UNA- SIA: 0600-17), and the Costa Rica Institute of Technology (ITCR-VIE 1490-021).

Rodríguez-Yáñez acknowledges the support of the Innovation and Human Capital for Competitiveness Program (PINN) of the Ministry of Science, Technology, and Telecommunications (MICITT) of Costa Rica.

References

Abdalah-Hernández M, Rodríguez-Yáñez J, Alvarado-González D. 2020. Gaussian mixture analysis of basic meteorological parameters: Temperature and relative humidity. Tecnología en Marcha 33:5-12. https://doi.org/10.18845/tm.v33i5.5068

Alcántara J, Chico B, de la Fuente D, Morcillo M. 2015. Airborne chloride deposit and its effect on marine atmospheric corrosion of mild steel. Corrosion Science 97:74-88. https://doi.org/10.1016/j.corsci.2015.04.015

Amador J. 2008. The Intra-Americas Sea low-level jet. Annals of the New York Academy of Sciences 1146 (1):153-188. https://doi.org/10.1196/annals.1446.012

ASTM International. 2017. ASTM G1-03(2017)e1 Standard Practice for Preparing, Cleaning, and Evaluating Corrosion Test Specimens. American Society for Testing and Materials International. West Conshohocken, PA, USA. https://doi.org/10.1520/G0001-03R17E01 (accessed 2018 June 20)

ASTM International. 2019. ASTM A36 / A36M-19 Standard Specification for Carbon Structural Steel. American Society for Testing and Materials International. West Conshohocken, PA, USA. https:// doi.org/10.1520/A0036_A0036M-19 (accessed 2018 June 20)

Barrantes J, Liao A, Rosales A. 1985. Atlas climatológico de Costa Rica. San José, Costa Rica: Instituto Meteorológico Nacional. Available at https://www.imn.ac.cr/atlas-climatologico (accessed 2019 Jun 12)

Caetano E, Iniestra R. 2008. Identificación de cuencas atmosféricas en México. Instituto de Ecología y Cambio Climático de México. Available at https://docplayer.es/58286477-Identificacion-de-cuencas-atmosfericas-en-mexico.html (accessed 2018 April 15)

Campos M, Castro V. 1992. El clima a sotavento de las montañas de Costa Rica. Tópicos Meteorológicos y Oceanográficos 2:1-21. Available at: https://hdl.handle.net/10669/551 (accessed 2021 March 3)

Corvo F, Pérez T, Martín Y, Reyes J, Dzib L, González-Sánchez J and Castañeda A. 2008. Time of wetness in tropical climate: Considerations on the estimation of TOW according to ISO 9223 standard. Corrosion Science 50:206-219. https://doi.org/10.1016/j.corsci.2007.06.012

Correa-Bedoya E, Botero-Vega C, Restrepo AH, Delgado J, Castaño JG, Echevarria F. 2007. Corrosión del acero al carbono, acero galvanizado y aluminio en diferentes atmósferas colombianas, Scientia et Technica, 13(36): 7-12.

Díaz I, Cano H, Lopesino P, de la Fuente D, Chico B, Jiménez J, Medina SF, Morcillo M. 2018. Five-year atmospheric corrosion of Cu, Cr and Ni weathering steels in a wide range of environments. Corrosion Science 141:146-157. https://doi.org/10.1016/j.corsci.2018.06.039

Feliu S, Morcillo M, Feliu S. 1993. The prediction of atmospheric corrosion from meteorological and pollution parameters. I. Annual corrosion. Corrosion Science 34:403-4014. https://doi.org/10.1016/0010-938X(93)90112-T

Fernández W, Campos M, Amador JA. 2003. Second progress report of the AIACC LA06 project: Assessment of impacts and ad¬aptation measures for the water resources sector due to extreme events under climate change conditions in Central America. AIACC. Available at https://sedac.ciesin.columbia.edu/aiacc/progress/LA06_July03.pdf (accessed 2019 June 11)

García-Reynoso JA, Ruiz-Suárez LG, García-Escalante JS, Reséndiz-Juárez NA. 2009. Comportamiento de los contaminantes en cuencas atmosféricas: Metodología y estudio de caso (INE/A1-004/2009), Mexico: INE.

Garita-Arce L, Rodríguez-Yáñez J, Robles-Cordero J. 2014. Modelado de la velocidad de corrosión de acero de baja aleación en Costa Rica. Revista Ingeniería 24:79-90. https://doi.org/10.15517/RING.V24I2.14624

Herrera-Murillo J, Rodríguez S, Rojas-Marín J, Báez A. 2012. Relations between bulk precipitation, PM10 composition and meteorological conditions in the metropolitan area of Costa Rica. The Open Journal of Atmospheric Sciences 6:19-32. https://doi.org/10.2174/1874282301206010019

Herrera J, Rojas JF, Beita VH, Chaves M. 2014. Composición química de muestras de depositación total colectadas en el área metropolitana de Costa Rica en 2012. Ciencias Ambientales 48:30-38. https://doi.org/10.15359/rca.48-2.3

IMN. 2008. Clima, variabilidad y cambio climático en Costa Rica. San José, Costa Rica: Comité Regional de Recursos Hidráulicos. Available at http://cglobal.imn.ac.cr/documentos/publicaciones/CambioClimatico/climaVariabilidadCambioClimaticoCR.pdf (accessed 2019 April 17)

INEC. 2011. Anuario estadístico 2010. San José, Costa Rica: Instituto Nacional de Estadística y Censos, Ministerio de Hacienda. Available at https://www.inec.cr/sites/default/files/documentos/anuario_estadistico/publicaciones/reanuarioestad2010-02.pdf (accessed 2019 May 27)

ISO. 1992. Corrosion of metals and alloys - Corrosivity of atmospheres - Classification (ISO 9223:1992). ISO. Available at https://www.iso.org/standard/16855.html (accessed 2018 June 20)

ISO. 2012a. Corrosion of metals and alloys - Corrosivity of atmospheres - Classification, determination and estimation (ISO 9223:2012). ISO. Available at https://www.iso.org/standard/53499.html (accessed 2018 June 20)

ISO. 2012b. Corrosion of metals and alloys – Corrosivity of atmospheres – Measurement of pollution (ISO 9225:2012). ISO. Available at https://www.iso.org/standard/53501.html (accessed 2018 June 20)

Magaña V, Amador JA, Medina S. 1999. The midsummer drought over Mexico and Central America. Journal of Climate 12 (6):1577-1588. https://doi.org/10.1175/1520-0442(1999)012<1577:TMDOMA>2.0.CO;2

Morcillo M, Almeida E, Rosales B, Uruchurtu J, Marrocos M. 1998. Corrosión y protección de metales en las atmósferas de Iberoamérica. Parte I: Mapas iberoamericanos de corrosión atmosférica (MICAT). Madrid, Spain: CYTED.

Morcillo M, De la Fuente D, Díaz I, Cano H. 2011. Atmospheric corrosion of mild steel. A review. Revista Metalurgia 47: 426–444. http://doi.org/10.3989/revmetalm.1125

Morcillo M, Chico B, de la Fuente D, and Simancas J. 2012. Looking back on contributions in the field of atmospheric corrosion offered by the MICAT Ibero-American testing network. International Journal of Corrosion 2012:1-24. https://doi.org/10.1155/2012/824365

Morcillo M, Chico B, Díaz I, Cano H, de la Fuente D. 2013. Atmospheric corrosion data of weathering steels. A review. Corrosion Science 77:6-24. https://doi.org/10.1016/j.corsci.2013.08.021

Morcillo M. 2017. Fundamental and research frontier of atmospheric corrosion. Materials, Madrid, Spain. https://doi.org/10.3390/books978-3-03842-642-4

Muñoz AC, Fernández W, Gutiérrez JA, Zárate E. 2002. Variación estacional del viento en Costa Rica y su relación con los regímenes de lluvia. Tópicos meteorológicos y oceanográficos 9: 1-13.

Murphy GM, Hurtado, RH. 2013. Agrometeorología. Buenos Aires, Argentina: Editorial Facultad de Agronomía, Universidad de Buenos Aires. 57-70.

NOAA. 2019. Cold and warm episodes by season. National Weather Service of the United States. Available at: http://origin.cpc.ncep.noaa.gov/products/analysis_monitoring/ensostuff/ONI_v5.php (accessed 2019 October 27)

Ortiz-Malavasi E. 2015. Atlas digital de Costa Rica 2014. Instituto Tecnológico de Costa Rica. Cartago, Cartago, Costa Rica. Available at http://hdl.handle.net/2238/7477 (accessed 2019 July 25)

OVSICORI. 2015. Estado de los volcanes. Observatorio Vulcanológico y Sismológico de Costa Rica. Available at http://www.ovsicori.una.ac.cr/index.php/extension/estado-de-los-volcanes (accessed 2019 October 21)

Ríos-Rojas JF, Aperador-Rodríguez D, Hernández-García EA, Arroyave-Posada CE. 2017. Annual atmospheric corrosion rate and dose-response function for carbon steel in Bogotá. Atmósfera 30:53-61. https://doi.org/10.20937/atm.2017.30.01.05

Roberge PR, Klassen RD, Haberecht PW. 2002. Atmospheric corrosivity modeling-A review. Materials and Design 23:321-330. https://doi.org/10.1016/S0261-3069(01)00051-6

Robles J. 2013. Evaluation of atmospheric corrosion in three geographic areas of Costa Rica by electrochemical and gravimetric techniques. Bachelor thesis, Universidad Nacional de Costa Rica.

Rodríguez-Yáñez JE, Garita-Arce L, Saborío-Leiva E. 2015. Mapas estimativos de la corrosión atmosférica de acero de baja aleación en Costa Rica. Cuadernos de Investigación 7:181-191. https://doi.org/10.22458/urj.v7i2.1144

SEMARNAT-INECC. 2016. Diagnóstico sobre la calidad del aire en cuencas atmosféricas de México. Instituto de Ecología y Cambio Climático de México. Mexico City, Mexico. Available at: http://biblioteca.semarnat.gob.mx/janium/Documentos/Ciga/Libros2013/CD002516.pdf (accessed 2019 January 17)

Sendiña-Nadal I, Pérez-Muñuzuri, V. 2006. Fundamentos de meteorología. Galicia, Spain: Universidad Santiago de Compostela.

Solano J., Villalobos R. (2000). Regiones y subregiones climáticas de Costa Rica. Instituto Meteorológico Nacional de Costa Rica. Available at: https://www.imn.ac.cr/documents/10179/20909/Regionalizaci%C3%B3n+clim%C3%A1tica+de+Costa+Rica (accessed 2018 January 17)

Vera R, Troconi de Rincón O, Bagnara M, Romero N, Araya R, Ossandón S. 2017. Tropical/non-tropical marine environments impact on the behaviour of carbon steel and galvanised steel. Materials corrosion 69:614-625. https://doi.org/10.1002/maco.201709873

Wilks DS. 2011. Statistical Methods in the Atmospheric Sciences. United States: Academic Press.

Zárate E. 1978. Comportamiento del viento en Costa Rica. Nota técnica de investigación Nº 2. Instituto Meteorológico Nacional de Costa Rica.

Zárate E. 1980. El viento en San José. Instituto Meteorológico Nacional de Costa Rica.